IPP-Report

Alexander von Müller

Towards a plasma-facing component design with melt infiltrated tungsten-copper composite heat sink materials

IPP 2020-02
Mai 2020

Technische Universität München
Fakultät für Maschinenwesen

Towards a plasma-facing component design with melt infiltrated tungsten-copper composite heat sink materials

Dipl.-Ing. Alexander von Müller, M.Sc.

Vollständiger Abdruck der von der Fakultät für Maschinenwesen der Technischen Universität München zur Erlangung des akademischen Grades eines

Doktor-Ingenieurs (Dr.-Ing.)

genehmigten Dissertation.

Vorsitzender:	Prof. Dr.-Ing. Oskar J. Haidn
Prüfer der Dissertation:	1. Prof. Dr. rer. nat. Rudolf Neu
	2. Prof. Dr.-Ing. Christoph Broeckmann

Die Dissertation wurde am 13.08.2019 bei der Technischen Universität München eingereicht und durch die Fakultät für Maschinenwesen am 06.11.2019 angenommen.

"We say that we will put the sun into a box. The idea is pretty. The problem is, we don't know how to make the box."

Pierre-Gilles de Gennes

Abstract

The exhaust of power and particles is currently considered as one of the ultimate challenges in view of the design of a future magnetic confinement thermonuclear demonstration fusion reactor (DEMO). One predominantly challenging aspect in this regard is the design and manufacture of divertor target plasma-facing components (PFCs) that have to sustain intense particle, heat and neutron fluxes during fusion operation. Current state-of-the-art water-cooled divertor target PFC designs make use of tungsten (W) as a plasma-facing material while copper (Cu) alloys are regarded as most appropriate candidate materials for the heat sink of such highly loaded PFCs. However, issues arise when such a design is applied to a DEMO environment. In this context, it has been underlined that the use of Cu alloys as structural heat sink materials in PFCs implies design engineering risks mainly due to the behaviour of these materials under neutron irradiation characterised by a pronounced loss of ductility at lower and a loss of strength at elevated operating temperatures.

Against this background, development work regarding tungsten-copper (W-Cu) composites as potentially advanced heat sink materials for highly loaded PFCs is discussed within the present work. In this context, different types of W-Cu composite materials were investigated: W particle-reinforced Cu composites, W fibre-reinforced Cu composites as well as W-Cu composites based on additively manufactured W preforms. The common feature of these materials is that they are all fabricated according to the same manufacturing approach, i.e. liquid Cu melt infiltration of open porous W preforms. In principle, W-Cu composite materials can combine a high conductivity due to the Cu matrix with good high-temperature strength properties due to reinforcing W inclusions within the material. Furthermore, the macroscopic properties of such materials can be tailored through adjusting the composite microstructure which can for example be exploited by adjusting the coefficient of thermal expansion (CTE) in order to minimise thermally induced stresses due a CTE mismatch within a component. The investigated composites were characterised and examined regarding their applicability as heat sink materials in highly loaded PFC designs. Overall, it has been found that the investigations reported on within the present work, including high-heat-flux (HHF) tests on PFC mock-ups, imply that W-Cu composites can be regarded a viable class of potentially advanced HHF materials for heat sink applications in highly loaded PFCs.

Acknowledgements

The present work could only come about because I had the possibility to cooperate fruitfully with and to count on the continuous support by numerous people.
Firstly, I have to express my profound gratitude to Prof. Dr. Rudolf Neu who during the past years was not only a very good academic supervisor with respect to the present work but also a very dependable and competent advisor in general regarding many scientific and technical aspects I encountered within the course of my research. I could count on his professional opinion anytime.
Furthermore, I want to thank Prof. Dr. Jeong-Ha You who gave me the possibility to work on the topic of tungsten-copper composites and who allowed me to be deeply involved in the EUROfusion DEMO divertor developments.
Moreover, I appreciated the day-to-day cooperation with many colleagues at IPP Garching in an excellent working atmosphere. Especially, I would like to thank: Mrs Gabriele Matern, Mrs Katja Hunger, Mr Stefan Elgeti and Dr. Martin Balden for support with metallography, material analyses and microscopy; Mr Henri Greuner and Mr Bernd Böswirth for support with high-heat-flux tests within the GLADIS facility; as well as Till Höschen, Dr. Johann Riesch and Dr. Hans Maier for regular technical and scientific support and discussions.
Apart from that, I enjoyed to be involved in the EUROfusion high-heat-flux materials and divertor projects that allowed me to cooperate with different institutions outside of IPP. In this context, I have to thank especially: Dr. Eliseo Visca from the Special Technologies Laboratory at ENEA Frascati Research Centre; Dr. Udo Siefken from Louis Renner GmbH; Mrs Dagmar Ewert from Deutsche Institute für Textil- und Faserforschung Denkendorf; as well as Dr. Georg Schlick from Fraunhofer-Einrichtung für Gießerei-, Composite- und Verarbeitungstechnik IGCV.
Moreover, I would like to thank several diligent students that I could supervise and that contributed to the research carried out within the course of the present work. In this regard, I would like to thank especially Mrs Marine Ilg, Mr Monty Mutschler and Mr Bailey Curzadd.
Furthermore, I would like to thank Prof. Dr. Christoph Broeckmann from the Lehrstuhl und Institut für Werkstoffanwendungen im Maschinenbau at Rheinisch-Westfälische Technische Hochschule Aachen for being the second examiner of the present work.
Finally, I would like to thank my wife and my son for being a bedrock in my life. Starting out from this basis, I could during the past years consistently follow my research work.

Contents

List of Figures

List of Tables

Abbreviations

3D	three-**d**imensional
2D	two-**d**imensional
AM	**a**dditive **m**anufacturing
ASDEX	**A**xially **S**ymmetric **D**ivertor **E**xperiment
bcc	**b**ody-**c**entred **c**ubic
BN	**b**oron **n**itride
CHF	**c**ritical **h**eat **f**lux
CTE	**c**oefficient of **t**hermal **e**xpansion
DBTT	**d**uctile-to-**b**rittle **t**ransition **t**emperature
DEMO	**DEMO**nstration fusion reactor
dpa	**d**isplacements **p**er **a**tom
DRA	**d**iscontinuously **r**einforced **a**luminium
EDM	**e**lectrical **d**ischarge **m**achining
EDX	**e**nergy **d**ispersive **X**-ray spectroscopy
ELM	**e**dge **l**ocalised **m**ode
EU	**E**uropean **U**nion
FE	**f**inite **e**lement
FEA	**f**inite **e**lement **a**nalysis
FIB	**f**ocused **i**on **b**eam
FPP	**f**usion **p**ower **p**lant
fpy	**f**ull **p**ower **y**ear
GLADIS	**G**arching **L**arge **D**ivertor **S**ample **T**est **F**acility
HHF	**h**igh-**h**eat-**f**lux
HIP	**h**ot **i**sostatic **p**ressing
HSM	**h**eat **s**ink **m**aterial

HV	**h**igh-**v**acuum
HV	**V**ickers **h**ardness
ICP-OES	**i**nductively **c**oupled **p**lasma with **o**ptical **e**mission **s**pectroscopy
IEA	**I**nternational **E**nergy **A**gency
IR	**i**nfra**r**ed
JET	**J**oint **E**uropean **T**orus
LFA	**l**aser **f**lash **a**nalysis
LPBF	**l**aser **p**owder **b**ed **f**usion
MFH	**m**ean-**f**ield **h**omogenisation
MMA	**m**ethod of **m**oving **a**symptotes
MMC	**m**etal **m**atrix **c**omposite
Mtoe	**m**illion **t**onnes of **o**il **e**quivalent
NASA	**N**ational **A**eronautics and **S**pace **A**dministration
NDT	**n**on-**d**estructive **t**esting
NS	**n**on-**s**ag
RT	**r**oom **t**emperature
RVE	**r**epresentative **v**olume **e**lement
PVD	**p**hysical **v**apour **d**eposition
PFC	**p**lasma-**f**acing **c**omponent
PFM	**p**lasma-**f**acing **m**aterial
SAA	**s**olution **a**nnealed and **a**ged
SEM	**s**canning **e**lectron **m**icroscopy
SiC$_f$-Ti	**si**licon **c**arbide **f**ibre-reinforced **ti**tanium
SOL	**s**crape-**o**ff **l**ayer
SSME	**s**pace **s**huttle **m**ain **e**ngine
UD	**u**ni**d**irectional
UTS	**u**ltimate **t**ensile **s**trength
VRE	**v**ariable **r**enewable **e**nergy
W7-X	**W**endelstein **7-X**
WEO	**W**orld **E**nergy **O**utlook
W$_{AM}$-Cu	**W-Cu** composite based on **a**dditively **m**anufactured W
W$_f$-Cu	**W** **f**ibre-reinforced **Cu**
W$_p$-Cu	**W** **p**article-reinforced **Cu**

Symbols

Latin	**meaning**
B	magnetic field
c_p	specific heat capacity
d	diameter
C_{ij}	effective stiffness tensor
E	Young's modulus
E_ρ	energy density
f	fibre volume fraction/frequency
f_{ij}, f_{ij0}	angular function
F	force
g	gravitational acceleration
I	current
k_B	Boltzmann constant
K_L	stress intensity factor
l	length
L	length
m	mass
M	average ion mass/bending moment
n	particle density/integer number
p	pressure
P	power
q	heat flux
Q	fusion power gain
Q_N	nominal heat load
r	radius

R	radius
$R_{p,0.2}$	0.2% yield strength
s	scan line spacing
S_{ij}	effective compliance tensor
t	thickness
T	temperature
T_0	reference temperature
v	flow velocity/scanning speed
V	volume
x	spatial coordinate

Greek	**meaning**
α	thermal diffusivity/coefficient of thermal expansion
ϵ	energy/inverse aspect ratio/strain
κ	plasma elongation
λ	thermal conductivity
λ_q	scrape-off layer power fall-off length
ν	Poisson's ratio
ρ	mass density
σ	stress
σ_0	constant stress term
$\langle \sigma v \rangle$	nuclear fusion reaction cross section
τ	characteristic time
ω	stress exponent/angular velocity

Sub-/Superscripts	**meaning**
c	composite/centrifugal
cool	cooling channel
D	deuterium
DT	deuterium-tritium
el	element
E	energy
f	fibre/fracture
g	gravitational

geo	geometrical
in	inlet
m	matrix
max	maximum
nom	nominal
$surf$	surface
th	thermal
T	tritium
TC	thermocouple
v	von Mises

Chapter 1

Introduction

1.1 Energy supply - current global situation

Our present civilised societies fundamentally rely on a secure and perpetual supply of energy that powers our industries, transportation and modern way of life with all its achievements.

According to the *World Energy Outlook* (WEO) 2015 [1], published by the *International Energy Agency* (IEA), the world-wide primary energy demand has increased by 55% between 1990 and 2013. Furthermore, the IEA predicts within their WEO 2015 that the world-wide primary energy demand can increase by up to 45% until the year 2040 within the so-called *Current Policies Scenario* as is illustrated in Figure 1.1a. The primary world-wide energy demand by fuel according to the central *New Policies Scenario* from the same study is shown in Figure 1.1b. It is predicted to grow for all fuels until the year 2040, including non-renewable fossil fuels like natural gas, oil and coal which still represent the dominating share of the world's energy demand at that time. Currently, the world-wide *Reserves-to-Production Ratios* for these fuels are predicted to be 52.6,

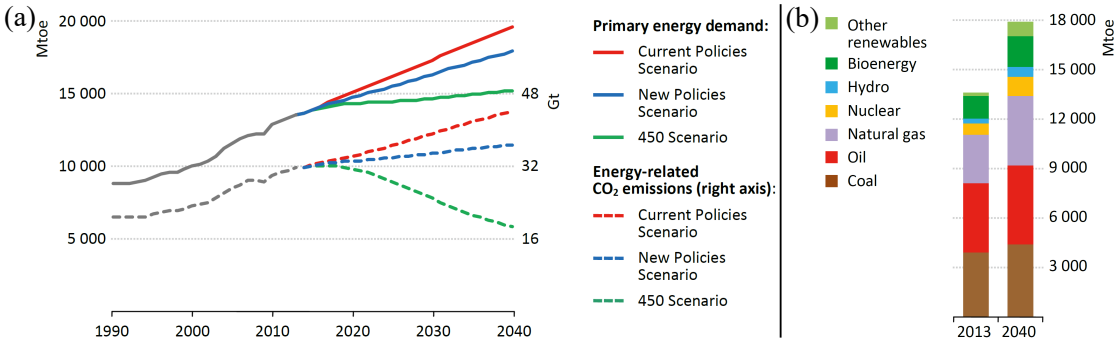

FIGURE 1.1: (a) World-wide primary energy demand in million tonnes of oil equivalent (Mtoe) with related CO_2 emissions for different scenarios and (b) world-wide primary energy demand by fuel in the *New Policies Scenario* according to the IEA WEO 2015 [1].

50.2 and 134 years, respectively [2]. Apart from that, the IEA states within the WEO 2015 that global electricity demand is expected to increase by more than 70% from 2013 to 2040 within the central *New Policies Scenario* though it is estimated that 550 million people still live without access to electricity at that time. This means that electricity demand is expected to exhibit the fastest growth among final energy sources raising its share to 24% until 2040.

The abovementioned figures illustrate that a fairly urgent and important question that humankind has to answer in time is: How can this substantial global energy demand in the future be satisfied in a sustainable and environmentally responsible way?

Many hopes are nowadays centred on renewable energy sources as alternative to technologies that rely on non-renewable fossil fuels. However, the drawbacks of these technologies are still not resolved, especially for *variable renewable energies* (VREs) like wind power and solar photovoltaics. That is the reason why the IEA mentions within their WEO 2016 [3] that if energy storage and demand-side response actions are not deployed within their decarbonisation scenario curtailment of VRE supply would start in the late 2020s in the *European Union* (EU).

Against the background of these upcoming challenges with respect to the global energy supply there could be a further option for the future energy system of mankind: The use of controlled nuclear fusion reactions as dispatchable energy source. The realisation of a technology that makes use of such energy releasing reactions has been the dream of researchers since many decades but has proven to be exceptionally challenging as will be described in more detail in the following sections.

1.2 Nuclear fusion

In nuclear physics, a commonly used quantity is the *binding energy per nucleon*. In Figure 1.2, this quantity is illustrated for stable and long-lived nuclei [4]. It shows a maximum of around 8.7 MeV at a mass number of approximately 56 which corresponds to iron (Fe). Towards heavier nuclei, the binding energy decreases slightly while towards very light nuclei there is also a decrease which is however much more pronounced. This steep decrease implies that a comparably large amount of energy can be released when two light atomic nuclei combine to a more stable heavier one. Such a combination process is called *nuclear fusion* while the energy released within such a reaction is due to the difference in the binding energies between the initial and final states. In order that nuclear fusion reactions can occur, the mutual *Coulomb repulsion* of the involved nuclei has to be overcome so that the short range attractive *nuclear force*[1] can become

[1] Nuclear forces are effective on short ranges on the order of 10^{-15} m and are stronger by a factor of 10^{36} compared to gravitational forces [5].

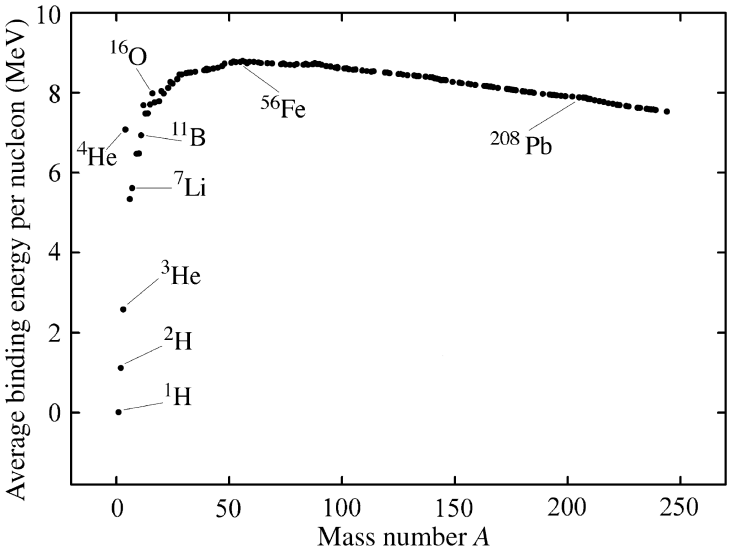

FIGURE 1.2: Binding energy per nucleon versus atomic mass number for stable and long-lived nuclei [4].

effective [5]. Hence, nuclei that are involved in nuclear fusion reactions need to exhibit sufficient energy in order to come into close contact with each other so that they can penetrate their mutual Coulomb barrier. This can be accomplished either by accelerating and bombarding them onto appropriate target nuclei or by raising them to very high temperatures so that they acquire such high energies that when they collide a portion of them fuses under energy release. To achieve the latter - which is also known as *thermonuclear fusion* - temperatures on the order of 10^8 K are needed [6][2].

Nuclear fusion is also the process that powers the Sun in our solar system as well as countless other stars within our universe. It is hence the ultimate energy source that made and still makes life on Earth possible. The primary nuclear fusion reaction that happens within the Sun is a *proton-proton* reaction [4]. However, this particular reaction is a rather slow process that is hence not considered useful for the realisation within a reactor on Earth.

Fortunately, more practicable alternatives, involving the hydrogen (H) isotopes *deuterium* (D) and *tritium* (T), with higher reaction rates exist. In this regard, the following nuclear reactions can for example be considered as relevant with respect to energy conversion through man-made nuclear fusion [7, 8]:

$$D + D \Rightarrow T + p + 4\ MeV \tag{1.1}$$

$$D + {}^3He \Rightarrow {}^4He + p + 18.3\ MeV \tag{1.2}$$

$$D + T \Rightarrow {}^4He + n + 17.6\ MeV \tag{1.3}$$

[2]By just considering the Coulomb repulsion, the temperatures expected for thermonuclear fusion reactions would be much higher. However, there are two circumstances that lead to the fact that thermonuclear fusion reactions take place at lower temperatures: They are on the one hand *Maxwell's Distribution of Colliding Particles* as well as on the other hand the *Tunneling of the Coulomb Barrier* [5].

The D-T reaction according to Equation 1.3 is favoured for use in earth-bound controlled nuclear fusion reactors because of the comparably large energy release of 17.6 MeV as well as the high nuclear fusion reaction *cross section*. In Figure 1.3, this quantity is illustrated for the abovementioned three nuclear fusion reactions [9] and it can be seen that the D-T reaction offers the largest cross section and hence the highest probability of fusion reactions, especially at lower particle energies. The nuclear reaction cross

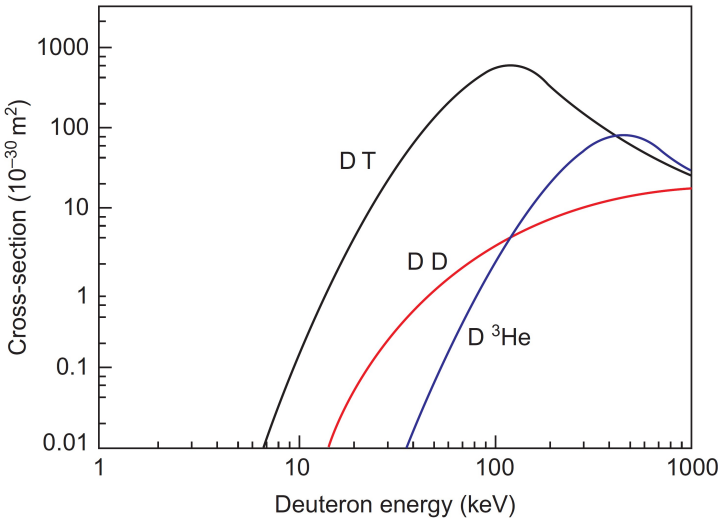

FIGURE 1.3: Nuclear reaction cross sections for D-D, D-T and D-^{3}He fusion reactions versus D ion energies [9]; it can be seen that at lower particle energies the reaction probability for the D-T reaction is orders of magnitude higher compared with the other two.

section is directly relevant for energy conversion within a nuclear fusion reactor as the corresponding overall energy release rate can be evaluated as

$$P_{DT} = \frac{\epsilon_{DT}}{4} \int n^2 \langle \sigma v \rangle_{DT} \, dV \tag{1.4}$$

where ϵ_{DT} is the energy released per fusion reaction, n is the particle density with $\frac{n}{2} = n_D = n_T$, $\langle \sigma v \rangle_{DT}$ is the D-T fusion reaction cross section and $\int dV$ is the integral over the reaction volume [10].

It has been mentioned that in order to realise thermonuclear fusion reactions the particles that are meant to undergo such reactions need to exhibit high energies, i.e. high temperatures on the order of 10^8 K. At such temperatures, the hydrogen isotopes to be fused are fully ionised[3] which means that the fusion fuel within a thermonuclear fusion reactor is not a neutral gas but is transformed into a *plasma*.

According to a textbook definition, the term plasma designates a gaseous mixture of charged particles, usually positive ions and electrons. Plasmas can be fully or partially ionised while their characteristic feature is that each plasma particle interacts with a

[3]Expressed in terms of mean kinetic energy $T = 10^8$ K correspond to $\frac{3}{2} k_B T \approx 13$ keV while the ionisation potential of hydrogen lies at only 13.6 eV [11].

comparatively large number of other particles within the plasma due to the *electrostatic interaction*. This interaction is effective on distances longer compared to the short range *van der Waals forces* that dominate the interactions in a neutral gas when the comprising particles collide[4]. That is the reason why plasmas exhibit a rather different behaviour compared to neutral gases [12].

To summarise, the abovementioned implies that thermonuclear fusion reactions can in principle be realised within a high-temperature plasma that contains fusion fuel in the form of hydrogen isotopes. The main difficulty of realising fusion reactions in such a way is the controlled containment of the energy stored within a high-temperature plasma. Several approaches have been devised during the past decades in order to adress this difficulty while the nowadays most promising approaches are based on plasma confinement by means of strong magnetic fields as will shortly be described within the following section.

1.3 Thermonuclear fusion through magnetic confinement

Plasmas can be confined by means of magnetic fields. In principle, charged particles can move freely within a uniform magnetic field in the direction parallel to the field. However, this does not hold true for the transverse direction as the *Lorentz force* compels the particles onto a circular orbit. The resulting motion of a plasma particle is hence a helical path along the direction of the magnetic field [9, 12]. This behaviour can be exploited in order to confine the charged particles of a plasma within a sufficiently strong magnetic field. The most promising approaches in this respect are ring-shaped toroidal devices as magnetic field lines around a torus do not exhibit open ends. In this context, two major concepts are nowadays being investigated in which precisely designed magnetic fields are used for the confinement of fusion plasmas. One of them is the confinement of a high-temperature plasma within a so-called *tokamak* device while this designation originates from the transliteration of a Russian acronym. The working principle of a tokamak is schematically illustrated in Figure 1.4 [9]. In principle, there are two main magnetic field components that are mostly important in such a device: The *toroidal field* which is produced by external coils enclosing the plasma as well as a *poloidal field* that is generated by means of an electric current that flows toroidally in the plasma itself and is induced by transformer action. The poloidal magnetic field must be superimposed on the toroidal magnetic field in order to compensate for particle drifts induced by the curvature of the toroidal magnetic field [13]. The two magnetic fields combine to form a field that twists helically around the torus. In a tokamak, the toroidal field that is

[4] Van der Waals forces decay with interparticle distance as r^{-6} while Coulomb forces decay according to r^{-2} [12].

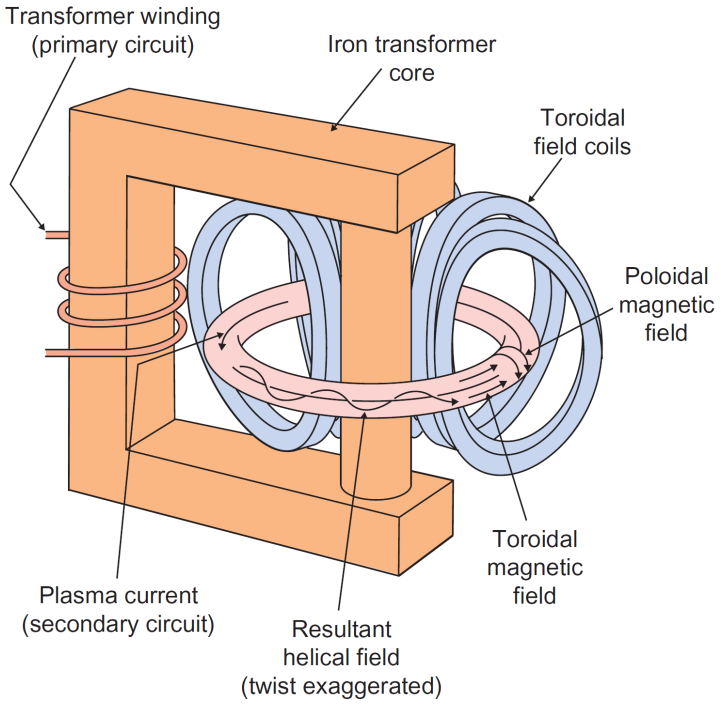

FIGURE 1.4: Schematic illustration of the working principle of a tokamak: The toroidal magnetic field is generated by external coils while the poloidal field component is generated by means of an induced current flowing in the plasma itself [9].

produced by the external coils is usually about 10 times stronger than the poloidal field that is generated by the plasma current [9].

Many experimental devices have been built according to the tokamak principle during the past decades and have demonstrated successful operation. In Figure 1.5a, the internal view of a tokamak experimental device, the *Joint European Torus* (JET), is illustrated [14]. In Figure 1.5b, a corresponding technical illustration of the device from the time of construction is shown [15]. Some main design parameters of the JET tokamak device

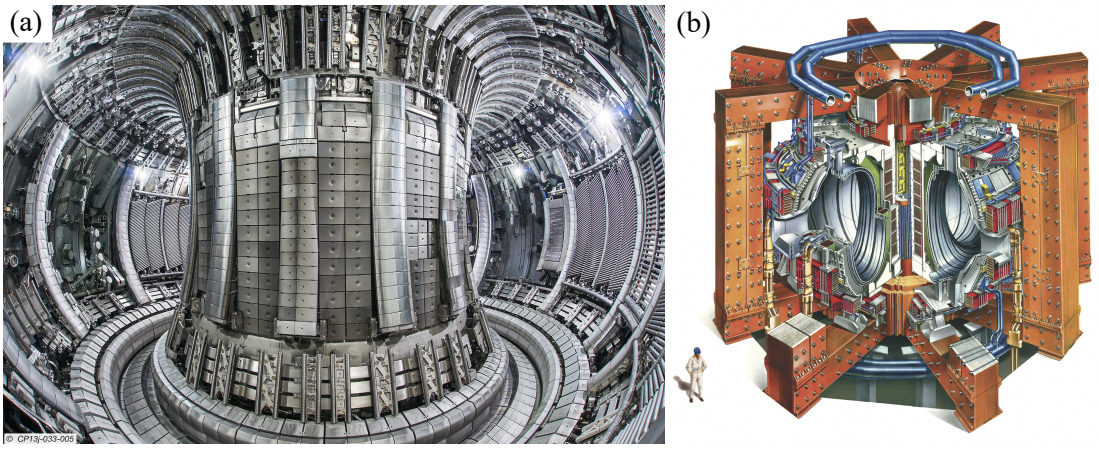

FIGURE 1.5: Tokamak experiment JET: (a) Internal view [14] as well as (b) technical illustration of the device from the time of construction [15].

are summarised in Table 1.1 [16].

TABLE 1.1: Main design parameters of the tokamak experiment JET [16].

Plasma major radius	2.96 m
Plasma minor radius (horizontal/vertical)	1.25 m/2.10 m
Toroidal magnetic field at plasma centre	3.45 T
Flattop pulse length	up to 20 s
Plasma current	up to 4.8 MA

A major achievement of the JET device was successful D-T operation with a resulting fusion power production of 16.1 MW in the late 1990s [17]. These experiments validated performance projections based on D-D tokamak operation as well as expected alpha particle plasma heating. Currently, the tokamak concept is the most extensively investigated magnetic confinement fusion device design.

Another toroidal device concept for the confinement of high-temperature plasmas is called *stellarator*. Unlike in a tokamak - where the magnetic confinement is generated with the help of currents flowing in the plasma itself - the magnetic field is generated entirely by means of external coils in a stellarator. In Figure 1.6, the basic device design of a classical stellarator is illustrated [9]. The stellarator concept offers advantages compared

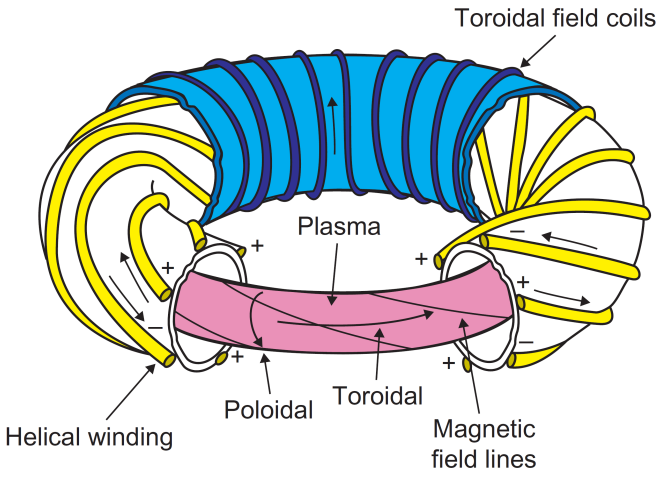

FIGURE 1.6: Schematic illustration of a stellarator device: There are outer windings that provide the toroidal magnetic field as well as inner helical windings that generate the poloidal magnetic field [9].

to the tokamak. There is no inherent limitation to the time of operation as there is no transformer action for the induction of a current within the plasma required. Hence, the stellarator concept is in principle capable of continuous operation. Furthermore, disruptive terminations of a plasma discharge - a troubling issue with tokamaks - do not seem to occur in stellarators [13]. However, the geometrical simplicity of axisymmetry is not given in a stellarator which makes it from the outset a significantly more complex device.

Currently, magnetic confinement fusion research on stellarators is pursued. An up-to-date stellarator device is *Wendelstein 7-X* (W7-X) which uses modular non-planar twisted toroidal field coils for the magnetic confinement. In Figure 1.7, this device is illustrated [18,19] while its main design parameters are summarised in Table 1.2 [20].

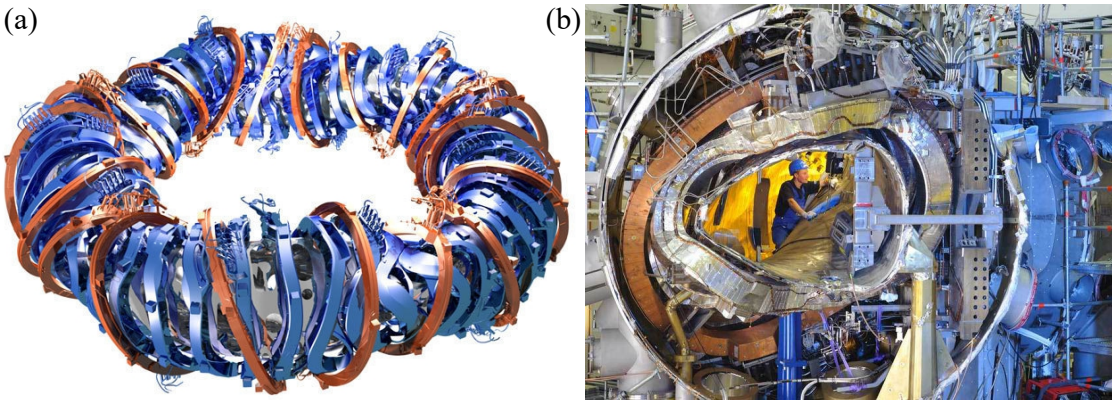

FIGURE 1.7: Stellarator experiment W7-X: (a) Technical illustration [18] and (b) picture taken during construction of the device [19].

TABLE 1.2: Main design parameters of the stellarator experiment W7-X [20].

Plasma major radius	5.5 m
Plasma minor radius (averaged)	0.55 m
Maximum magnetic field	up to 3 T
Pulse length	up to 30 min

The stellarator experiment W7-X has been put into operation during recent years [21] and early plasma discharges of W7-X have shown that its energy confinement is among the highest attained in world-wide stellarator devices [22].

1.4 Prospects of thermonuclear fusion as energy source

Within the sections above, the basic principles and concepts with respect to magnetic confinement thermonuclear fusion have been described briefly. In the following, the potential benefits and prospects that nuclear fusion power could provide are summarised:

- Per nuclear fusion reaction, energy on the order of a few MeV is released while a chemical reaction releases energy on the order of a few eV [5]. Hence, nuclear fusion power converts significantly more energy for a given amount of fuel than any fossil fuelled, combustion based energy source.

- Nuclear fusion reactors could provide uninterrupted and dispatchable high power density energy supply as e.g. required in urban areas with high population density. Within the WEO 2017 [23], the IEA predicts that the share of the global population living in cities and towns is increasing with a projected global urbanisation rate of 63% in 2040 having enormous implications for world-wide energy use.

- For D-T fusion, the basic fuels are readily extractable, not radioactive and available for long timescales:

  - *Deuterium* (D) is a stable isotope and occurs in natural compounds that comprise H, as e.g. water, with an average abundance of 0.015 mol% [8]. These resources are enormously plentiful and easy to access.

  - *Tritium* (T) does not occur in larger quantities naturally on Earth. However, T can be produced from lithium (Li) through neutron absorption in situ in a nuclear fusion reactor using the high-energy neutrons released from the D-T reaction (cf. Equation 1.3) [9]:

$$^{6}Li + n \Rightarrow {}^{4}He + T + 4.8\ MeV \tag{1.5}$$

$$^{7}Li + n \Rightarrow {}^{4}He + T + n - 2.5\ MeV \tag{1.6}$$

  According to the German *Federal Institute for Geosciences and Natural Resources*[5] Li is classified as a worldwide abundant metal [24].

- The nuclear end product of the D-T fusion reaction is ^{4}He (cf. Equation 1.3) which is a light and stable nucleus. The fuel cycle of nuclear fusion reactors does hence not create long-lasting radioactive waste which imposes a burden on future generations.

- Regarding emission of pollutants as well as greenhouse gases, nuclear fusion can be regarded as a technology with a low global environmental impact. In contrast to fossil fuelled, combustion based power sources the primary energy releasing reaction does not produce atmospheric pollutants, as e.g. nitrous oxides (NO_x), or greenhouse gases, as e.g. carbon dioxide (CO_2).

- Magnetic confinement nuclear fusion reactors exhibit inherent safety in the sense that any malfunction of the nuclear fusion reaction cools the plasma and stops the reaction.

- The density of the nuclear fusion fuel within the reaction chamber is rather low at around a few gram of fuel per 1000 m^3 [25] which is regarded as beneficial in terms of the safety characteristics of nuclear fusion reactors.

[5] The original German name reads *Bundesanstalt für Geowissenschaften und Rohstoffe*.

- T as part of the fusion fuel is radioactive but decays with a rather short half-life of 12.36 y [8]. Furthermore, T will only be produced and used enclosed within the reactor fuel cycle. This means that no transport of radioactive fuels is needed for a nuclear fusion power plant.

- The energetic neutrons produced during the D-T fusion reaction (cf. Equation 1.3) will interact with the materials the reactor is built from and induce radioactivity. However, careful choice of the materials placed around the fusion plasma can ensure that no long-term radioactive waste is produced which imposes a burden on future generations [9].

- In the far future, also other more favourable *aneutronic* nuclear fusion reactions could be realised in order to minimise neutron irradiation damage and activation within the reactor wall materials. A well-known example for such a nuclear reaction is [26]:

$$H + {}^{11}B \;\Rightarrow\; 3\ {}^{4}He + 8.7\ MeV \tag{1.7}$$

The appealing prospects mentioned above raise the question what the current status and outlook of thermonuclear magnetic confinement fusion research with respect to the development of power-producing reactors is. In Figure 1.8, the historical development of a decisively important quantity regarding that - the so-called *fusion triple product* - is illustrated [27]. The fusion triple product is a figure of merit with which the performance of magnetic confinement thermonuclear fusion experiments can be compared against each other. Within Figure 1.8, various past, current and future magnetic confinement thermonuclear fusion experiments are indicated. On the one hand, it can be seen that a significant performance improvement in terms of the fusion triple product has been achieved during the past decades. On the other hand, it can be seen that the fusion triple product is nowadays within striking distance to fusion power plant plasma conditions. In order that a fusion device reaches ignition with D-T fuel at a temperature of about 20 keV - meaning that the nuclear fusion reaction is self-sustained through alpha particle heating - a triple product of approximately

$$n_{DT}\, T_{ion}\, \tau_E > 6 \times 10^{21}\,\mathrm{m^{-3}\,keV\,s} \tag{1.8}$$

is required, with n_{DT} as the *plasma density*, T_{ion} as the *plasma ion temperature* and τ_E as the *energy confinement time* which characterises the rate of energy loss from a confined plasma [28].

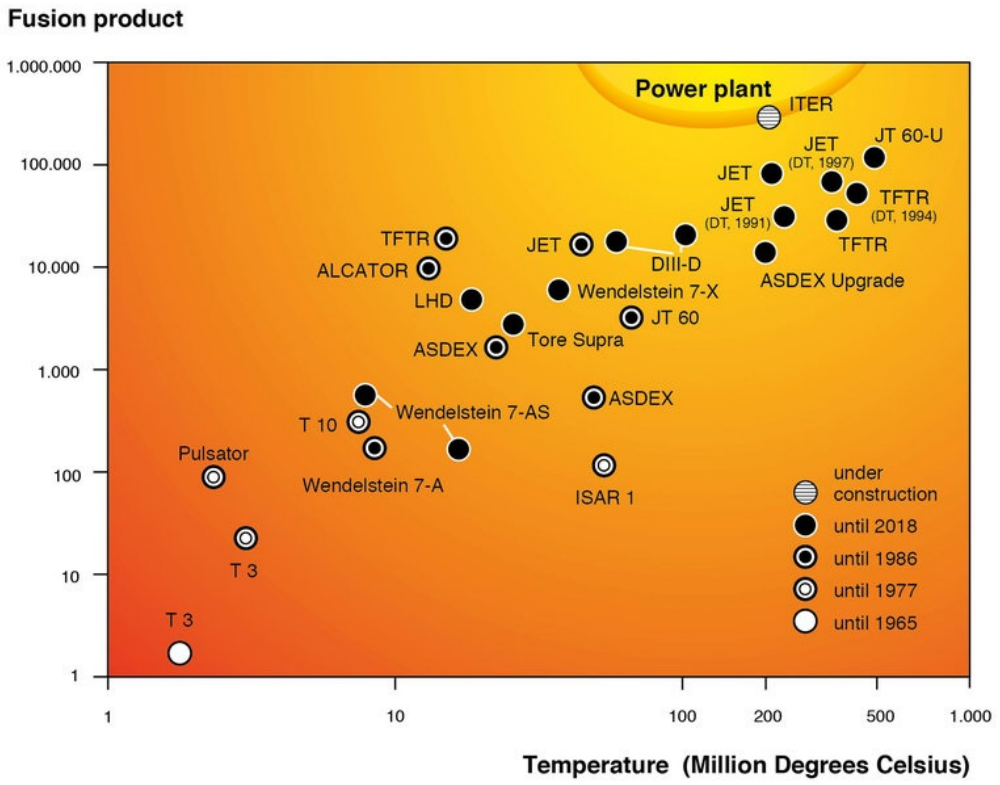

FIGURE 1.8: Fusion triple product [10^{17} particles per cubic centimetre $\times$ second $\times$ degree Celsius] for past, current and future magnetic confinement thermonuclear fusion experiments; the plot illustrates the performance improvements that have been achieved over the past decades [27].

In Figure 1.9, the latter quantity is illustrated. More precisely, the characteristic thermal global *H-mode*[6] energy confinement time versus an empirical power law scaling based on appropriate experimental data from world-wide existing tokamak experiments is illustrated [31]. The underlying scaling expression is

$$\tau_{E,th} = 0.0365\ I^{0.97} B^{0.08} P^{-0.63} n^{0.41} M^{0.20} R^{1.93} \epsilon^{0.23} \kappa^{0.67} \tag{1.9}$$

with the following variables: R $[m]$ is the major radius, I $[MA]$ is the plasma current, B $[T]$ is the toroidal magnetic field at major radius, P $[MW]$ is the loss power, n $[10^{19} m^{-3}]$ is the line average density, κ is the plasma elongation, ϵ is the inverse aspect ratio and M $[AMU]$ is the average ion mass[7]. Figure 1.9 illustrates the predictive capabilities of the power law scaling according to Equation 1.9 while also the prediction

[6] The *H-mode* is a magnetic confinement mode of toroidal plasmas that exhibits comparably high confinement characteristics [29,30]. Future magnetic confinement thermonuclear fusion devices are supposed to be operated in H-mode in order to realise a high fusion energy gain.

[7] For further details regarding the definition of all these quantities the reader is referred to [31].

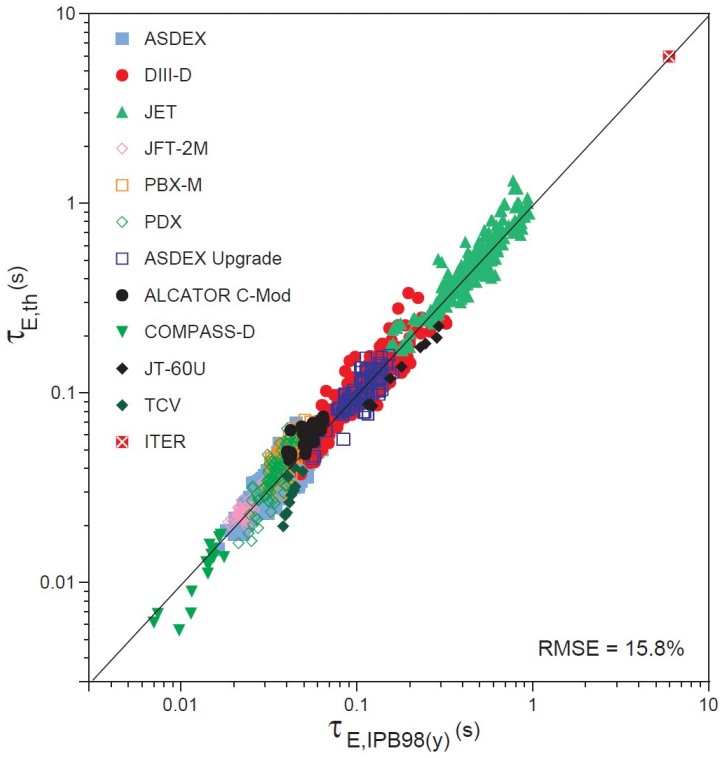

FIGURE 1.9: Comparison of H-mode thermal energy confinement time with the scaling expression according to Equation 1.9 based on appropriate data from a variety of different tokamak experiments; the good agreement between experimentally determined data and the scaling law can be seen while also a prediction for the next step magnetic confinement fusion device *ITER* is included [31].

for the next step magnetic confinement fusion device *ITER* with a characteristic confinement time of 6 s is included[8].

The scaling expression according to Equation 1.9 implies that the major radius of the tokamak device has a considerable influence on the energy confinement. This means that future devices with improved confinement need to be comparably large which in turn implies that the construction of such devices is expensive. Because of the highly complex nature of the physical processes that determine the heat and particle transport in thermonuclear plasmas it is not possible to provide a derivation of the dependence of energy confinement properties on plasma parameters from first principles. The energy confinement properties are hence described by means of empirical scalings, like Equation 1.9, based on appropriate experimental data. This approach represents the key tool for the extrapolation of plasma performance to future magnetic confinement fusion devices [31].

On the one hand, the abovementioned arguments indicate that thermonuclear fusion power has the potential to provide a sustainable, environmentally responsible and dispatchable high power density energy supply solution for the future of mankind. On the

[8] An energy confinement time of 6 s was predicted for ITER when [31] was issued in 1999. Later, however, this value has been corrected to 3.7 s [32].

other hand, the abovementioned points imply that magnetic confinement fusion research has made remarkable progress over the past decades so that a device that is capable of realising a net energy gain is within reach.

1.5 Outline of the present work

The present work deals with material developments regarding highly loaded *plasma-facing components* (PFCs) for future magnetic confinement thermonuclear fusion reactors. In this context, the work focuses on the investigation of *tungsten-copper* (W-Cu) composite materials as potentially advanced PFC *heat sink materials* (HSMs). In the following chapters, different types of such W-Cu composites will hence be discussed while their common feature is that they are all fabricated according to the same manufacturing approach, i.e. liquid copper (Cu) melt infiltration of open porous tungsten (W) preforms. In the subsequent Chapter 2, the environment and boundary conditions for highly loaded PFCs in future magnetic confinement thermonuclear fusion reactors are first discussed. Furthermore, the current state-of-the-art design solution for highly loaded PFCs is described as well as the potential risks that are implied when such a technology is directly applied to PFCs in future D-T fusion reactors. In Chapter 3, the material scientific background relevant with respect to the present work is described while also the specific interest in the W-Cu composite material system is discussed. In Chapter 4, work performed regarding *W particle-reinforced Cu* (W_p-Cu) composites is described. This includes discussion of the material manufacturing and characterisation as well the application of these materials to PFC mock-ups that were tested under relevant *high-heat-flux* (HHF) loadings. In Chapter 5, work performed regarding *W fibre-reinforced Cu* (W_f-Cu) composites is described. Again, the material manufacturing and characterisation as well as the application of these materials to PFC mock-ups that were HHF tested is discussed. In Chapter 6, development work performed regarding the realisation of *W-Cu composites based on additively manufactured W preforms* (W_{AM}-Cu) is discussed. This approach makes use of state-of-the-art *additive manufacturing* (AM) technology and represents a versatile way for the realisation of tailored W-Cu composites. In this regard, the AM of pure W by means of *laser powder bed fusion* (LPBF) is described as well as the fabrication of a W_{AM}-Cu composite based on an additively manufactured thin-walled W honeycomb structure. Furthermore, it is discussed how the design freedom allowed by AM can be exploited in order to realise tailored W_{AM}-Cu structures that can enhance the performance and integrity of HHF loaded PFCs. Finally, in Chapter 7 it is subsumed, based on the results of the present work, whether the investigated W-Cu composites can be appraised as materials suitable for PFC applications in future magnetic confinement

fusion devices. This discussion will emphasise the potential effects of fusion neutron irradiation on the materials as this represents a crucial criterion regarding PFC operation in future thermonuclear D-T fusion reactors.

Chapter 2

Divertor target plasma-facing components in future fusion devices

2.1 ITER and DEMO

To date, the best-performing magnetic confinement fusion device design is the tokamak. That is the reason why this design concept is currently regarded to offer the highest potential with respect to the realisation of a technologically feasible and commercially viable thermonuclear fusion reactor.
In this context, the next device on the way to realising such a thermonuclear fusion reactor is the tokamak experiment *ITER*[1]. In November 1985, during the Geneva Summit, United States President Ronald Reagan and Soviet General Secretary Mikhail Gorbachev proposed an international effort concerning the development of nuclear fusion *"as an inexhaustible source of energy for the benefit of mankind"* [33]. This can be regarded as a starting point for the ITER project. Currently, ITER is being assembled in southern France in the framework of an international collaboration by the ITER members China, the EU (plus Switzerland), India, Japan, the Republic of Korea, Russia and the United States [34]. ITER will be the largest magnetic confinement thermonuclear fusion experiment world-wide capable of better confinement compared to any other fusion experiment. The first plasma in ITER is announced for 2025 [35]. In Figure 2.1, a technical illustration of the ITER tokamak is shown [36] while its main design parameters are summarised in Table 2.1 [37].

[1] *Iter* means *the way* in Latin.

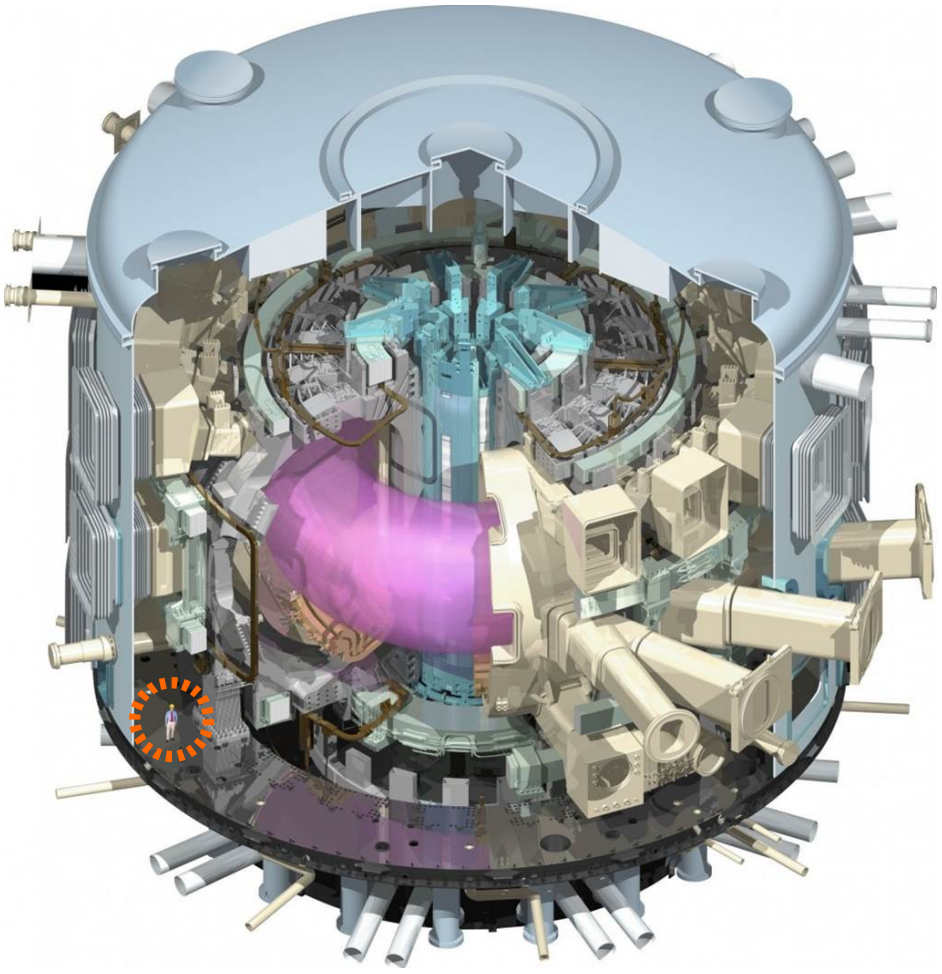

FIGURE 2.1: Technical illustration of the tokamak experiment ITER [36]; on the lower left, a human is included for scale (highlighted in dashed orange circle) in order to illustrate the size of the device.

TABLE 2.1: Main design parameters of the tokamak experiment ITER [37].

Plasma major radius	6.2 m
Plasma minor radius	2.0 m
Toroidal magnetic field at plasma centre	5.3 T
Plasma inductive burn time	$\geq$ 400 s
Plasma current	15 MA

ITER is a device designed to break new ground in thermonuclear fusion research and to prove the feasibility of nuclear fusion as a large-scale energy source [35]. Furthermore, ITER is the experimental step between current fusion experiments and future power-producing magnetic confinement fusion reactors. In more detail, ITER is specifically designed to achieve the following [38]:

- Produce 500 MW of fusion power for pulses with a duration of 400 s and with a fusion power gain[2] of $Q \geq 10$.
- Demonstrate the integrated operation of technologies for a fusion power plant.
- Create a D-T plasma in which the reaction is sustained through internal heating, meaning that heating due to the alpha particles is large enough to exceed the plasma heating that is injected from external sources.
- Test T breeding on mock-up blankets in a real nuclear fusion environment.
- Demonstrate the safety characteristics of a fusion device.

Within the EU nuclear fusion research strategy, a *demonstration fusion reactor* (DEMO) is envisaged as successor of the ITER experiment. DEMO is regarded as the remaining and crucial step towards a fully commercial thermonuclear *fusion power plant* (FPP). The principal goals of DEMO are [39, 40]:

- Production of net grid electricity on the order of a few hundred MW.
- Breeding the amount of T needed to close its fuel cycle, i.e. achieve T self-sufficiency.
- Demonstration of all the technologies needed for the construction of a commercial FPP.
- Demonstration of an adequate level of availability of several *full power year* (fpy).
- Minimisation of activation waste resulting from reactor operation in order that no long-term storage is required.
- DEMO as a component test facility and pathfinder to a first-of-a-kind FPP.

DEMO as a facility is foreseen to start operation in the 2050s [41]. The current EU DEMO key device parameters are summarised in Table 2.2 [40].

TABLE 2.2: Some current EU DEMO key device parameters [40].

Plasma major radius	9.0 m
Plasma minor radius	2.9 m
Toroidal magnetic field	5.9 T
Burn time	7200 s
Plasma current	18 MA
Fusion power	2000 MW

[2] The fusion power gain is defined as $Q = P_{fusion}/P_{heating}$, i.e. the ratio of the fusion power produced within the reaction chamber divided by the power injected into the reaction chamber through external heating systems.

The principal challenges associated with the realisation of a DEMO device are outlined within reference [39]. Two of those major challenges are the topics of *power exhaust* as well as *neutron resistant materials*. As the present work can be regarded as related to these issues they are adressed in some detail in the following sections.

2.2 Power exhaust in future magnetic confinement fusion devices

2.2.1 Plasma physical considerations

Issues related to plasma energy confinement have been a main working place for thermonuclear fusion research during the past decades. However, regarding future devices - first and foremost ITER and DEMO - such issues are likely to be increasingly overshadowed by those related to the topic of *power exhaust* [10].
When a thermonuclear fusion plasma is created and maintained within a reactor injected heating power as well as the energy released within the reaction chamber need to be exhausted safely and in a controlled manner during steady state operation. Furthermore, similar exhaust considerations do also have to be taken into account with respect to the fusion fuel and ash. D and T must be continuously introduced into the reaction chamber due to the fact that they are consumed by the fusion reaction. At the same time, the alpha particles - as the primary fusion reaction product (cf. Equation 1.3) - have to be exhausted in order to avoid dilution of the plasma which would cause a reduction of the overall reactivity. Moreover, impurities released from the reactor walls have to be exhausted as well at the rate they are created. Eventually, it turns out that the topic of power and particle exhaust in a thermonuclear fusion reactor represents a very special problem due to the field topology of magnetically confined high-temperature plasmas [42]. In this regard, the exhaust of power and particles is currently deemed one of the main challenges in view of the design of a future magnetic confinement fusion reactor, like DEMO [39]. When discussing the topic of power exhaust in magnetic confinement thermonuclear fusion reactors one has to distinguish three different channels of heat loadings on PFCs [10]:

- Neutrons released in the D-T fusion reaction (cf. Equation 1.3) deposit their energy volumetrically in the bulk of the PFC materials; they do not interact with the magnetically confined plasma.
- Photon energy due to bremsstrahlung, synchrotron and line radiation generates a rather uniformly distributed surface heat load on PFCs.

- A substantial fraction of the plasma thermal/kinetic energy is conducted along magnetic field lines to specifically designed heat load bearing PFCs, the so-called *divertor targets*.

The most severe heat loadings that components facing a thermonuclear plasma have to withstand is represented by the third of the abovementioned channels.
Historically, thermonuclear magnetic confinement fusion experiments were equipped with so-called *limiters*. Such components limit the plasma geometrically inside the reaction chamber while the magnetic field lines impinge directly onto the limiter material. Limiters in early tokamaks were typically manufactured from metals with high melting points, as e.g. molybdenum (Mo) or W [13]. However, when such high-Z materials are sputter eroded and migrate into the plasma core as impurities they have a deleterious effect and cool the plasma rapidly due to radiation losses caused by partially stripped ions [43, 44]. Suggestions to overcome the issues associated with limiters have been proposed already in the 1950s with a confinement system in which the magnetic field lines at the plasma edge are diverted into a separate chamber where they interact with the wall. Such a system is hence called a *divertor* [9]. The concept of a divertor has been applied to tokamaks rather successfully and can nowadays be regarded as state-of-the-art device design feature that brings about a distinct separation between the confined hot plasma core and the edge plasma that is in contact with wall material surfaces. In this context, the introduction of the divertor has led to the discovery of the H-mode which improved the confinement characteristics of fusion plasmas by a factor of two [30, 42, 45].
In Figure 2.2, a schematic section view of a tokamak with a so-called single-null divertor configuration is illustrated [9]. It can be seen that the divertor with its target plates is

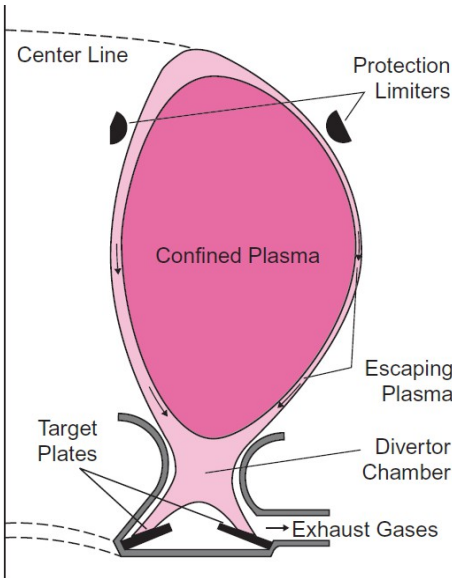

FIGURE 2.2: Schematic illustration of a tokamak with a single-null divertor where the target plates are located at the bottom of the reaction chamber [9].

located at the bottom of the reaction chamber. Moreover, it can be seen that at the target plates exhaust gases are pumped out of the reactor as at this position the plasma particles form a neutral gas after impinging on the target plates. In Figure 2.3, a section view of the current EU DEMO design is illustrated [46]. It can be seen that this device is also foreseen to be operated as a tokamak with a single-null divertor which can hence be regarded as a state-of-the-art design feature in tokamaks. In general, a divertor

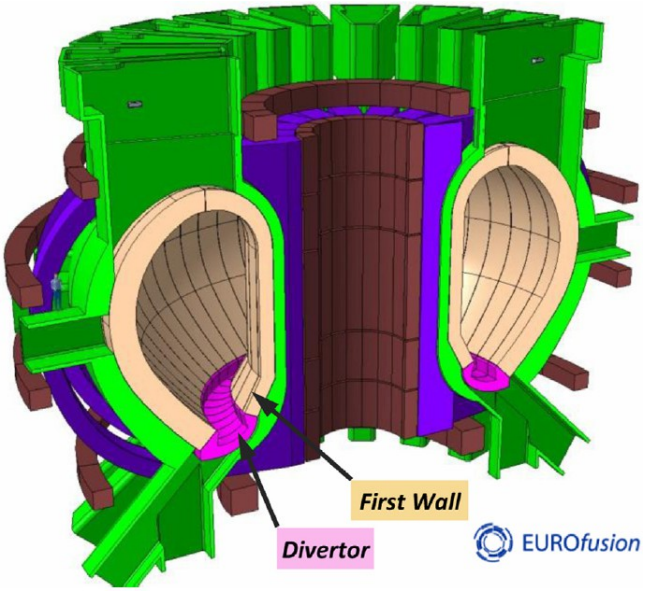

FIGURE 2.3: Section view of the current EU DEMO design [46]; the location of the first wall and divertor PFCs are highlighted.

configuration is realised by means of magnetic field topologies that direct field lines to areas that are adequately remote from the hot confined core plasma. In principle, this works through the modification of the magnetic field at the plasma edge. The poloidal magnetic field is distorted in a way which creates a magnetic *separatrix* which separates the confined thermonuclear plasma and the divertor PFCs through a region of open magnetic field lines, the so-called *scrape-off layer* (SOL).

In Figure 2.4, the difference between a tokamak in limiter and divertor configuration is illustrated schematically [42]. In the limiter configuration, the plasma contacts the reactor wall in the main chamber while in the divertor configuration the confined plasma does not get into contact with the reactor walls as the magnetic field topology diverts the edge plasma towards the target plates.

The physical background behind the abovementioned high heat loadings on the divertor target plates due to the transport of the plasma energy along the magnetic field lines in the SOL is that most of the power passing through the separatrix flows inside a narrow channel. The characteristic width of this channel - the so-called *scrape-off layer power fall-off length* λ_q which is determined at the tokamak outboard midplane [47] - is an important parameter as the size of λ_q defines the tolerable power P_{SOL} that crosses the

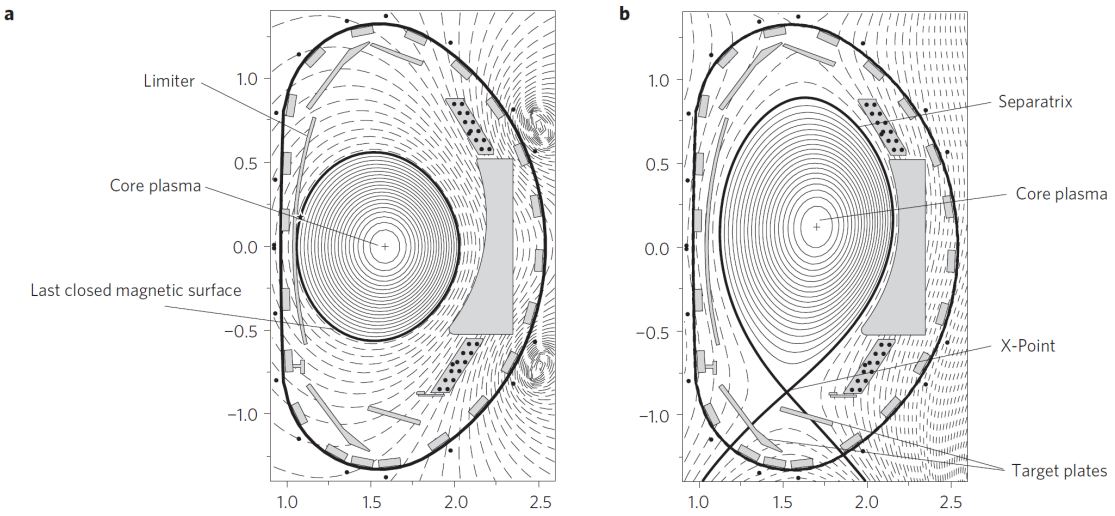

FIGURE 2.4: The difference between limiter and divertor configuration: (a) In a limiter configuration the plasma contacts the reactor wall in the main chamber; (b) in a divertor configuration the magnetic field topology diverts the edge plasma towards the target plates [42].

separatrix and impinges on the divertor target plates. Hence, a small λ_q represents a concern as this directly results in high power fluxes to the divertor target plates. Scaling expressions for λ_q have been derived in the literature. According to [48], the following scaling based on appropriate data from existing tokamak experiments can be used in order to describe dependencies on machine size and on P_{SOL}:

$$\lambda_q \propto P_{SOL}^{0.1} \, R_{geo}^{0} \tag{2.1}$$

where P_{SOL} is the power crossing the separatrix and R_{geo} is the major radius of the device. It can be seen that there is only a rather weak dependence on P_{SOL} while a pronounced positive dependence on P_{SOL} would be beneficial for future tokamak devices, like e.g. ITER where P_{SOL} is approximately 100 MW which is about 20 times higher than the values usually found in current tokamak experiments [48]. A further important implication of the scaling expression according to Equation 2.1 is the absence of a machine size scaling. This fact represents a significant issue regarding the power exhaust in large-scale tokamaks, like DEMO, where P_{SOL} will be significantly higher compared to existing devices.

When extrapolating existing tokamak results to ITER baseline H-mode operation a value of $\lambda_q \approx 1\,\text{mm}$ is found. Furthermore, extrapolation to a fusion power plant shows that without any countermeasures the power loadings on the divertor target plates will be beyond the technologically realisable heat removal capabilities of PFCs. Therefore, countermeasures will have to be implemented in future tokamaks in order to reduce the heat fluxes to the divertor targets to acceptable levels. In this regard, current research focuses on three approaches [42, 49]:

- Modification of the magnetic field topology in the divertor region in order that the length of and the area covered by the field lines are maximised; this reduces the heat flux geometrically and increases the effect of perpendicular plasma transport; in this context several advanced divertor configurations are being investigated.
- Seeding controlled amounts of impurities into the plasma, preferably noble gases, that dissipate power by radiating volumetrically in the plasma which distributes the heat fluxes more homogeneously over the first wall; the total radiation fraction expected during operation of a future thermonuclear fusion power plant will be around 90% of the overall heating power.
- Creating a "cold" edge plasma close to the *plasma-facing material* (PFM) surfaces by minimising the plasma temperature and maximising the plasma density in front of the divertor targets in order that a neutral gas accumulation can form that cushions the energy of the plasma particles that impinge on the target surfaces; at sufficiently low plasma temperatures at the divertor target surfaces the plasma can effectively be extinguished; this state is usually referred to as *detachment*.

To summarise, it can be underlined that the topic of power exhaust is currently regarded as a decisive concern for the design of any future magnetic confinement thermonuclear fusion device, including ITER and DEMO. This statement does not only hold true for plasma physical exhaust considerations but also for the design and engineering of divertor target PFCs as will be discussed in the following sections.

2.2.2 Boundary conditions for divertor target plasma-facing components

Above, it has been described that tokamak operation with a divertor configuration has advantages but comes at the expense of high particle fluxes onto the divertor target plates which in turn generate HHF loads. It is intuitively reasonable that the maximum heat fluxes a divertor target PFC can safely handle are limited due to physical-technical boundary conditions. In this respect, design HHF loads that are currently regarded as appropriate for the ITER as well as DEMO divertor targets are $10\,\mathrm{MW\,m^{-2}}$ for steady state operation as well as $20\,\mathrm{MW\,m^{-2}}$ for slow transient events [50–52]. These values exceed heat flux loads that occur in established power engineering applications by approximately one order of magnitude[3]. Typical heat loads on heat exchangers of fossil-fired

[3]There are applications where surface heat loadings exceed the design heat flux loads for divertor PFCs. One prominent example are *space shuttle main engine* (SSME) combustion chambers where throat heat fluxes higher than $100\,\mathrm{MW\,m^{-2}}$ occur [53]. However, one has to bear in mind that the boundary conditions and constraints for the design of such components are significantly different compared to PFCs.

power plants are on the order of a few hundred $\mathrm{kW\,m^{-2}}$ [54] while maximum heat loadings on the surface of fuel rods in nuclear fission reactors are on the order of $1\,\mathrm{MW\,m^{-2}}$ [55]. A basic requirement for a thermonuclear fusion reactor is that the divertor PFCs can ensure reliable operation by providing safe power exhaust handling capabilities. Eventually, it turns out that this requirement is the limiting factor for the energy flow across the outer plasma boundary. In this sense, the tolerable peak power load on highly heat loaded divertor PFCs represents a key constraint for the design of a future fusion reactor like DEMO and will determine its operating scenario [56].
The origin of the HHF loads that PFCs have to withstand lies mainly in the interactions of plasma particles with the PFM. These interactions can according to [57] be classified with respect to the particles under consideration:

- Bombardment by atomic particles, i.e. ions, neutral atoms or molecules,
- electron bombardment,
- interaction with electromagnetic radiation and
- fusion neutron irradiation.

The bombardment of PFMs with electrons and photons results in near-surface heating. The effects of fusion neutron irradiation are in principle related to the bulk of the PFC materials where they mainly cause material damage while near-surface effects like sputter erosion can be neglected. The impact of atomic particles induces a number of interaction and transformation processes within PFMs which can lead to a change of material structure and composition. In this respect, various processes have to be considered, like e.g. erosion or diffusion processes. For more details regarding these phenomena the reader is referred to references [57,58].
In view of these considerations, one aspect of paramount importance regarding the design of divertor PFCs is the choice of a suitable PFM. Nowadays, W is considered as the preferred PFM for future magnetic confinement thermonuclear fusion devices, including DEMO [40]. W is a metal with unique properties as it for example exhibits the highest melting point as well as the lowest vapour pressure of all metals. Typically, W and W based materials are used and of interest with regard to rather demanding applications, including e.g. anode materials in X-ray tubes or welding electrodes. Some basic properties of monolithic W are summarised in Table 2.3 [59,60].

TABLE 2.3: Basic properties of monolithic W [59, 60].

Melting point	3400 °C
Density (20 °C)	19.3 g cm^{-3}
Thermal conductivity (0 °C to 100 °C)	174 W m^{-1} K^{-1}
CTE (0 °C to 100 °C)	4.5×10^{-6} K^{-1}
Young's modulus (20 °C)	411 GPa
Vapour pressure (2000 °C)	8.15×10^{-8} Pa
Hardness (polycrystalline)	up to 650 HV_{30}

For PFM applications, W is mainly chosen because of its high threshold energy for sputtering by H isotopes as well as its low retention of H isotopes within the material [61]. The former ensures that material erosion by impinging particle fluxes is sufficiently small[4]. The latter ensures that the amount of retained radioactive T within the PFM is acceptably small.

Historically, carbon (C) based materials were preferably used as PFM in magnetic confinement fusion experiments. This choice was mainly due to the following reasons: Such materials do not melt and exhibit a rather high sublimation temperature as well as a good thermal conductivity. Furthermore, at high plasma temperatures C is fully ionised and does hence only cause minor impurity radiation losses. However, the chemical reactivity of C with hydrogen plasmas leads to high erosion rates. Moreover, hydrocarbon compounds can form that are deposited all over the reaction chamber. With respect to T, this is not acceptable from a safety point of view [42, 62]. Against this background, W as a high-Z metal is nowadays favoured over C based PFMs. Pioneering work regarding the use of W as PFM was performed in the *Axially Symmetric Divertor Experiment Upgrade* (ASDEX Upgrade) tokamak which is located in Garching, Germany [42, 63–65]. However, a PFC does not only and entirely consist of the W PFM which according to current PFC design rationales cannot act as structural material for ensuring component integrity. This is mainly due to the inherent brittleness of W while this issue is discussed in more detail in section 2.4. Hence, a divertor PFC is formed through the combination of a W PFM with an actively cooled heat sink that provides structural function. Priority requirements for PFC HSMs are a high thermal conductivity as well as adequate mechanical properties regarding all envisaged operating conditions in order to provide a high heat removal capability as well as mechanical integrity for the PFC. In this respect, Cu alloys are currently regarded as preferred HSMs for highly loaded PFCs [66].

During fusion operation, divertor PFCs have to face not only severe cyclic particle and

[4] On the one hand, this ensures a reasonable lifetime of a PFC. On the other hand, this keeps the plasma contamination by impurities - which is inevitably caused by the plasma-wall interaction - sufficiently low.

heat flux loads but also considerable fusion neutron irradiation (cf. Equation 1.3). The latter is regarded as a crucial issue for future D-T fusion devices, including DEMO, as such a neutron irradiation inevitably leads to degradation of thermophysical and mechanical properties of the PFC materials [61,67,68].
As a PFC is a joint structure comprising PFM and HSM, joining of these differing materials is an important aspect and technologies to reliably combine them to a component need to exist. The PFC materials have to be bonded intimately to ensure a flawless thermal contact as well as a high joint strength in order that the joined PFC can sustain cyclic HHF loading during fusion operation.
According to our current understanding, future thermonuclear fusion reactors like DEMO will be large power stations. This means that materials and components used for the design of such devices need to be capable of being produced in an industrial environment and on a corresponding scale. Hence, a basic requirement for current material and PFC developments with respect to DEMO and beyond is that they have to demonstrate essential elements of industrial scale fabrication.
All in all, the abovementioned points imply that the design and realisation of highly loaded divertor PFCs represents a key engineering challenge with respect to future power-producing thermonuclear fusion devices, like DEMO.

2.3 State-of-the-art divertor target design

It has been mentioned that currently W is the preferred PFM and Cu alloys are the preferred HSMs for actively cooled divertor target PFCs. The current state-of-the-art divertor target PFC design that makes use of such materials and will be used within the ITER divertor is a so-called *monoblock design* where W armour tiles are joined to a water-cooled *copper-chromium-zirconium* (CuCrZr) heat sink pipe with the help of a soft Cu interlayer. This design is illustrated in Figure 2.5 [69] and has proven to fulfil the ITER divertor target qualification criteria [70, 71]. In principle, these criteria comprise the demonstration of component integrity for 5000 HHF load cycles at $10\,\mathrm{MW\,m^{-2}}$ and additionally 300 HHF load cycles at $20\,\mathrm{MW\,m^{-2}}$ [50, 69]. Apart from that, the manufacturing of a full-scale ITER divertor target prototype has recently been demonstrated. In Figure 2.6, such a prototype which is armoured with 1104 W monoblocks is illustrated [72].

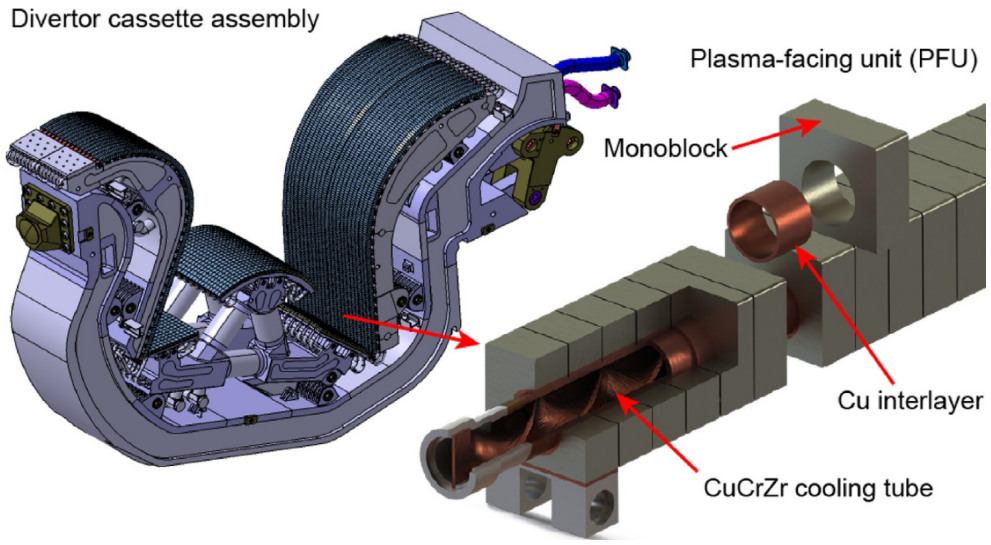

FIGURE 2.5: Illustration of an ITER divertor cassette (left) as well as an exploded view of a plasma-facing unit (right) showing the W monoblock design; the width of the W monoblocks is 28 mm; the ITER divertor will consist of 54 cassettes in total [69].

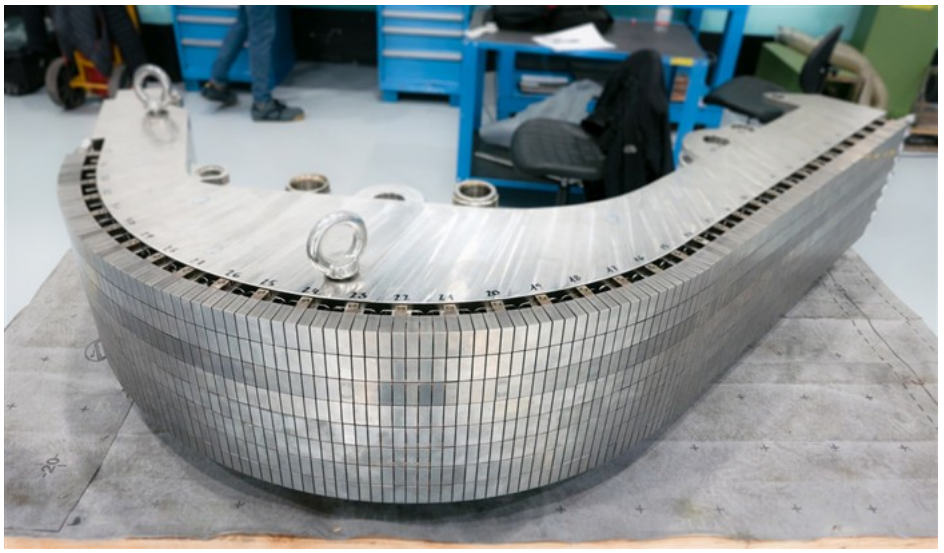

FIGURE 2.6: Successfully manufactured full-scale ITER vertical divertor target prototype [72].

2.4 Risks associated with the state-of-the-art divertor target design

Above, it has been mentioned that the W monoblock design has been validated through HHF tests according to the ITER divertor target qualification criteria. However, regarding the application of this design to a DEMO environment issues arise mainly due to the fact that divertor PFCs in DEMO are foreseen to be in operation for 2 fpy meaning that they will be exposed to high fusion neutron doses leading to significant PFC material damage [67, 73]. In the following, these issues are briefly discussed with a distinct focus

on the PFC heat sink as the present work deals with PFC HSMs.

It has been mentioned that W is currently regarded as the preferred PFM for divertor PFCs. However, W is an inherently brittle metal with a high *ductile-to-brittle transition temperature* (DBTT) which makes it a challenging material from an engineering point of view. Furthermore, the DBTT of W typically depends strongly on the manufacturing route of the material. For example, a comprehensive study regarding the impact bending properties of different W material grades revealed that none of the investigated materials exhibited ductile fracture behaviour below 450 °C while some of the materials showed brittle fracture behaviour up to 1000 °C [74]. For PFM applications, it has been recommended that W should not be operated at temperatures below approximately 800 °C [61]. The situation, however, is likely to be even worse under fusion neutron irradiation. It has been predicted that for a DEMO reactor neutron irradiation induced damage levels in the divertor W PFM can reach values up to 6-7 *displacements per atom/full power year* (dpa/fpy) which is a dose high enough to lead to pronounced degradation of material properties. Moreover, there is a lack of neutron irradiation embrittlement data for W which is regarded as a high design engineering risk with respect to DEMO [61]. The brittleness and embrittlement issue of W might not only be critical regarding the cyclic quasi-steady-state HHF loading within a tokamak type reactor but also regarding loadings due to plasma instabilities, like e.g. so-called *edge localised modes* (ELMs), where energies on the order of $\mathrm{GW\,m^{-2}}$ can impinge on the divertor targets during ms periods which results in intense loadings that can damage the W PFM [61].

The precipitation hardened Cu alloy CuCrZr is currently regarded as the most appropriate HSM for highly loaded water-cooled PFCs in present-day and future magnetic confinement fusion devices [50, 51, 75–77]. Some basic properties of CuCrZr[5] are summarised in Table 2.4 [78].

Table 2.4: Basic properties of CuCrZr in aged condition [78].

Chemical composition	Cr: 0.5-1.2wt.%, Zr: 0.03-0.3wt.%
Melting range	1070 °C to 1080 °C
Density (20 °C)	$8.91\,\mathrm{g\,cm^{-3}}$
Thermal conductivity (100 °C)	$315\,\mathrm{W\,m^{-1}\,K^{-1}}$
CTE (0 °C to 100 °C)	$16.3 \times 10^{-6}\,\mathrm{K^{-1}}$
Young's modulus (20 °C)	110 GPa to 130 GPa
Hardness	up to 200 *HV*

The advantage of this specific alloy with regard to structural PFC heat sink application

[5] EN material designation: CuCr1Zr, CW106C

in comparison with other existing Cu alloys is mainly its superior fracture toughness behaviour [66]. However, it has been underlined that there are high-impact design engineering risks regarding the use of Cu alloys, particularly CuCrZr, in a DEMO environment. The most serious issues concerning CuCrZr relate to the behaviour of this material under neutron irradiation characterised by a pronounced loss of ductility at lower and a loss of strength at elevated operating temperatures [61,66,79,80]. In the literature, a lower operating temperature limit of 180 °C [61] as well as a maximum operating temperature of approximately 300 °C [66] have been recommended for the use of CuCrZr in DEMO divertor PFCs. However, within a recent analysis on the applicability of Cu alloys for DEMO HHF components [66] it is even stated that neutron irradiation at temperatures below approximately 275 °C leads to pronounced radiation hardening and loss of ductility and that "*existing Cu alloys have a vanishingly small potential operating temperature window where they would retain good ductility, fracture toughness and resistance to creep deformation under DEMO reactor conditions*".

The abovementioned operating temperature limitations impose a strong constraint on the design of divertor PFCs for DEMO as they imply that the structural Cu alloy PFC HSM has to be operated within a rather narrow temperature window in order to ensure reliable operation. However, *finite element analysis* (FEA) studies of an "ITER-like" W monoblock divertor target design indicate that this can hardly be assured in view of the substantial HHF loadings that have to be exhausted by the divertor target. In reference [52], it is reported that during stationary HHF loading with 15 $\mathrm{MW\,m^{-2}}$ the temperature in the CuCrZr pipe locally exceeds the allowed upper operating temperature limit (376 °C at the bond interface). Furthermore, it is stated that for stationary HHF loading with 20 $\mathrm{MW\,m^{-2}}$ the entire apex region of the CuCrZr pipe experiences temperatures significantly higher than the abovementioned temperature limit (432 °C at the bond interface). Against this background, the need for an advanced HSM solution that ensures sufficient integrity of a divertor target PFC at elevated temperatures becomes visible.

In Figure 2.5, it can be seen that the W monoblock design makes use of a pure Cu interlayer between the W armour and the CuCrZr pipe which is supposed to act as a compliant layer to reduce thermally induced stresses at the joint interface [71]. However, pure Cu does also suffer from neutron irradiation induced loss of ductility at temperatures below approximately 200 °C [66]. Such a loss of ductility is presumably not acceptable with respect to DEMO divertor applications as an embrittled Cu interlayer cannot maintain its functionality as a soft and stress-relieving layer. Moreover, dimensional changes due to void swelling are regarded as a further potential concern regarding pure Cu. The steady-state volumetric swelling rate in neutron irradiated pure Cu has been reported to be approximately 0.5%/dpa while the swelling level can be higher than 70% [66,81].

Maximum swelling in pure Cu has under fission neutron irradiation conditions been determined at approximately 300 °C to 325 °C which can be regarded a relevant operating temperature range. CuCrZr exhibits superior void swelling resistance compared to pure Cu under neutron irradiation which appears to be acceptably low for applications in a DEMO reactor [66, 79].

Apart from that, within a divertor PFC as illustrated in Figure 2.5 W armour monoblocks have to be combined with a CuCrZr heat sink pipe which gives rise to two issues. On the one hand, these materials exhibit inherently different thermomechanical properties, especially CTEs. This mismatch is a driving force that inevitably leads to high thermal stresses during cyclic HHF loading. On the other hand, the abovementioned operating temperature limits for W and CuCrZr cannot be satisfied simultaneously which implies that with such a design PFC materials are to some extent operated under unfavourable conditions and the corresponding property degradation has to be accepted and taken into account.

It has been mentioned that the W monoblock design has been validated through HHF tests according to the ITER divertor target qualification criteria. However, post HHF exposure metallographic analyses revealed that the following defects could be observed on the tested PFC mock-ups [70, 71]:

- Microcrack formation at the inside of the CuCrZr heat sink pipe,
- mechanical deformation of the CuCrZr heat sink pipe,
- crack formation at the W/Cu bond interface,
- porosity formation in the pure Cu interlayer,
- microstructural changes in W down to the W/Cu bond interface,
- macrocrack formation in W monoblocks and
- strong surface modification on the W monoblocks.

These results indicate that the W monoblock design - although satisfying the ITER divertor qualification criteria - clearly experiences defects and damage due to cyclic HHF loading. In this regard, it should be stressed that the tests in references [70, 71] have been performed on unirradiated PFC mock-ups while the behaviour under and after fusion neutron irradiation might be notably worse due to the degradation of the PFC material properties. Hence, it is questionable if an "ITER-like" divertor target design is applicable to a DEMO divertor. In this context, the "show-stopper" nature of the divertor [61] requires that alternatives to existing materials for divertor PFC applications are developed.

Chapter 3

Material scientific background

3.1 Composite materials

According to a textbook definition [82], *composites* are manufactured materials that consist of at least two suitably arranged or distributed phases which are separated by an interface and characterised by notably different physical and/or chemical properties. A further characteristic aspect according to this definition is that composite materials exhibit properties that are not depicted by any of the constituents in isolation.
Nowadays, composites constitute a rather diverse and important class of engineering materials that are frequently classified according to the applied matrix material in which some reinforcing phase is embedded. In this respect, one example of conventional composites that are widely used for various applications are polymeric matrix composites [83]. Another distinguished class is represented by composites based on ceramic matrix materials while there is also the category of *metal matrix composites* (MMCs) [84]. Aside from that, a categorisation of composite materials can also be made according to the reinforcements which are used. These reinforcements can come in the form of particles, whiskers, short fibers, continuous fibers or sheets as is schematically illustrated in Figure 3.1 [85]. Very often, reinforcements are used in the form of fibres as materials are usually stronger and stiffer in fibrous shape than in any other form. For many a long year, glass fibres have for example been used to produce fibre-reinforced composites but nowadays there are many other high-performance fibres with high strength and stiffness available as e.g. boron, silicon carbide, carbon or alumina fibres [82].
Apart from that, many materials that are well-known to us are effectively composites. In particular, this is true for various natural biological materials such as wood, bone or hide [84]. Such biological materials are all complex composites with sophisticated

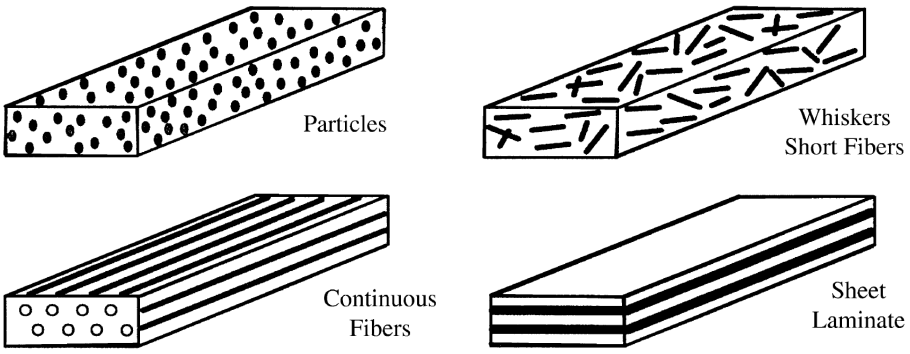

FIGURE 3.1: Schematic illustration of different types of composite materials classified according to the shape of the applied reinforcements [85].

structures that ensure material properties tailored according to specific performance requirements. One particular example for such tailored biological materials is *bamboo* which is effectively a fibre-reinforced composite material [86,87]. Bamboo comprises cellulose fibres embedded in a lignin–hemicellulose matrix shaped into honeycomb-like cells while the fibres are aligned parallel to the stem. The distribution of the load-bearing fibres in bamboo is not uniform but graded with fibre density being highest at the outer periphery of the stem where the highest stresses occur. In Figure 3.2, the hierarchical composite structure of bamboo is illustrated [86]. With this composite architecture optimised at each structural level bamboo achieves very high efficiency in terms of mechanical performance per unit weight.

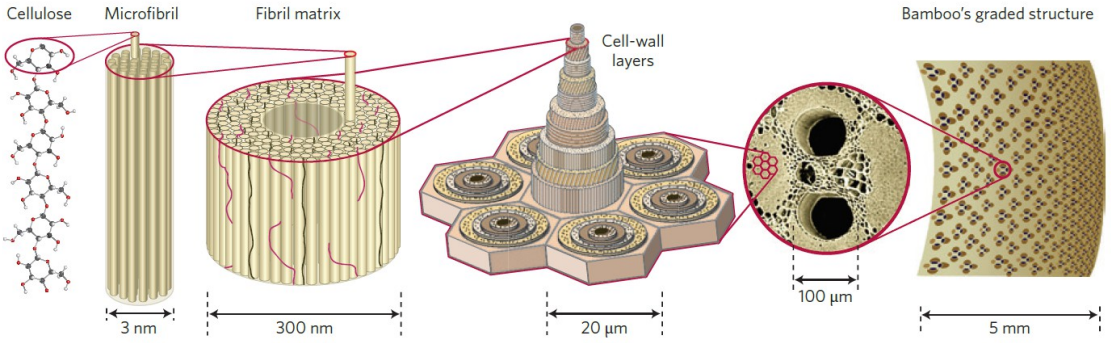

FIGURE 3.2: Hierarchical structure of bamboo as an example for a complex composite material occuring in nature; it is composed of cellulose fibres embedded in a lignin-hemicellulose matrix while the distribution of load-bearing fibres is graded with fibre density being highest at the outer periphery of the stem. [86].

3.2 Metal matrix composites

As the present work is focused on MMCs, a more detailed description of such composite materials is provided within this section. MMCs are materials that are typically of interest with respect to rather specific and demanding applications. One example illustrating the capabilities of MMCs is the use of a carbon fibre-reinforced aluminium composite as antenna waveguide/boom on the *Hubble Space Telescope* as is illustrated in Figure 3.3 [88]. This fibre-reinforced material offers an outstanding property com-

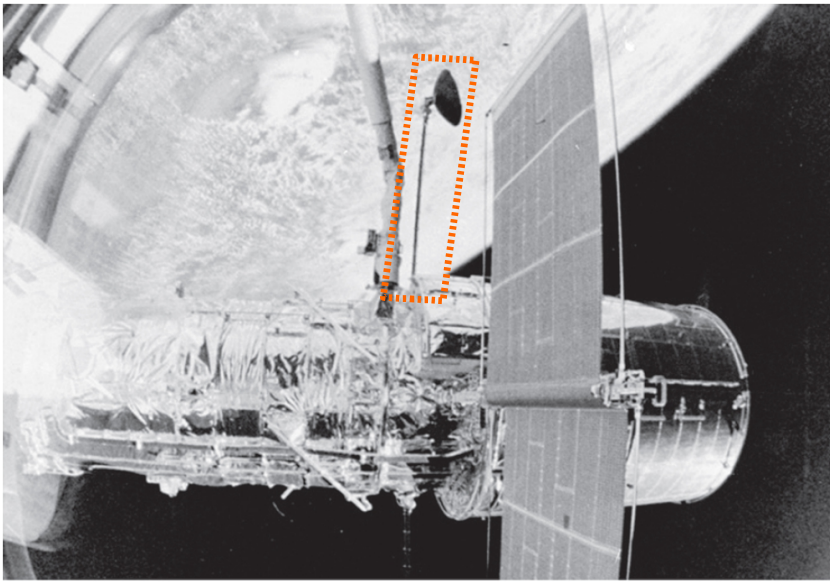

FIGURE 3.3: Carbon fibre-reinforced aluminium MMC antenna wave guide/boom on the Hubble Space Telescope (highlighted in dashed orange rectangle) as it is deployed from the space shuttle orbiter [88].

bination of high specific stiffness and low CTE for the realisation of a lightweight and dimensionally stable structure. Furthermore, with an excellent electrical conductivity this material provides waveguide function for signal transmission. This example illustrates the appeal and high potential of metallic composite materials rather well as with such materials property combinations can be realised that can hardly be achieved with monolithic materials.

There are also MMCs intended for high-temperature applications. One example in this respect are titanium (Ti) based composites reinforced with continuous silicon carbide fibres (SiC_f-Ti). These composites were developed as lightweight and damage tolerant materials capable of handling extreme mechanical loadings at elevated temperature [89–93]. An exemplary microsection of a *unidirectionally* (UD) reinforced SiC_f-Ti MMC is shown in Figure 3.4 [93]. SiC_f-Ti has mainly been investigated as high-performance material with regard to aerospace applications while it has been reported in the literature that SiC_f-Ti composites demonstrate expected mechanical properties in terms of high

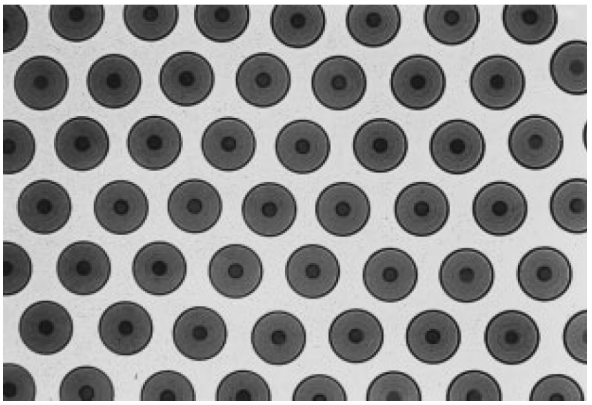

FIGURE 3.4: Microsection of a UD SiC_f-Ti MMC [93].

strength, stiffness, creep and fatigue resistance. However, extremely high material costs as well as a lack of knowledge of material properties have limited the use of SiC_f-Ti composites in competition with established materials, as e.g. nickel-based alloys or steels.
Apart from that, there are also mass production examples of MMCs, as e.g. *discontinuously reinforced aluminium* (DRA) MMCs which are applied in the automotive sector [94]. In this respect, a specific example is the application of selectively reinforced cylinder liners in internal combustion engine blocks. Such MMC components are manufactured through a liquid infiltration process where a preform from chopped alumina and carbon fibres is infiltrated during the engine block casting. The use of such MMC cylinder liners results in improved wear properties and cooling efficiency as well as 50% weight savings compared to cast iron without increasing the engine package size [85]. An illustration of such a selectively reinforced engine block together with a microsection of the MMC material is shown in Figure 3.5 [82,94].
There exists a variety of methods and technologies for the fabrication of MMCs including processes that make use of all different states of matter [85]:

- *Solid-state* as for example used in powder metallurgical processing,
- *liquid-state* as e.g. used in liquid infiltration methods and
- *gaseous-state* processing as for example used in physical vapour deposition (PVD) methods.

The MMCs described within the present work are manufactured by means of liquid infiltration. Such a liquid-state processing means combining reinforcements with the matrix at processing temperatures above the melting point of the matrix material which is then solidified after the infiltration process. Commercial MMC products manufactured through liquid-state routes such as infiltration account for the largest volume in primary MMC production [94].

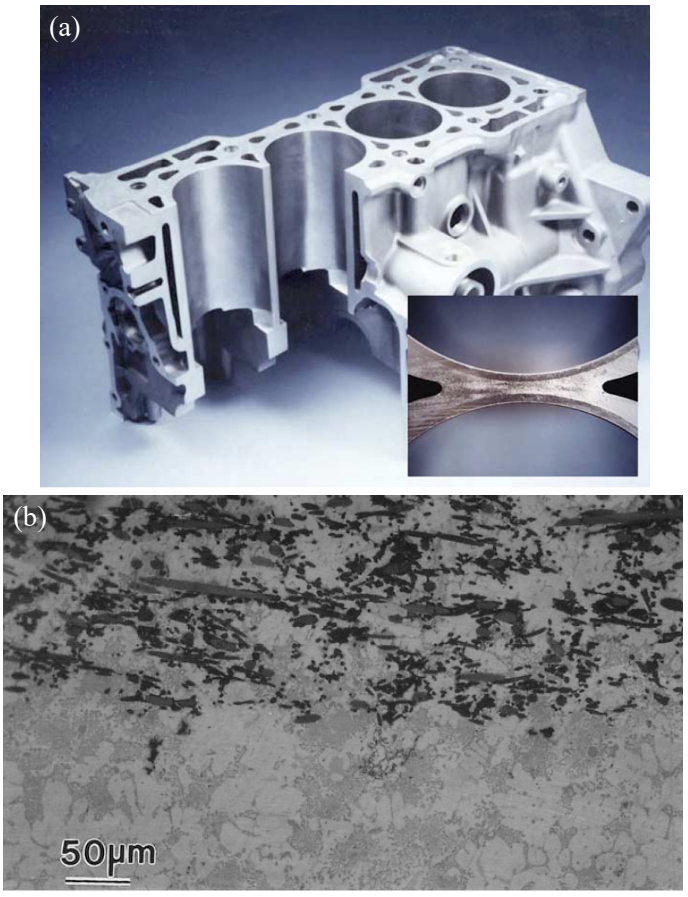

FIGURE 3.5: (a) Internal combustion engine block with selectively reinforced DRA cylinder liners (the magnified insert illustrates the selective reinforcement) and (b) microstructure of the cylinder liner showing the unreinforced Al alloy as well as the alumina and carbon fibre-reinforced MMC [82, 94].

3.3 Properties of composites

It is intuitively reasonable that the introduction of reinforcements, i.e. an additional phase, into a matrix material alters the overall properties of this material which thus becomes a composite. According to [95], the properties of a composite material are primarily determined by:

- The properties of the constituent materials,
- their geometrical distribution and
- their interactions.

In order to describe a composite material and its behaviour it is hence necessary to specify the properties of the constituents, their geometry (size & shape), their distribution (concentration & orientation) as well as the nature of the matrix-reinforcement interface.

The concentration of a reinforcing phase within a composite is an important parameter determining the characteristics of a composite material and is typically given in terms of volume or weight fraction. Moreover, composite material properties can depend strongly on the orientation of the reinforcements as for example in UD fibre-reinforced composites where the fibre orientation determines the *anisotropic behaviour* of the composite material. Certain properties of a composite can also be sensitive to the nature of the matrix-reinforcement interface which e.g. determines the interfacial bond strength which in turn influences the overall mechanical properties of the composite.
The abovementioned correlations indicate one of the main advantages of composite materials. The macroscopic behaviour of such materials can to a notable extent be tailored by customising the structure of the composite given by the arrangement of the constituing phases. Compared with monolithic materials, this offers considerable flexibility as the properties of composites can specifically be tailored to meet service conditions.
When discussing composites as engineering materials one is mainly interested in the effective properties of the composite, i.e. the response of the materials on a *macroscopic* scale, as structures built from such materials typically exhibit macroscopic dimensions. At a sufficiently small scale, however, composites - as well as most other practical engineering materials - are in principle heterogeneous. Nevertheless, a proven and reasonable approach is to treat these materials as *continuum*. This means that the actual constitution of the material is considered to be continuous and that this continuum is characterised by properties that are identical at every material point [95]. This concept is schematically illustrated in Figure 3.6 [96]. Moreover, this implies that a characteristic dimension for

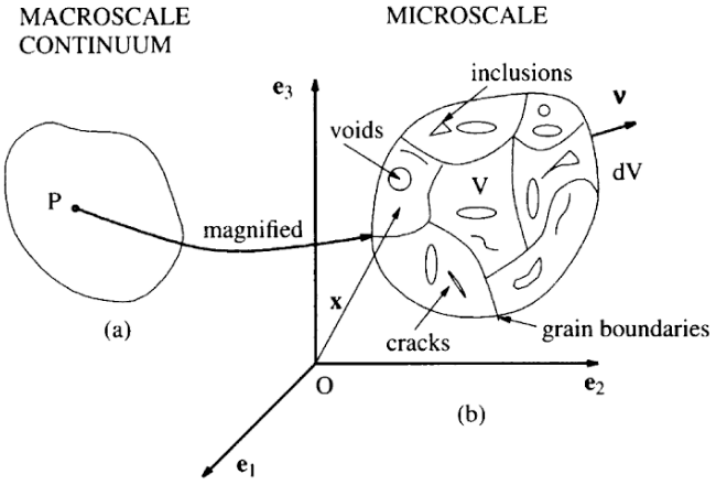

FIGURE 3.6: Illustration of the transition between macroscale continuum and microscale: (a) P is a typical material point surrounded by a small material volume and (b) shows a corresponding magnification with a possible heterogeneous microstructure for the neighbourhood of material point P [96].

the heterogeneity of a composite material can be defined and that there generally exists a scale - intermediate between the microscopic scale of the composite constituents and

the scale of the structure - at which the macroscopic properties of a composite can be described by spatial averaging to yield a proper approximation for the effective material properties. The corresponding material volume which is considered to be representative for the determination of averaged composite material properties is usually referred to as *representative volume element* (RVE). On this scale, the material can be regarded as *macroscopically homogeneous* while the corresponding homogenised properties can e.g. be used as input for component design. Exemplarily, the determination of the homogenised stiffness and compliance properties for a heterogeneous composite material will be discussed in the following in order to illustrate the concept of homogenisation mathematically [95]. In equilibrium, external loads applied to a composite material must be equal to the sum of the volume averaged loads carried by the composite constituents. Hence, when stress and strain conditions are imposed on the boundary of an RVE, the average stress is defined by

$$\overline{\sigma}_i = \frac{1}{V}\int_V \sigma_i(x)\, dV, \quad i = 1, ..., 6 \tag{3.1}$$

while the average strain is defined by

$$\overline{\epsilon}_j = \frac{1}{V}\int_V \epsilon_j(x)\, dV, \quad j = 1, ..., 6 \tag{3.2}$$

where σ_i and ϵ_j are the elements of the stress and strain tensors at position x and $\int_V dV$ is the volume integral over the RVE. These correlations are general and allow the definition of the effective stiffness C_{ij} and compliance S_{ij} tensors through

$$\overline{\sigma}_i = C_{ij}\overline{\epsilon}_j, \quad i, j = 1, ..., 6 \tag{3.3}$$

and

$$\overline{\epsilon}_i = S_{ij}\overline{\sigma}_j, \quad i, j = 1, ..., 6. \tag{3.4}$$

From the above equations, it can be seen that in order to determine homogenised properties of a microscopically heterogeneous material it is necessary to calculate the average quantities over the RVE and then derive from them effective material properties. This problem seems to be simple in principle but can be very complex in practice. In order to apply Equation 3.1 and Equation 3.2, one has to know the detailed stress and strain fields for each point of a heterogeneous material. Similar considerations and formulations can be found in the literature for the derivation of other homogenised material properties of interest, as e.g. CTE or thermal conductivity [97–105].

Apart from the general idea of the homogenisation concept regarding the macroscopic response of composite materials as an averaged property behaviour a few more aspects regarding composite behaviour will be discussed briefly in the following.

One important feature of composite materials is the *load sharing* between the matrix and the reinforcing phase as probably the most central objective regarding the use of reinforcements in composite materials is the enhancement of mechanical properties. The rigorous and detailed description of this enhancement effect can be rather complex and difficult. However, a simplified example regarding the elastic behaviour of a composite with UD continuous fibre-reinforcement is described in the following in order to illustrate the concept of load sharing. We consider a composite as illustrated in Figure 3.7 where the two constituents have the same lengths parallel to the fibre-matrix interface [84]. If a

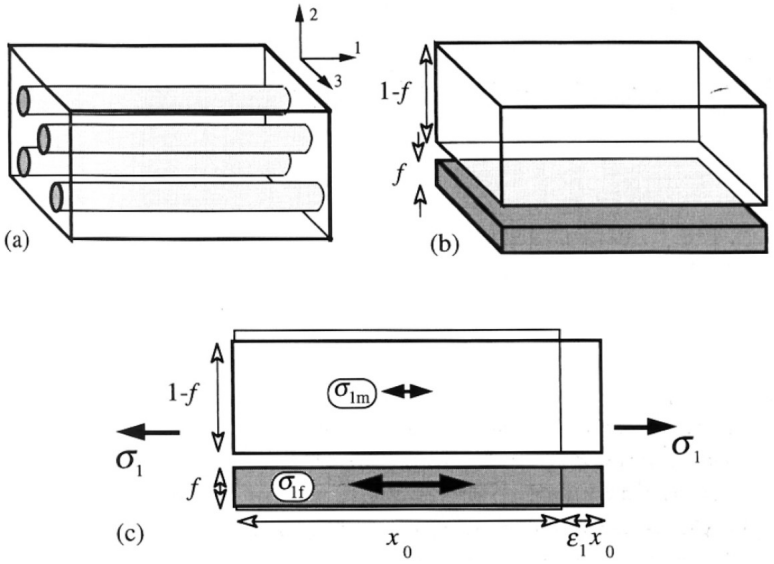

FIGURE 3.7: Schematic illustration of (a) a UD continuous fibre-reinforced composite, (b) a simplified representation of the composite in terms of slabs taking into account the volume fraction f of the fibre reinforcement and (c) the response of the composite if a stress is applied parallel to the fibre orientation [84].

stress is applied in the direction parallel to the fibre alignment (1-direction in Figure 3.7) both constituents exhibit the same strain in loading direction. Under this equal strain condition, the strain of the fibres as well as the matrix must correspond to the ratio between the stress and the Young's modulus for each of the two constituents:

$$\epsilon_{c,1} = \epsilon_{f,1} = \frac{\sigma_{f,1}}{E_{f,1}} = \epsilon_{m,1} = \frac{\sigma_{m,1}}{E_{m,1}} \tag{3.5}$$

where σ, ϵ and E denote stress, strain and Young's modulus, respectively. The subscripts c, f and m denote *composite*, *fibre* and *matrix*, respectively. This means that for a composite in which the fibres are much stiffer than the matrix - which is usually the case - the reinforcing fibres are subject to much higher stresses than the matrix. This is desired as it implies that the load is distributed while the high modulus fibres absorb a high proportion of the applied load. The overall or average stress and Young's modulus

of the composite can then be described as follows:

$$\sigma_c = (1 - f)\, \sigma_m + f\, \sigma_f \tag{3.6}$$

and

$$E_c = (1 - f)\, E_m + f\, E_f \tag{3.7}$$

where f denotes the volume fraction of the reinforcing fibres. Equation 3.6 and Equation 3.7 represent well-known *rules-of-mixture* which describe a weighted mean of the two composite constituent properties. These relations are however only valid in the direction of the fibre alignment due to the anisotropic behaviour of such a composite. When loaded in other directions, the composite material response has to be described by means of other relations.

The mechanism of mechanical load transfer between phases is a general feature and does not only occur in fibre-reinforced composite materials. Fibres as composite reinforcements are especially known for their effective load transfer capabilities as they can carry a high proportion of the applied loads. However, other composites including interpenetrating phase particle-reinforced composites exhibit similar load transfer capabilities although the effect is expectedly not as pronounced as in fibre-reinforced materials [106]. Furthermore, there are many other important and decisive aspects determining and influencing the overall properties of composite materials. One example in this respect would be fracture and failure mechanisms in composite materials which, however, can be regarded as an extensive research subject of its own. Details regarding these topics will not be covered within the present work while more information on these topics can for example be found in references [107–109].

3.4 Motivation for the use of tungsten-copper composites in plasma-facing components

The performance of a highly loaded divertor target PFC is most closely linked to the properties of the materials that are used for its design. A notable improvement of the performance of such a component can hence first and foremost be achieved by applying advanced materials with superior behaviour compared to existing and established PFC materials. Regarding the heat sink of highly loaded PFCs for future magnetic confinement thermonuclear fusion devices W-Cu MMCs can be regarded as suitable advanced materials due to the following reasons:

- W reinforcements in the W-Cu composite enhance the strength properties of the material, especially at elevated temperatures; this can be exploited in order to

overcome the issue of limited upper operating temperature of Cu alloys described in section 2.4.

- The Cu matrix leads to a high overall thermal conductivity of the composite, as well as an acceptably ductile material behaviour for sufficiently high Cu contents.
- The W-Cu material properties can - to some extent - be tailored by adjustment of the composite structure; this can for example be exploited by reducing the CTE mismatch with respect to W in order to minimise thermal stress levels at PFM to heat sink joints.
- The material system W-Cu is particularly suited for MMC fabrication by means of liquid infiltration of open porous W preforms due to the following reasons [59, 110]:
  - The binary system W-Cu does not show any interfacial reaction or mutual solubility. This means that there is no excessive matrix/inclusion interaction leading to dissolution of W in the matrix or the formation of intermetallic phases that make the material weak and/or brittle. Furthermore, no diffusion barrier coatings are necessary that would increase the cost of material fabrication.
  - There is a distinct difference in the melting points of Cu ($T_{m,Cu} = 1083\,°C$) and W ($T_{m,W} = 3400\,°C$).
  - The wettability of W with Cu melt is good.
- The basic constituent materials for W-Cu composites are readily and commercially available as semi-finished products.

The liquid Cu melt infiltration manufacturing approach for the W-Cu MMCs investigated within the present work is schematically illustrated in Figure 3.8.
Above, mainly the beneficial features of MMCs have been mentioned. However, the use of such composite materials does also implicate disadvantages. They can in principle be summarised as follows [84, 111]:

- The manufacturing of MMCs is comparably complicated. Therefore, the costs of fabrication are in general high.
- The characterisation of composites is typically more complicated compared with monolithic materials, especially if a composite exhibits anisotropic behaviour[1].

[1] This might also lead to the fact that the implementation of MMCs into design codes or standards is more difficult.

- Property mismatch between the different composite constituents can have a notable effect on the overall composite behaviour. For example, differential thermal expansivities can generate unfavourable internal stresses during material manufacturing or in service.

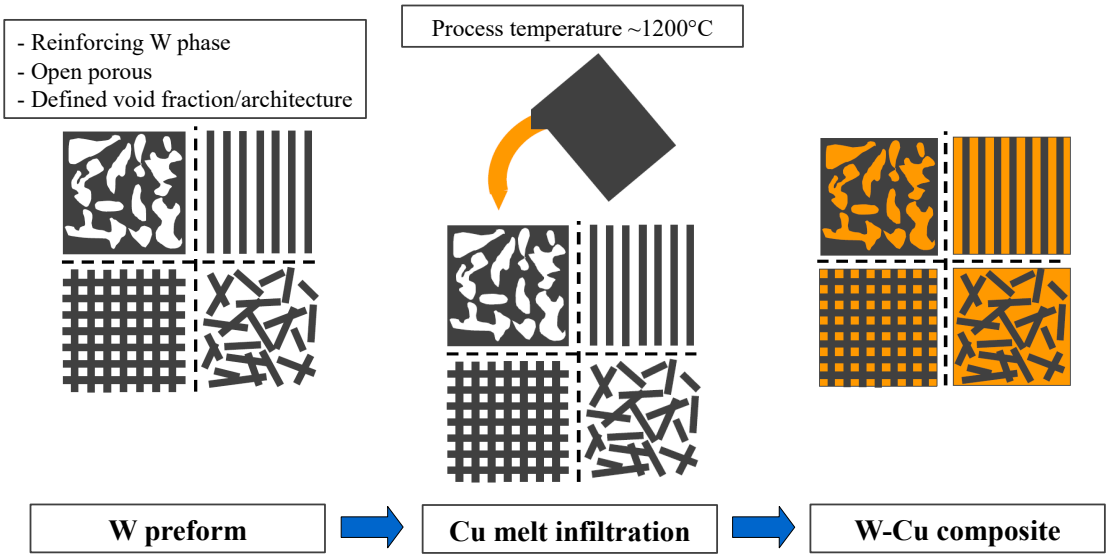

FIGURE 3.8: Schematic illustration of the W-Cu MMC manufacturing approach through liquid Cu infiltration followed within the present work.

Chapter 4

Tungsten particle-reinforced copper

4.1 General remarks

As mentioned within the outline in Chapter 1, one class of W-Cu MMCs of interest with regard to PFC heat sink application and investigated within the present work are *W particle-reinforced Cu* (W_p-Cu) composites [112]. Such MMCs are in principle known as it has long been recognised that these composite metals offer an interesting combination of material properties [113,114]. W_p-Cu composites can be fabricated by means of Cu melt infiltration of powder metallurgically produced open porous W compacts. Following such an approach, viable materials with compositions ranging from typically 60-40wt.% to 90-10wt.% W-Cu [60] - which corresponds to approximately 40-60vol.% to 80-20vol.% W-Cu - can be fabricated. This composition range offers notable flexibility in terms of realisable macroscopic material properties. Nowadays, W_p-Cu MMCs are for example used as circuit breakers in high voltage applications due to their high thermal and electrical conductivity, their high-temperature stability as well as their high ablation resistance [115].

4.2 Material manufacturing

The manufacturing of W_p-Cu materials can in principle be described as follows: W powder is pressed to a porous compact and subsequently sintered at comparably low temperatures. The resulting porosity of the W compact - which determines the amount of infiltrate within the later MMC - can be adjusted through the pressing and sintering parameters of the compact as well as by the sizing distribution of the used W powder. Infiltration with the Cu matrix is typically performed under hydrogen (H_2) atmosphere in order to reduce and hence avoid oxide layers that hinder the wetting of the porous W

preform and disturb the infiltration process [60].
Within the present work, W_p-Cu materials with differing W-Cu compositions were fabricated in cooperation with industry[1] according to the following process:

- Powder metallurgical production of an open porous W compact by means of uniaxial cold pressing[2].
- Sintering of the preform for 2 h at 1150 °C under H_2 or *high vacuum* (HV) atmosphere.
- Melt infiltration of the preform for 2 h at 1150 °C under H_2 or HV atmosphere.

Apart from that, W_p-Cu materials were fabricated with the following different Cu alloys[3] as matrix materials [116, 117]:

- Cu-OFE (EN material designation: Cu-OFE, CW009A)
- CuCrZr (EN material designation: CuCr1Zr, CW106C)
- CuCr (EN material designation: CuCr1, CW105C)

The infiltration of W_p-Cu materials with the precipitation hardenable alloys CuCrZr and CuCr was investigated due to the known issues with pure Cu under neutron irradiation as has been discussed in section 2.4. Especially, it was mentioned that CuCrZr exhibits superior void swelling resistance compared to pure Cu under neutron irradiation [66, 79] which means that a W-Cu composite with a Cu alloy matrix might be more suitable with respect to PFC applications in a D-T fusion environment. Furthermore, the infiltration of W-Cu composites with CuCrZr or CuCr is expected to be beneficial in terms of the mechanical properties of the material.
For material characterisation purposes, W_p-Cu plates with dimensions of 150 mm × 30 mm × 3 mm were manufactured as is exemplarily illustrated in Figure 4.1.

[1] Louis Renner GmbH, Bergkirchen, Germany
[2] As raw powder material for the compacts, a mixture of W powders with an average grain size of 4.0 ± 0.3 µm, as well as $12.0 + 1.0 \backslash -1.5$ µm measured by means of a *Fisher Subsieve Sizer* [115] according to ASTM B 330 was used.
[3] Conventional W_p-Cu materials are typically fabricated with addition of up to 2wt.% Nickel (Ni) in order to improve the wetting and hence the infiltration process [60, 114]. The W_p-Cu materials investigated within the present work, however, have been fabricated without the addition of Ni due to the following two reasons: On the one hand, the addition of Ni reduces the thermal conductivity of the material. On the other hand, Ni is a highly activating element under neutron irradiation that should hence be avoided strictly within a D-T fusion environment.

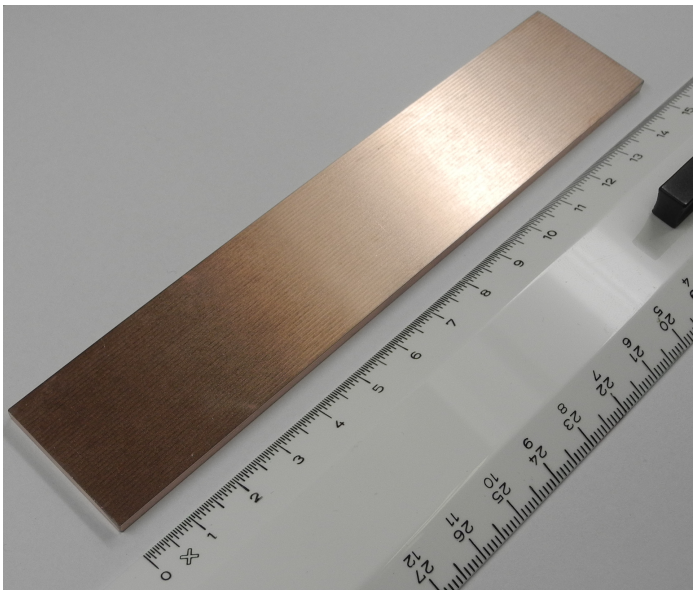

FIGURE 4.1: W_p-Cu MMC plate (nominal composition: 70-30wt.% W-Cu, infiltrated matrix: Cu-OFE) with dimensions of 150 mm x 30 mm x 3 mm.

4.3 Microstructure

Typical optical microsections[4] of W_p-Cu materials investigated within the present work are illustrated in Figure 4.2. In Figure 4.2a, a material with a nominal composition of 85–15wt.% W-Cu is shown while in Figure 4.2b a material with a nominal composition of 60–40wt.% W-Cu is illustrated. These materials do also represent the compositional boundaries for the W_p-Cu composites investigated within the present work. The microsections in Figure 4.2 illustrate the two different phases of the MMCs which can clearly be distinguished. Furthermore, it can be seen that the material is fully infiltrated with the Cu matrix and that it does not show plainly visible porosity which is an important prerequisite for adequate thermophysical and -mechanical properties of the material in general.

In Figure 4.3, typical *scanning electron microscopy* (SEM) images (backscattered electron images) of a W_p-Cu composite microsection of a material with a nominal composition of 60–40wt.% W-Cu is shown. As expected, a similar material constitution as in Figure 4.2 can be seen with no pronounced preferential direction of the reinforcing W phase. Moreover, Figure 4.3 illustrates that the typical size of the reinforcing W inclusions can be identified as on the order of $\leq 10\,\mu m$.

[4] The W_p-Cu microsections shown within this chapter were prepared plane parallel to the 150 mm × 30 mm dimensions into the thickness ($t = 3$ mm) of the plate material (cf. Figure 4.1). In general, the metallographic preparation of W-Cu MMC material samples was within the present work performed by wet grinding with SiC abrasives up to a grit of P4000 and polishing with diamond suspension with a grain size of 1 µm.

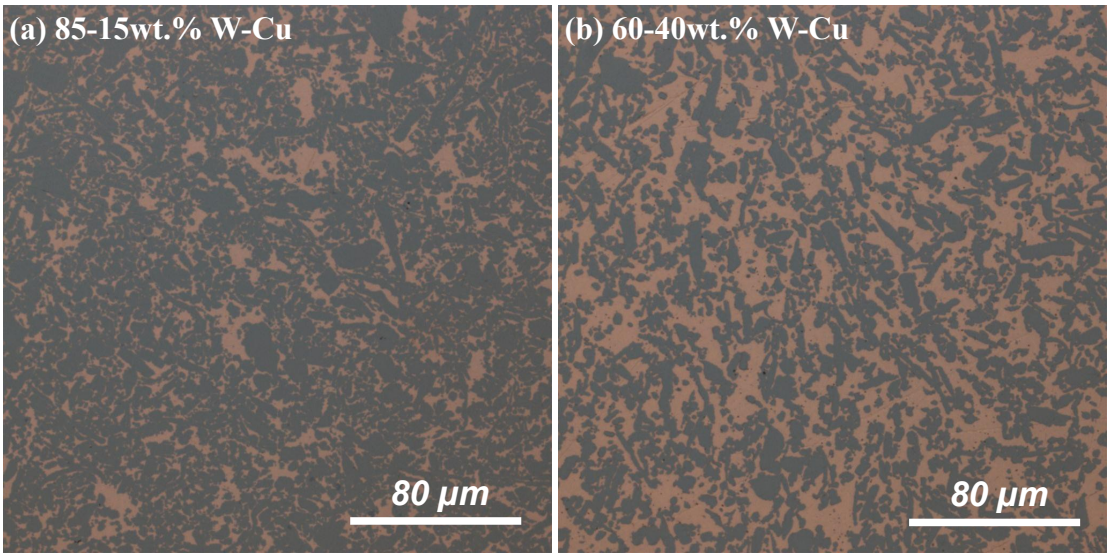

FIGURE 4.2: Typical optical microsections of W_p-Cu MMCs (infiltrated matrix: Cu-OFE) with (a) a nominal composition of 85–15wt.% W-Cu and (b) a nominal composition of 60–40wt.% W-Cu.

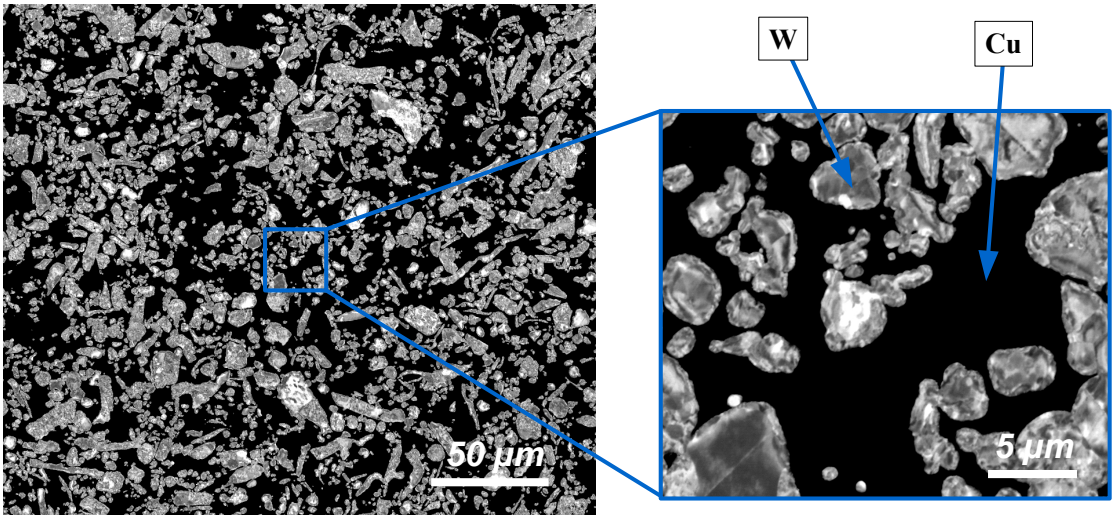

FIGURE 4.3: Typical SEM microsection (backscattered electron images) of a W_p-Cu MMC (infiltrated matrix: Cu-OFE) with a nominal composition of 60–40wt.% W-Cu.

4.4 Melt infiltration with copper alloys

As mentioned within section 4.2, melt infiltration of W_p-Cu materials was also investigated with the precipitation hardenable alloys CuCrZr and CuCr[5]. W_p-Cu materials infiltrated with these Cu alloys are expected to exhibit improved neutron irradiation resistance as well as superior mechanical properties compared to material infiltrated with pure Cu grades.

[5]W-Cu composites infiltrated with the Cu alloys CuCrZr or CuCr will in the following explicitly be referred to as *W-CuCrZr* and *W-CuCr*. The designation *W-Cu* is used as a general term for the composites under investigation or if the infiltrated matrix material is pure Cu, i.e. Cu-OFE.

In the course of the present work, three batches of W_p-CuCrZr materials with a nominal composition of 70–30wt.% W-CuCrZr were produced. In Figure 4.4, corresponding optical microsections are shown together with the measured *Vickers hardness*[6] (HV) of the materials. Batch III was additionally *solution annealed and aged* (SAA)[7] after

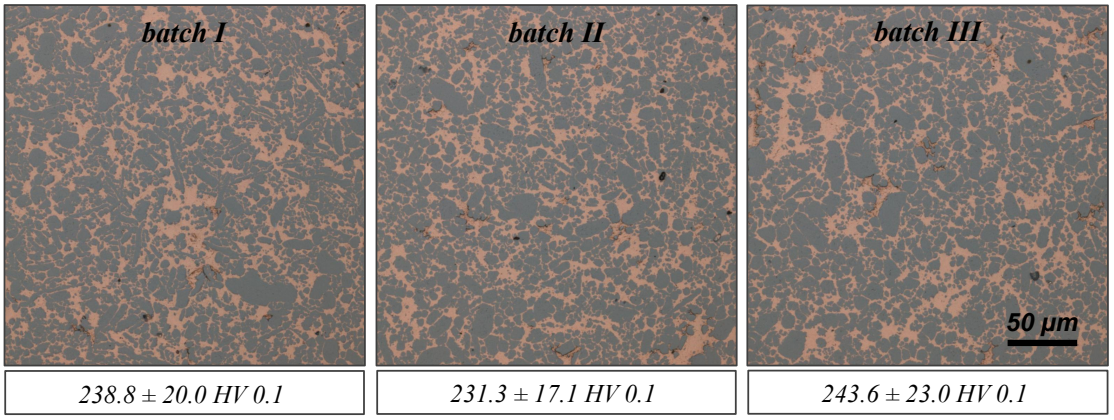

FIGURE 4.4: Optical microsections as well as measured HV of three different batches of W_p-CuCrZr with a nominal composition of 70–30wt.% W-CuCrZr.

the infiltration process. It can be seen that the different material batches exhibit a comparable, i.e. a reproducible, microstructure. Furthermore, it can be seen that the material with additional SAA treatment (batch III) does only exhibit a slightly higher hardness compared with the other two batches in as-infiltrated condition[8]. Moreover, chemical composition analyses[9] were performed on the W_p-CuCrZr materials illustrated in Figure 4.4. The corresponding results are given in Table 4.1.

TABLE 4.1: Results of chemical composition analyses for W_p-CuCrZr materials with a nominal composition of 70–30wt.% W-CuCrZr (standard deviations of the measurements are given in parentheses).

wt.%	*C*	*O*	*N*	*H*	*W*	*Cu*	*Cr*	*Zr*
batch I	0.0049 (0.0006)	0.0017 (0.0012)	< 0.0016	< 0.0002	68.0 (0.6)	30.8 (0.4)	0.195 (0.012)	0.203 (0.007)
batch II	0.0012 (0.0002)	0.0023 (0.0005)	< 0.002	< 0.0002	67.4 (0.4)	31.6 (0.5)	0.226 (0.017)	0.185 (0.003)
batch III	0.0011 (0.0003)	0.0016 (0.0005)	< 0.0018	< 0.0002	68.6 (0.7)	29 (0.4)	0.209 (0.019)	0.209 (0.006)

[6] The HV of the materials was evaluated based on 10 measurements with an applied load of 981 mN (0.1 *kp*) for a loading time of 30 s.

[7] A SAA heat treatment of CuCrZr typically comprises solution annealing at 950 °C to 1000 °C and subsequent ageing at 450 °C for 4 h [118].

[8] For comparison: The HV of a W_p-Cu material infiltrated with Cu-OFE and with the same nominal composition of 70–30wt.% W-Cu was measured as 197 ± 12.9 *HV* 0.1.

[9] The measurements were performed at Forschungszentrum Jülich, Zentralinstitut für Engineering, Elektronik und Analytik (ZEA-3). The following equipment/methods were used: Leco CS 600 C/S determinator; Leco TCH 600 N/O/H determinator; *inductively coupled plasma with optical emission spectroscopy* (ICP-OES) for W, Cu, Cr and Zr determination.

In principle, the results of the chemical composition analyses demonstrate that W_p-CuCrZr materials can be fabricated reasonably reproducible with a conclusive content of the alloying elements Cr and Zr within the material. Apart from that, the C, O, N and H contaminations can be regared as adequately low.

In order to get more insights into the microstructure of the W_p-CuCrZr material SEM and *energy dispersive X-ray spectroscopy* (EDX) analyses were performed. In Figure 4.5, an SEM microsection of a W_p-CuCrZr material with a nominal composition of 70–30wt.% W-CuCrZr (batch III according to Figure 4.4) with corresponding EDX maps for W, Cr and Zr are illustrated. It can be seen that submicrometre-sized Cr and Zr precipitates can be identified within the EDX maps while there are significantly more Cr than Zr precipitates visible in Figure 4.5. Furthermore, it can be seen from the stacked EDX maps (W+Cr & W+Zr) that these precipitates are only found at W-Cu interfaces[10].

With respect to W_p-CuCrZr material fabrication, however, it was found that on the surface of the molten and resolidified CuCrZr a slag layer was formed during the infiltration process. This phenomenon was further investigated as the formation of such layers could hinder the melt infiltration process. In Figure 4.6a, a cross section of a W_p-CuCrZr material assembly after infiltration is shown. A dark layer can be seen on the surface of the molten and resolidified CuCrZr. In Figure 4.6b, a corresponding SEM image of a *focused ion beam* (FIB) cross section through the CuCrZr surface for EDX analysis is illustrated. It can be seen that there is a closed layer on the surface of the CuCrZr with a thickness of approximately 1 µm. Results of the EDX analysis are illustrated in Figure 4.7 while from Figure 4.7a (Zr Lα) and Figure 4.7c (Pt Lα) it can be seen that the closed layer on the surface of the CuCrZr consists of Zr whereas Figure 4.7b (O Kα) shows that this is not an oxide layer which could be attributed to residual O contamination during the melt infiltration process[11]. Hence, the abovementioned figures illustrate that there is segregation of a Zr layer on the surface of molten and resolidified CuCrZr.

Based on these findings, melt infiltration experiments were performed with the binary alloy CuCr which does not contain Zr and could serve as a possible Cu alloy matrix material to ensure neutron irradiation resistance, adequate mechanical material properties as well as melt infiltration process stability. In Figure 4.8, a direct comparison between molten and resolidified CuCr and CuCrZr materials after an infiltration process is illustrated. It can unambiguously be seen that in contrast to CuCrZr (Figure 4.8b) the infiltration processing with binary CuCr (Figure 4.8a) does not create a segregated opaque layer on the surface of the molten and resolidified Cu alloy.

[10] The very small spots that are rather uniformly distributed over the Cr and Zr EDX maps in Figure 4.5 are attributed to noise.

[11] The characterisitc Zr Lα X-ray lines lie with 2.0424 keV (Lα_1) and 2.0399 keV (Lα_2) very close to the Pt Mα_1 line with 2.0505 keV. That is the reason why the Pt Lα lines with 9.4423 keV (Lα_1) and 9.3618 keV (Lα_2) were used to distinguish the Zr from the Pt layer that is needed for sample preparation [119].

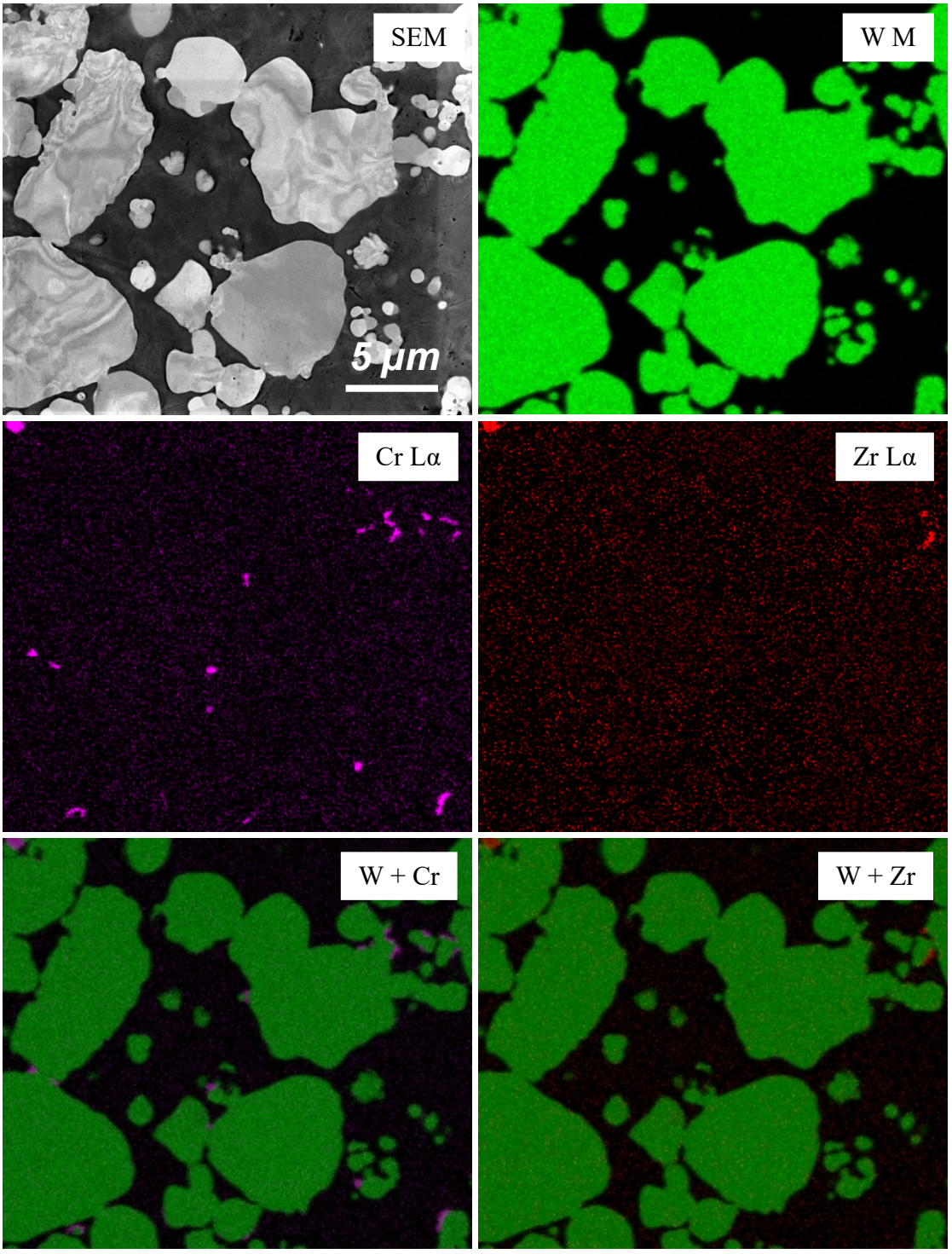

FIGURE 4.5: SEM microsection of a W_p-CuCrZr material with a nominal composition of 70–30wt.% W-CuCrZr (batch III according to Figure 4.4) with corresponding W, Cr and Zr EDX maps.

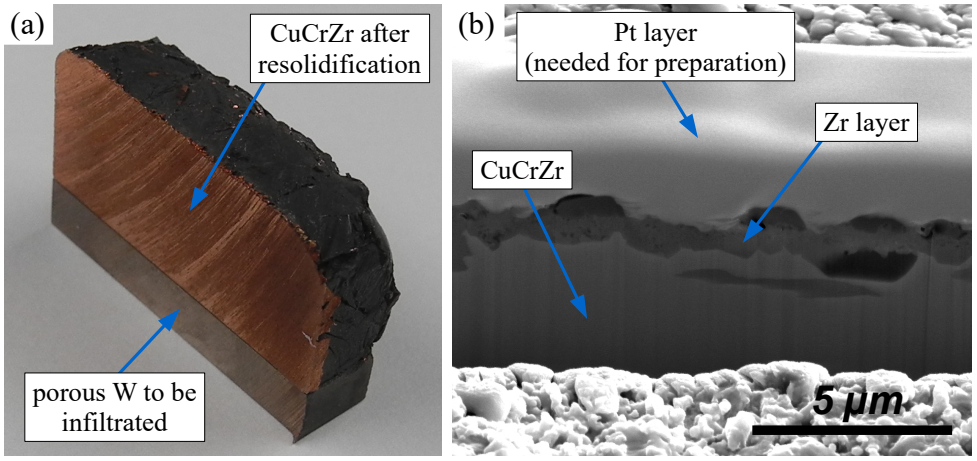

FIGURE 4.6: (a) Cross section through a W_p-CuCrZr material after infiltration and (b) corresponding SEM image of a FIB cross section through the CuCrZr surface for EDX analysis.

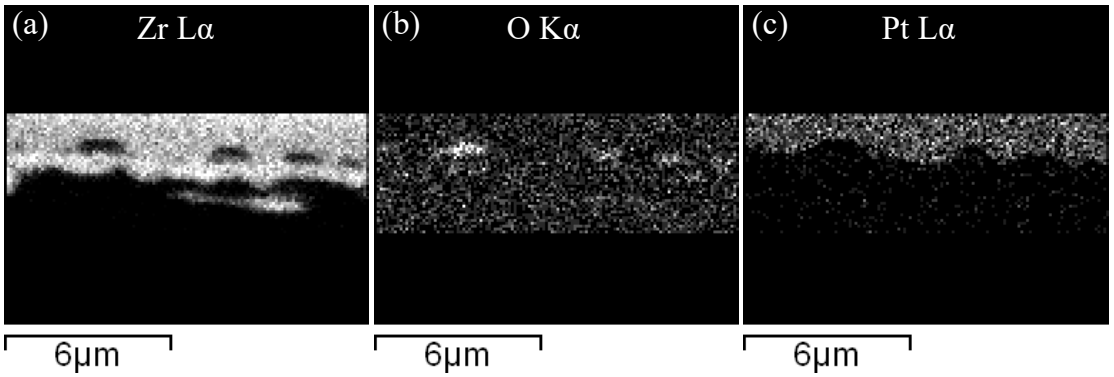

FIGURE 4.7: EDX maps for the cross section illustrated in Figure 4.6b: (a) Zr Lα, (b) O Kα and (c) Pt Lα.

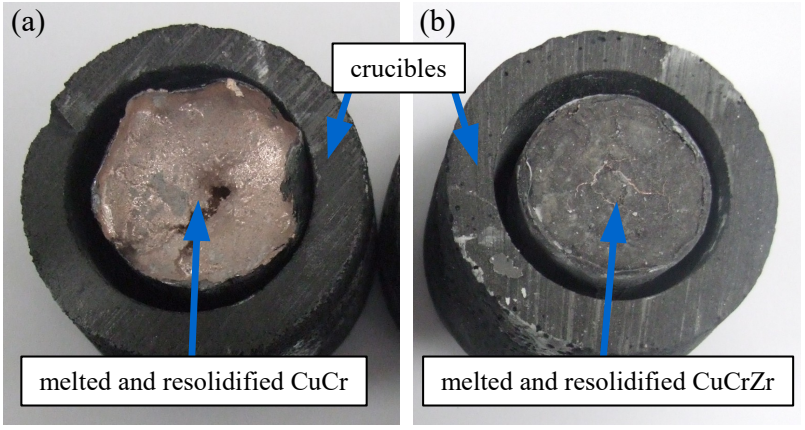

FIGURE 4.8: (a) CuCr and (b) CuCrZr material samples after melt infiltration processing; binary CuCr does not create a segregated opaque layer on the surface of the melted and resolidified Cu alloy.

4.5 Thermophysical and -mechanical properties

A high thermal conductivity is a paramount requirement for divertor PFC HSMs. Hence, this property has been determined experimentally based on *laser flash analysis* (LFA) measurements for W_p-Cu materials with different compositions (60-40wt.% W-Cu, 70-30wt.% W-Cu, 70-30wt.% W-CuCrZr[12], 85-15wt.% W-Cu)[13]. In Figure 4.9a, the measured *thermal diffusivities* for temperatures up to 1000 °C are shown while in Figure 4.9b corresponding *conductivities* for temperatures up to 900 °C are illustrated[14]. The thermal conductivity can be determined from the thermal diffusivity according to the following relationship [120]:

$$\lambda = \alpha \, \rho \, c_p \tag{4.1}$$

where λ $\left[\mathrm{W\,m^{-1}\,K^{-1}}\right]$ is the thermal conductivity, α $\left[\mathrm{m^2\,s^{-1}}\right]$ is the thermal diffusivity, ρ $\left[\mathrm{kg\,m^{-3}}\right]$ is the mass density and c_p $\left[\mathrm{J\,kg^{-1}\,K^{-1}}\right]$ is the specific heat capacity[15]. The thermal conductivity is a material property that defines the magnitude of the heat rate that can be transferred within a material in the direction of a flux per unit length and per unit temperature difference. The thermal diffusivity, which is quantity that is accessible through LFA measurements, is a material characteristic that describes how quickly the temperature distribution within a body changes when cooled or heated from the outside [120].

In Figure 4.9a, it can be seen that, as expected, the thermal diffusivities of the investigated W_p-Cu materials are decreasing with increasing W content as well as decreasing with increasing test temperature. Specifically, it can be seen that the material with a composition of 60-40wt.% W-Cu exhibits a thermal diffusivity of nearly $85\,\mathrm{mm^2\,s^{-1}}$ at 50 °C while this value decreases to somewhat below $60\,\mathrm{mm^2\,s^{-1}}$ at 1000 °C. Furthermore, it can be seen that the material with a composition of 85-15wt.% W-Cu exhibits a thermal diffusivity of up to approximately $65\,\mathrm{mm^2\,s^{-1}}$ at 50 °C while this value decreases to below $50\,\mathrm{mm^2\,s^{-1}}$ at 1000 °C. Moreover, data regarding W_p-CuCrZr material with a composition of 70-30wt.% is included in Figure 4.9a. It can be seen that this material shows overall a lower thermal diffusivity compared to the material with the same nominal composition but with an infiltrated Cu-OFE matrix.

The thermal conductivities of the investigated W_p-Cu materials illustrated in Figure 4.9b exhibit in general the same trends as the thermal diffusivities shown in Figure 4.9a. It can be seen that the material with a composition of 60-40wt.% W-Cu exhibits a thermal

[12] As-infiltrated W_p-CuCrZr material without SAA heat treatment (batch I according to Figure 4.4)

[13] The LFA measurements on W_p-Cu materials were performed in the framework of research activities within the EUROfusion work package materials (WPMAT) at the National Institute of Materials Physics, Bucharest-Magurele, Romania. For each material composition four samples were measured.

[14] The data illustrated in Figure 4.9 is given as tabulated values in Appendix B.

[15] The thermal conductivities illustrated in Figure 4.9b were calculated with mass density and specific heat capacity values determined with a linear rule-of-mixture based on data from [121]. These values are also given in tabular form in Appendix B.

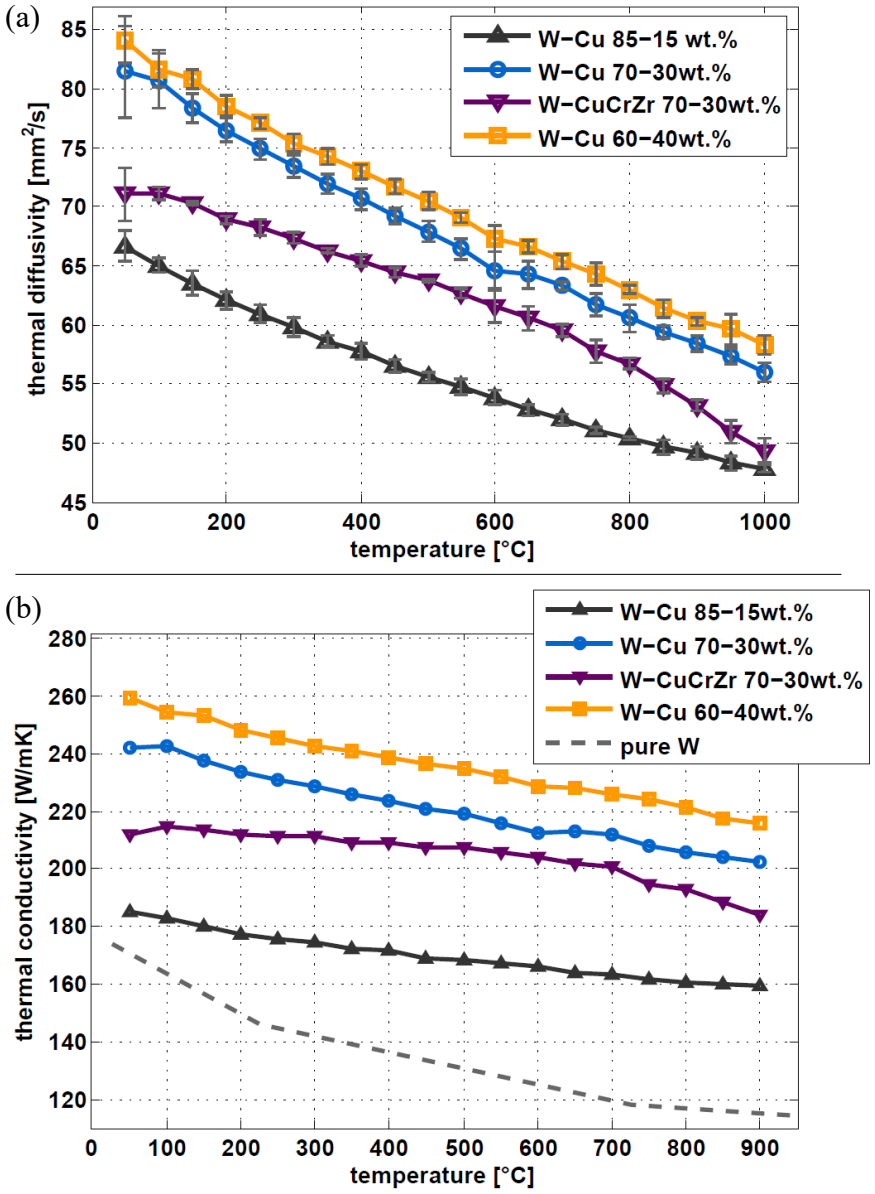

FIGURE 4.9: (a) Measured thermal diffusivities (errorbars indicate the standard deviation of the measured values) as well as (b) thermal conductivities of W_p-Cu materials with differing compositions (60-40wt.% W-Cu, 70-30wt.% W-Cu, 70-30wt.% W-CuCrZr, 85-15wt.% W-Cu).

conductivity of up to approximately $260\,W\,m^{-1}\,K^{-1}$ at 50 °C while this value decreases to somewhat below $220\,W\,m^{-1}\,K^{-1}$ at 900 °C. Furthermore, it can be seen that the material with a composition of 85-15wt.% W-Cu exhibits a thermal conductivity of up to approximately $185\,W\,m^{-1}\,K^{-1}$ at 50 °C while this value decreases to slightly below $160\,W\,m^{-1}\,K^{-1}$ at 900 °C. For reasons of comparison, the thermal conductivity of pure W is also included in Figure 4.9b [60] and it can be seen that, as expected, the W_p-Cu composites exhibit in general a substantially higher thermal conductivity compared with

pure W[16]. Moreover, the data regarding the W_p-CuCrZr material with a composition of 70-30wt.% included in Figure 4.9b illustrates that this material shows overall a lower thermal conductivity compared to the material with the same nominal composition but with an infiltrated Cu-OFE matrix. This behaviour is plausible as CuCrZr alloy exhibits a notably lower thermal conductivity compared with Cu-OFE [78, 122].

In Figure 4.10, the CTEs of W_p-Cu materials with three different compositions (60-40wt.% W-Cu, 70-30wt.% W-Cu, 85-15wt.% W-Cu) based on dilatometer measurements[17] are illustrated for temperatures ranging from 150 °C up to 900 °C[18]. For reasons

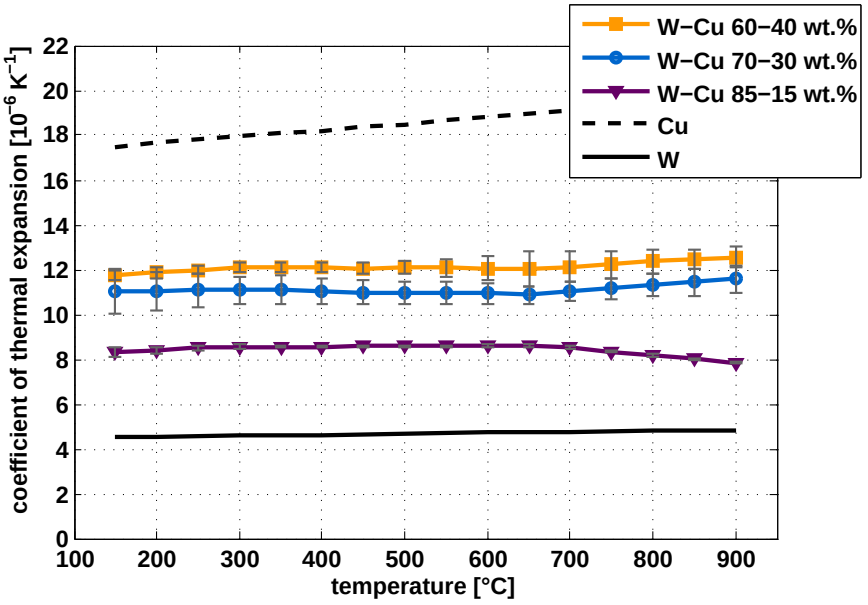

FIGURE 4.10: Measured CTEs of W_p-Cu materials (errorbars indicate the standard deviation of the measured values) with differing compositions (60-40wt.% W-Cu, 70-30wt.% W-Cu, 85-15wt.% W-Cu) in comparison to monolithic Cu and W [121].

of comparison, the CTEs of monolithic Cu and W [121] are also included in Figure 4.10. It can be seen that the W_p-Cu composites exhibit a significantly reduced macroscopic CTE compared with monolithic Cu. For example, it can be deduced from Figure 4.10 that the material with a composition of 70-30wt.% W-Cu exhibits a CTE of approximately $11 \times 10^{-6}\,\mathrm{K}^{-1}$. It can hence be concluded that the investigated W_p-Cu materials can indeed be used to effectively mitigate thermal stresses due to CTE mismatch at W PFM to PFC heat sink joints.

[16] Pure Cu exhibits a thermal conductivity of $401\,\mathrm{W\,m^{-1}\,K^{-1}}$ at 20 °C and $340\,\mathrm{W\,m^{-1}\,K^{-1}}$ at 900 °C [121].

[17] The CTE measurements on W_p-Cu materials were performed in the framework of research activities within the EUROfusion work package materials (WPMAT) at the National Institute of Materials Physics, Bucharest-Magurele, Romania. The CTE was determined from heating curves with a reference temperature of 30 °C while three samples were measured for each material composition.

[18] The data illustrated in Figure 4.10 is given as tabulated values in Appendix B.

Furthermore, the mechanical properties of W_p-Cu composites were investigated[19]. Especially, the influence of differing Cu matrix contents as well as the influence of an infiltrated CuCrZr matrix[20] on the mechanical properties were investigated. Exemplarily, the tensile properties of the investigated W_p-Cu materials are illustrated in Figure 4.11 and discussed in the following. For further details regarding the mechanical characterisation and properties of the investigated W_p-Cu materials the reader is referred to [112,123,124]. In Figure 4.11a and Figure 4.11b, the 0.2% yield as well as *ultimate tensile strength* (UTS) of the W_p-Cu composites for test temperatures up to 800 °C are shown. It can be seen

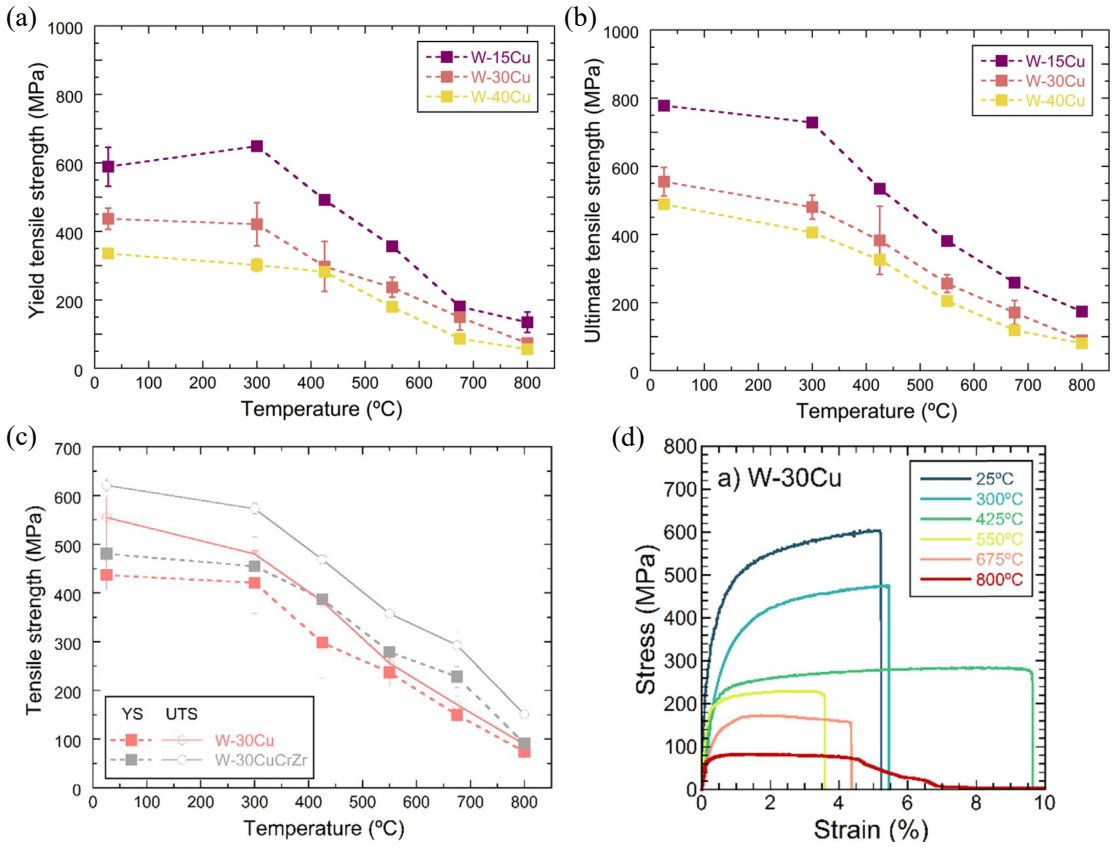

FIGURE 4.11: (a) 0.2% yield tensile strength of W_p-Cu composites (60-40wt.% W-Cu, 70-30wt.% W-Cu, 85-15wt.% W-Cu) as a function of composition and test temperature and (b) corresponding UTS; (c) comparison of yield tensile strength and UTS for 70-30wt.% W_p-Cu and 70-30wt.% W_p-CuCrZr; (d) typical stress-strain curves for a 70-30wt.% W_p-Cu composite at different test temperatures [123,124].

that, as expected, there is an increase in strength for increasing W contents as well as a decrease in strength for increasing test temperatures. In particular, it can be seen that the material with a composition of 70-30wt.% W-Cu - which corresponds to approximately 50-50vol.% W-Cu - exhibits a UTS of around 550 MPa at *room temperature* (RT) as well as approximately 400 MPa at a test temperature of 425 °C. In textbook

[19] These investigations were conducted in cooperation with the Departamento de Ciencia de Materiales-CIME, Universidad Politécnica de Madrid, C/ Profesor Aranguren 3, E28040 Madrid, Spain and have been published within [123,124].

[20] As-infiltrated W_p-CuCrZr material without SAA heat treatment (batch I according to Figure 4.4)

literature, a tensile strength of 390 MPa at RT is reported for a W_p-Cu material with a composition of 70-30wt.% W-Cu [60]. It can hence be concluded that the W_p-Cu materials investigated within this work exhibit comparably high strength properties. In Figure 4.11c, the influence of an infiltrated CuCrZr matrix on the tensile strength properties of a W_p-Cu material with a nominal composition of 70-30wt.% W-Cu is illustrated. It can be seen that there is a notable impact and that the yield and UTS properties of the material with an infiltrated CuCrZr matrix are superior. This holds true over the entire investigated temperature range up to 800 °C while the general trend of decreasing strength properties over test temperature is similar for both materials. In particular, the W_p-CuCrZr material investigated within the present work exhibits a tensile strength of more than 550 MPa at 300 °C as well as approximately 350 MPa at 550 °C. These numbers are notably higher compared to data for W_p-CuCrZr from [125] where material with a comparable composition exhibited a tensile strength of approximately 450 MPa at 300 °C and 250 MPa at 550 °C. It can hence be concluded that the W_p-CuCrZr materials investigated within the present work exhibit comparably high strength properties. In Figure 4.11d, typical stress-strain curves for a W_p-Cu material with a nominal composition of 70-30wt.% W-Cu and for different test temperatures are illustrated. In principle, the curves indicate that the material exhibits several percent of fracture strain, also at RT, which can be considered a reasonably ductile behaviour.

For reasons of comparison, the tensile strength properties of CuCrZr alloy for PFC heat sink applications are illustrated in Figure 4.12 [126]. The data illustrated refers to Cu-

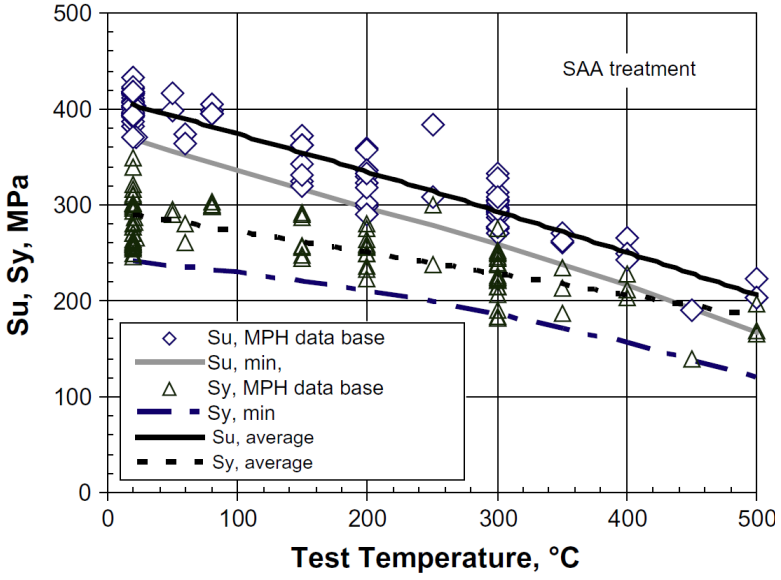

FIGURE 4.12: UTS (Su) and yield tensile strength (Sy) of CuCrZr alloy in SAA condition according to [126].

CrZr alloy in SAA condition which can be regarded as the most common and relevant treatment. In Figure 4.12, it can be seen that the average UTS for CuCrZr ranges

from approximately 400 MPa at RT down to 200 MPa at 500 °C while the average yield strength ranges from approximately 300 MPa at RT down to below 200 MPa at 500 °C. This means that these average strength properties of CuCrZr in SAA condition are lower compared to all the W_p-Cu and W_p-CuCrZr materials investigated within the present work (cf. Figure 4.11).

4.6 Flat-tile type plasma-facing component mock-ups

The investigated W_p-Cu materials have not only been characterised with respect to their basic thermophysical and -mechanical properties. They have also been examined by means of HHF tests. To that end, flat-tile type PFC mock-ups that comprised a W_p-Cu heat sink block with a composition of 70-30wt.% W-Cu were manufactured. In Figure 4.13, the dimensions of the manufactured mock-ups are illustrated. The main

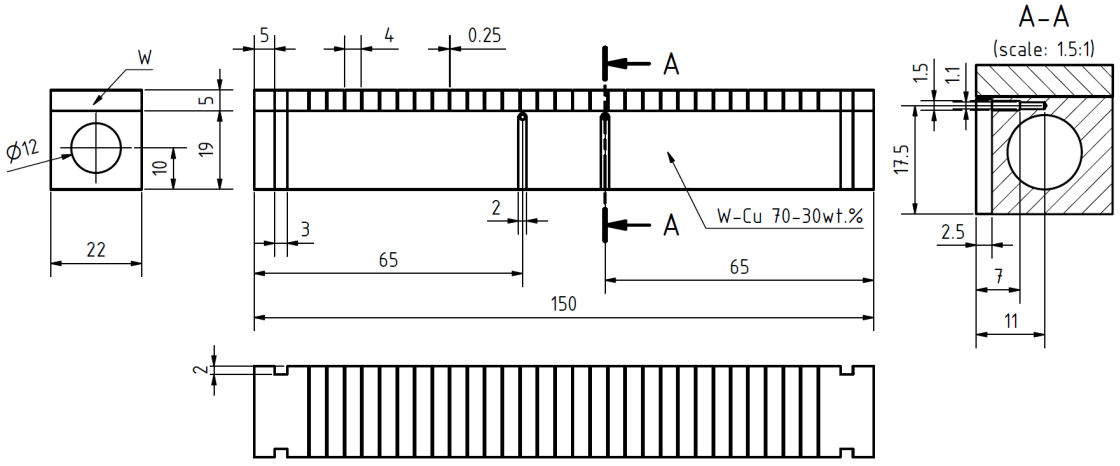

FIGURE 4.13: Dimensions of flat-tile type PFC mock-ups for HHF testing with W_p-Cu MMC heat sink; the sectional view on the right illustrates machinings for the insertion of thermocouples.

expected beneficial effect of such a design lies in a reduced CTE mismatch between the W PFM tiles and the W_p-Cu MMC heat sink. Ultimately, this mitigates the risk of failure at or near the bonding interface as stress concentrations occurring at the free edges of the bond interface are relaxed. The issue with stress singularities at the interface of bonded dissimilar materials under mechanical and thermal loading was investigated in [127, 128] and applied to joints of highly heat loaded PFCs in [129]. When considering a *two-dimensional* (2D) problem as illustrated in Figure 4.14 the stresses σ_{ij} near the free edge of the joint exhibiting contact angles of $\theta_1 = \theta_2 = 90°$ can be described by the following relation [128]:

$$\sigma_{ij} = -\Delta T \Delta\alpha \left[\frac{1}{E_1^*} - \frac{1}{E_2^*}\right]^{-1} \left[\frac{-K_L/\sigma_0}{(r/L)^{\omega}} f_{ij} - f_{ij0}\right] \tag{4.2}$$

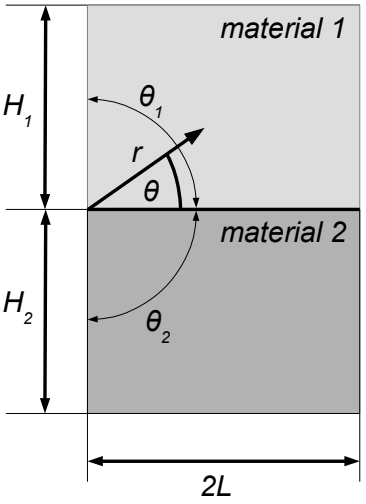

FIGURE 4.14: Schematic illustration of a bimaterial joint with contact angles of $\theta_1 = \theta_2 = 90°$.

where ΔT is a change in temperature, $\Delta\alpha$ is defined as

$$\Delta\alpha = \begin{cases} \alpha_1 - \alpha_2 & \text{for plane stress} \\ \alpha_1 (1+\nu_1) - \alpha_2 (1+\nu_2) & \text{for plane strain} \end{cases} \tag{4.3}$$

and E_i^* are the effective moduli that can be determined as

$$E_i^* = \begin{cases} \dfrac{E_i}{\nu_i} & \text{for plane stress} \\ \dfrac{E_i}{\nu_i(1+\nu_i)} & \text{for plane strain} \end{cases} \tag{4.4}$$

K_L is the stress intensity factor and σ_0 is a constant stress term. Both these quantities are proportional to ΔT and $\Delta\alpha$ while they also dependent on the elastic properties of the materials. Furthermore, K_L depends on the external loading and has in principle to be determined from numerical stress analysis. The quantity r/L is the normalised distance from the free edge of the bonding interface (cf. Figure 4.14), ω is the stress exponent and f_{ij}/f_{ij0} are angular functions. The latter two quantities depend on the so-called *Dundurs' parameters* which in turn are functions of the Young's moduli as well as the Poisson's ratios of both materials [128]. In Equation 4.3 and Equation 4.4, ν denotes the Poisson's ratio and E denotes the Young's modulus of the materials. Equation 4.2 is derived under the following assumptions:

- Perfect bonding between the joined materials,
- isotropic, linear-elastic material behaviour[21] and

[21] The assumption of linear-elastic material behaviour is typically not fulfilled close to the free edge of the joint where high stresses occur. However, linear-elastic calculations indicate the general effect of material properties and very often the plastic zone may be considered to be negligibly small.

- temperature-independent material properties.

From Equation 4.2, it can be seen that the interface stresses are directly proportional to $\Delta\alpha$, the CTE mismatch between the bonded materials. This means that minimising the CTE mismatch between a W PFM tile and the PFC heat sink mitigates thermal stresses at the joint straightforwardly. Moreover, it can be seen that there is a size effect due to the term L^{ω} which implies that smaller dimensions do in general result in lower interface stresses. For further details regarding the definition of all the quantities that appear in Equation 4.2 as well as their behaviour the reader is referred to [127–129].

As the high stresses at the free edges of a bonding interface in a flat-tile type PFC design may cause failure of or near the interface these free edges are considered the weakest site in a flat-tile design. Associated with this, there exists also the basic concern that the detachment of a single tile could affect neighbouring tiles and trigger a cascade failure that ultimately limits the overall integrity of the PFC [52, 130]. Nevertheless, a PFC armoured with W flat tiles joined to a CuCrZr heat sink block will be used for the ITER divertor *dome* [50]. This flat-tile design concept allows a relatively straightforward fabrication process as well as the application of a hypervapotron[22] cooling structure. However, due to the abovementioned issues, the ITER dome flat-tile type PFCs are only used in regions where they face reduced heat flux loadings of $5\,\mathrm{MW\,m^{-2}}$ during steady state operation [133].

As already mentioned in section 2.2.2, joining of differing materials for the manufacture of a highly loaded PFC is a critical and technologically challenging issue. Regarding the mock-ups with W_p-Cu composite heat sink, the bonding of the W PFM tiles was realised simultaneously during the melt infiltration of the MMC heat sink within a one-temperature process. The manufacturing procedure for the mock-ups can accordingly be described as follows:

- The porous W compact for the W_p-Cu composite heat sink block is assembled together with a W plate within a mould.
- The assembly is Cu infiltrated bonding simultaneously the W PFM to the W_p-Cu composite heat sink block.
- The joined assembly is machined to the desired dimensions, including the cooling channel as well as the castellation[23] of the W plate.

In Figure 4.15, a picture of a flat-tile type PFC mock-up manufactured according the abovementioned procedure as well as a corresponding side view are shown. In Figure 4.16,

[22] A hypervapotron is an actively cooled device in which the coolant flows over a perpendicularly finned surface [131]. Due to boiling/condensation effects, such a cooling channel design offers very good cooling capabilities, especially in terms of *critical heat flux* (CHF) [132].

[23] In general, small W PFM armour tiles are desired in a PFC as has also been mentioned in the context of Equation 4.2 that contains the size term L^{ω}. That is the reason why a W castellation is typically applied in PFCs in order to mitigate thermally induced stresses under HHF loading.

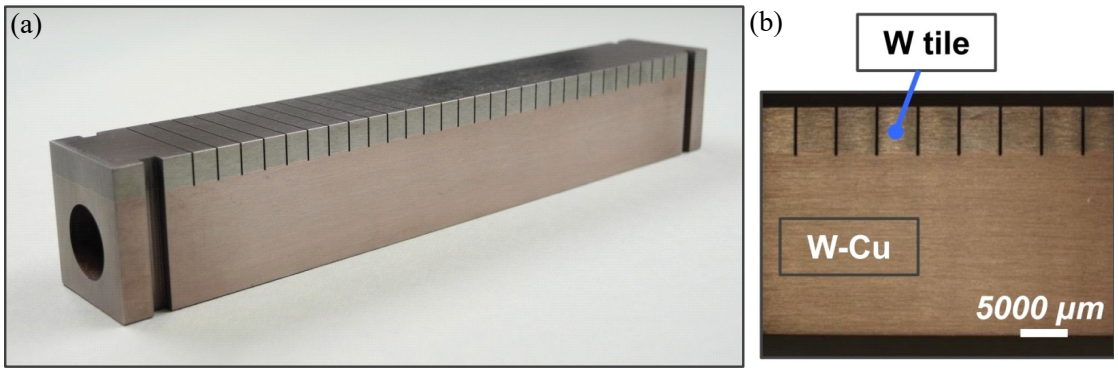

FIGURE 4.15: (a) Flat-tile type PFC mock-up for HHF testing with W_p-Cu MMC heat sink (70-30wt.% W-Cu) and (b) side view of the mock-up.

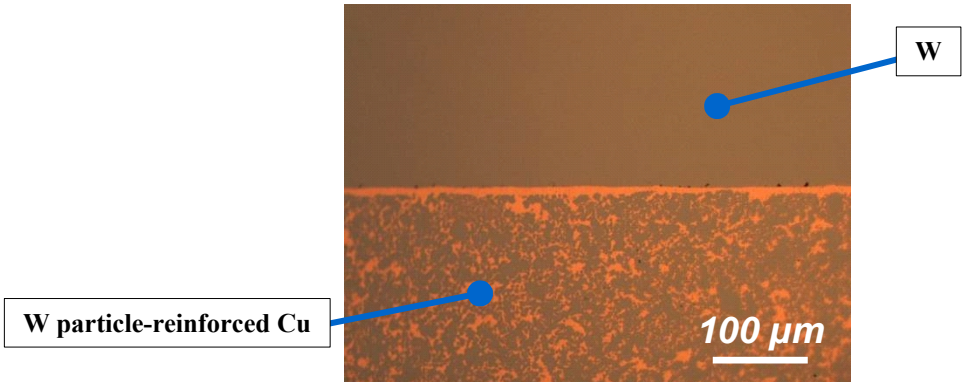

FIGURE 4.16: Optical microsection of a W/W_p-Cu joint produced through bonding monolithic W to the W_p-Cu material during the Cu melt infiltration process.

an optical microsection of a W/W_p-Cu joint that has been produced with the melt infiltration procedure applied during mock-up fabrication is illustrated. It can be seen that the joint quality is sound demonstrating the viability of the applied joining procedure. Furthermore, it can be seen that a Cu layer with a thickness of approximately 10 µm develops in between the materials during the melt infiltration/joining.

The mock-up as illustrated in Figure 4.15 was loaded within the HHF test facility *GLADIS* (Garching Large Divertor Sample Test Facility)[24,25] with the following *cold-water* cooling conditions:

- Coolant inlet temperature of $T_{in} = 20\,°C$,
- static coolant pressure of $p_{static} = 10\,bar$,
- coolant flow velocity of $v = 12\,m\,s^{-1}$ and
- use of a swirl tape insert with a twist ratio[26] of 2 and a tape thickness of 0.8 mm.

[24] A description of the HHF test facility GLADIS can be found in Appendix A.

[25] The HHF tests reported on in the present work were performed in the framework of research activities within the EUROfusion work package divertor (WPDIV).

[26] The twist ratio is defined as the number of diameter lengths per 180° twist [130].

HHF loading was applied as follows[27]:

- HHF screening up to 22 MW m^{-2} as well as
- cyclic HHF loading up to 370 cycles at 20 MW m^{-2}.

Complementary to the HHF testing, 2D thermal FEA was performed[28] for which the W_p-Cu material property data discussed above in section 4.5 was used as input. In Figure 4.17, the main results of the FEA are illustrated: Maximum surface temperature ($T_{max,surf}$), maximum temperature at the W/W_p-Cu joint ($T_{max,joint}$), maximum temperature at the cooling channel surface ($T_{max,cool}$) and temperature at the thermocouple tip position (T_{TC}) versus applied heat load. Furthermore, experimentally determined data is included in the plot: Measured thermocouple temperatures ($T_{TC,1}, T_{TC,2}$) as well as pyrometric surface temperature measurements ($T_{pyrometer}$). It can be seen that for a

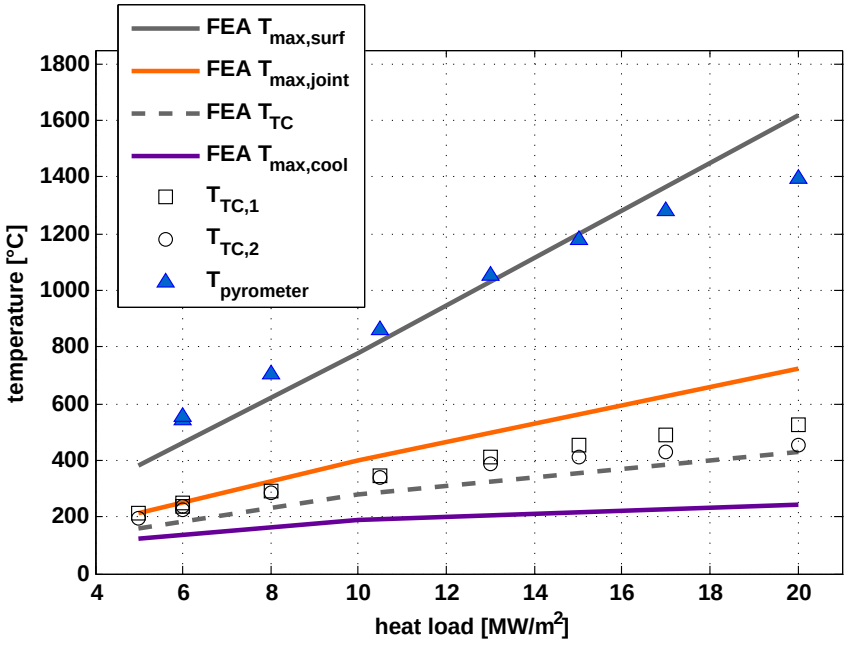

FIGURE 4.17: Results of 2D thermal FEA of W flat-tile type PFC mock-up with W_p-Cu MMC heat sink and dimensions as illustrated in Figure 4.13 under HHF loading: Maximum surface temperature ($T_{max,surf}$), maximum temperature at the W/W_p-Cu joint ($T_{max,joint}$), maximum temperature at the cooling channel surface ($T_{max,cool}$) and temperature at the thermocouple tip position (T_{TC}) versus applied heat load. Furthermore, experimentally determined data is included in the plot: Measured thermocouple temperatures ($T_{TC,1}, T_{TC,2}$) as well as pyrometric surface temperature measurements ($T_{pyrometer}$).

heat loading of 20 MW m^{-2} the maximum surface temperature is predicted to be slightly higher than 1600 °C and the maximum temperature at the W/W_p-Cu joint - which also

[27] During all the HHF tests reported on in the present work applied heat pulses had a duration of 10 s.

[28] The simulations were performed with Abaqus/CAE 2016. The mesh had a total number of 1820 elements (1783 linear quadrilateral elements of type DC2D4, 37 linear triangular elements of type DC2D3) and a total number of 1931 nodes. The heat transfer at the cooling channel surface was modeled as surface film condition with the heat transfer coefficient given in Appendix B.

corresponds to the maximum temperature the W_p-Cu MMC is subjected to - is predicted to reach more than 700 °C. Furthermore, it can be stated that the agreement between the temperatures predicted by FEA and the experimentally determined values can be regarded as reasonable. In general, it should be considered that pyrometric surface temperature measurements can only be regarded as indicative as they depend sensitively on the emissivity of the heat loaded surface. In turn, the emissivity is a quantity that depends strongly on temperature, wavelength as well as surface condition. Therefore, pyrometric surface temperature measurements on PFC mock-ups during HHF testing are typically not considered as quantitatively reliable. Apart from that, it can be seen that the thermocouple measurements included in Figure 4.17 follow the temperature trend predicted by the FEA although there seems to be a rather constant offset. This behaviour is attributed to the high temperature gradients that occur in the measurement region[29] in combination with the fact that the thermocouple wire exhibits in this respect a comparably large diameter of 1 mm[30]. Moreover, in Figure 4.18 exemplary FEA results are illustrated for a HHF loading with 10 MW m^{-2}. In Figure 4.18a, the temperature distribution is illustrated while in Figure 4.18b the heat flux distribution is shown. It

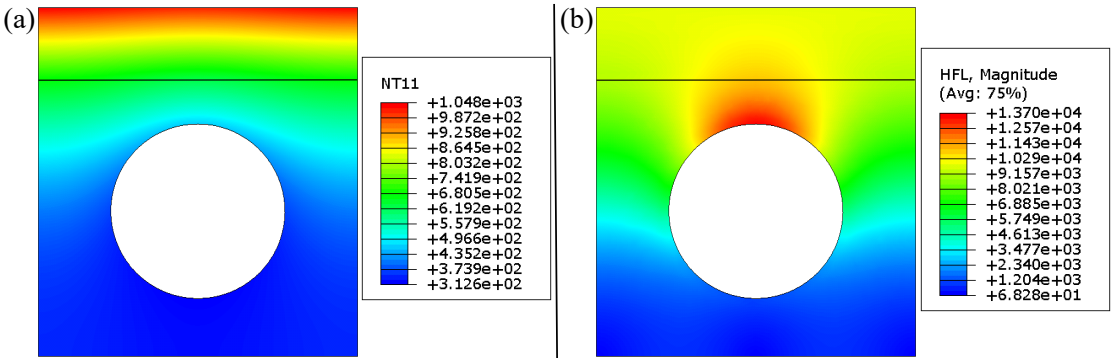

FIGURE 4.18: Exemplary thermal FEA results of W flat-tile type PFC mock-up with W_p-Cu MMC heat sink for a HHF loading with 10 MW m^{-2}: (a) Temperature distribution (scale in K) and (b) heat flux distribution (scale in kW).

can be seen that, as expected, the highest temperatures ($T_{max,surf}$ = 775.35 °C) occur at the W PFM tile surface edges and that heat flux peaking occurs at the apex of the cooling channel (q_{max} = 13.7 MW m^{-2}, q_{max}/q_{nom} = 1.37).

The main results of the HHF testing can be summarised as follows: The mock-up exhibited a stable behaviour during scrennning up to 22 MW m^{-2} which indicated a good manufacturing quality of the W_p-Cu MMC as well as the W/W_p-Cu joint. During the cyclic loading with 20 MW m^{-2} no deterioration of HHF performance was detected up

[29] For a heat loading of 20 MW m^{-2}, a temperature gradient of (726.7 °C − 431.98 °C/1.5 mm) = 196.48 K mm^{-1} is predicted by FEA for the region in between the W/W_p-Cu joint and the thermocouple tip position.

[30] The following K type thermocouples were used: THERMOCOAX 2ABI 10/750MM/TI/MFM9M.

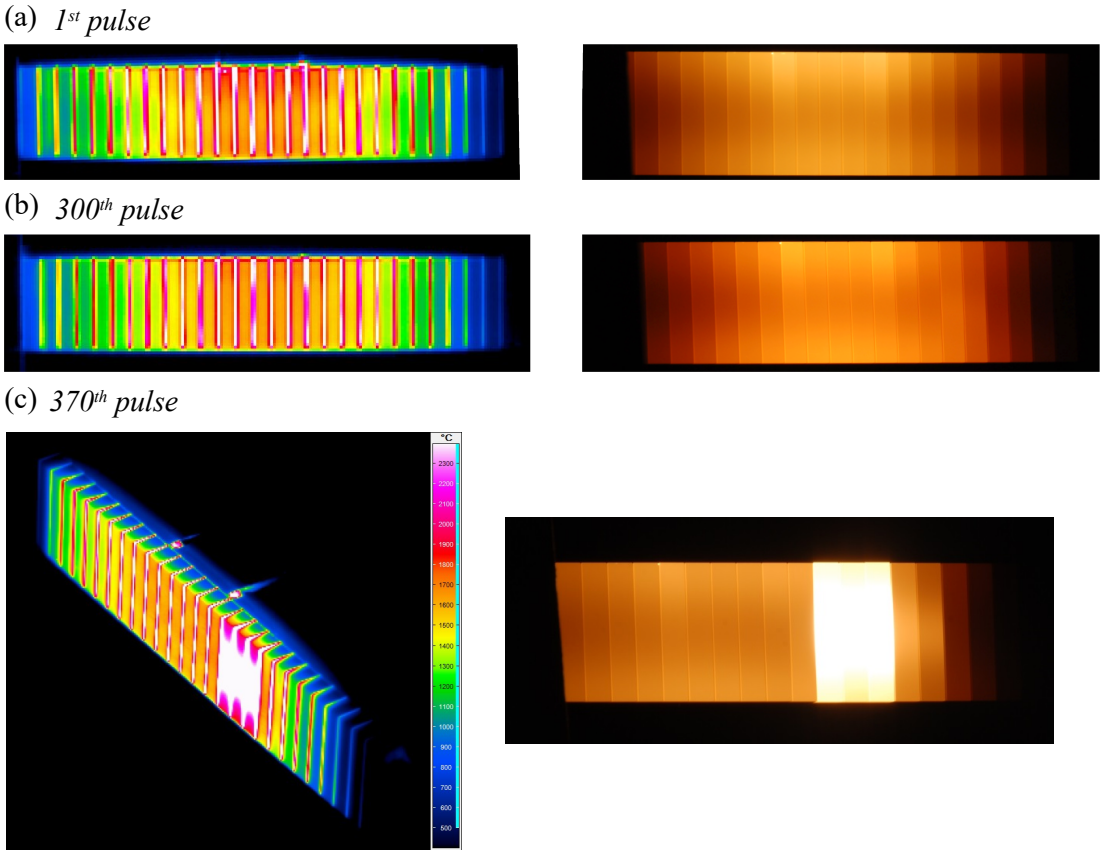

FIGURE 4.19: IR and optical images of W flat-tile type PFC mock-up with W_p-Cu MMC heat sink (illustrated in Figure 4.15) during HHF testing: (a) 1st pulse, (b) 300th pulse and (c) 370th pulse.

to 300 pulses which corresponds to the design qualification criterion for the ITER divertor target at 20 MW m^{-2} [50, 69]. Further cyclic loading of the mock-up lead to the development of bonding defects at the W/W_p-Cu joint. The experiment was continued up to 370 load cycles at 20 MW m^{-2} where W tile overheating due to detachment was unambiguously visible. In Figure 4.19, optical as well as *infrared* (IR) images during the HHF loading of the mock-up for pulse numbers 1, 300 and 370 are illustrated. It can be seen that the temperature distributions are homogeneous and qualitatively similar for pulse numbers 1 and 300 but that there are hot spots, i.e. overheating W tiles, visible during pulse number 370. In Figure 4.20, post HHF images of the mock-up after 370 applied load cycles at 20 MW m^{-2} are shown. In Figure 4.20a, the centred top view on the heat loaded W tiles of the mock-up is shown. No significant material degradation or macroscopic cracking can be seen. In Figure 4.20b, a side view on the partially detached W armour tiles and the W/W_p-Cu bond interfaces is illustrated. The magnified image shows the W tile debonding that developed during the cyclic HHF loading. Furthermore, it can be seen that melting of the Cu layer occured at the bond interface due to tile overheating. In Figure 4.20c, a metallographic cross section of the mock-up through a partially detached W tile - as indicated by the white arrow in Figure 4.20b - is shown.

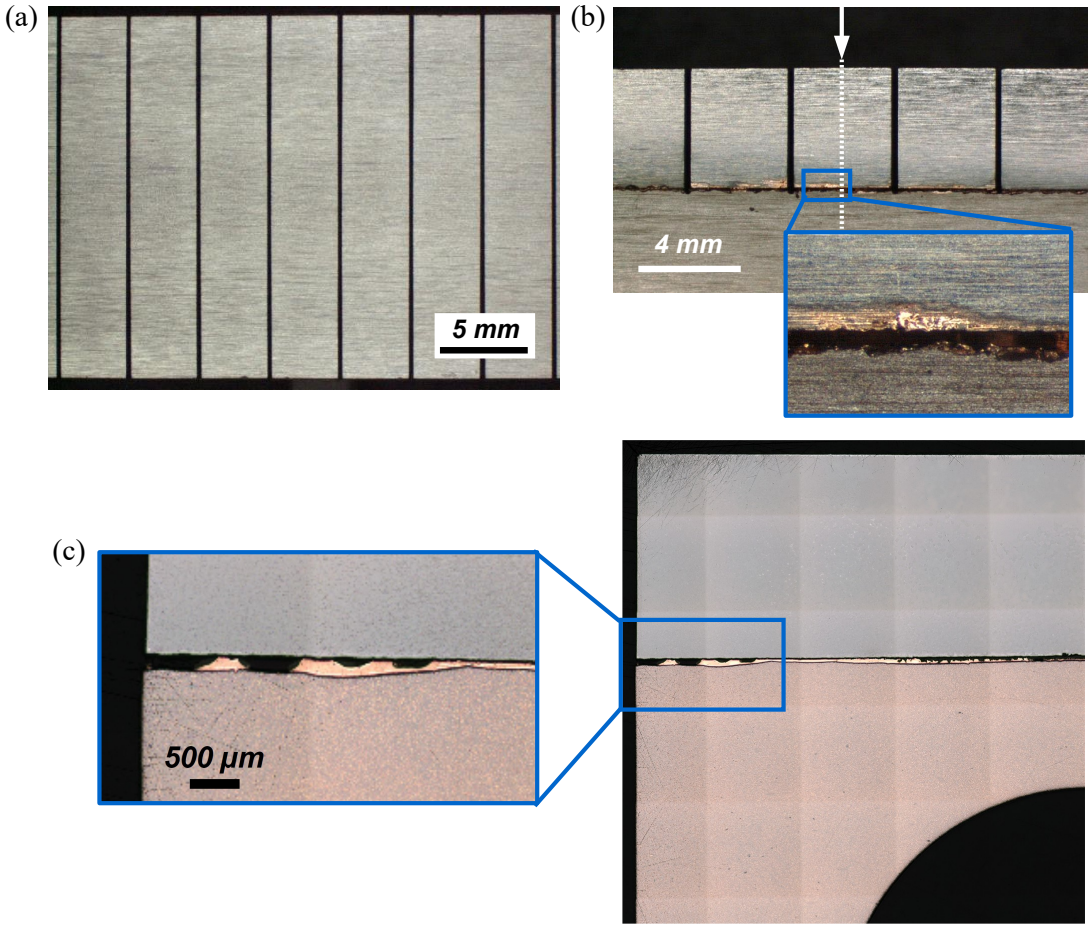

FIGURE 4.20: Images of W flat-tile type PFC mock-up with W_p-Cu MMC heat sink (illustrated in Figure 4.15) after 370 applied HHF load cycles at $20\,MW\,m^{-2}$: (a) Centred top view on HHF loaded W tiles, (b) side view on defective W/W_p-Cu bond interfaces and (c) metallographic cross section through a partially detached W tile.

The magnified image unambiguously shows the defective W/W_p-Cu bond interface. Two more W flat-tile type PFC mock-ups with a W_p-Cu heat sink were manufactured according to the fabrication procedure described above. However, during HHF testing these mock-ups exhibited premature crack defects within the loaded W tiles parallel to the heat loaded surface and the HHF tests were concluded accordingly[31]. In Figure 4.21a, a side view on the failed W tiles of such a mock-up is shown. The macroscopic cracks that developed during the HHF loading are plainly visible while at the same time it can be seen that the W/W_p-Cu bond interfaces are flawlessly intact. Hence, no experimental conclusion about the performance of these mock-ups - especially in terms of the fatigue lifetime of the W/W_p-Cu joint - under cyclic HHF loading was possible. In Figure 4.21b, a metallographic cross section through a cracked W tile can be seen while in Figure 4.21c a corresponding optical microsection of such a crack is shown[32]. Figure 4.21c reveals that

[31] One of the mock-ups was HHF screened up to a heat loading of $22\,MW\,m^{-2}$ and then loaded up to 100 HHF cycles at $20\,MW\,m^{-2}$. The second mock-up was only HHF screened up to a heat flux of $22\,MW\,m^{-2}$ without subsequent cyclic HHF loading.

[32] The sample was etched with *Murakami's reagent* in order to make the grain structure visible.

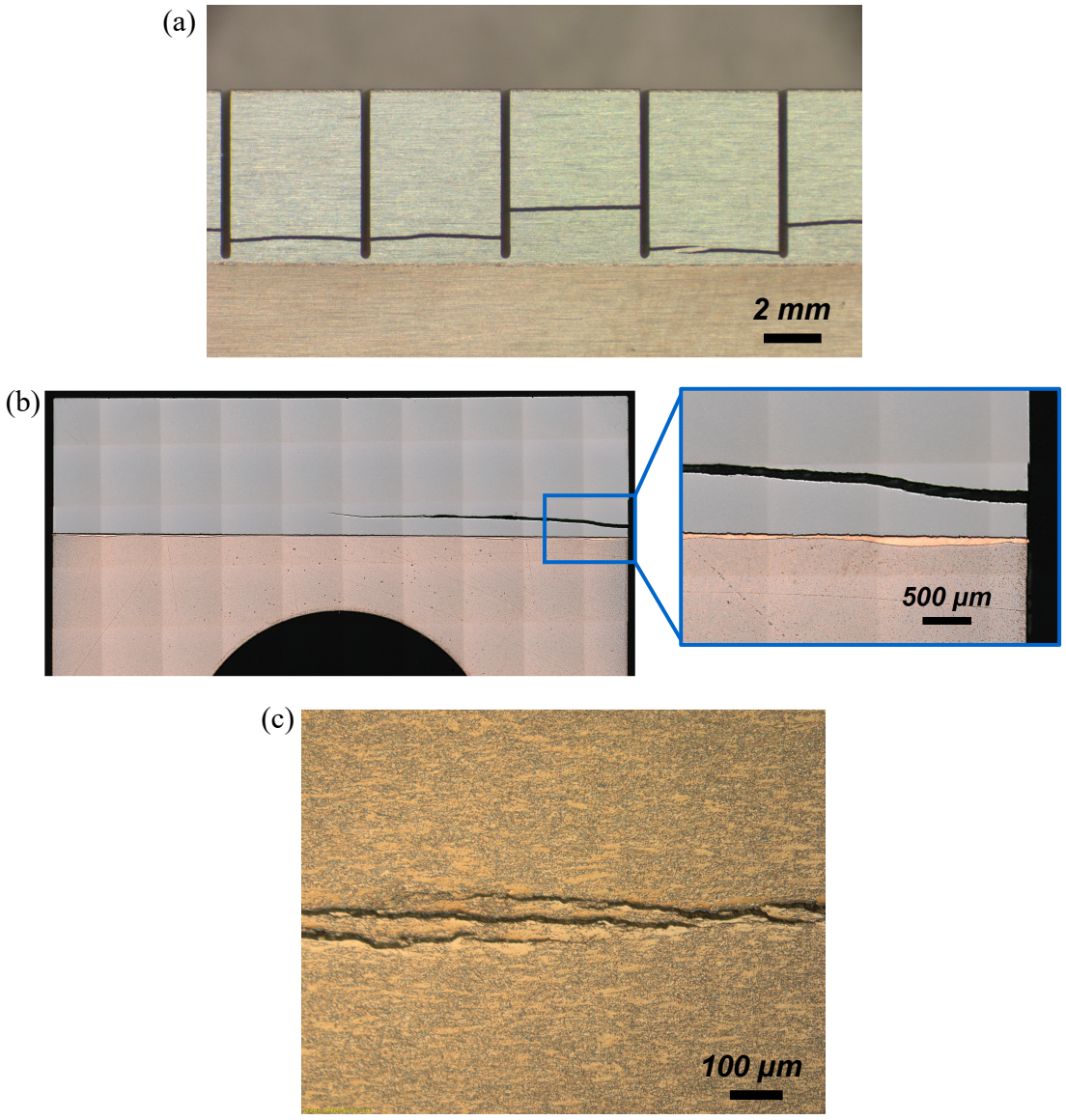

FIGURE 4.21: (a) Side view on prematurely cracked W tiles of a W flat-tile type PFC mock-up with W_p-Cu MMC heat sink, (b) metallographic cross section through a cracked W tile and (c) corresponding optical microsection of such a crack.

the W tile material exhibits a preferential grain orientation parallel to the heat loaded surface. The observed failure of the W tiles was attributed to this grain orientation. Typically, W armoured PFCs are designed in such a way that the grain orientation of the W PFM is perpendicular to the plasma-facing surface. Such a configuration is chosen as it is well-known that the grain orientation of a wrought W material plays a decisive role regarding the mechanical properties. Typically, a deformed W material consisting of elongated grains does not only exhibit higher strength properties in deformation direction but also corresponding anisotropic fracture behaviour [60, 134–136]. That is the reason why W armour materials for the ITER divertor target (cf. section 2.3) shall have a specified grain orientation with deformation direction perpendicular to the plasma-facing

surface as is schematically illustrated in Figure 4.22 [137].

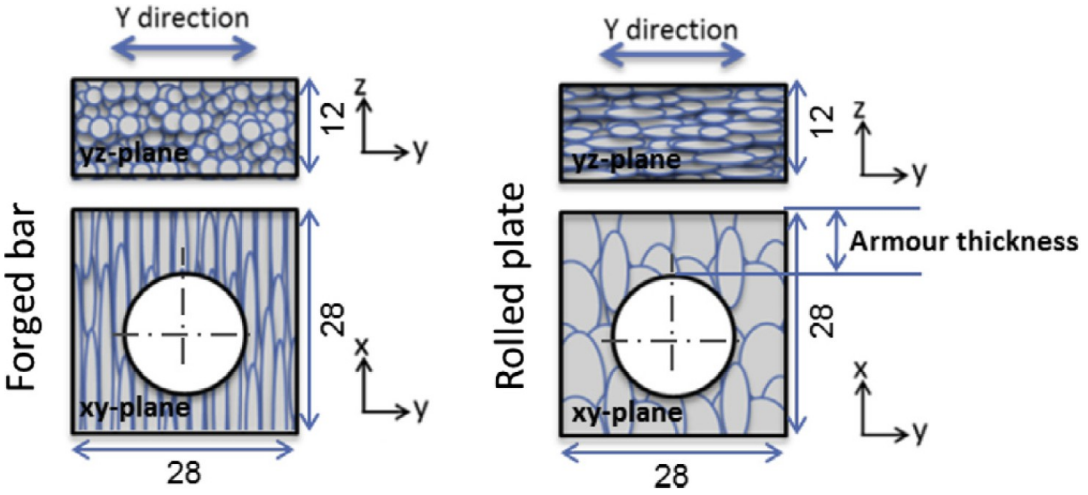

FIGURE 4.22: Schematic illustration of wrougth W monoblock microstructures for ITER divertor target application with grain orientation/deformation direction perpendicular to the plasma-facing surface according to [137].

4.7 Chapter 4 Summary

Within this chapter, work performed regarding the development of W_p-Cu MMCs intended for use as potentially advanced HSMs in highly loaded PFCs is described. In this respect, the material manufacturing as well as the characterisation of thermophysical and -mechanical properties were discussed. Furthermore, the application of W_p-Cu to W flat-tile type PFC mock-ups that were HHF tested was described.
To summarise, it can be stated that the investigated W_p-Cu MMCs can be regarded as viable materials for PFC heat sink applications due to the following reasons:

- It has been shown that W_p-Cu MMCs can be fabricated with good material quality, i.e. with material properties acceptable for HHF applications. Furthermore, it has been demonstrated that W_p-Cu MMCs can also be fabricated through melt infiltration with Cu alloys that might improve the behaviour of the materials under fusion neutron irradiation.

- Material property investigations showed that through composition variation W_p-Cu MMCs can exhibit beneficial properties with respect to PFC applications, as e.g. a reduced CTE or superior tensile strength properties compared with monolithic Cu alloys.

- Moreover, the HHF tests performed on W flat-tile type PFC mock-ups with W_p-Cu MMC heat sink demonstrated the potential of these composite materials for

PFC applications. The tested design survived more than 300 HHF load cycles[33] at a heat load of $20\,\mathrm{MW\,m^{-2}}$. However, it was found that typical flat-tile design issues with stress concentrations at the W PFM to heat sink joint induced failure. In this respect, the high temperatures occuring at the $\mathrm{W/W_p}$-Cu bond interfaces ($> 700\,^{\circ}\mathrm{C}$) are considered as a main issue. It seems that at such temperatures, the $\mathrm{W/W_p}$-Cu bond interface, which essentially is a thin Cu layer (cf. Figure 4.16), suffers from fatigue damage and can hence not withstand the cyclic HHF loading.

[33] In section 2.3, it has been mentioned that the ITER divertor target qualification criteria comprise the demonstration of component integrity for 300 HHF load cycles at $20\,\mathrm{MW\,m^{-2}}$ [50, 69].

Chapter 5

Tungsten fibre-reinforced copper

5.1 General remarks

As mentioned within the outline in Chapter 1, another class of W-Cu MMCs of interest with regard to PFC heat sink application and investigated within the present work are *W fibre-reinforced Cu* (W_f-Cu) composites [112]. In principle, W_f-Cu MMCs are of specific interest as potentially advanced PFC heat sink materials due to the well-known eligibility of fibrous reinforcements in composites. Fibres are especially suitable as composite material reinforcement as they exhibit the following characteristics [82]:

- Fibrous reinforcements can exhibit a small diameter with respect to the materials microstructure unit, as e.g. the grain size, which allows a higher fraction of the theoretical material strength to be attained. This can be regarded a direct result of the so-called *size effect*: The smaller the diameter of a fibre, the lower the probability of having imperfections within the material that lead to premature failure.

- Within a composite material, the high aspect ratio (length/diameter) of fibres allows a large fraction of the applied loads to be transferred through the matrix material to the typically stiff and strong fibre.

- The high flexibility of fibres allows their processing to preforms for composite material fabrication with a variety of techniques, as is e.g. described within section 5.4.1.

The potential of W_f-Cu materials has been analysed in the literature within several studies which are briefly reviewed in the following section 5.2. However, these studies considered W_f-Cu mainly as a model system for the investigation of the basic behaviour of fibre-reinforced MMCs. Such materials have hence remained exceptions while there

has no viable application of W_f-Cu materials or components using W_f-Cu been reported in the literature[1].

5.2 Literature survey

Several decades ago, the W_f-Cu material system was used within research work at the *National Aeronautics and Space Administration* (NASA) as a model system to study the fundamental behaviour of fibre-reinforced MMCs [110, 139–141]. This choice was mainly due to the good-naturedness of the W-Cu material system as has been described within section 3.4 of the present work. Against this background, basic material property characterisation was performed on W_f-Cu while also the potential of this fibre-reinforced, high-strength, high-conductivity composite with regard to demanding HHF applications was recognised. In this respect, W_f-Cu was considered as a potentially advanced thrust chamber liner material for use in high-temperature, high-pressure rocket propulsion engines [138]. The intention behind the use of W_f-Cu as a liner material was to make the thrust chamber more damage tolerant and long-life reusable as the use of state-of-the-art high performance Cu alloys limited the lifetime due to low-cycle fatigue failure issues.
Kelly and Tyson [142] investigated the temperature dependent tensile behaviour of continuous and discontinuous UD fibre-reinforced W_f-Cu. Their study confirmed that the strength of a W_f-Cu MMC can be described by a linear relationship correlating the strength and the fibre volume fraction for a particular aspect ratio of the reinforcing fibres.
Regarding W_f-Cu for PFC applications, work was performed by *Herrmann et al.* with a focus on the optimisation of the fibre-matrix interface properties [143, 144]. These investigations confirmed that there are no reactions at the W-Cu fibre-matrix interface and that hence the interfacial adhesion between a W fibre and the Cu matrix is determined through the mechanical interlocking. Furthermore, different interface concepts were investigated while a graded W-Cu transition interface was found to yield the highest interfacial shear strength. Apart from that, the investigated W_f-Cu MMC, which was fabricated by means of *hot isostatic pressing* (HIP), was tested in W monoblock type PFC mock-ups as reinforcing interlayer between the monoblocks and a CuCrZr heat sink pipe [145]. Although the HHF performance of the mock-ups was rather poor the W_f-Cu MMC interlayer itself survived cyclic heat loading at $10.5\,\mathrm{MW\,m^{-2}}$ without damage.
Moreover, a study regarding the use of W_f-Cu as a kinetic energy penetrator material can be found in the literature [146]. For these investigations, W_f-Cu penetrator specimens were fabricated through liquid infiltration of closely packed UD aligned W fibres with a

[1] It should be mentioned that in the context of research work performed by NASA subscale rocket thrust chamber mock-ups lined with W_f-Cu were tested. However, it was reported that the investigated chambers failed prematurely due to material and manufacturing flaws [138].

CuZn alloy. In terms of material fabrication, it is reported that no interfacial reaction between the W fibres and the CuZn alloy could be observed and that the composite exhibited good interfacial bonding.

5.3 The reinforcing tungsten fibres

It is well-known that the microstructure of polycrystalline W materials influences the mechanical properties strongly. The microstructural parameters, however, can be controlled through the fabrication process of the material, e.g. the sintering conditions, the degree and type of deformation, or the applied annealing processes. According to [60], the following basic correlations between the mechanical material behaviour of polycrystalline W and the applied fabrication process can be described:

- A wrought microstructure that consists of grains elongated in deformation direction is stronger than an annealed or recrystallised one. Especially, this is valid for the strength in deformation direction[2].
- The lower the working temperature and the higher the energy that is stored during deformation, the higher is the resulting strength of the material[3].
- The smaller the grain size, the higher is the strength of the material[4].
- Different fabrication processes result in different properties. For example, there remain origin-related differences in the properties of arc-melted and powder metallurgical materials, even after final working.

A specific form of worked polycrystalline W are W fibres fabricated by means of drawing. With such a processing, W fibres can be fabricated down to diameters of approximately 10 µm [147]. Drawn W fibres exhibit a highly worked characteristic fibrous microstructure and a correspondingly high strength. Furthermore, they exhibit reasonably ductile behaviour already at RT. Since many a long year, W fibres are used as filaments in incandescent lamps where they exhibit high service temperatures of up to 3000 °C which corresponds to nearly 0.9 T_m [60]. Pure W fibres would fail quickly at such operating temperatures due to recrystallisation and grain boundary sliding. Therefore, so-called *non-sag* (NS) W fibres were developed that exhibit an extended lifetime while the term refers to the resistance of the material against deformation at incandescent temperatures. NS W is sometimes also called *doped W* and owes its outstanding properties to potassium (K) filled bubbles which act as grain boundary migration barriers that are typically aligned in rows along the drawing direction of the fibre. Eventually, these K bubbles

[2] This is typically referred to as *texture strengthening*.
[3] This is typically referred to as *work hardening*.
[4] This is typically referred to as *fine-grain strengthening*.

affect the recrystallisation of the material in such a way that they preserve an interlocking long-grained microstructure that is the underlying reason for the NS properties. Furthermore, it is known that finely dispersed K bubbles contribute to the outstanding creep resistance of NS W fibres through pinning of dislocations. Usually, 50 µg g^{-1} K are required to produce NS W fibres in which a large number of small-diameter K bubbles is favoured for obtaining a high material quality. For further details regarding the manufacturing of drawn W fibres the reader is referred to references [60, 147].

The preferred reinforcing fibres for the W_f-Cu MMCs investigated within the present work are commercially available drawn K doped W fibres. An SEM image (backscattered electron image) of a characteristic longitudinal microsection of such a W fibre in as-fabricated condition[5] is illustrated in Figure 5.1. As has been mentioned above, the

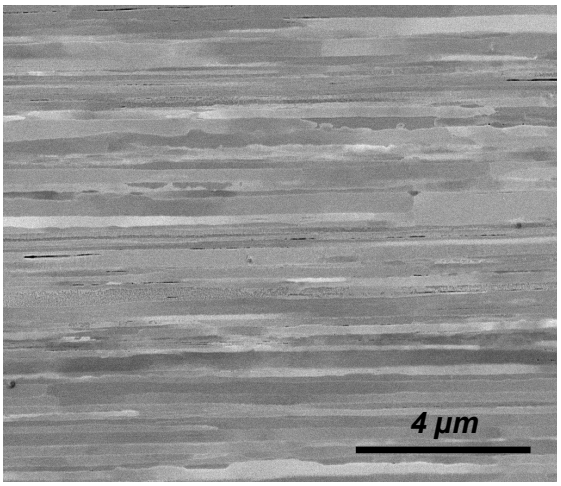

FIGURE 5.1: Longitudinal SEM microsection (backscattered electron image) of a drawn K doped W fibre in as-fabricated condition illustrating the characteristic fibrous grain microstructure.

mechanical properties of K doped W fibres can be regarded as very beneficial. It has been reported that material with a diameter of 150 µm exhibits a tensile strength of about 2.7 GPa in as-fabricated condition and tested at RT as well as a ductile fracture behaviour even after heat treatment at temperatures of up to 1900 °C. In Figure 5.2 and Figure 5.3, these benign properties are illustrated. Figure 5.2 shows typical single fibre tensile curves of as-fabricated and heat treated K doped W fibres [148]. Figure 5.3 shows a typical fracture surface of a K doped W fibre tensile tested at RT after heat treatment at 1900 °C for 30 min [148]. The picture illustrates that the specimen fractured with local necking in a ductile manner even after heat treatment at this considerably high temperature. Moreover, the strength of drawn W fibres varies with their diameter while the strength increases with decreasing fibre diameter. This is due to the abovementioned size effect but also due to the fact that the smaller the diameter of a drawn fibre, the more worked is the microstructure. In Figure 5.4, the dependence of the tensile strength

[5] K doped W fibre, nominal diameter 150 µm, OSRAM GmbH, wire BSD-OG 68,610 mg S3D bare

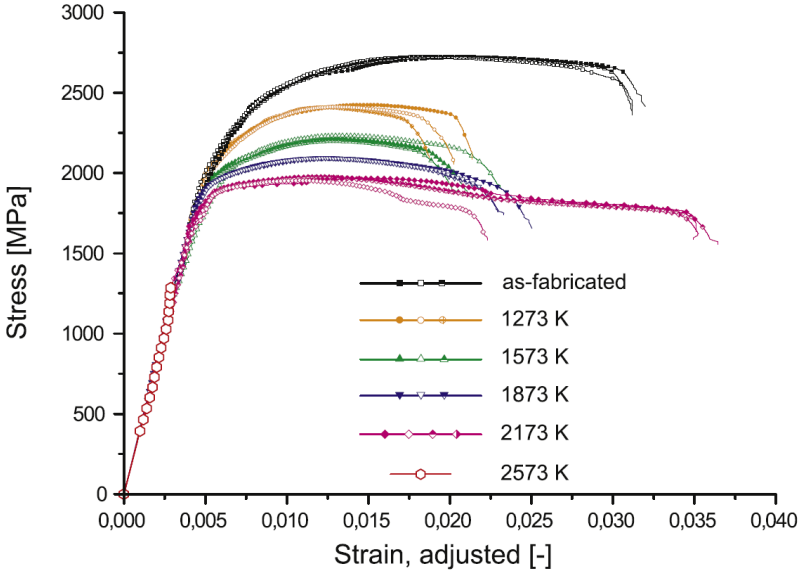

FIGURE 5.2: Typical stress-strain curves for single fibre tensile tests at RT of as-fabricated and heat treated drawn K doped W fibres with a diameter of 150 µm [148].

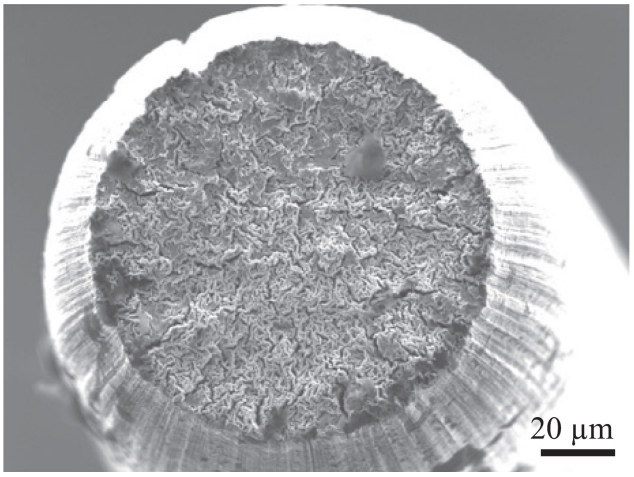

FIGURE 5.3: Typical fracture surface of a drawn K doped W fibre tensile tested at RT after heat treatment at 1900 °C for 30 min [148].

of drawn W fibres versus fibre diameter based on experimental data from different studies is illustrated [149]. Especially, it can be seen that there is a steep increase in tensile strength for W fibres with diameters of approximately 100 µm and less while fibres with a diameter of 20 µm can reach a tensile strength of approximately 4 GPa. Furthermore, drawn W fibres do also maintain rather high strength properties at elevated temperature. In [150], it was reported that K doped W fibres with a diameter of 150 µm and in as-fabricated condition exhibit a UTS of approximately 2.3 GPa at RT and 1.5 GPa at 600 °C. These numbers illustrate that drawn W fibres are indeed a suitable composite material reinforcement, also for elevated temperature applications.

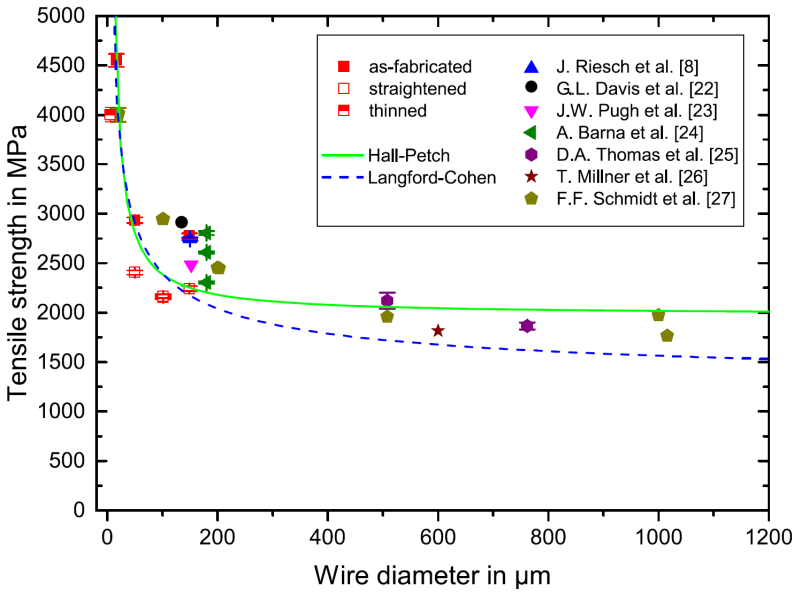

FIGURE 5.4: Tensile strength of drawn W fibres with varying diameters [149].

Due to the substantial strength properties and the achievable microstructural stability of drawn W fibres these reinforcements have also attracted interest regarding fibre-reinforcement of other high-temperature materials. With respect to PFC applications, drawn W fibres are also used within *W fibre-reinforced W* composites [148,149,151,152]. Another example are *W fibre-reinforced superalloys* which were investigated by NASA as high-strength materials intended for use above the temperatures at which the strengthening mechanisms in superalloys typically begin to fail [60,153–160].

5.4 Material manufacturing

5.4.1 Continuous tungsten fibre processing

The starting point for the manufacturing of the W_f-Cu MMCs investigated within the present work is the fabrication of suitable fibrous preforms. Regarding an actively cooled PFC heat sink, a W_f-Cu material in pipe configuration is of main interest. That is the reason why within the present work an appropriate method to produce cylindrical W fibre preforms was investigated in the first place. As described within section 2.2.2, material developments with regard to future magnetic confinement thermonuclear fusion reactors need to demonstrate essential elements of industrial scale fabrication. Therefore, the processing of continuous W fibres to cylindrical preforms by means of *circular braiding* - which represents a well-established fibre-processing technology - was investigated.
Within the German standard DIN 60000, braids are defined as: *Two- or three-dimensional fabrics with even thread density and closed fabric appearance whose braiding*

threads cross each other in diagonal direction to the selvedges[6] [161, 162]. Since many a long year, braiding has been used for the fabrication of textile structures as e.g. shoelaces or ropes. Nowadays, braiding is also used for the fabrication of various industrial products such as hydraulic hoses or electrical cables. In recent years, technological applications of braided structures in fibre-reinforced composite materials have gained substantial interest also in demanding areas as for example aerospace technology [163]. One specific example in this respect is the application of braided composite fan casings for gas turbine engines. In state-of-the-art high-bypass gas turbine engines, the fan casing represents one of the largest and heaviest components which must be able to contain a released fan blade during a so-called blade-out event. It has been reported that for this application braided composites can be fabricated efficiently, offer design flexibility, lead to weight reduction compared to metal cases and ultimately exhibit improved impact performance in terms of crack propagation resistance [164].

Braided structures can be classified into 2D and *three-dimensional* (3D) braids [163]. 2D braids refer to single-layered structures while 3D braids refer to interconnected multi-layered structures. 2D braids can be *biaxial* or *triaxial* in configuration while biaxial construction is the most commonly applied and is characterised by two sets of interlacing yarns. A triaxial braid comprises additionally a third set of longitudinal yarns in the production direction which are also referred to as axial yarns. The difference between bi- and triaxial braids is illustrated in Figure 5.5 [163]. Within the present work, 2D biaxial

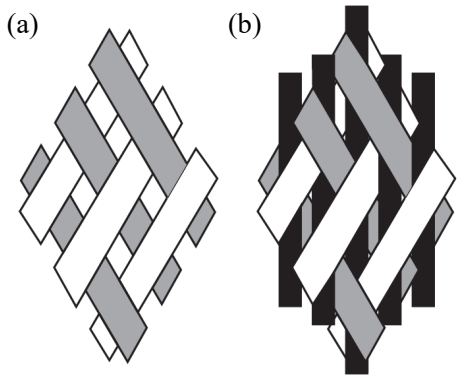

FIGURE 5.5: Illustration of (a) biaxial and (b) triaxial braid construction [163].

braids were investigated. Geometrically, such braided structures are characterised by a number of parallelograms - equal to half of the number of the braiding machine yarn carriers - that form in circumferential direction. The basic geometrical features of a 2D biaxial braid are schematically illustrated in Figure 5.6 [163]. The *braiding angle* θ is an important parameter that measures the angle of interlacing yarns with respect to the braid axis. Although circular braids are 3D objects, their yarn architecture is 2D

[6] Original German definition: *Flächen- oder Körpergebilde mit regelmäßiger Fadendichte und geschlossenem Warenbild, deren Flecht-(Klöppel-)Fäden sich in schräger Richtung zu den Warenkanten verkreuzen* [161].

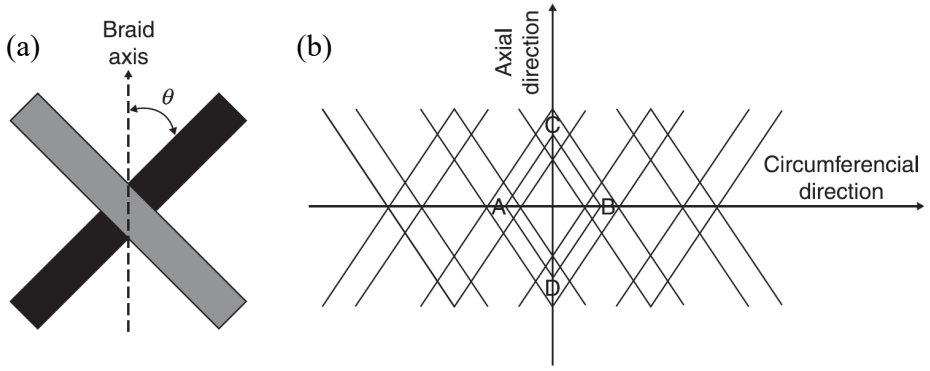

FIGURE 5.6: Illustration of the geometrical features of a braid: (a) Braiding angle and (b) braid unit cell [163].

which means that braided structures are similar to woven structures in terms of the yarn interlacement topology. Furthermore, different braiding patterns can be realised as is illustrated in Figure 5.7 [163].

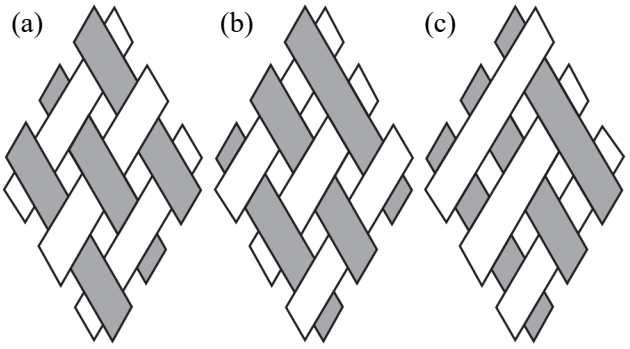

FIGURE 5.7: Illustration of different braiding patterns: (a) Diamond braid, (b) regular braid and (c) Hercules braid [163].

In general, the following parameters characterise a braid [162]:

- The number of braiding yarns,
- the braiding pattern (cf. Figure 5.7),
- the number of plies,
- the braiding angle (cf. Figure 5.6) and
- the braid density, i.e. the number of braiding points per length.

Braided structures exhibit a number of advantages with respect to fibre-reinforced composite material fabrication if compared to other competing processes, as e.g. filament winding and weaving. The most important with respect to the present work are [163,165]:

- Braided composites exhibit superior toughness and fatigue strength when compared to filament wound composites. In filament wound composites, cracks can propagate

easily along the fibres whereas in braided composites the points of interlacement act as crack arresters.

- Braiding is a versatile process with which a wide range of yarn interlacement angles can be realised. Furthermore, axial yarns can additionally be introduced to the braiding process in order to form triaxial braids which can exhibit quasi-isotropic properties.

In a conventional circular braiding machine, yarn carriers rotate along a circular sinusoidal track around the center of the device while half the carriers move in a clockwise direction and the remaining half of the carriers moves in a counterclockwise direction as is schematically illustrated in Figure 5.8 [166]. Such a process results in an interlacement

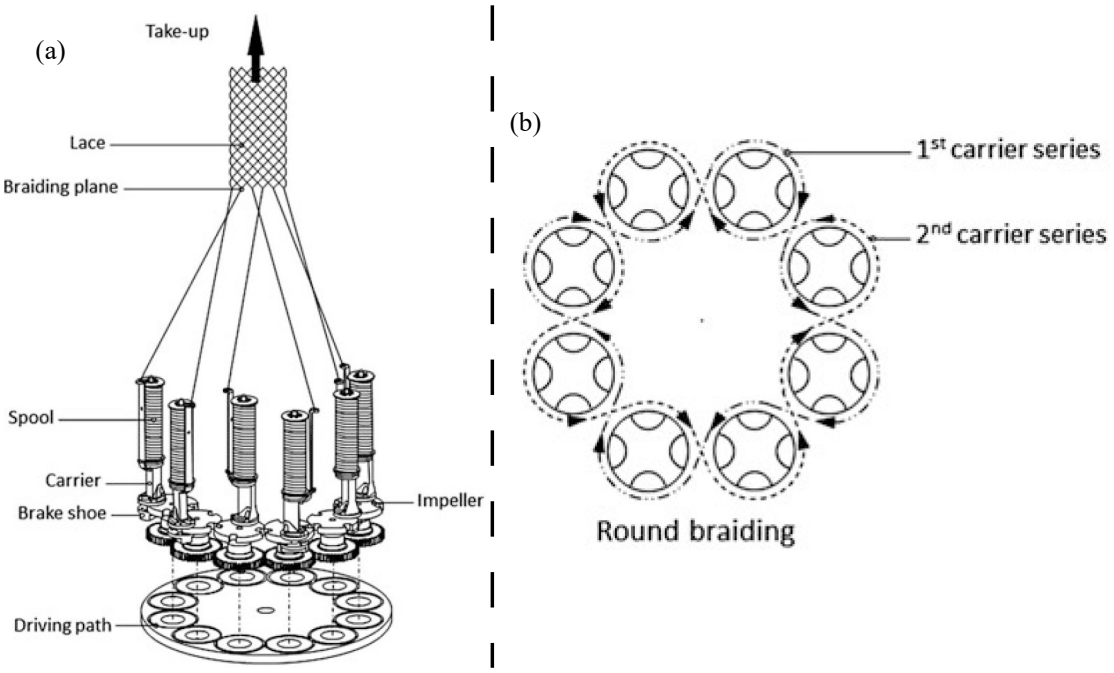

FIGURE 5.8: (a) Braiding principle and (b) movement of yarn carriers in a circular braiding machine [166].

of two sets of yarns at a biased angle to the axis of the braiding machine and forms a tubular structure which is continuously moved forward by an appropriate take-up mechanism. A braid can either be created as a continuous sleeve or be deposited on a mandrel where multiple plies can be braided on top of each other in order to create a structure or preform with a required thickness [163].

The braiding device that was used for producing the continuous W fibre preforms described within the present work is a vertical maypole braider[7] equipped with 48 bobbins and is illustrated in Figure 5.9. With this braider, cylindrical continuous W fibre preforms were fabricated by means of circular mandrel overbraiding.

[7] Körting Nachfolger Wilhelm Steeger GmbH & Co. KG, Wuppertal, Germany; located at Deutsche Institute für Textil- und Faserforschung (DITF) Denkendorf, Germany

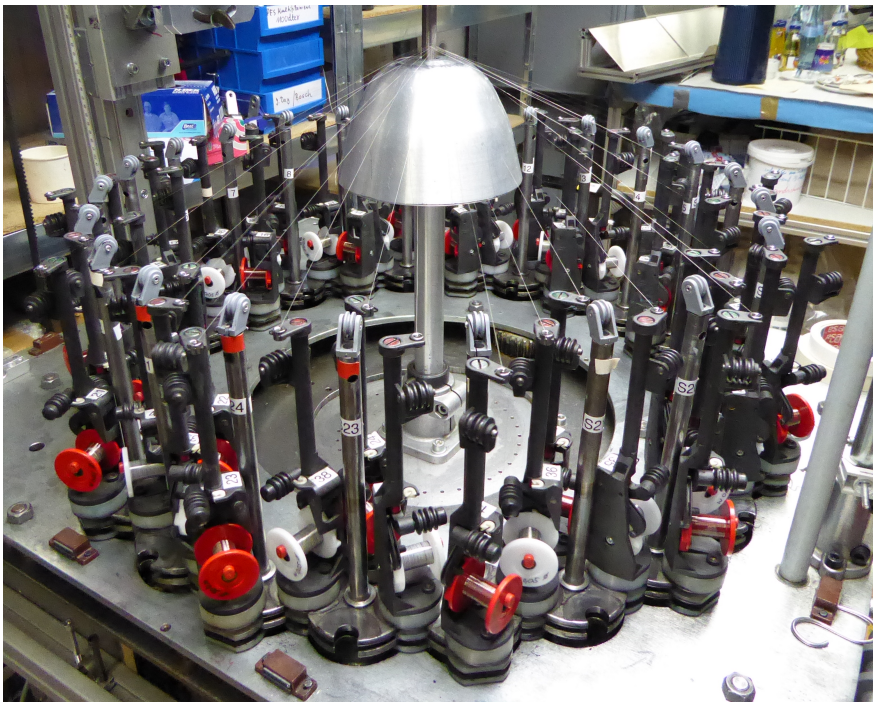

FIGURE 5.9: Vertical braiding machine (Körting Nachfolger Wilhelm Steeger GmbH & Co. KG, Wuppertal, Germany) used within the present work for the fabrication of cylindrical continuous W fibre preforms.

In Figure 5.10, microscopic images of two circular single-layered W fibre braids are shown [167]. Figure 5.10a illustrates a braid that consists of W fibres with a diameter 150 µm[8] while Figure 5.10b shows a braid that consists of W fibres with a diameter of 50 µm[9]. It can be seen that the fibres with the smaller diameter of 50 µm are much

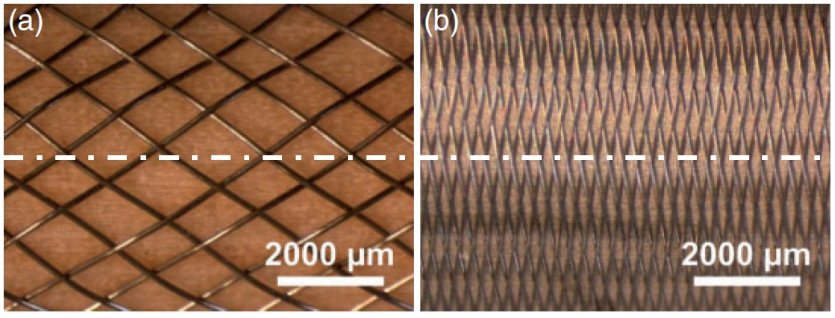

FIGURE 5.10: Microscopic images of regular biaxial circular braids made out of drawn K doped W fibres with a diameter of (a) 150 µm and (b) 50 µm (the white dashed lines represent the braid axis) [167].

more suited for such a processing as the braid shows significantly less perturbing undulations which allows higher braiding angles and a higher braid cover factor to be achieved[10].

[8] K doped W fibre, nominal diameter 150 µm, OSRAM GmbH, wire BSD-OG 68,610 mg S3D bare

[9] K doped W fibre, nominal diameter 50 µm, OSRAM GmbH, wire BSD-OG 7,647 mg S1B bare

[10] A high braiding angle is in principle desired for a braided preform to be used in a PFC heat sink pipe as this implies that the braid provides adequate reinforcement and macroscopic CTE reduction in circumferential direction.

Following these results, multi-layered circular braids as preforms for W_f-Cu MMC material fabrication were manufactured successfully. In Figure 5.11, two such preforms with differing architecture are illustrated [167]. They are both manufactured from the same

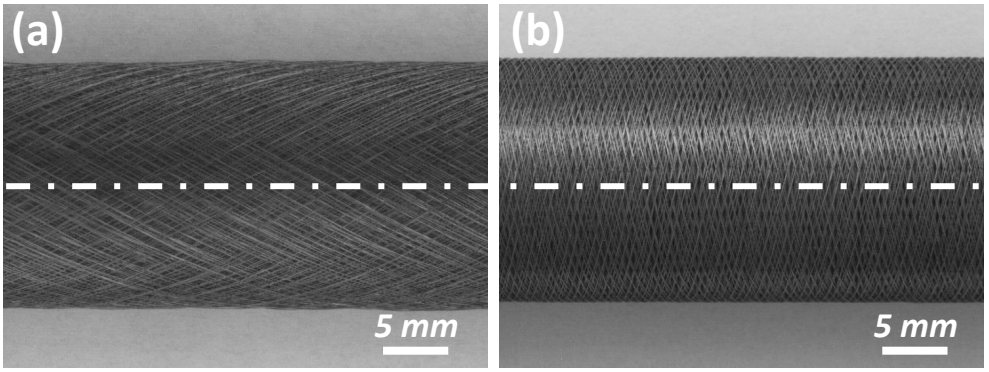

FIGURE 5.11: Images of multi-layered circular braids as preforms for W_f-Cu MMC fabrication made of drawn K doped W fibres with a diameter of 50 µm with a braiding angle of (a) ca. 30° and (b) ca. 78° (the white dashed lines represent the braid axis) [167].

W fibres with a diameter of 50 µm. Figure 5.11a shows a multilayered preform with a braiding angle of approximately 30° while Figure 5.11b illustrates a braid with a significantly higher braiding angle of about 78° (cf. Figure 5.6). These preforms demonstrate the direct possibility to influence the preform architecture and hence the later composite material properties by varying the braiding parameters during the preform production process. If the circumference shall be reinforced a higher braiding angle is preferred while a lower braiding angle is desired if the axial direction of the composite needs reinforcement.

In order to further leverage the potential of W_f-Cu MMCs, continuous W fibre preform fabrication was improved through the use of even thinner W fibres with a diameter of 20 µm[11]. The advantage of applying such thin filaments is twofold:

- The use of thin W filaments is beneficial in terms of strength properties as has been discussed in section 5.3 and is illustrated in Figure 5.4. Hence, the application of thinner W filaments can improve the overall performance of W_f-Cu MMCs.

- The flexibility of an elongated elastic beam with circular cross section can be described as follows [82]:

$$\frac{1}{M\,R} = \frac{64}{E\,\pi\,d^4} \tag{5.1}$$

  where M is a bending moment, R is the bending radius, E is Young's modulus and d is the fibre diameter. Equation 5.1 implies that the flexibility of fibres is a sensitive

[11] K doped W fibre, nominal diameter 20 µm, OSRAM GmbH, Draht BSD-OG 1,216 mg S2E bare

inverse function of their diameter. This means that the handling and processing of fibres is improved and facilitated by using filaments with small diameters[12].

However, thin W filaments with diameters of around 20 µm and less cannot be processed individually to a preform in a practicable manner. Hence, they have to be processed to multifilaments which can then subsequently be used for further processing to preforms for composite material fabrication. Within the present work, W multifilaments were fabricated[13] by means of twisting $2 \times 7 = 14$ filaments, each with a diameter of 20 µm. Twisting is a well-known textile processing method for the production of multifilamentary yarns [162]. In Figure 5.12, microscopic images of such a 14×20 µm W yarn in comparison with single W fibres with diameters of 150 µm and 50 µm are shown. Furthermore, in

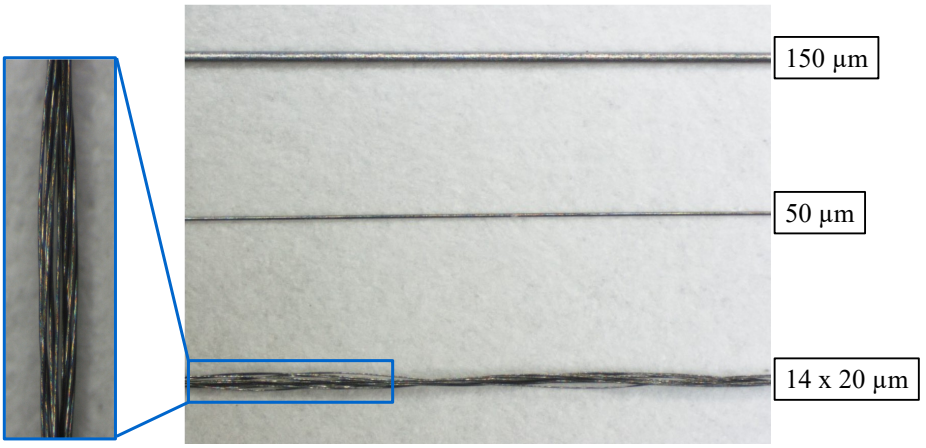

FIGURE 5.12: Microscopic images of a twisted 14×20 µm W yarn in comparison with single W fibres with diameters of 150 µm and 50 µm.

Figure 5.13 a typical tensile curve of a W yarn in as-fabricated condition as illustrated in Figure 5.12 and measured at RT is shown. For reasons of comparison, the tensile behaviour of a W fibre in as-fabricated condition with a diameter of 150 µm is included in the plot[14]. It can be seen that compared with the single W fibre the W yarn exhibits not only a significantly higher UTS, but also a notably higher yield strength. At RT, the UTS of the yarn was measured as $\sigma_{UTS} = 3935 \pm 4.1$ MPa while the 0.2% yield strength was determined as $R_{p,0.2} = 3450 \pm 110$ MPa[15]. Furthermore, it can be seen that the W yarn exhibits a fracture strain of approximately $\epsilon_f = 3\%$ and that there is a

[12] Equation 5.1 also implies that practically one can realise very flexible fibres out of inherently brittle materials, as e.g. glass, SiC or alumina, provided one can shape such brittle materials into fine diameter fibres.

[13] The multifilamentary W yarn fabrication was performed at TEC-KNIT GmbH, Rhede, Germany.

[14] The tensile data for the W fibre with a diameter of 150 µm was taken from [168].

[15] The evaluation of these numbers was based on seven uniaxial tensile tests (plus/minus values correspond to the standard deviation of the measurements) which were performed with an electromechanical universal testing machine (TIRA Test 2820) that was equipped with a 200 N load cell. The tests were conducted at RT with a constant cross-head displacement speed of 5 µm s^{-1}. The specimens had a gauge length of 30 mm and the fibres were clamped with glued ends in order to improve the grip and to protect the samples from damage by clamping. The strain measurement was performed optically by means of digital image correlation.

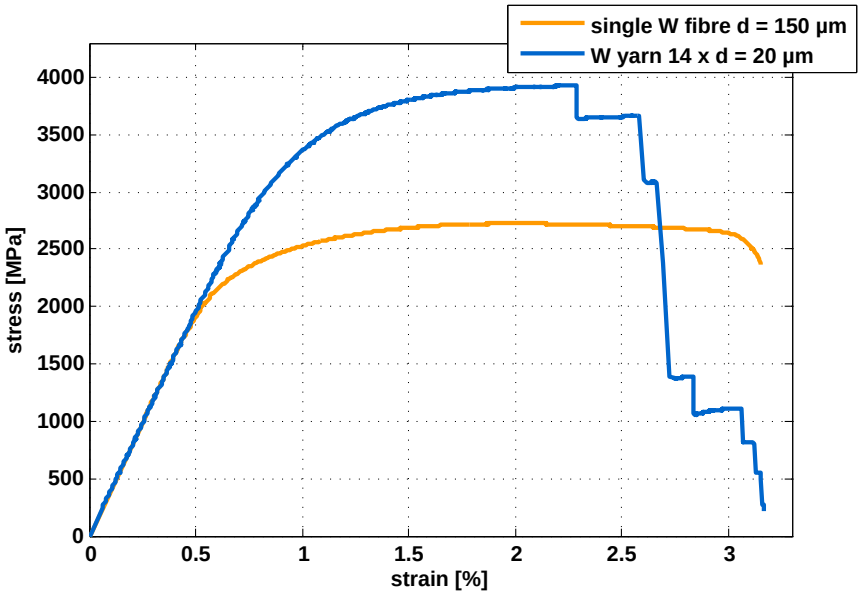

FIGURE 5.13: Typical tensile behaviour of a W yarn with 14 × 20 µm filaments in as-fabricated condition at RT; for reasons of comparison the tensile behaviour of a single W fibre with a diameter of 150 µm in as-fabricated condition is included in the plot [168].

characteristic stepwise failure of the yarn due to gradual failure of individual filaments. Moreover, in Figure 5.14 fractographic SEM images of a W yarn after tensile testing at RT are shown. Figure 5.14a illustrates several fractured W filaments of the yarn. In Figure 5.14b, a W filament fracture surface is shown and it can be seen that as expected the filament exhibits a ductile knife edge fracture surface with characteristic local necking. The fabrication of circular braids with the discussed W yarns was also investigated. In Figure 5.15a, an image illustrating the braiding process with W yarns is shown. In Figure 5.15b, microscopic images of a W yarn braid are illustrated while the yarn strands with the individual filaments can be identified within the magnified

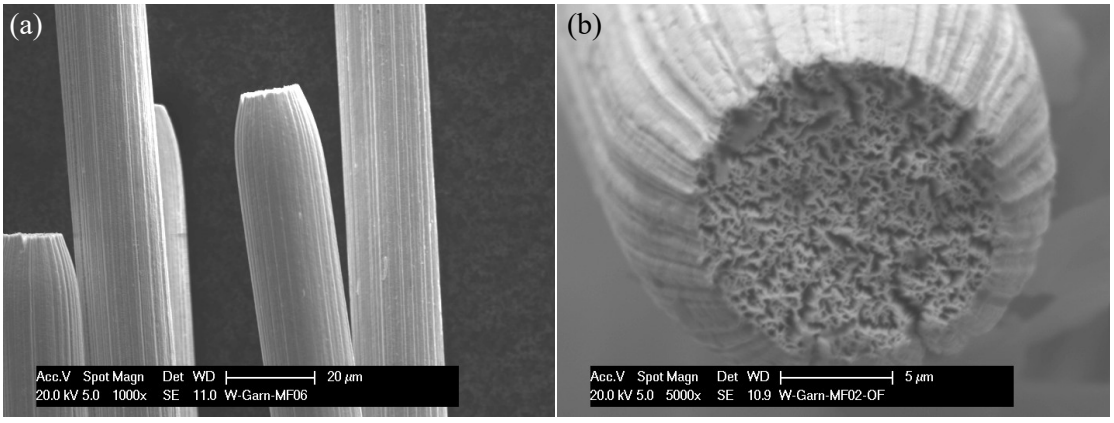

FIGURE 5.14: Fractographic SEM images of a W yarn after tensile testing at RT: (a) Several fractured filaments of the yarn and (b) fracture surface of an individual filament.

image. Figure 5.15 demonstrates the viability of yarns made out of thin W filaments with respect to continuous W fibre preform preparation for MMC fabrication.

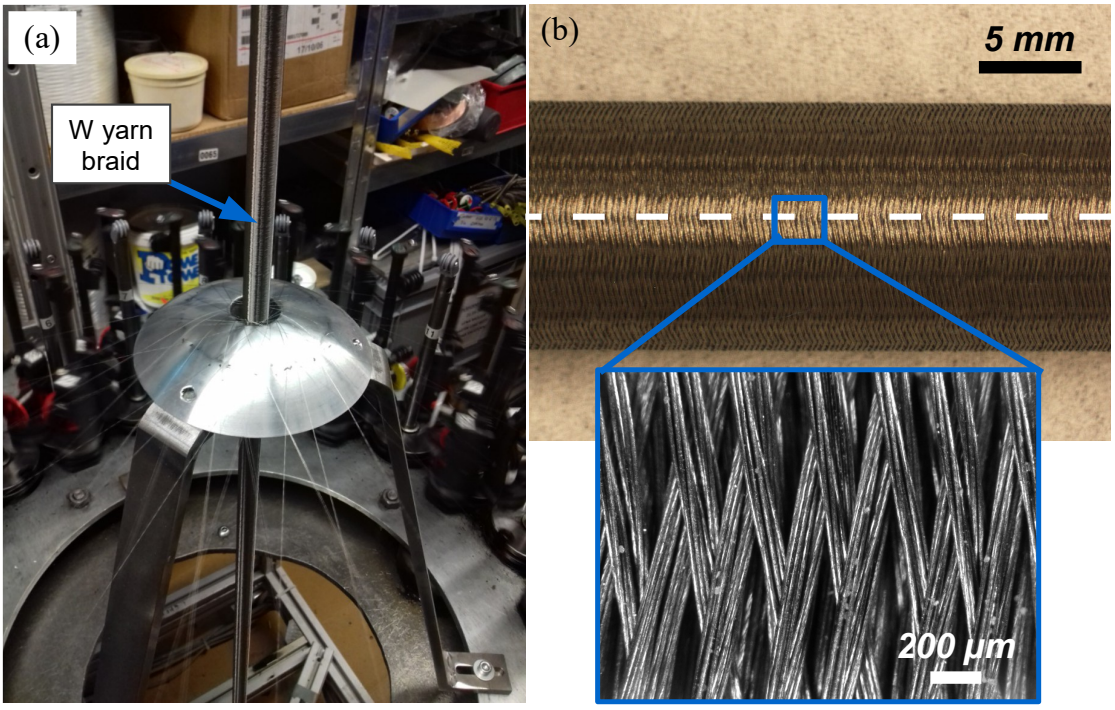

FIGURE 5.15: (a) Image illustrating the circular braiding with the investigated W yarns and (b) microscopic images of a corresponding W yarn braid.

5.4.2 Copper melt infiltration

With the braided continuous W fibre preforms as discussed above, W_f-Cu MMC fabrication by means liquid Cu infiltration was investigated. In this respect, two approaches were followed:

- Gravity/capillarity assisted infiltration[16] and
- centrifugal infiltration, for which a dedicated laboratory experiment was designed.

5.4.2.1 Gravity/capillarity assisted infiltration

The principle idea of the first of the abovementioned fabrication approaches is illustrated in Figure 5.16 and can be described as follows:

- Preparing a fibrous W preform with defined architecture,
- embedding the preform on a mandrel in a suitable mould,
- Cu melt infiltration of the preform as well as

[16] These fabrication trials were performed in cooperation with industry, Louis Renner GmbH, Bergkirchen, Germany.

- demoulding and machining of the part to final dimensions.

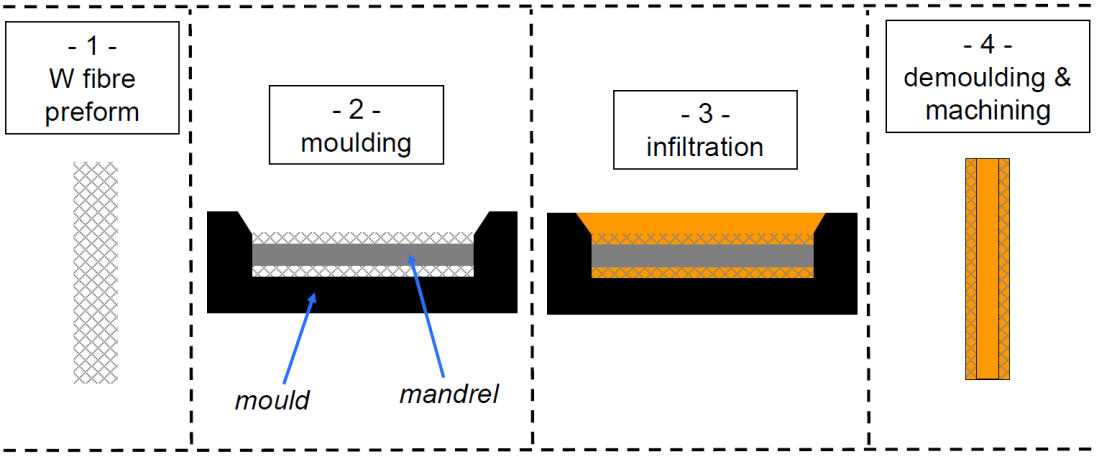

FIGURE 5.16: Schematic illustration of the fabrication of a W_f-Cu MMC pipe through liquid Cu infiltration of a fibrous W preform.

In Figure 5.17, images of early manufacturing trials according to this approach can be seen. These fabrication experiments were performed by using graphite as a mould and mandrel material during the infiltration process. Furthermore, the infiltration was performed with a maximum process temperature of 1220 °C and under H_2 atmosphere. In Figure 5.17a, an assembly before the Cu infiltration process is illustrated where the braided W fibre preform can be seen within the mould. In Figure 5.17b, the assembly after the infiltration process is shown (infiltrated matrix: Cu-OFE). In Figure 5.18, re-

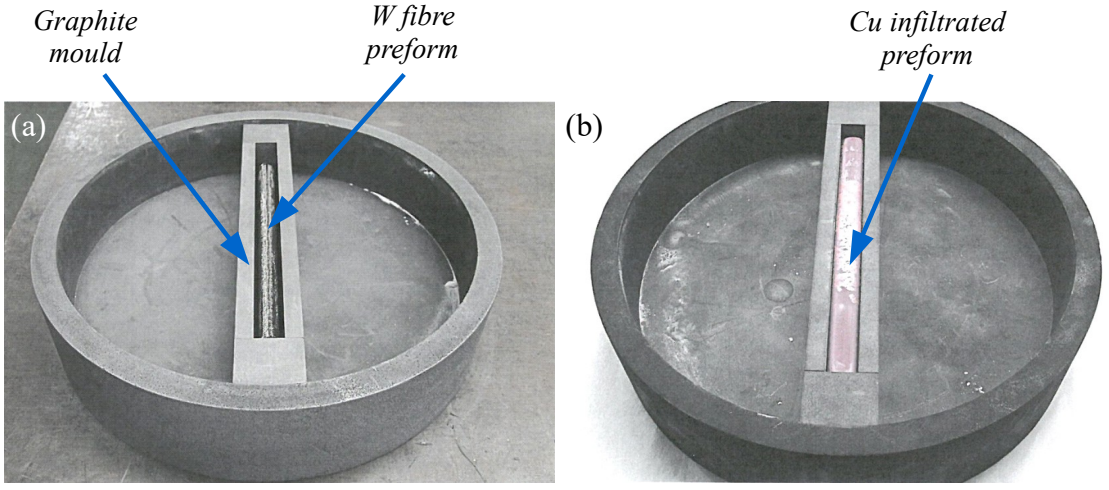

FIGURE 5.17: Early fabrication trials of W_f-Cu MMC pipe specimens: Assembly (a) before and (b) after the Cu infiltration process (infiltrated matrix: Cu-OFE).

sults of such a fabrication process are illustrated. Figure 5.18a shows a braided W fibre[17] preform used for these infiltrations. In Figure 5.18b, a specimen with a partly dissolved Cu matrix[18] is shown illustrating the embedded W fibre preform within the matrix. In

[17] K doped W fibre, nominal diameter 150 µm, OSRAM GmbH, wire BSD-OG 68,610 mg S3D bare
[18] The Cu matrix was dissolved with nitric acid (30wt.% aqueous solution).

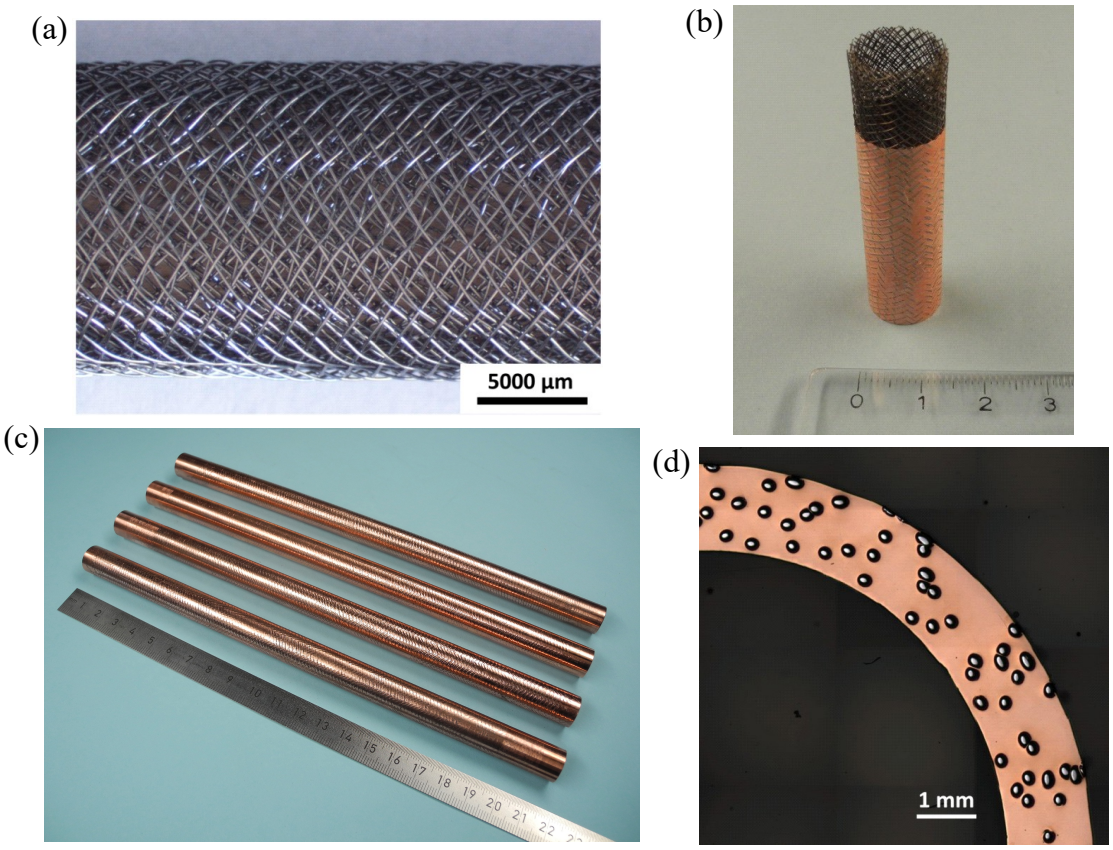

FIGURE 5.18: Results of early W_f-Cu MMC pipe specimen fabrication trials: (a) Braided W fibre preform used for the Cu infiltrations (diameter of W fibres: 150 µm), (b) specimen with partly dissolved Cu matrix, (c) W_f-Cu MMC pipe specimens after Cu infiltration and machining as well as (d) optical transversal microsection of a W_f-Cu pipe specimen.

Figure 5.18c, W_f-Cu MMC pipe specimens after Cu infiltration and machining are shown while in Figure 5.18d an optical transversal microsection of such a W_f-Cu pipe specimen is illustrated. The material depicted in Figure 5.18 demonstrated the viability of the elaborated W_f-Cu MMC fabrication procedure. In particular, metallographic investigations revealed that W_f-Cu material with high quality can be realised in such a way as the material did not exhibit porosity or voids (cf. Figure 5.18d) which is an important prerequisite for adequate thermophysical and -mechanical properties of MMCs.
However, during handling of the W_f-Cu MMC samples as illustrated in Figure 5.18 a significant deterioration of the mechanical properties of the infiltrated W fibres was found. After the Cu infiltration processing, the W fibres behaved unambiguously brittle at RT although the process temperatures during the Cu infiltration were considerably lower than the temperatures at which material property degradation due to recrystallisation and grain growth typically occurs in K doped drawn W fibres (cf. Figure 5.3 in which the ductile fracture behaviour of a drawn K doped W fibre after heat treatment at 1900 °C is illustrated).

In order to investigate these contradictory findings, dedicated experiments were performed on W fibre samples in order to examine the effect of the W_f-Cu MMC material manufacturing process on the properties of these high-strength reinforcements [169]. In more detail, single fibre tensile tests, microstructural investigations as well as chemical composition analyses were conducted on as-fabricated and heat treated W fibre samples as is described in the following.

As raw material for the investigations drawn K doped W fibres with a diameter of 150 µm[19] were used. Various heat treatments relevant with respect to a W_f-Cu MMC manufacturing process were performed in different furnaces and for different W fibre sample arrangements both in a laboratory[20] as well as an industrial environment[21]. The heat treatments were performed with temperatures in the range of 1100 °C to 1300 °C and dwell times in the range of 1 h to 8 h. In Table 5.1, an overview regarding the used furnaces is given.

TABLE 5.1: Details regarding the furnaces used for the heat treatments on W fibre samples.

environment	*atmosphere*	*purity/pressure*
laboratory	He 5.0	$\geq$ 99.999%
industry	H_2 3.0	$\geq$ 99.9%
industry	high vacuum (turbomolecular pump)	$\approx 10^{-5}$ mbar
industry	high vacuum (oil diffusion pump)	$\approx 10^{-5}$ mbar

In order to examine the mechanical performance of the W fibre samples uniaxial single fibre tensile tests were performed. For further experimental details, the reader is referred to [169].

In Figure 5.19, measured UTS values for all tested heat treated W fibre samples are shown [169]. In principle, it can be seen that there is some noticeable variety in the data. For the sake of clarity, the boundaries of the tensile performance of the samples in terms of mean UTS are highlighted. The *blue (round)* data points correspond to the samples exhibiting the best tensile performance with $\sigma_{UTS} = 2356 \pm 23.6$ MPa[22]. The *orange (triangle)* data points correspond to the samples exhibiting the worst tensile performance with $\sigma_{UTS} = 1909 \pm 196.6$ MPa. Furthermore, the *purple (diamond)* data points correspond to samples that underwent nominally the same heat treatment as the orange (triangle) samples in terms of maximum temperature and dwell time but exhibit a tensile performance of $\sigma_{UTS} = 2288 \pm 62.9$ MPa. The horizontal dashed lines within Figure 5.19 indicate the mean UTS values of the three highlighted sample types. The *grey (cross)* data points correspond to measured UTS values of all other heat treated

[19] K doped W fibre, nominal diameter 150 µm, OSRAM GmbH, Draht BSD-OG 68,610 mg S3D bare
[20] Max-Planck-Institut für Plasmaphysik, Garching, Germany
[21] Louis Renner GmbH, Bergkirchen, Germany
[22] plus/minus values correspond to the standard deviation of the measurements

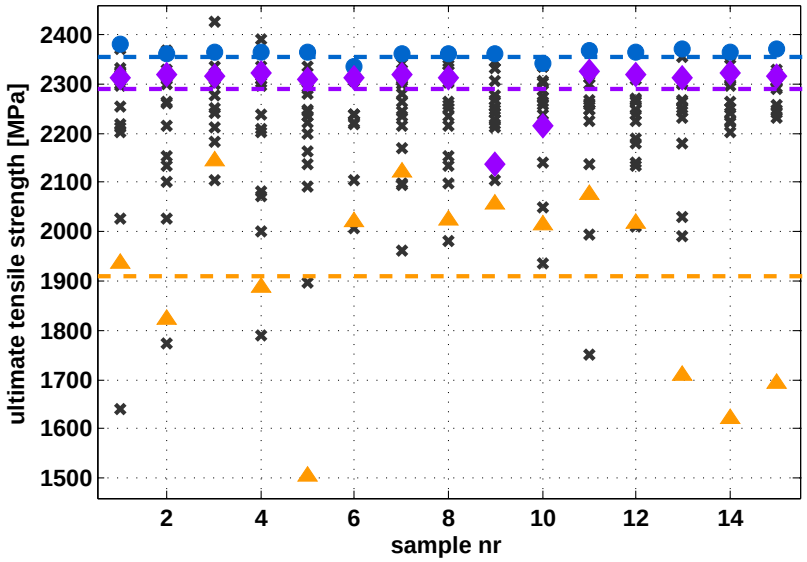

FIGURE 5.19: UTS of different heat treated W fibre samples (annealing temperatures: 1100 °C to 1300 °C, dwell times: 1 h to 8 h); blue (round) data points correspond to samples exhibiting the best tensile performance; orange (triangle) data points correspond to samples exhibiting the worst tensile performance; purple (diamond) data points correspond to samples that underwent nominally the same heat treatment as the orange (triangle) samples in terms of maximum temperature and dwell time but exhibit a different tensile behaviour; grey (cross) data points correspond to measured UTS values of all other heat treated W fibre samples [169].

W fibre samples and are shown in order to illustrate the overall amount of investigated samples.

The heat treatment corresponding to the blue (round) data was as follows:

- Heat treatment at 1100 °C for a dwell time of 1 h.
- Laboratory furnace with protective He atmosphere.
- Samples in protective Tantalum (Ta) foil envelope during the heat treatment.

The heat treatment corresponding to the orange (triangle) data was as follows:

- Heat treatment at 1220 °C for a dwell time of 2 h.
- Industrial furnace with protective H_2 atmosphere.
- Samples placed barely on a graphite crucible during the heat treatment.

The heat treatment corresponding to the purple (diamond) data was as follows:

- Heat treatment at 1220 °C for a dwell time of 2 h.
- Laboratory furnace with protective He atmosphere.
- Samples in protective Ta foil envelope during the heat treatment.

It can be seen from Figure 5.19 that there is considerably more scatter in the orange (triangle) data compared to the blue (round) and purple (diamond) data points which indicates that the former samples do not only exhibit a lower mean UTS but also a more brittle behaviour.

In Figure 5.20, measured stress-strain curves for the orange (triangle) and purple (diamond) samples illustrated in Figure 5.19 are shown [169]. The continuous orange curves correspond to the data highlighted with the same colour (triangle data points) in Figure 5.19 while the dashed purple curves correspond again to the data highlighted with the same colour (diamond data points) in Figure 5.19. It can be seen that the tensile

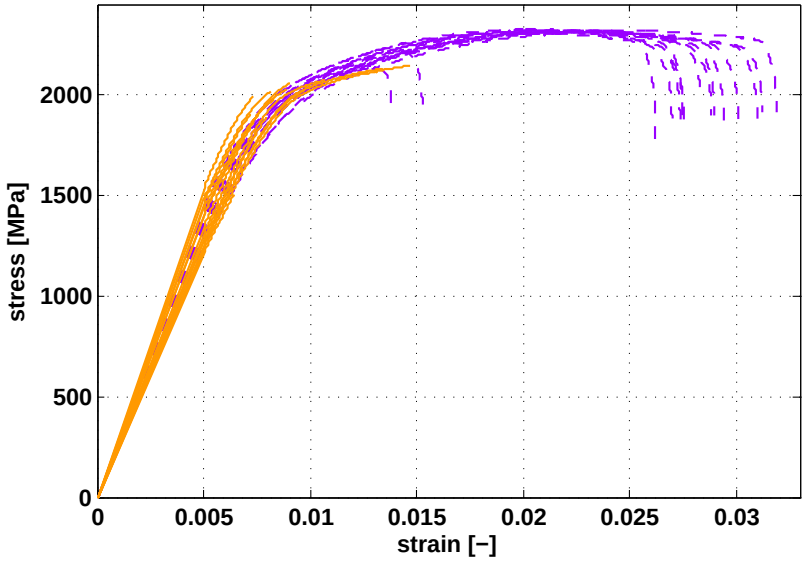

FIGURE 5.20: Tensile curves for two different W fibre sample types with nominally identical heat treatments in terms of maximum temperature and dwell time, namely 1220 °C for 2 h [169].

behaviour of these two samples differs significantly. While the dashed purple curves show a *ductile* behaviour, the orange curves indicate a rather *brittle* behaviour with most of the samples failing almost without plastic deformation. This finding is in line with the results for the UTS as illustrated in Figure 5.19. Nominally the two sample types illustrated in Figure 5.20 have been heat treated in the same way in terms of maximum temperature and dwell time, namely 1220 °C for 2 h. The difference between the two cases illustrated in Figure 5.20 was as follows: The samples corresponding to the continuous orange curves have been heat treated in an industrial furnace with protective H_2 atmosphere while the samples were placed barely on a graphite crucible during the heat treatment. The samples corresponding to the dashed purple curves have been heat treated in a laboratory furnace with protective He atmosphere while the samples were inside a protective Ta foil envelope during the heat treatment.

The result highlighted in Figure 5.20 is intriguing and indicates that apart from the maximum temperature and dwell time, additional heat treatment conditions regarding the sample arrangement or protection can have a strong impact on the post heat treatment mechanical performance of the investigated W fibres.
Fracture surfaces of tensile tested W fibre samples were imaged by means of SEM. Exemplary images can be seen in Figure 5.21 in which fracture surfaces of the samples pointed out in Figure 5.20 are shown [169]. In Figure 5.21a, a fracture surface of a sample corresponding to the dashed purple curves in Figure 5.20 is shown. It can be seen that the fracture surface indicates a ductile failure behaviour with local necking which is in line with the corresponding tensile curves illustrated in Figure 5.20. In Figure 5.21b, a fracture surface of a sample corresponding to the continuous orange curves in Figure 5.20 is shown. It can be seen that the fracture surface does not indicate a ductile failure behaviour but a brittle cleavage fracture. This result is also in line with the corresponding

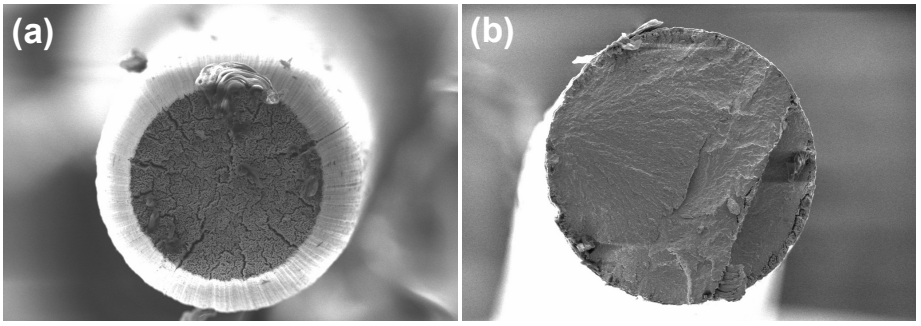

FIGURE 5.21: Exemplary fracture surfaces of the two W fibre sample types illustrated in Figure 5.20 that underwent nominally the same heat treatment (maximum temperature 1220 °C, dwell time 2 h): (a) Sample identified as *ductile* within tensile tests, (b) sample identified as *brittle* within tensile tests [169].

tensile behaviour illustrated in Figure 5.20. In Figure 5.22, exemplary longitudinal SEM microsections[23] (backscattered electron images) are shown for four different investigated W fibre samples [169]. Figure 5.22a shows an as-fabricated W fibre sample without any heat treatment. As expected, this fibre exhibits a comparably fine microstructure of elongated grains along the fibre drawing direction. Figure 5.22b shows a microsection of a W fibre sample corresponding to the orange (triangle) data points in Figure 5.19 and the continuous orange curves in Figure 5.20. This sample has been identified as worst performing and *brittle* within the tensile tests. Compared to Figure 5.22a, some grain coarsening can be observed. However, the microstructure still shows characteristic elongated grains and no extensive grain growth can be seen. For reasons of comparison, two microsections of samples heat treated in the laboratory furnace with protective He atmosphere within a protective Ta foil envelope during heat treatment and identified as *ductile*

[23] Details regarding the metallographic preparation of the samples illustrated in Figure 5.22 can be found in [170] which is a *Diplomarbeit* that was supervised by the author in the course of the present work.

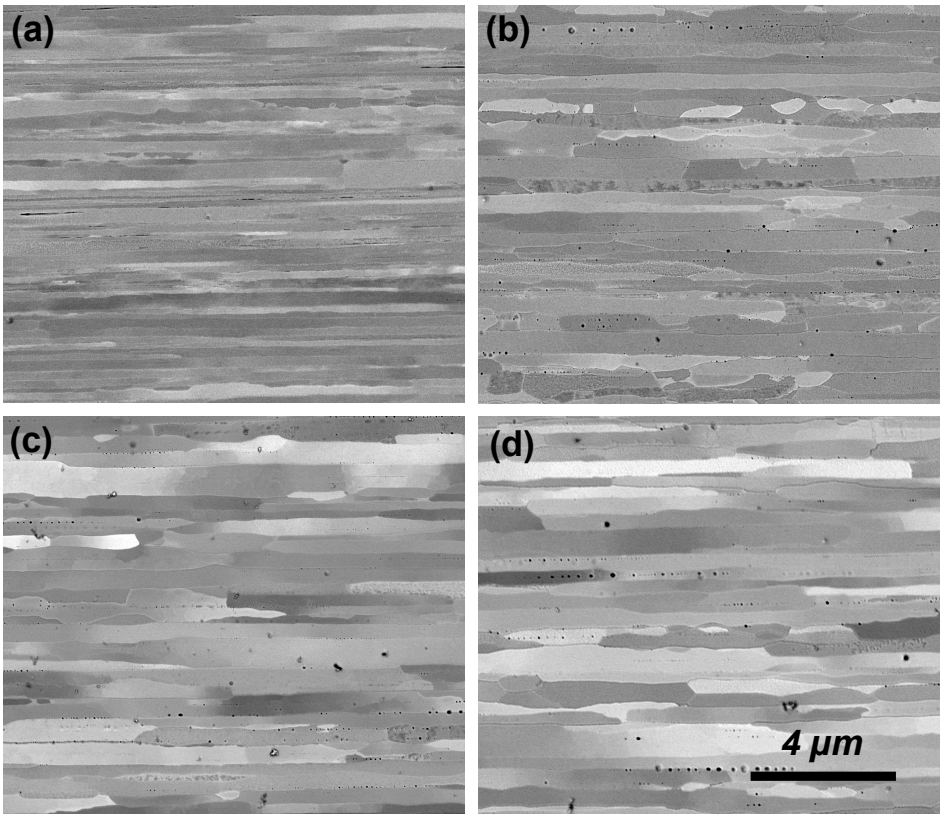

FIGURE 5.22: Longitudinal SEM microsections (backscattered electron images) of W fibre samples: (a) As-fabricated, (b) heat treated at 1220 °C for 2 h and identified as *brittle* within tensile tests (orange data in Figure 5.19 & Figure 5.20), (c) heat treated at 1300 °C for 2 h and identified as *ductile* within tensile tests and (d) heat treated at 1300 °C for 8 h and identified as *ductile* within tensile tests [169].

within tensile tests are included in Figure 5.22. These samples have been heat treated at 1300 °C with dwell times of 2 h (Figure 5.22c) and 8 h (Figure 5.22d). Figure 5.22c and Figure 5.22d also show slight grain coarsening compared to the as-fabricated W fibre illustrated in Figure 5.22a but again the characteristic elongated grain structure is unambiguously visible similar to Figure 5.22b. Hence, it can be stated that there is no fundamental difference in microstructure between the heat treated sample identified as *brittle* (Figure 5.22b) and the heat treated samples identified as *ductile* (Figure 5.22c,d) plainly visible. No additional phases or precipitates can be identified nor within nor at the boundaries of the grains.

As discussed above, the investigated heat treated W fibres can exhibit significantly differing tensile properties even if the samples undergo nominally the same heat treatment in terms of maximum temperature and dwell time. This finding has led to the conclusion that chemical composition analyses on heat treated samples are required in order to provide information about the incorporation of impurities into the samples during heat treatments that in turn might be related to the observed mechanical property degradation. Hence, C, N, O, H chemical composition analyses were performed on the following

W fibre samples[24]:

- No. 1: as-fabricated *reference* sample
- No. 2: sample heat treated in laboratory furnace with protective He atmosphere and in protective Ta foil envelope; maximum temperature 1220 °C; identified as *ductile* during manual handling of the sample and tensile testing (dashed *purple* curves in Figure 5.20).
- No. 3: sample heat treated in industrial furnace with protective H_2 atmosphere and barely on graphite crucible; maximum temperature 1220 °C; identified as *brittle* during manual handling of the sample and tensile testing (continuous *orange* curves in Figure 5.20).
- No. 4: sample directly dissolved from a W_f-Cu composite material[25] infiltrated in an industrial furnace under protective H_2 atmosphere within a graphite crucible; maximum temperature 1220 °C; identified as *brittle* during manual handling of the sample.
- No. 5: sample heat treated in laboratory furnace with protective He atmosphere within protective Ta foil envelope; maximum temperature 1300 °C; identified as *ductile* during manual handling of the sample and tensile testing.
- No. 6: sample heat treated in industrial furnace with protective H_2 atmosphere on a W sample holder placed on a Mo plate; maximum temperature 1220 °C; identified as *ductile* during manual handling of the sample and tensile testing.

The results of the C, N, O, H chemical composition analyses are summarised within Table 5.2.

[24] The measurements were performed at Forschungszentrum Jülich, Zentralinstitut für Engineering, Elektronik und Analytik (ZEA-3). The following equipment was used: Leco CS 600 C/S determinator; Leco TCH 600 N/O/H determinator.

[25] The Cu matrix was dissolved with nitric acid (30wt.% aqueous solution).

TABLE 5.2: Results of the C, N, O, H chemical composition analyses for different W fibre samples.

sample	T_{max}	*behaviour at RT*	*C [wt.%]*	*N [wt.%]*	*O [wt.%]*	*H [wt.%]*
No. 1 - as-fabricated	-	ductile	< 0.0024	< 0.0009	0.0031	< 0.0002
No. 2 - annealed	1220 °C	ductile	< 0.0013	< 0.0008	0.009	0.00024
No. 3 - annealed	1220 °C	brittle	0.0034	< 0.0006	0.109	0.00082
No. 4 - annealed	1220 °C	brittle	0.0586	< 0.0009	0.0081	0.00029
No. 5 - annealed	1300 °C	ductile	< 0.001	< 0.0006	0.0033	0.000156
No. 6 - annealed	1220 °C	ductile	< 0.0012	< 0.0006	0.0024	0.00009

The conclusions that can be drawn from the results of the chemical composition analyses are as follows:

- For all samples, the **N** content is below the detection limit.
- For all samples, the **H** content is low, for sample No. 1 even below the detection limit; the highest H content has been measured for sample No. 3 with a maximum value of 0.00082 *wt.%*.
- For all samples, an **O** content has been measured; sample No. 3 shows an outstanding O content with 0.109 *wt.%*.
- All samples categorised as *brittle* exhibit an increased **C** content - with a maximum value of 0.0586 *wt.%* for sample No. 4 - but not necessarily an increased O content.
- For all samples categorised as *ductile* the **C** content is below the detection limit.

In addition, the measured C content of samples No. 3 and 4 seems to be plausible as these samples were heat treated in contact with graphite crucibles that presumably act as a source of C contaminations that are incorporated into the W fibres during heat treatment.

To summarise, it can be stated that the tensile test results regarding heat treated W fibres showed a rather strong variety even for samples that underwent nominally identical heat treatments in terms of temperature and dwell time. As microstructural SEM

investigations did not reveal any plainly visible difference between samples that behaved rather differently during tensile testing, chemical composition analyses were performed on selected samples. These analyses indicate that impurities incorporated into the material during the heat treatments are the underlying reason for the deterioration of the W fibre mechanical properties. Especially, all W fibre samples identified as *embrittled* exhibited an increased C impurity content.

This result seems to be reasonable as it is known that the mechanical properties of W materials are strongly influenced by the presence of impurity elements [60]. Within a comprehensive study [171], the effects of O and C impurities with respect to the mechanical properties of polycrystalline and high-purity single crystal W was investigated. This study revealed that already additions of a few 10 ppm, of both O and C, to polycrystalline W induce a significant increase in the DBTT. For the case of C impurities this is illustrated in Figure 5.23 [171]. Furthermore, it was concluded within that study that

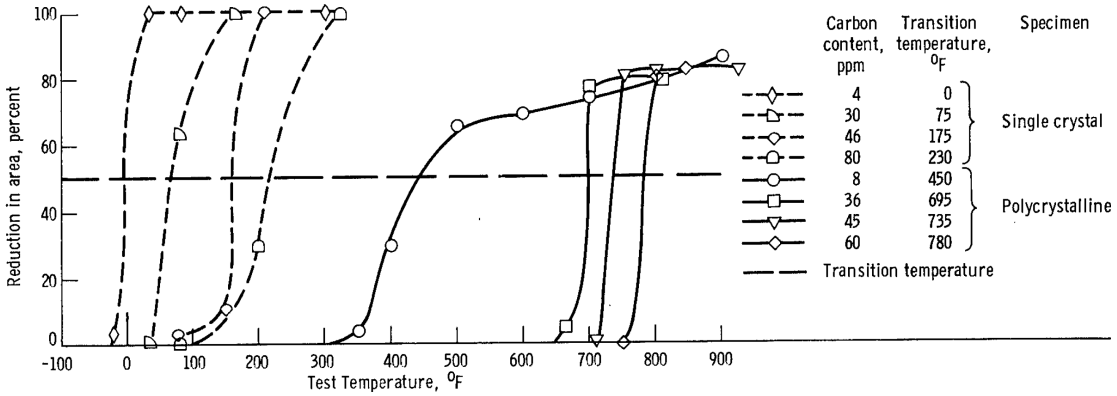

FIGURE 5.23: Effect of C impurities on the ductility of W according to [171] (temperature scale in °F).

embrittlement arising from O contamination is due to grain boundary segregation facilitating intergranular fracture while embrittlement arising from C impurities is primarily due to the interaction between dislocations and the C impurity atoms.

Furthermore, recent work regarding W fibre-reinforced W materials [172] indicates that during field assisted sintering of such materials there is a direct influence of the used die lining material on the properties of the W fibres within the consolidated composite material. Specifically, it was found that if graphite sheets are used as a lining material the W fibres show brittle cleavage fracture while they exhibit a more ductile behaviour with necking and knife edge fracture for material processed with a W foil die lining. This finding can be regarded in line with the results described within the present work and confirms that sources of C impurities can deteriorate the mechanical properties of W fibres sensibly.

The main practical implication of the abovementioned is that for the investigated drawn W fibres the conditions for processing have to be considered carefully and that sources

of contamination, especially C based materials like graphite, have to be avoided at all during W fibre-reinforced composite material manufacturing processes that involve high temperatures.

As a conclusion, the W_f-Cu MMC fabrication process was adapted by avoiding possible sources of W fibre contamination, in particular C based mould and mandrel materials, during the Cu infiltration process. Hence, a mould and mandrel material similarly practical as graphite and compatible with the process conditions had to be applied. A *boron nitride* (BN) material grade[26] was chosen in this respect as a material that is compatible with high process temperatures as well as molten Cu. Corresponding material manufacturing experiments were conducted as is illustrated in Figure 5.24. Figure 5.24a shows a W fibre[27] braid on a BN rod, Figure 5.24b shows the braid illustrated in Figure 5.24a within a BN mould and Figure 5.24c shows the assembly before Cu infiltration. The

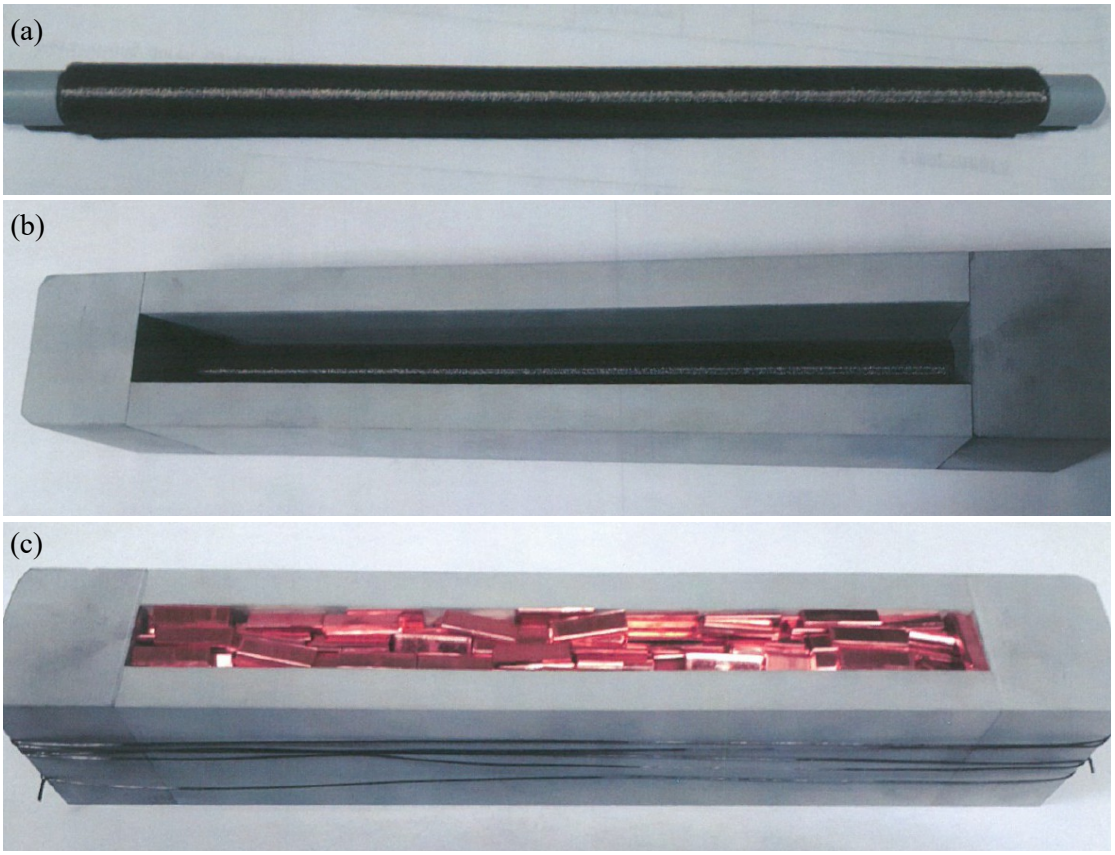

FIGURE 5.24: W_f-Cu MMC pipe specimen fabrication trial: W fibre braid (a) on BN rod and (b) within BN mould as well as (c) the final assembly before Cu infiltration.

experimental proof for the preservation of the W fibre ductility through a W_f-Cu MMC fabrication as illustrated in Figure 5.24 is given in Figure 5.25. Figure 5.25a shows the fractured part of a W_f-Cu MMC pipe specimens that was infiltrated[28] as illustrated in

[26] HeBoSint® O120, Henze BNP AG, Lauben, Germany

[27] K doped W fibre, nominal diameter 50 µm, OSRAM GmbH, wire BSD-OG 7,647 mg S1B bare

[28] The infiltration was performed with a maximum process temperature of 1200 °C and under HV atmosphere ($\approx 10^{-5}$ mbar).

Figure 5.24 and subsequently tensile tested in axial direction at RT[29]. In Figure 5.25b, fractographic SEM images of the W_f-Cu pipe specimens are shown. It can be seen that the W fibres failed in a ductile manner with local necking.

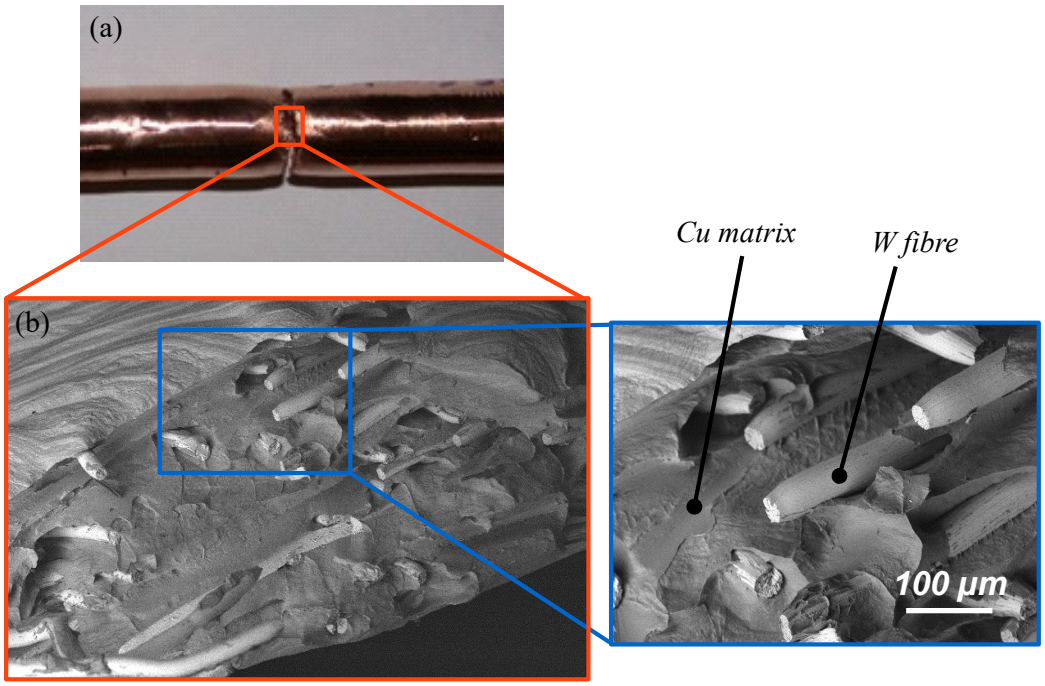

FIGURE 5.25: (a) Fractured part of a W_f-Cu MMC pipe specimen (inner diameter: 12 mm, wall thickness: 1.5 mm, length: 150 mm) that was tensile tested in axial direction at RT and (b) corresponding fractographic SEM images.

5.4.2.2 Centrifugal infiltration

In section 3.4, it has been mentioned that compared with monolithic materials the manufacturing of MMCs is typically more complicated. Within reference [111] it is in this context explicitly stated that the difficulties in MMC production technology are - among other things - due to the following requirements:

- A strong bond of the reinforcing fibres with the matrix material needs to be ensured.
- The MMC has to be realised with a strength reasonably near to theoretical expectation, i.e. with high material quality.
- The required shape and dimensions of the MMC need to be achieved.

Against this background, a process for liquid Cu infiltration of cylindrical fibrous W preforms in a centrifugal force field was investigated within the present work. This approach makes use of the tubular geometry of the W_f-Cu MMC of interest and represents

[29] The tensile test on the W_f-Cu MMC pipe specimen was performed in the framework of research activities within the EUROfusion work package materials (WPMAT) at ENEA Frascati Research Center, Italy.

a straightforward fabrication method where the centrifugal forces promote the infiltration of the preform to yield a high quality MMC without cavities or residual porosity similar to *centrifugal casting*.

Centrifugal casting is a well-known manufacturing process for the fabrication of rotationally symmetric products. By inserting melt into a rotating mould friction and centrifugal forces push the melt against the wall of the mould. The melt is then solidified while the centrifugal force field is sustained. Such a solidification typically results in a high quality material microstructure without cavities and with low residual porosity as such casting defects are less dense than the melt and hence gather at the inner diameter of the part during the rotation. The outer diameter of a centrifugally cast part is defined by the inner diameter of the mould while the wall thickness of the part can be adjusted straightforwardly by altering the amount of inserted melt. For further information regarding the topic of centrifugal casting the reader is referred to [173].

The use of centrifugal forces to promote the liquid infiltration of porous preforms is well suited for MMC fabrication and has also been proposed elsewhere [174, 175]. Furthermore, the process of liquid infiltration of fibrous preforms in a centrifugal force field has been described theoretically in [176]. The general idea behind the centrifugal infiltration process of W_f-Cu MMCs discussed within the present work is illustrated in Figure 5.26 and can be described as follows:

- Preparing a fibrous W preform with defined architecture,
- inserting the preform into a rotatable mould together with the Cu infiltrate,
- centrifugal Cu melt infiltration of the preform through heating and rotating the mould as well as
- demoulding and machining of the part to final dimensions.

For the investigation of the viability of such a fabrication process for W_f-Cu MMC pipe specimens a dedicated experiment has been designed and set up in the course of the present work[30]. In principle, such a device has to comprise a rotatable mould that provides a sufficient centrifugal force field and contains the constituents of the MMC at temperatures above the melting point of Cu[31]. Furthermore, a protective atmosphere has to be created inside the mould in order to avoid pronounced oxidation of the MMC constituents during the infiltration process.

In general, by varying the angular velocity ω of a rotating mould the centrifugal force F_c acting on a mass m can be adjusted for a given radius r according to

$$F_c = m\,\omega^2\,r. \tag{5.2}$$

[30] The experiment was designed and constructed in the framework of a *Semesterarbeit* that was supervised by the author in the course of the present work [177].

[31] $T_{m,Cu} = 1083\,°C$ [59]

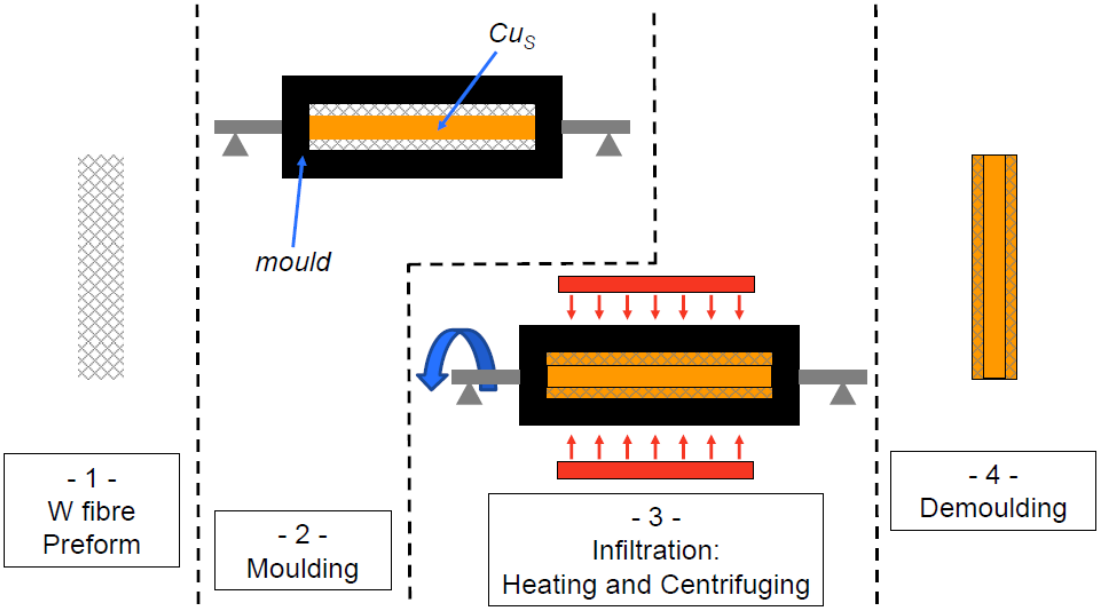

FIGURE 5.26: Schematic illustration of the fabrication of a W_f-Cu MMC pipe through centrifugal liquid Cu infiltration of a fibrous W preform.

Apart from that, it can be stated that during a melt infiltration the centrifugal force has to be very high compared to the gravitational force $F_g = m\,g$. By using $\omega = 2\,\pi\,f$, Equation 5.2 and

$$F_c = n\,F_g \tag{5.3}$$

the following relation between the angular frequency f and a factor n describing how much the centrifugal force exceeds the gravitational force can be derived:

$$f_n = \frac{1}{2\,\pi}\sqrt{\frac{n\,g}{r}} \tag{5.4}$$

With an inner diameter of 12 mm of the preform to be infiltrated one can calculate frequencies for different multiples of g according to Equation 5.4 as is summarised in Table 5.3.

TABLE 5.3: Rotational speeds for $n = 1, 10, 100$ calculated according to Equation 5.4.

n	f
1	$386.13\,\mathrm{min}^{-1}$
10	$1221.04\,\mathrm{min}^{-1}$
100	$3861.27\,\mathrm{min}^{-1}$

It can be stated that the rotational speeds given in Table 5.3 are technologically well realisable.

The central part of the centrifugal infiltration device set up in the course of the present work is the *rotating mould* which must be able to contain the MMC constituents during the centrifugal infiltration process. A schematic illustration of the rotating mould design

is shown in Figure 5.27. It can be seen that the basic structural element is a ceramic tube which is loaded with a liner that in turn contains the MMC constituents and gives the infiltrated MMC its shape. The torque is transferred to the rotating mould via O-ring clamping connections. To compensate for the differing thermal expansivities of the ceramic tube and spacers that hold the liner in position a thermal compensator is implemented. For further information regarding the detailed thermal and mechanical

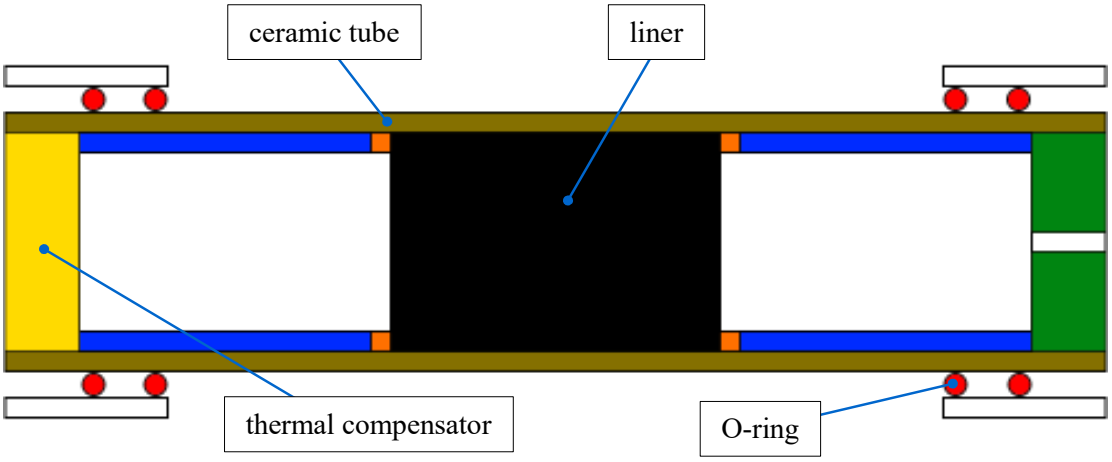

FIGURE 5.27: Schematic design of the rotating mould.

design of the centrifugal infiltration device the reader is referred to [177].
In Figure 5.28, an image of the assembled centrifugal infilatration device is illustrated and the following most important features are highlighted:

- The tube furnace through which the rotating mould passes,
- on the left and right sides, the bearings with the corresponding flanges edging the ceramic tube by means of O-ring clampings,
- at the left-hand flange, the rotary union that is needed in order to maintain HV conditions during the mould rotation,
- at the right-hand flange, the electric motor that drives the mould by means of a belt as well as
- two hinged protective covers that were installed for safety reasons.

In Figure 5.29, the centrifugal infiltration procedure of a W_f-Cu MMC pipe specimen is illustrated. In Figure 5.29a, a braided W fibre[32] preform before Cu infiltration is illustrated. In Figure 5.29b, the assembly of such a preform inside a BN[33] liner and a corresponding Cu infiltrate rod is shown. In Figure 5.29c, the assembly with inserted

[32] K doped W fibre, nominal diameter 50 µm, OSRAM GmbH, wire BSD-OG 7,647 mg S1B bare
[33] HeBoSint® O120, Henze BNP AG, Lauben, Germany

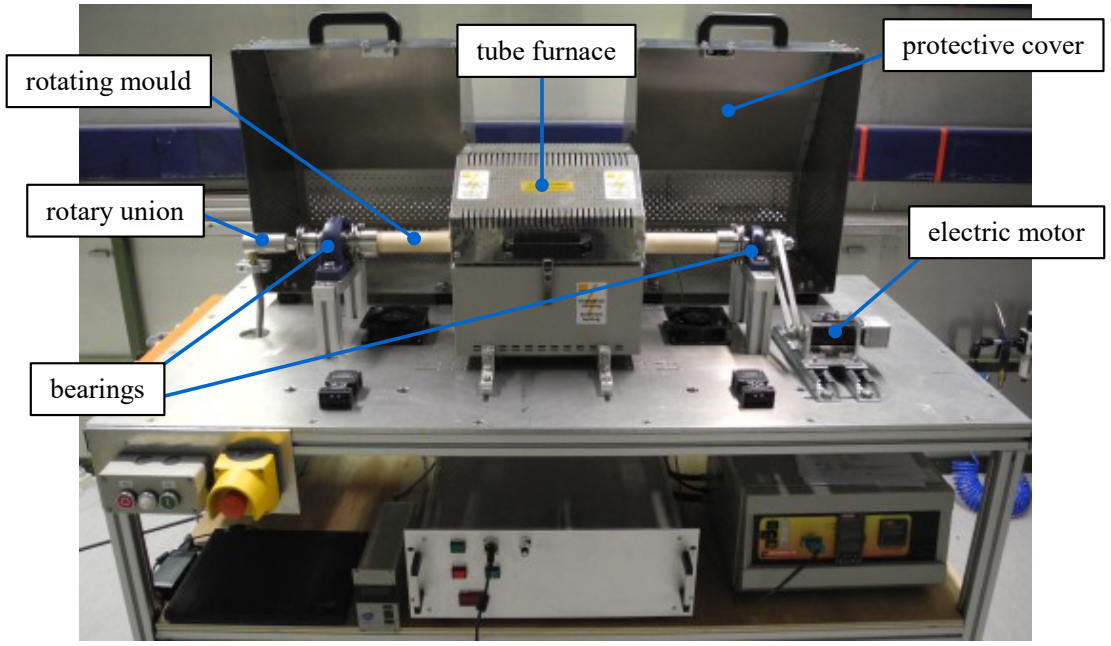

FIGURE 5.28: Assembled centrifugal infiltration device for the fabrication of W_f-Cu MMC pipe specimens.

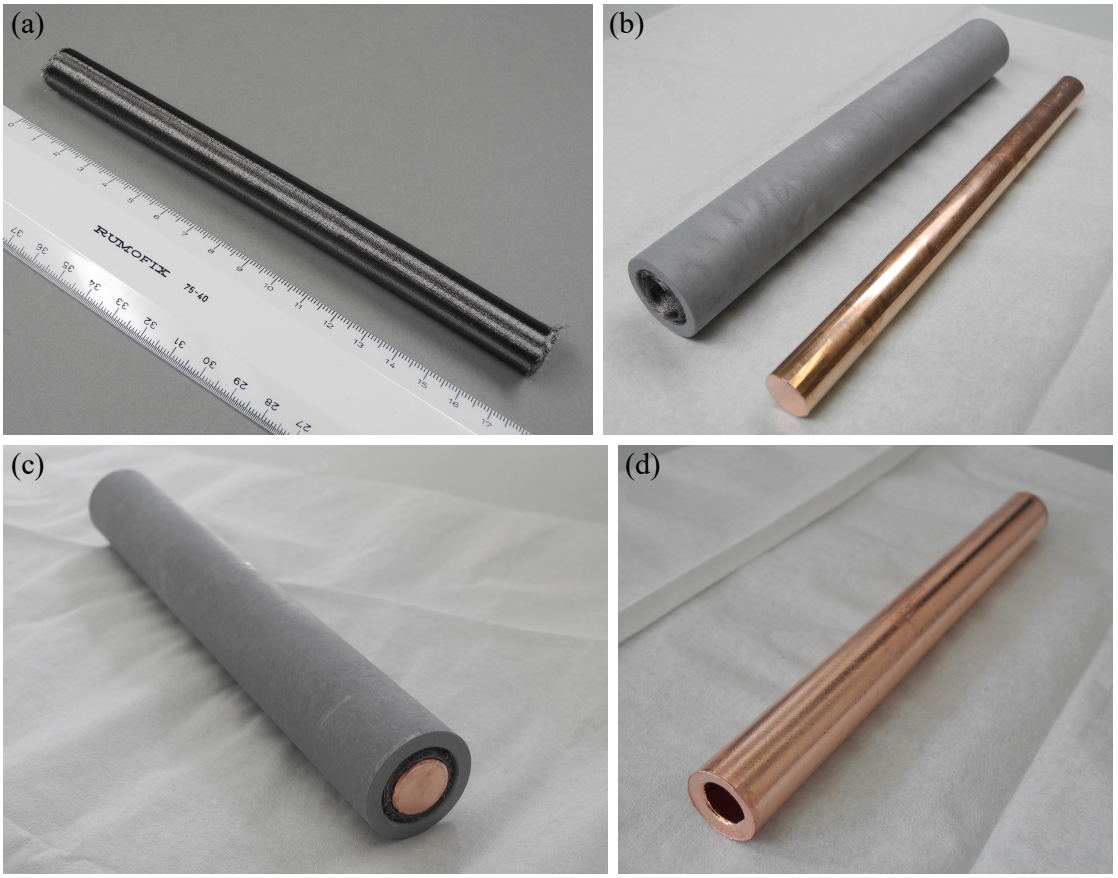

FIGURE 5.29: Illustration of the centrifugal infiltration procedure of a W_f-Cu MMC pipe specimen: (a) Braided W fibre preform, (b) preform in BN liner and Cu infiltrate rod, (c) assembly with inserted W fibre preform and Cu rod as well as (d) centrifugally infiltrated preform after liner removal.

Cu rod is shown[34]. In Figure 5.29d, the result of a centrifugal infiltration process[35] is illustrated after liner removal.

5.5 Material property predictions through mean-field homogenisation

It has been mentioned that W_f-Cu materials exhibit potentially superior properties compared with monolithic Cu alloys due to the incorporation of the reinforcing W fibres and that this aspect is regarded a central consideration concerning the application of these materials to highly loaded PFCs. However, the question arises what properties can be expected from and achieved with a W_f-Cu MMC material and how they compare with properties of existing Cu alloys.

In order to adress this question, computations based on *mean-field homogenisation* (MFH) were performed to predict the thermophysical and -mechanical properties of W_f-Cu MMCs. MFH is a well-established method for the prediction of multiphase composite material behaviour based on per-phase properties and microstructure definition. Furthermore, MFH is based on analytical expressions which implies that corresponding computational tools are rather efficient. The MFH code used within the present work is *DIGIMAT-MF*[36] with a *Mori-Tanaka* homogenisation scheme [178]. As input for the computations, the properties of the individual W_f-Cu composite material constituents, the W fibres and the Cu (alloy) matrix material, were used[37]. Output of the computations was then a parametric analysis of the following effective macroscopic properties of W_f-Cu:

- Thermal conductivity,
- CTE as well as
- stress-strain behaviour from which the 0.2% yield strength was determined.

For UD W_f-Cu material (pure Cu matrix) the thermal conductivity at 20 °C and 500 °C in longitudinal and transverse direction versus fibre volume fraction is illustrated in Figure 5.30. As expected, it can be seen that the fibre volume fraction is a determining factor for the effective thermal conductivity of the composite. Furthermore, it can be seen that the behaviour in longitudinal direction can in principle be described by a simple linear rule-of-mixture and that the differences in orientation are reasonably small. An-

[34] During the centrifugal infiltration process, the assembly as illustrated in Figure 5.29c is closed at the ends with suitable sockets made out of BN.

[35] The sample illustrated in Figure 5.29d was infiltrated with Cu-OFE at a maximum process temperature of 1200 °C, a maximum rotational speed of 2200 min^{-1} and under HV conditions of $\approx 10^{-5}$ mbar.

[36] Version 6.0.1

[37] The W_f-Cu MMC constituent's properties used for the MFH computations are given as tabulated values in Appendix B.

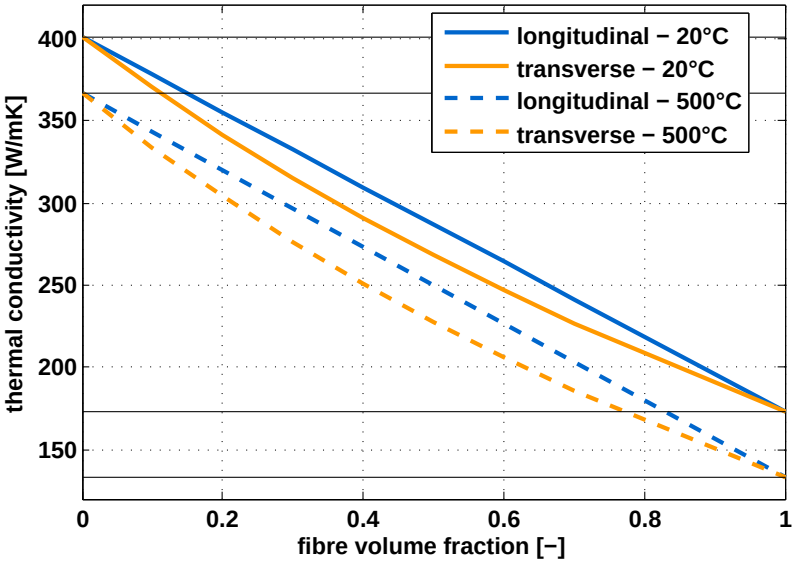

FIGURE 5.30: Longitudinal and transverse thermal conductivity of UD W_f-Cu (pure Cu matrix) at 20 °C and 500 °C predicted by means of MFH versus fibre volume fraction (the black horizontal lines indicate the thermal conductivities of pure W and pure Cu at 20 °C and 500 °C).

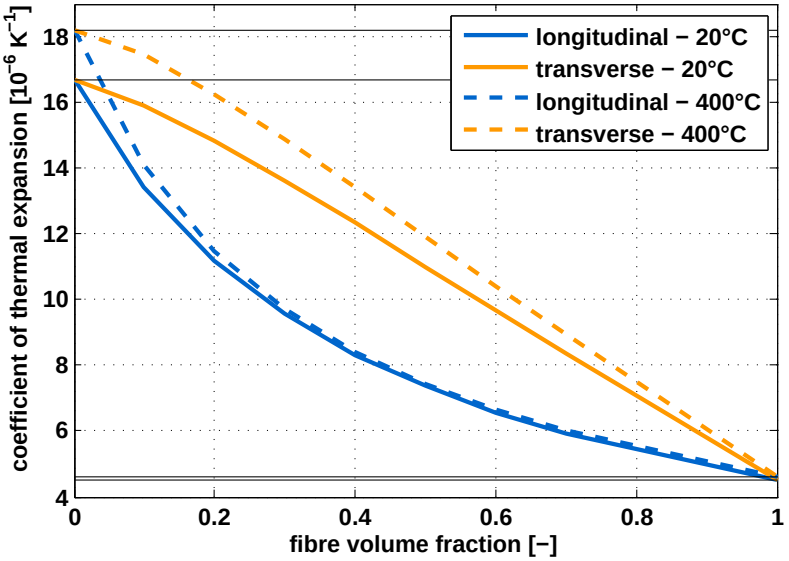

FIGURE 5.31: Longitudinal and transverse CTE of UD W_f-Cu (pure Cu matrix) at 20 °C and 400 °C predicted by means of MFH versus fibre volume fraction (the black horizontal lines indicate the CTEs of pure W and pure Cu at 20 °C and 400 °C).

other material property of importance with regard to HHF applications is the CTE. This quantity is illustrated in Figure 5.31, again for UD W_f-Cu material (pure Cu matrix) at 20 °C and 400 °C in longitudinal and transverse direction versus fibre volume fraction[38]. It can be seen that the CTE differences regarding the two perpendicular directions are

[38] For these computations, both composite material phases were modelled as thermoelastic material.

rather pronounced implicating that macroscopic CTE reduction in a W_f-Cu material is especially effective in longitudinal direction, i.e. along the fibre orientation. Figure 5.31 furthermore indicates that for a fibre volume fraction of 0.3 the longitudinal CTE is reduced by approximately 40% with respect to the pure Cu matrix material. This can be regarded a notable reduction that can be exploited in order to mitigate thermally induced stresses at W PFM to heat sink joints in PFCs.

The mechanical performance of W_f-Cu was estimated in terms of the 0.2% yield strength which was determined from computed stress-strain curves. In Figure 5.32, such stress-strain curves for UD W_f-CuCrZr (CuCrZr matrix in SAA condition, heat treatment B according to reference [121]) at 20 °C are exemplarily illustrated. For these computa-

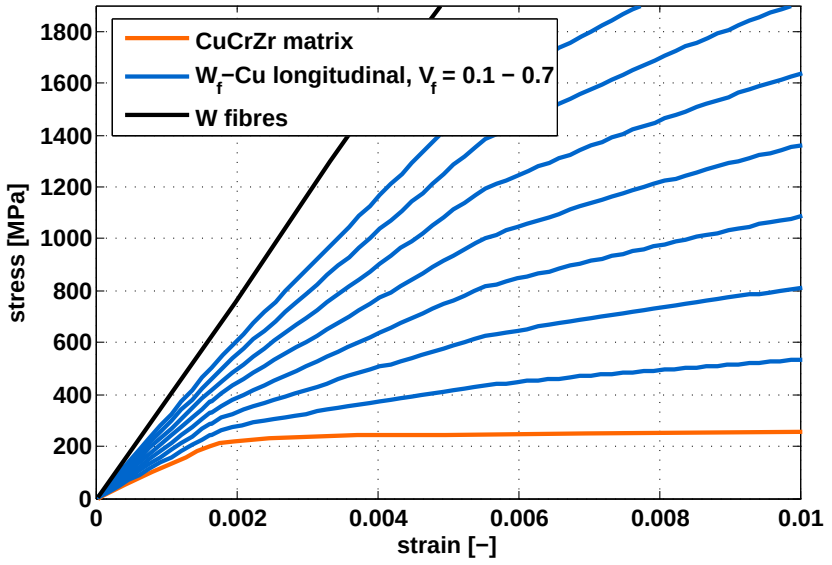

FIGURE 5.32: Longitudinal stress-strain behaviour of UD W_f-CuCrZr (CuCrZr matrix in SAA condition, heat treatment B according to reference [121]) at 20 °C predicted by means of MFH for different fibre volume fractions ranging from 0.1 to 0.7.

tions, both the matrix material and the reinforcing fibres were modelled as elastoplastic material[39]. The blue curves in Figure 5.32 illustrate the computed W_f-CuCrZr stress-strain behaviour for different fibre volume fractions, ranging from 0.1 to 0.7. The black curve shows the experimentally determined behaviour of the reinforcing W fibres[40]. The orange curve illustrates the stress-strain behaviour of the CuCrZr matrix material according to reference [121]. The W_f-CuCrZr stress-strain curves in Figure 5.32 show a typical behaviour of ductile-fiber/ductile-matrix composites which is characterised by different stages of deformation [110]. First, the fibres and the matrix are both elastically strained meaning that also the composite exhibits overall elastic behaviour. When the composite is further loaded the matrix begins to deform plastically while the fibres continue to

[39] J_2 plasticity with isotropic hardening (pure Cu and CuCrZr: power law according to $R(p) = kp^m$; W fibre: exponential law according to $R(p) = R_\infty[1 - \exp(-mp)]$)

[40] W yarn made out of filaments with a diameter of 20 µm as described above in section 5.4

deform elastically[41]. When the composite is even further loaded, both the fibres and the matrix material are deforming plastically while this behaviour continues until the UTS of the composite is reached. From stress-strain curves as illustrated in Figure 5.32 the 0.2% yield strength was determined in order to compare the W_f-Cu behaviour with Cu alloy property data from literature. In Figure 5.33, such a comparison based on data for different Cu alloys from [79] is shown in terms of thermal conductivity versus 0.2% yield strength at 20 °C. Results for UD W fibre-reinforced material loaded in longitudinal and

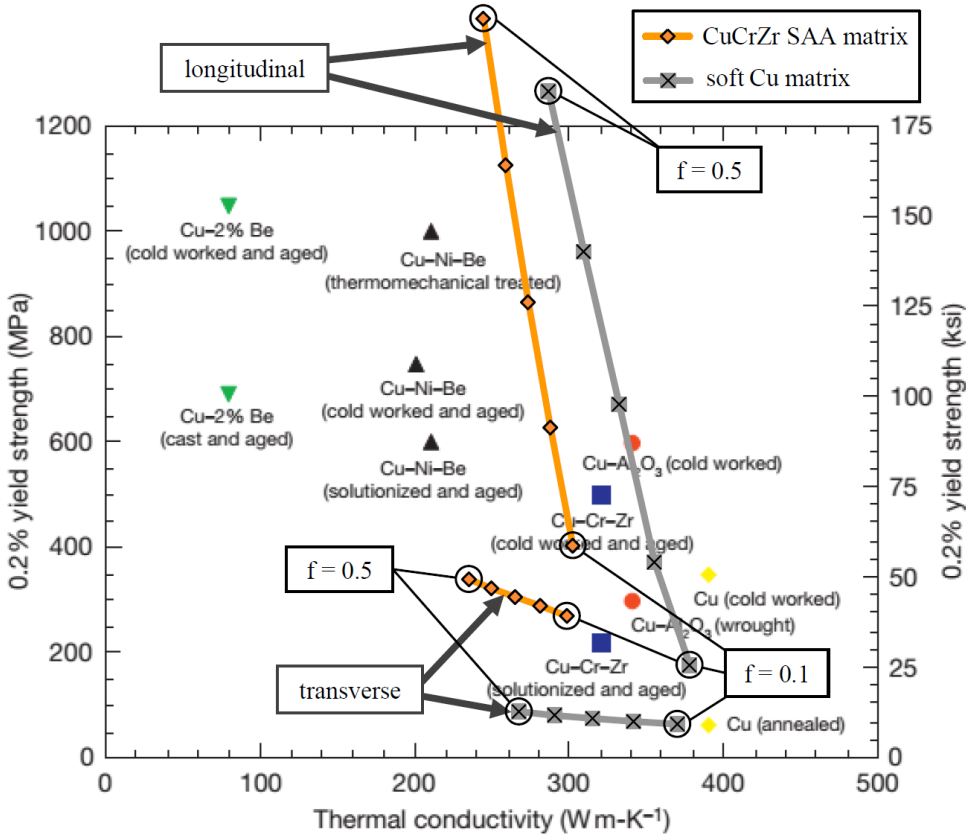

FIGURE 5.33: 0.2% yield strength versus thermal conductivity at 20 °C for UD W_f-Cu (longitudinal and transverse direction, pure Cu and CuCrZr (SAA condition; heat treatment B according to reference [121]) matrix, fibre volume fractions ranging from 0.1 - 0.5) predicted by means of MFH in comparison with Cu alloys [79].

transverse direction, with a pure Cu and a CuCrZr (SAA condition, heat treatment B according to reference [121]) matrix, and for fibre volume fractions ranging from 0.1 - 0.5 are illustrated. As expected, a significant difference can be identified regarding the loading direction. Furthermore, it can be seen that an increase in yield strength is associated with a decrease in thermal conductivity that in turn is related to the increase in W fibre volume fraction. Apart from that, it can be seen that within this representation longitudinal UD W_f-Cu materials in principle open up a parameter space of significantly

[41] According to uniaxial tensile tests at RT, drawn W fibres in an as-fabricated condition can be loaded elastically up to about 0.5% strain (cf. Figure 5.13) while CuCrZr can according to reference [121] be loaded elastically only up to approximately 0.1% strain.

higher yield strength compared with CuCrZr and Cu-Al_2O_3 material grades while at the same time ensuring thermal conductivities higher compared with high-strength CuNiBe alloys. Related to Figure 5.33, it should be mentioned that deformation hardened Cu alloys, like the indicated cold worked material grades, are not considered as strictly relevant with respect to elevated temperature PFC application as their strengthening is usually lost during short-period annealing at temperatures above 300 °C to 400 °C due to recrystallisation processes and dislocation recovery [66]. Numerically, it can be seen that longitudinal UD W_f-Cu with a pure, i.e. soft, Cu matrix and a fibre volume fraction of 0.2 outperforms CuCrZr in SAA condition both in terms of yield strength and thermal conductivity.

An entirely UD fibre-reinforced material is typically not given in a practical and realistic component or application. Within the present work, W_f-Cu MMC heat sink pipes were fabricated based on braided preforms as described within section 5.4.1. These preforms exhibit a certain fibre orientation - as can e.g. be seen in Figure 5.11 - which influences the anisotropic properties of the composite material strongly. Hence, W_f-Cu property estimation was done for such a fibre architecture. Therefore, the composite material was modelled as a multi-layered microstructure[42] according to the braid as illustrated in Figure 5.11b, i.e. with fibres oriented with a braiding angle of 78°. Analoguous to Figure 5.33, the 0.2% yield strength in braid hoop direction - which is the main reinforcement direction - versus thermal conductivity in radial direction through the multi-layered braided composite structure at 20 °C is illustrated in Figure 5.34. Again, results for material with a pure Cu and a CuCrZr (SAA condition; heat treatment B according to reference [121]) matrix, and for fibre volume fractions ranging from 0.1 - 0.5 are illustrated. It can be seen that the situation is somewhat different compared to the UD reinforcement case illustrated in Figure 5.33. As expected, the slope of the curves is more shallow and the yield strength values are in principle lower due to the fibre orientation that deviates from the loading direction by 12°. However, the main conclusions that have been drawn above for the UD fibre-reinforced material can still be regarded as valid. This means that a significantly higher yield strength compared with CuCrZr and Cu-Al_2O_3 material grades can be achieved while at the same time higher thermal conductivities compared with high-strength CuNiBe alloys can be ensured. Furthermore, it can be seen that the W_f-Cu material with a soft Cu matrix and a fibre volume fraction of 0.2 still outperforms SAA CuCrZr both in terms of yield strength and thermal conductivity.

The macroscopic CTE in hoop direction for a W_f-Cu material (pure Cu matrix) based on a braided preform as discussed above is illustrated in Figure 5.35 at 20 °C and 400 °C

[42] For these computations, the W fibres were, due to limitations of the used DIGIMAT-MF software, conservatively modelled as ideally plastic material (experimentally determined W fibre yield strain at RT: 0.546%) while the pure Cu and CuCrZr matrix materials were modelled as elastoplastic materials with J_2 plasticity and isotropic hardening.

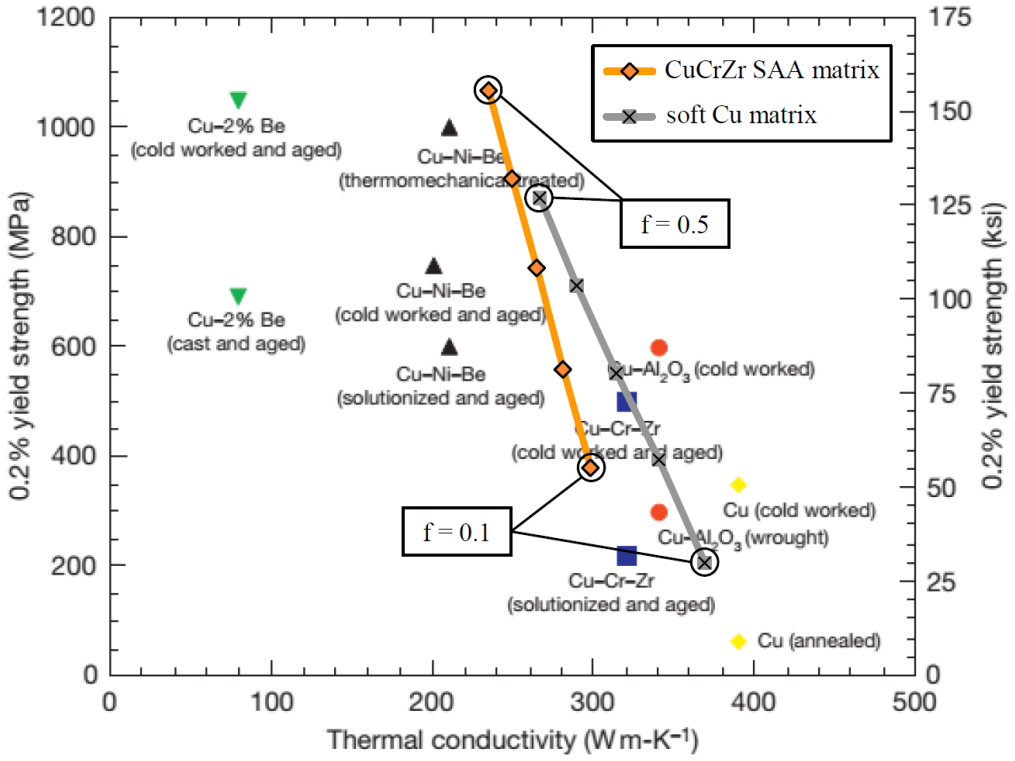

FIGURE 5.34: 0.2% yield strength in hoop direction versus thermal conductivity in radial direction at 20 °C for W_f-Cu (soft Cu and CuCrZr (SAA condition; heat treatment B according to reference [121]) matrix, fibre volume fractions ranging from 0.1 - 0.5) based on braided preform (braiding angle 78°) as illustrated in Figure 5.11b predicted by means of MFH in comparison with Cu alloys [79].

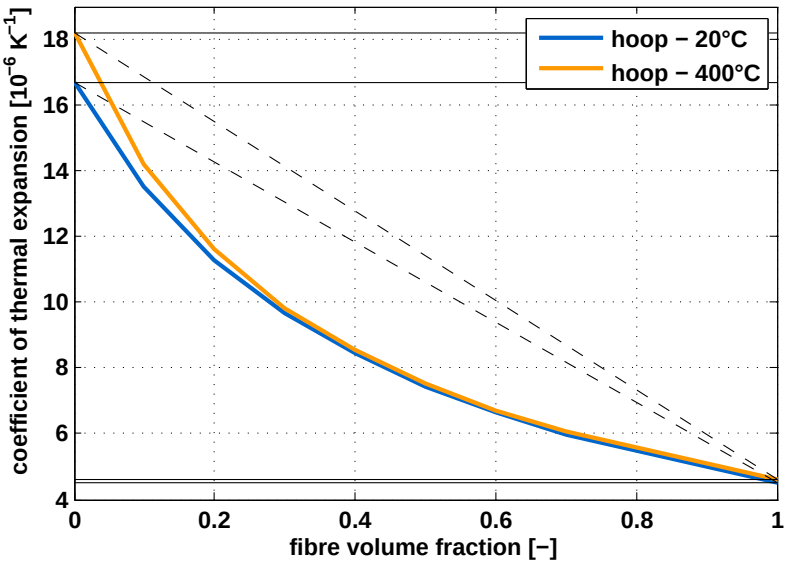

FIGURE 5.35: CTE of W_f-Cu (pure Cu matrix) based on braided preform (braiding angle 78°) as illustrated in Figure 5.11b in hoop direction at 20 °C and 400 °C predicted by means of MFH versus fibre volume fraction (the black horizontal lines indicate the CTEs of pure W and pure Cu at 20 °C and 400 °C).

versus fibre volume fraction[43]. Rather effective macroscopic CTE reduction, nearly as high as for UD W_f-Cu material in longitudinal direction (cf. Figure 5.31), can still be found.

5.6 High-heat-flux testing

5.6.1 Tungsten fibre-reinforced copper pipe

In order to test the integrity of the investigated W_f-Cu MMC in pipe configuration a specimen[44] as illustrated in Figure 5.36 was loaded within the HHF test facility GLADIS. During the experiment, cold-water cooling conditions were applied. The testing proce-

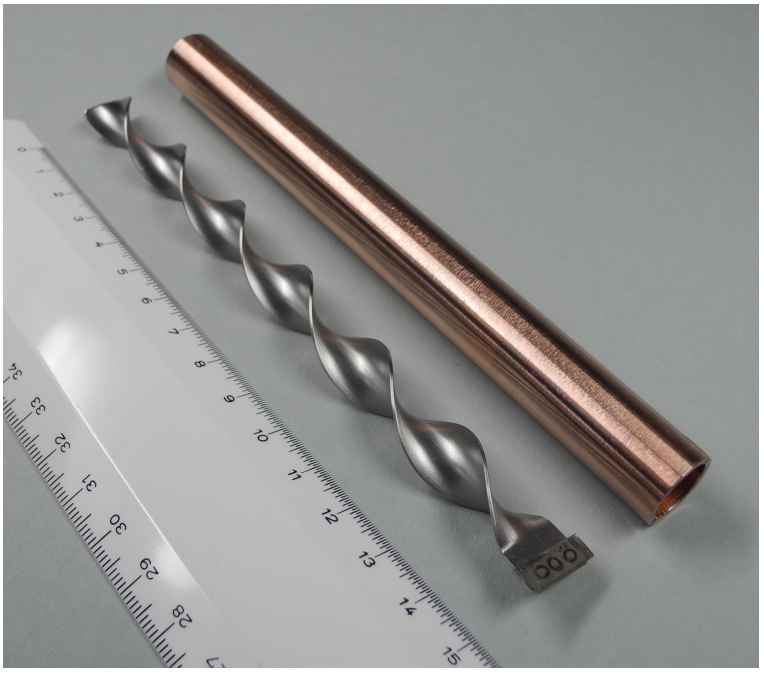

FIGURE 5.36: W_f-Cu MMC pipe specimen (inner diameter: 12 mm, wall thickness: 1.5 mm, length: 150 mm) with swirl tape insert (twist ratio: 2, tape thickness: 0.8 mm) before HHF testing.

dure was as follows with HHF loading perpendicular to the axis of the pipe specimen:

- HHF screening up to 25 MW m^{-2} as well as
- cyclic HHF loading up to 10 pulses at 25 MW m^{-2}.

[43] Again, for these computations, both composite material phases were modelled as thermoelastic material.

[44] This specific specimen was fabricated according to the centrifugal Cu infiltration process as described in section 5.4.2.2. The matrix material used for the infiltration was Cu-OFE and a braided W fibre preform as illustrated in Figure 5.11b was used for the MMC fabrication.

In Figure 5.37, images of the specimen during the HHF test as well as after the experiment are shown[45]. The performed HHF testing demonstrated primarily the integrity of

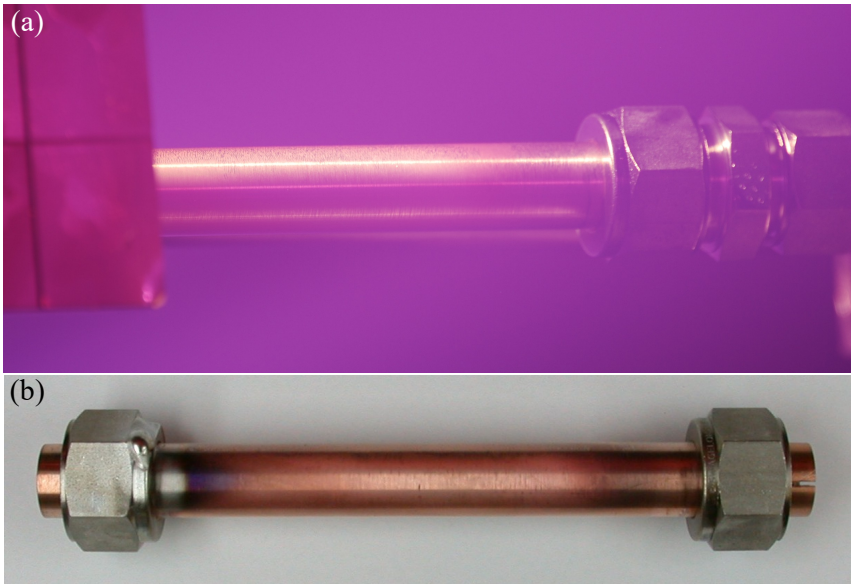

FIGURE 5.37: W_f-Cu MMC pipe specimen (a) during as well as (b) after HHF testing (top view on heat loaded side).

the investigated W_f-Cu MMC in pipe configuration as the specimen remained well intact during the experiment and by this confirmed the viability of W_f-Cu for elevated temperature HHF applications. Complementary to the HHF testing, 2D thermal FEA was performed[46]. To that end, homogenised W_f-Cu composite material properties, determined by means of MFH as described above in section 5.5, were used for the computations[47]. In Figure 5.38, results of the FEA are illustrated. In Figure 5.38a, maximum surface (outer diameter) temperatures ($T_{max,surf}$) as well as maximum cooling channel (inner diameter) temperatures ($T_{max,cool}$) are illustrated as a function of the applied HHF loading. In Figure 5.38b, a temperature distribution within the W_f-Cu MMC pipe for a heat loading of $25\,\mathrm{MW\,m^{-2}}$ is illustrated where it can be seen that the W_f-Cu material reaches a maximum surface temperature of approximately 360 °C. In Figure 5.39, a transversal optical microsection of the loaded half of the HHF tested W_f-Cu pipe specimen is shown. The section has been cut in the middle of the tube which corresponds to the most highly loaded part in the beam centre during the HHF testing. It can be seen that the microstructure of the W_f-Cu MMC is well intact without any plainly visible fibre failure

[45] On the left side of the specimen the clamping connection was melted during the initial heat pulses as the beam scraper of the HHF test facility was not inserted far enough. After adjustment, however, sufficient protection of the clamping could be ensured.

[46] The simulations were performed with Abaqus/CAE 6.14-1. The mesh had a total number of 1888 linear quadrilateral elements of type DC2D4 and a total number of 2124 nodes. The heat transfer at the cooling channel surface was modeled as surface film condition with the heat transfer coefficient given in Appendix B.

[47] The used W_f-Cu material property data is given in Appendix B in the form of tabulated values.

or debonding from the matrix which confirms both the manufacturing quality and the suitability of the investigated W_f-Cu material for HHF applications.

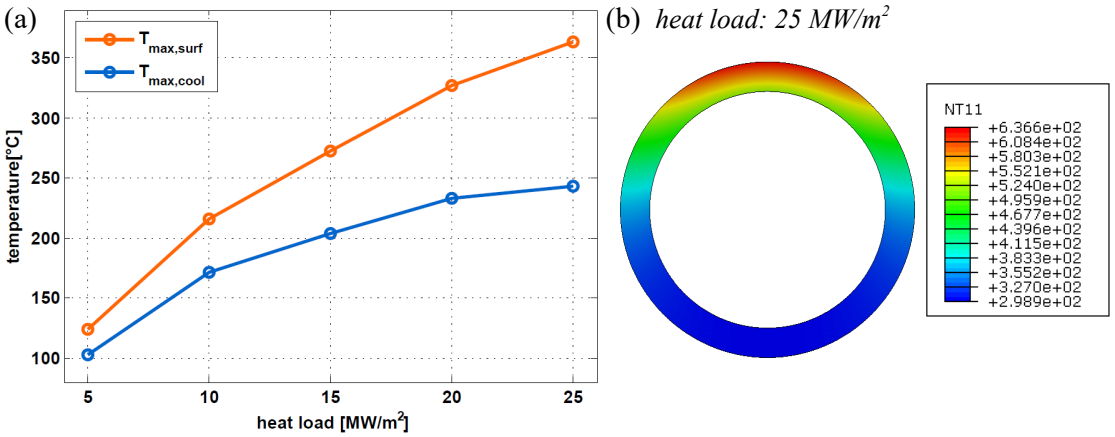

FIGURE 5.38: Results of 2D thermal FEA of W_f-Cu MMC pipe under HHF loading: (a) Maximum surface temperature ($T_{max,surf}$) and maximum cooling channel temperature ($T_{max,cool}$) as a function of applied HHF loading as well as (b) temperature distribution for a HHF loading of 25 MW m^{-2} (scale in K).

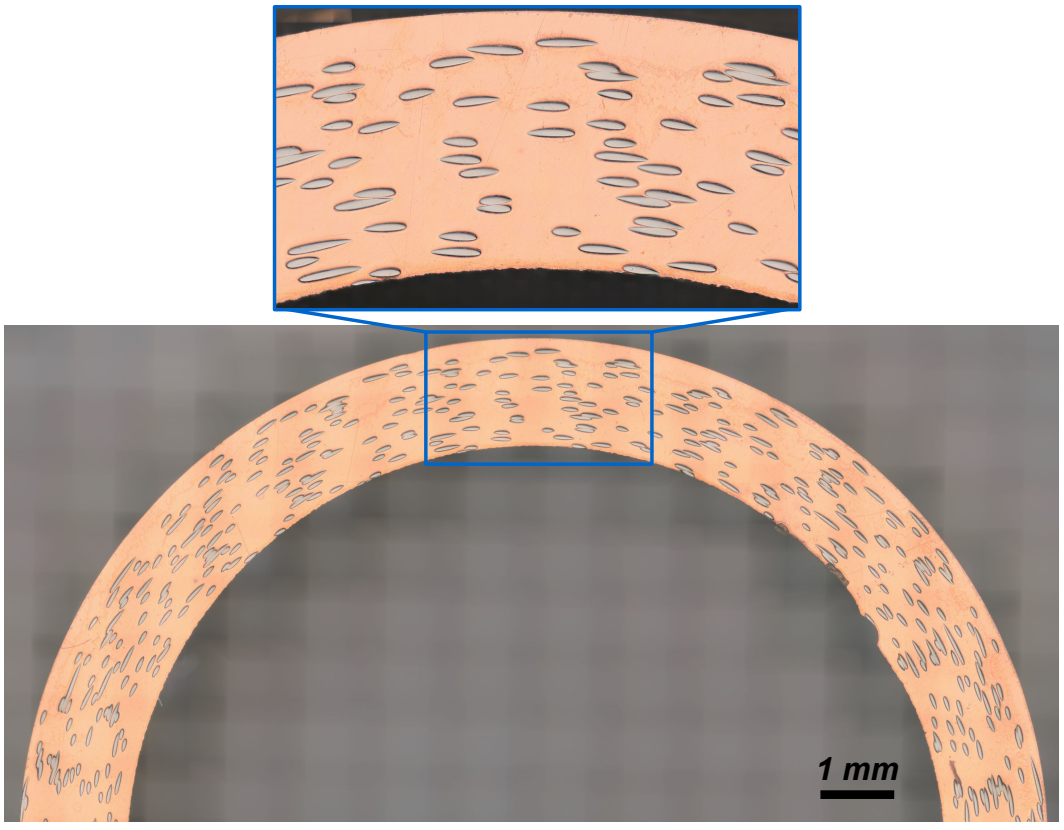

FIGURE 5.39: Transversal optical microsection of the loaded half of the HHF tested W_f-Cu MMC pipe specimen; the section was cut in the middle of the tube which corresponds to the most highly loaded part in the beam centre during the HHF testing.

5.6.2 Monoblock type plasma-facing component mock-ups

Furthermore, HHF tests on monoblock type PFC mock-ups with W_f-Cu MMC heat sink pipe were performed. In this regard, two types of mock-ups with differing dimensions were tested. On the one hand, a mock-up with W armour monoblocks with a thickness of 4 mm and dimensions as illustrated in Figure 5.40 was fabricated and loaded within the HHF test facility GLADIS. The following materials were used for the manufacturing

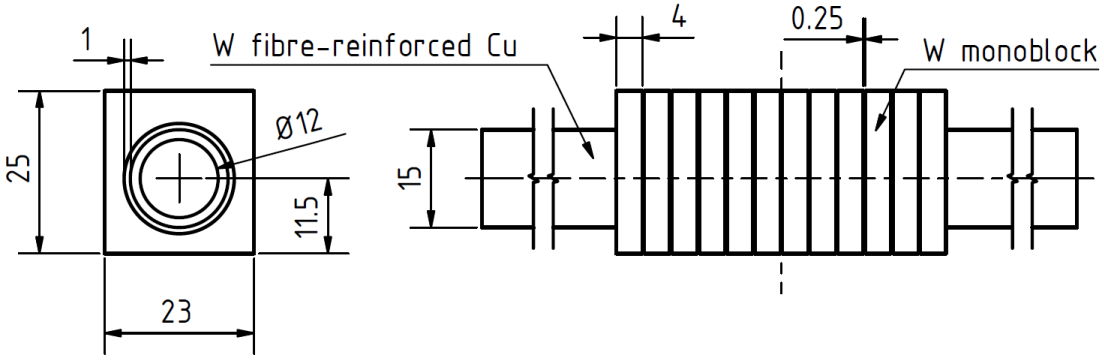

FIGURE 5.40: Dimensions of manufactured and HHF tested monoblock type PFC mock-up comprising W armour monoblocks with a thickness of 4 mm and a W_f-Cu MMC heat sink pipe.

of the mock-up:

- W monoblocks with Cu interlayer (thickness: 1 mm)[48]
- W_f-Cu MMC pipe (inner diameter: 12 mm, wall thickness: 1.5 mm, length: 150 mm)[49]
- Brazing alloy foil with 80wt.% Au, 20wt.% Cu[50]

The mock-up was joined through brazing the W monoblocks at the Cu interlayer to the W_f-Cu MMC pipe[51]. For the brazing procedure, a maximum process temperature of 950 °C was applied under HV conditions of approximately 10^{-5} mbar. In Figure 5.41, the manufactured mock-up is illustrated before HHF testing. The following HHF test procedure was then applied with cold-water cooling conditions:

- HHF screening up to 20 MW m^{-2} as well as
- cyclic HHF loading up to 100 pulses at 10 MW m^{-2}.

[48] supplier: AT&M Co., Ltd, China

[49] This specific specimen was fabricated according to the centrifugal Cu infiltration process as described in section 5.4.2.2. The matrix material used for the infiltration was Cu-OFE and a braided W fibre preform as illustrated in Figure 5.11b was used for the MMC fabrication.

[50] eutectic AuCu alloy; supplier: LOT-TEK GmbH, Germany

[51] The joining of the mock-up was performed in the framework of research activities within the EU-ROfusion work package divertor (WPDIV) at ENEA Frascati Research Center, Italy.

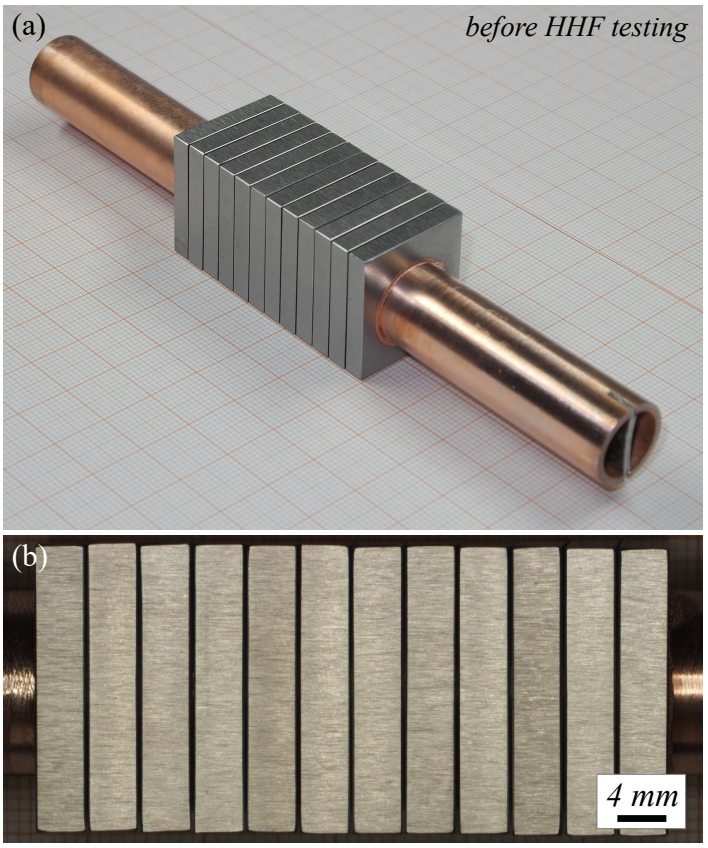

FIGURE 5.41: W monoblock type PFC mock-up comprising W armour monoblocks with a thickness of 4 mm and a W_f-Cu MMC heat sink pipe before HHF testing: (a) Oblique specimen view as well as (b) top view on W monoblock surfaces to be heat loaded.

Subsequently, the mock-up was HHF tested with the following DEMO relevant *hot-water* cooling conditions:

- Coolant inlet temperature of $T_{in} = 130\,°C$,
- coolant inlet pressure of $p_{in} = 40\,bar$,
- coolant flow velocity of $v = 16\,m\,s^{-1}$ and
- use of a swirl tape insert with a twist ratio of 2 and a tape thickness of 0.8 mm.

With these cooling conditions the following HHF loading was applied:

- HHF screening up to $20\,MW\,m^{-2}$ as well as
- cyclic HHF loading up to 500 pulses at $20\,MW\,m^{-2}$.

In Figure 5.42, IR and optical images of the mock-up during the cyclic HHF loading with $20\,MW\,m^{-2}$ and hot-water cooling conditions are shown for pulse numbers 1, 100 and 500. It can be seen that the mock-up exhibits a stable behaviour under HHF loading throughout the accumulating pulses without the development of hot spots. This

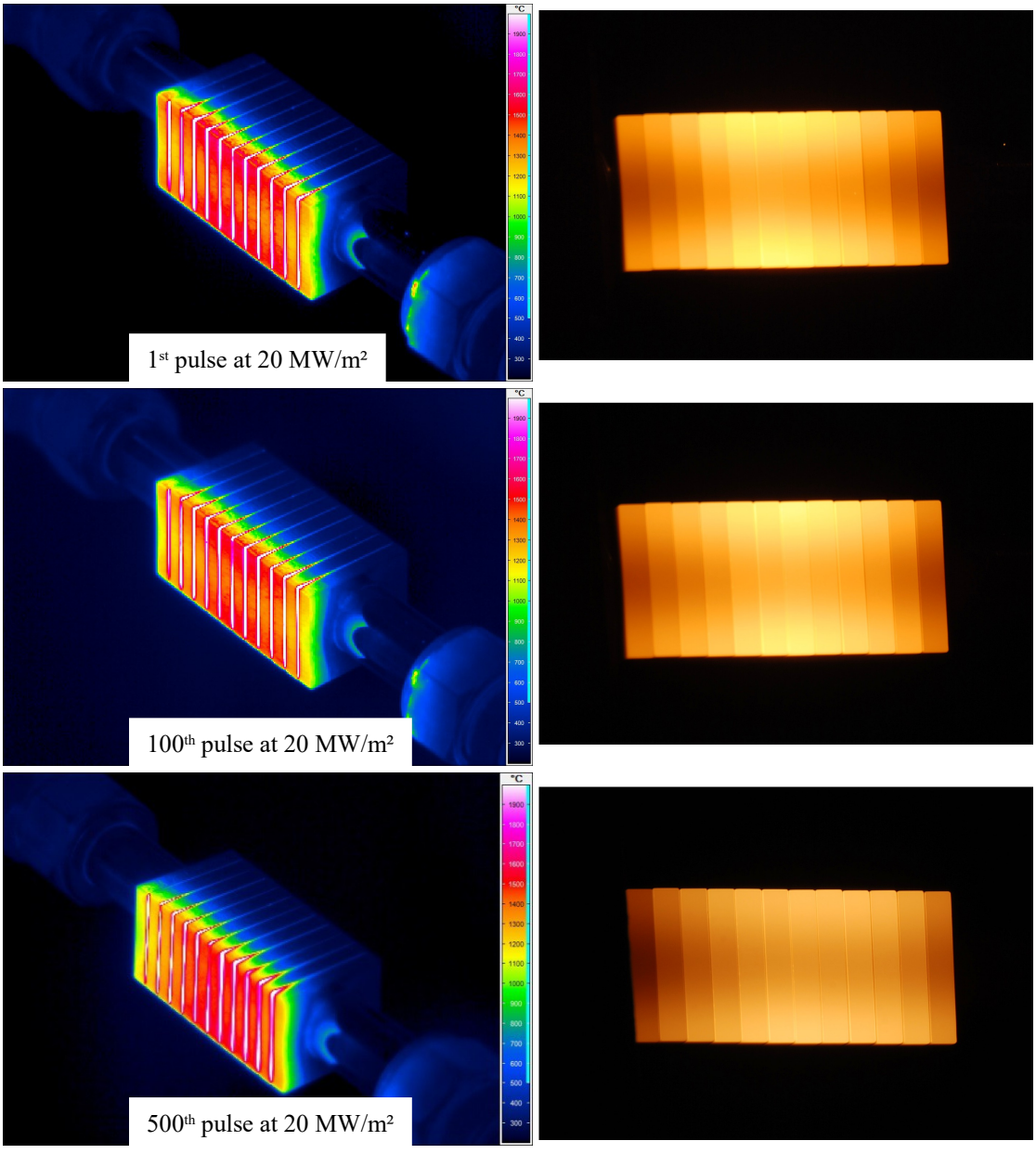

FIGURE 5.42: IR and optical images of W monoblock type PFC mock-up comprising W armour monoblocks with a thickness of 4 mm and a W_f-Cu MMC heat sink pipe during cyclic HHF loading with 20 MW m^{-2} and hot-water cooling conditions for pulse numbers 1, 100 and 500.

indicates that no hampering material or joint defects occured that would lead to HHF performance degradation. In Figure 5.43, images of the mock-up after HHF testing are shown and it can be seen that the mock-up is well intact. Furthermore, it can be

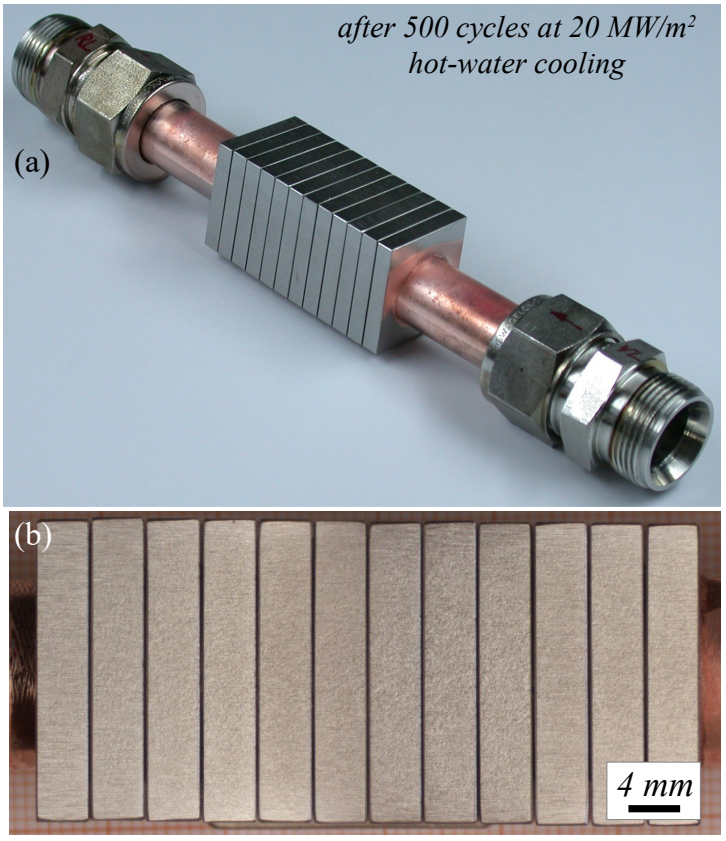

FIGURE 5.43: W monoblock type PFC mock-up comprising W armour monoblocks with a thickness of 4 mm and a W_f-Cu MMC heat sink pipe after cyclic HHF loading with 500 pulses at 20 MW m^{-2} and hot-water cooling conditions: (a) Oblique specimen view as well as (b) top view on heat loaded W monoblock surfaces.

seen in Figure 5.43b that the heat loaded surface of the mock-up does not exhibit plainly visible macroscopic defects. In Figure 5.44, results of 2D thermal FEA of the mock-up are shown[52]. Predicted maximum W surface temperatures ($T_{max,surf}$) and maximum W_f-Cu MMC pipe temperatures ($T_{max,pipe}$) are illustrated as a function of the applied heat flux both for cold- and hot-water cooling conditions. Furthermore, experimentally determined pyrometric surface temperature measurements are included in the plot ($T_{pyrometer}$). For a heat loading of 20 MW m^{-2} and hot-water cooling conditions it is predicted that the W monoblock surface reaches a maximum temperature of more than 1700 °C while the W_f-Cu pipe material reaches a maximum temperature of approximately 430 °C.

[52] The simulations were performed with Abaqus/CAE 6.14-1. The mesh had a total number of 2075 elements (1986 linear quadrilateral elements of type DC2D4, 89 linear triangular elements of type DC2D3) and a total number of 2164 nodes. The heat transfer at the cooling channel surface was modeled as surface film condition with the heat transfer coefficients given in Appendix B. The material properties used for the computations are given in Appendix B in the form of tabulated values.

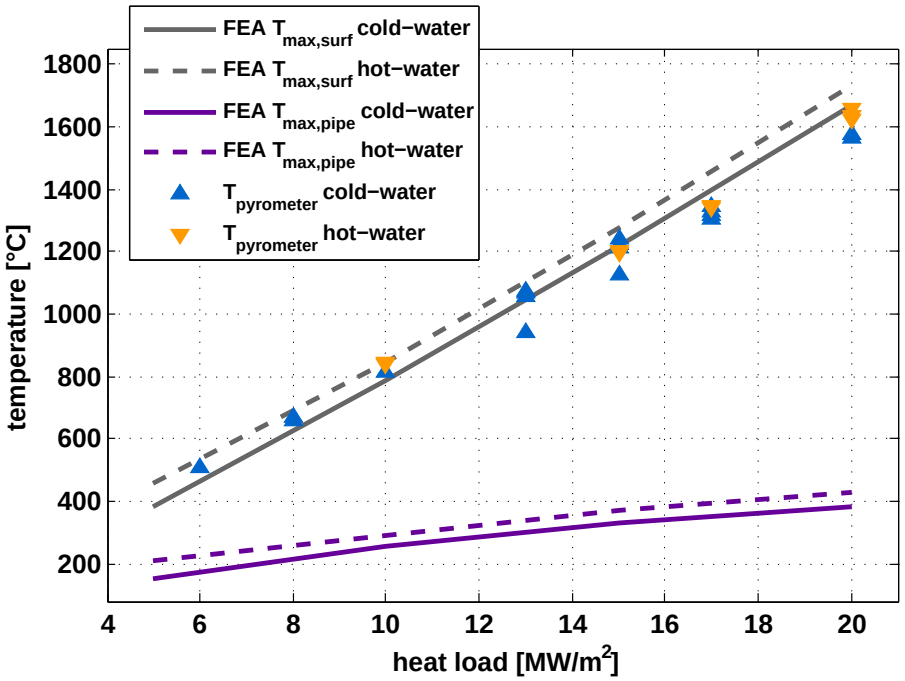

FIGURE 5.44: Results of 2D thermal FEA of W monoblock type PFC mock-up with W_f-Cu MMC heat sink pipe and dimensions as illustrated in Figure 5.40 under HHF loading: Maximum surface temperature ($T_{max,surf}$) and maximum W_f-Cu MMC pipe temperature ($T_{max,pipe}$) versus applied heat load. Furthermore, pyrometrically measured surface temperatures ($T_{pyrometer}$) are included in the plot.

Further PFC mock-ups with W_f-Cu MMC heat sink pipe and W armour monoblocks with a thickness of 12 mm were manufactured and loaded within the HHF test facility GLADIS. The dimensions of these mock-ups which comprised 4 W armour monoblocks are illustrated in Figure 5.45. In principle, these mock-ups were fabricated with the same

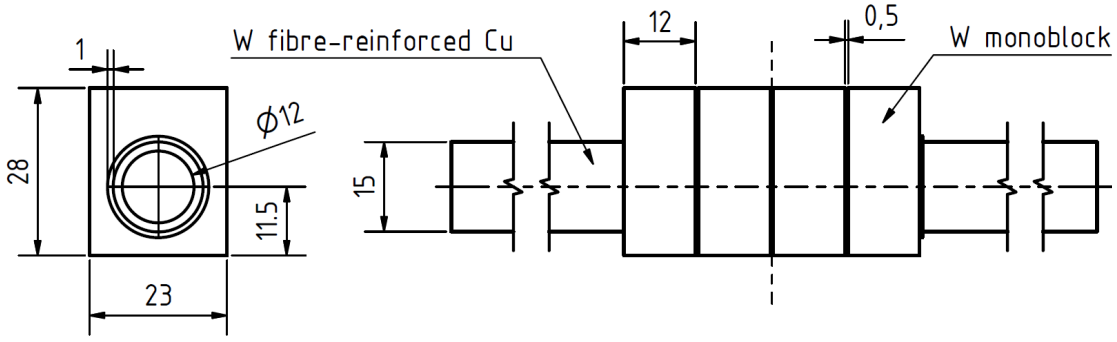

FIGURE 5.45: Dimensions of manufactured and HHF tested monoblock type PFC mock-ups comprising W armour monoblocks with a thickness of 12 mm and a W_f-Cu MMC heat sink pipe.

materials and procedure as described above regarding the mock-up comprising W armour monoblocks with a thickness of 4 mm. Only, the dimensions of the parts were different.

One of these mock-ups[53] was tested under HHF loading with high cycle numbers and is illustrated in Figure 5.46 before the HHF testing. Figure 5.46a shows the top view on the W monoblock surfaces to be heat loaded while in Figure 5.46b a side view on the mock-up is illustrated. For the HHF testing, the following loading was applied initially

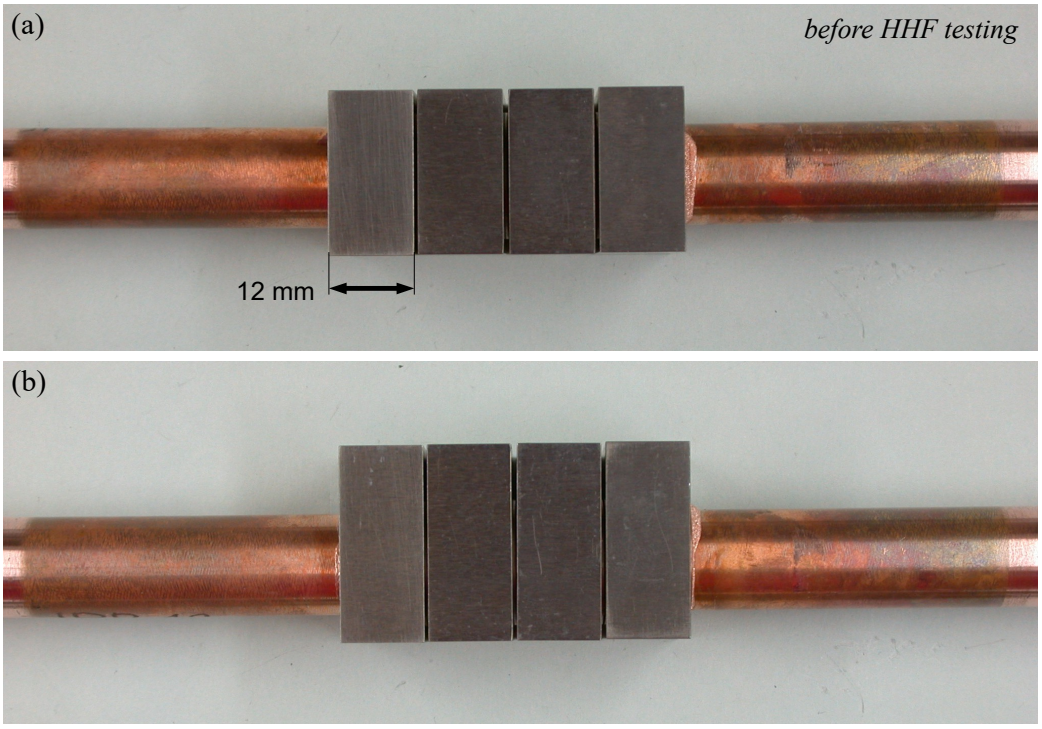

FIGURE 5.46: W monoblock type PFC mock-up comprising W armour monoblocks with a thickness of 12 mm and a W_f-Cu MMC heat sink pipe before HHF testing: (a) Top view on W monoblock surfaces to be heat loaded as well as (b) side view on the mock-up.

with cold-water cooling conditions:

- HHF screening up to 25 MW m^{-2} as well as
- cyclic HHF loading up to 100 cycles at 10 MW m^{-2}.

Subsequently, the following HHF loading was applied with hot-water cooling:

- HHF screening up to 20 MW m^{-2} as well as
- cyclic HHF loading up to 1000 cycles at 20 MW m^{-2}.

In Figure 5.47, IR and optical images of the mock-up during the cyclic HHF loading at 20 MW m^{-2} with hot-water cooling conditions are shown for pulse numbers 1, 100, 500 and 1000. It can be seen that the mock-up exhibits a stable behaviour under HHF load-

[53] The W_f-Cu MMC heat sink pipe specimen used for the manufacturing of this mock-up was fabricated according to the conventional Cu infiltration process as described within section 5.4.2.1. The matrix material used for the infiltration was Cu-OFE and a braided W fibre preform as illustrated in Figure 5.11b was used for the MMC fabrication.

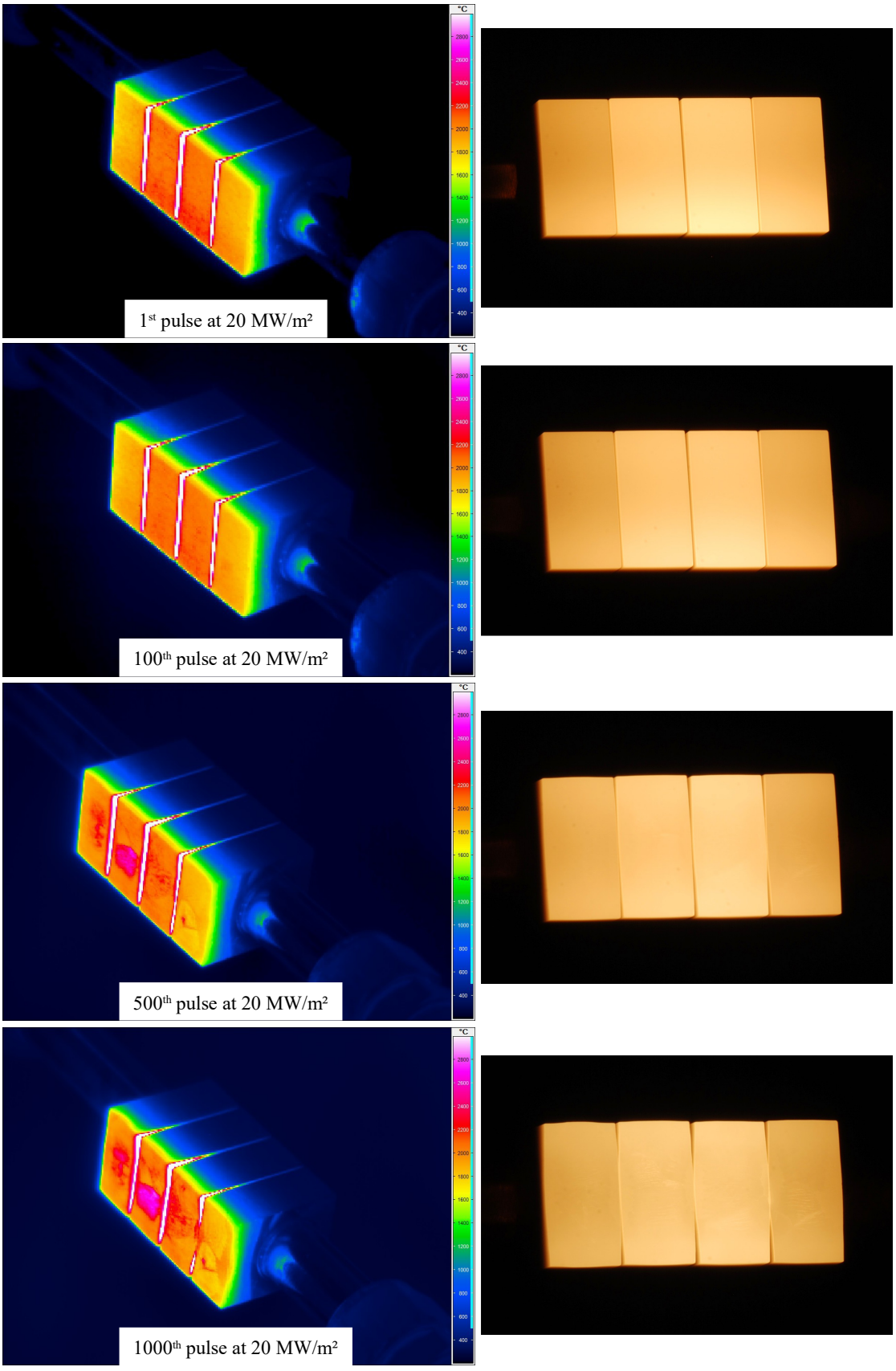

FIGURE 5.47: IR and optical images of W monoblock type PFC mock-up comprising W armour monoblocks with a thickness of 12 mm and a W_f-Cu MMC heat sink pipe during cyclic HHF loading with 20 MW m^{-2} and hot-water cooling conditions for pulse numbers 1, 100, 500 and 1000.

ing throughout the accumulating pulses without the development of hot spots. Again, this indicates that no hampering material or joint defects occured that would lead to HHF performance degradation. Furthermore, Figure 5.47 indicates two more findings. The IR images suggest that strong surface modifications occur during the accumulating heat pulses as is indicated by the seemingly higher temperatures of the loaded W monoblock surfaces for high pulse numbers. However, this is rather attributed to a change in emissivity of the modified W surfaces than due to a real increase of the surface temperatures. Apart from that, it can be seen that the W monoblocks underwent accumulated plastic deformation as it can be seen that the monoblock surfaces do after 1000 heat pulses not exhibit a shape as rectangular as can be seen within the images for heat pulse number 1. In Figure 5.48, images of the mock-up illustrated in Figure 5.46 and Figure 5.47 after HHF testing are shown. These images confirm that the cyclic heat

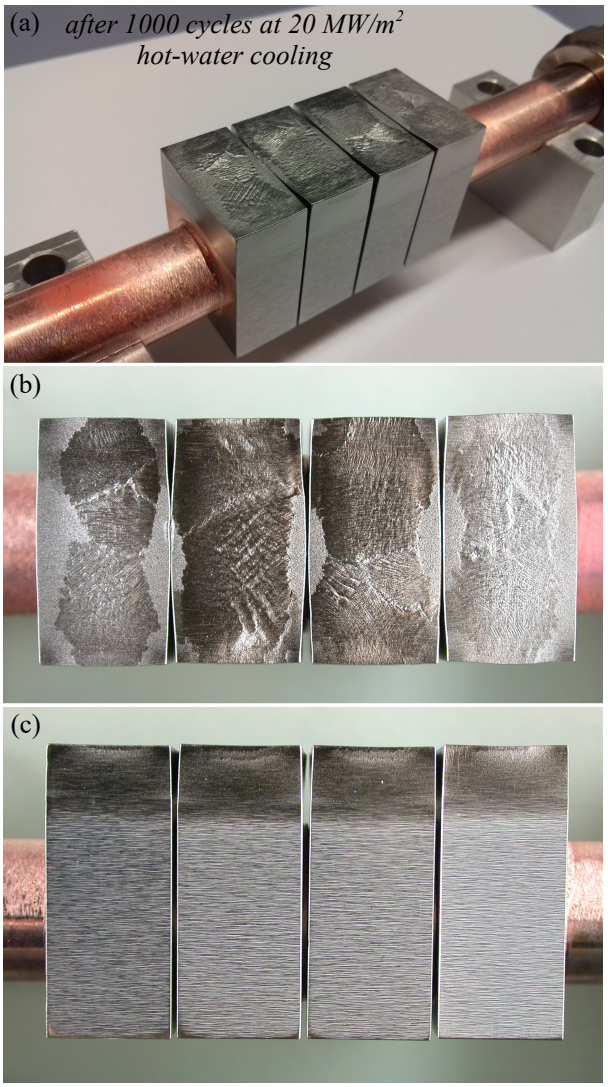

FIGURE 5.48: W monoblock type PFC mock-up comprising W armour monoblocks with a thickness of 12 mm and a W_f-Cu MMC heat sink pipe after cyclic HHF loading with 1000 pulses at 20 MW m^{-2} and hot-water cooling conditions: (a) Oblique specimen view, (b) top view on heat loaded surface and (c) side view.

loading induced strong surface modifications on as well as plastic deformation of the W monoblocks. Nevertheless, it is found that the mock-up and especially the W_f-Cu MMC heat sink pipe are well intact. In Figure 5.49, an axial metallographic cross section of one half (two W monoblocks) of the mock-up loaded up to 1000 pulses at $20\,MW\,m^{-2}$ with hot-water cooling conditions and illustrated in Figure 5.48 is shown. The magnifications in Figure 5.49 illustrate a cut through one W monoblock including the W_f-Cu MMC pipe as well as the joint interfaces. The upper image shows the heat loaded side while the lower image shows the unloaded side of the mock-up.

In general, it can be seen that there are no major material or joint defects of the mock-up. Apart from that, Figure 5.49 confirms that the W armour monoblocks exhibit plainly visible plastic deformation on the heat loaded side which is especially visible through the narrowing gap between the monoblocks towards the heat loaded surface. Furthermore, plastic deformation can also be identified regarding the joint interface including the Cu interlayer, especially at the W monoblock edges. Moreover, if the joint interface at the heat loaded side is compared with that at the unloaded side it can be seen that roughening of the braze layer seems to have occured due to the cyclic heat loading. Apart from that, some porosity can be identified within the braze layer at the heat loaded side while it is not clear if these joint defects were present from the beginning or if and how they evolved during the cyclic HHF loading. Regarding the W_f-Cu MMC pipe, it can be seen that it is well intact overall without significant plastic deformation or plainly visible crack or debonding defects. In Figure 5.50, an optical microsection of the W_f-Cu MMC heat sink pipe at the position as indicated by the white rectangle in Figure 5.49 at the heat loaded side of the mock-up below the centre of the W monoblock is illustrated. It can be seen that the material microstructure is in principle well intact without plainly visible defects that could hamper the performance of the MMC pipe. This result confirms the suitability of the investigated W_f-Cu MMC material for HHF applications.

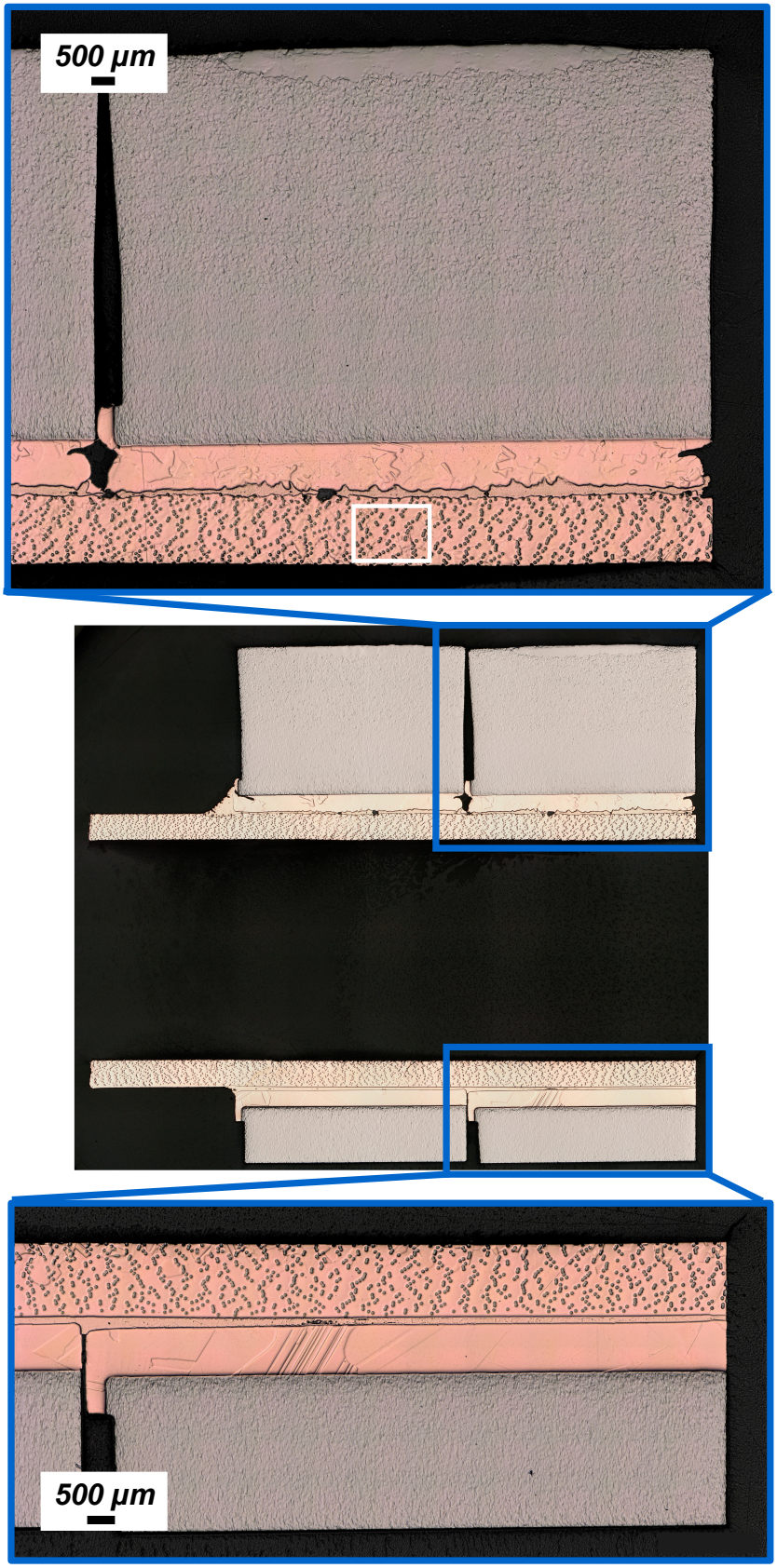

FIGURE 5.49: Axial metallographic cross section of W monoblock type PFC mock-up comprising a W_f-Cu MMC heat sink pipe after cyclic HHF loading with 1000 pulses at $20\,MW\,m^{-2}$ and hot-water cooling conditions.

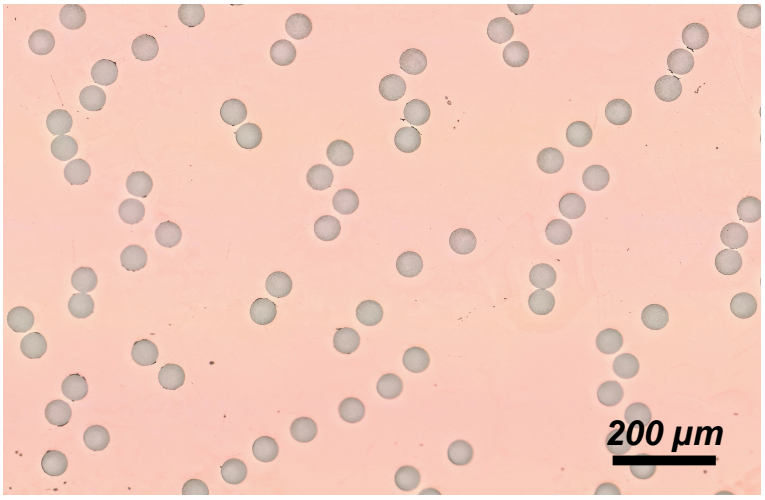

FIGURE 5.50: Optical microsection of W_f-Cu MMC heat sink pipe at the position indicated by the white rectangle in Figure 5.49.

Another PFC mock-up with W_f-Cu MMC heat sink pipe[54] and W armour monoblocks with a thickness of 12 mm, i.e. dimensions as illustrated in Figure 5.45, was investigated through HHF overload testing within the GLADIS facility. During these experiments, the following HHF loads were applied with cold-water cooling conditions[55]:

- HHF screening up to 25 MW m^{-2} as well as
- cyclic HHF loading up to 100 cycles at 10 MW m^{-2}.

Subsequently, the mock-up was overloaded as follows:

- HHF screening up to 32 MW m^{-2} as well as
- cyclic HHF loading up to 100 cycles at 25 MW m^{-2}.

In Figure 5.51, IR and optical images of the mock-up during the cyclic HHF overload testing at 25 MW m^{-2} are shown for pulse numbers 1 and 100. The qualitatively very similar temperature distributions for pulse numbers 1 and 100 indicate that the mock-up exhibits a stable behaviour under HHF loading throughout the accumulating pulses without the development of hot spots. Again, this indicates that no hampering material or joint defects occured that would lead to HHF performance degradation. Furthermore, Figure 5.51 confirms the findings discussed above. The IR images suggest again that strong surface modifications occur during the accumulating heat pulses as it can be seen that the emissivity of the loaded W monoblock surfaces changes locally. In Figure 5.52, images of the heat loaded side of the overload tested mock-up before and after the

[54] The W_f-Cu MMC heat sink pipe specimen used for the manufacturing of this mock-up was fabricated according to the centrifugal Cu infiltration process as described within section 5.4.2.2. The matrix material used for the infiltration was Cu-OFE and a braided W fibre preform as illustrated in Figure 5.11b was used for the MMC fabrication.

[55] coolant flow velocity of 16 m s^{-1}

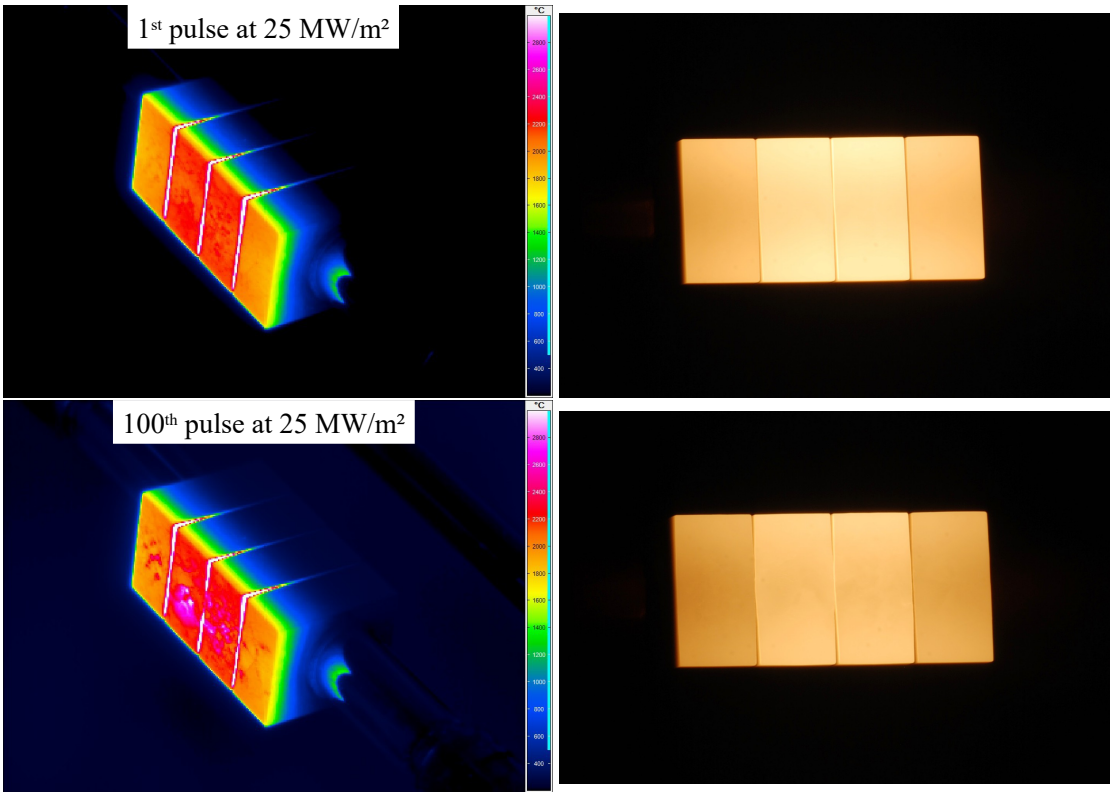

FIGURE 5.51: IR and optical images of W monoblock type PFC mock-up comprising W armour monoblocks with a thickness of 12 mm and a W_f-Cu MMC heat sink pipe during cyclic HHF overload testing with 25 MW m^{-2} for pulse numbers 1 and 100.

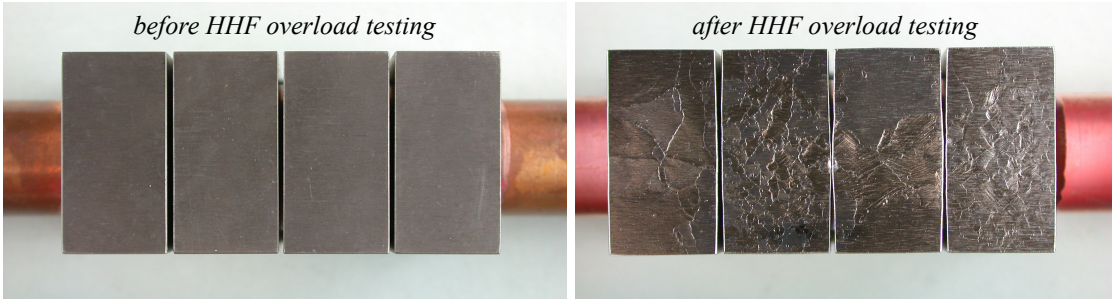

FIGURE 5.52: W monoblock type PFC mock-up comprising W armour monoblocks with a thickness of 12 mm and a W_f-Cu MMC heat sink pipe (a) before and (b) after HHF overload testing (screening up to 32 MW m^{-2} and 100 cycles at 25 MW m^{-2} with cold-water cooling conditions).

experiment are shown. These images confirm that the cyclic heat loading induced strong surface modifications as seen in the IR images on the loaded W monoblock surfaces. However, it can again be seen that overall the mock-up is in principle well intact. This test result confirms the previously encountered stable HHF performance of W monoblock type PFC mock-ups with W_f-Cu MMC heat sink pipe.

In Figure 5.53, results of 2D thermal FEA of the HHF tested mock-ups with dimensions

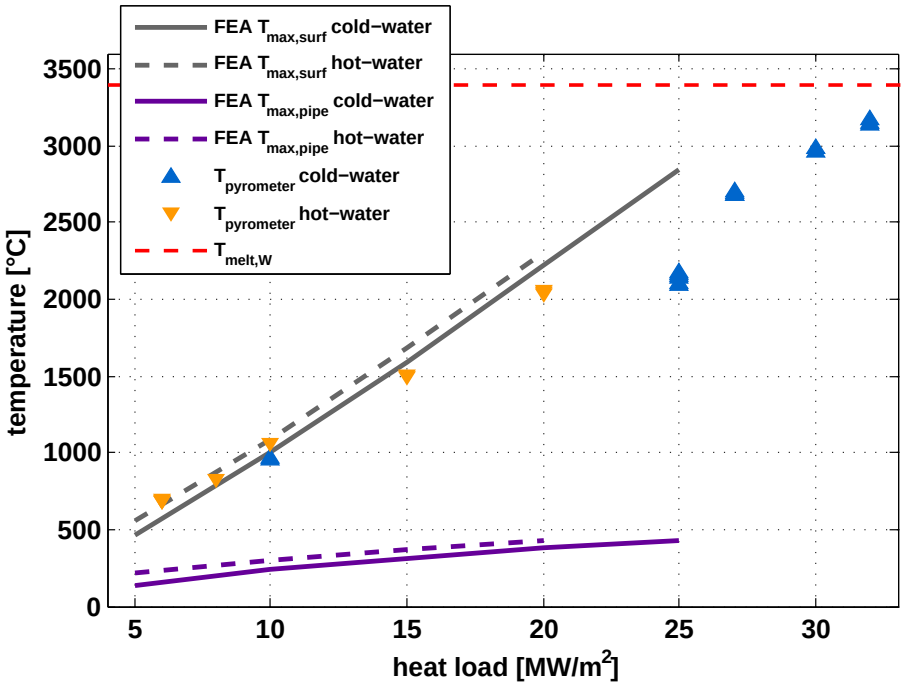

FIGURE 5.53: Results of 2D thermal FEA of W monoblock type PFC mock-up with W_f-Cu MMC heat sink pipe and dimensions as illustrated in Figure 5.45 under HHF loading: Maximum surface temperature ($T_{max,surf}$) and maximum W_f-Cu MMC pipe temperature ($T_{max,pipe}$) versus applied heat load. Furthermore, pyrometrically measured surface temperatures are included in the plot ($T_{pyrometer}$).

as illustrated in Figure 5.45 are shown[56]. Predicted maximum W surface temperatures ($T_{max,surf}$) and maximum W_f-Cu MMC heat sink pipe temperatures ($T_{max,pipe}$) are illustrated as a function of the applied heat load for both cold- and hot-water cooling conditions. Apart from that, experimentally determined pyrometric surface temperature measurements are included in the plot ($T_{pyrometer}$). It can be seen that for a heat loading with 25 MW m^{-2} and cold-water cooling conditions it is predicted that the W monoblock surface reaches a maximum temperature of more than 2800 °C while the W_f-Cu MMC pipe material reaches a maximum temperature of approximately 430 °C.

[56]The simulations were performed with Abaqus/CAE 6.14-1. The mesh had a total number of 2413 elements (2300 linear quadrilateral elements of type DC2D4, 113 linear triangular elements of type DC2D3) and a total number of 2496 nodes. The heat transfer at the cooling channel surface was modeled as surface film condition with the heat transfer coefficients given in Appendix B. The material properties used for the computations are given in Appendix B in the form of tabulated values.

5.7 Tungsten short fibre-reinforced copper

In section 3.2, it has been mentioned that there are mass production examples of MMCs in which discontinuous, i.e. short, fibres are used as reinforcement [94]. Compared with continuous fibre-reinforced composites, the fabrication of short fibre-reinforced materials is typically less expensive as the processing of short fibres is less effortful compared with continuous fibre processing. Against this background, short W_f-Cu could represent an attractive MMC that combines the outstanding properties of drawn W fibres with a rather simple and straightforward material fabrication procedure.

The possibility to realise short W_f-Cu MMCs has been investigated in principle within the present work but without detailed material characterisation and without the application of such materials to PFC mock-ups for HHF testing. In this regard, a method to produce short W fibre preforms for Cu melt infiltration was tested: Short W fibre nonwovens were produced by means of a *wet-laying process*[57]. In principle, wet-laid nonwovens are formed through filtering an aqueous suspension of fibres onto a sieve conveyor belt similar to a papermaking process from which this technology originated [179]. Hence, other references also use the term *hydroentangled nonwoven formation* to describe this processing technology [166].

For the investigations, short W fibres[58] with a diameter of 40 µm and lengths of 5 mm ($l/d = 125$) as well as 10 mm ($l/d = 250$) were used in equal weight shares. In Figure 5.54, the result of a wet-laying process with such W short fibres is shown which is a nonwoven sheet with a width of approximately 300 mm. In Figure 5.55a, a microscopic top view on such a wet-laid W short fibre nonwoven is illustrated. In Figure 5.55b, a typical microsection of a Cu infiltrated W short fibre nonwoven as illustrated in Figure 5.55a is shown. Both images illustrate the rather random orientation of the W short fibres. Furthermore, it can be seen in Figure 5.55b that the W fibres are well embedded within the Cu matrix. Apart from that, it can be seen that the fibre volume fraction is rather low. This means that for a viable MMC with reasonably reinforced properties the short fibre preforms should be prepared with a higher fibre density, possibly by compacting the preform through pressing before infiltration.

[57] For the fabrication of short W fibre nonwovens within the present work, a wet-laying facility at Hochschule Reutlingen, Fakultät Textil & Design, Germany was used.

[58] cut K doped W fibre, nominal diameter 40 µm, length 5 mm/10 mm, OSRAM GmbH

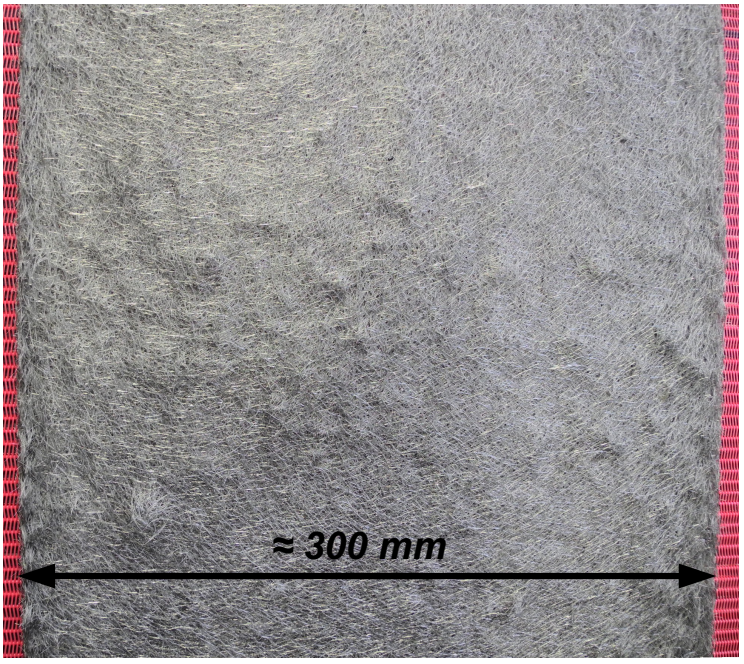

FIGURE 5.54: Wet-laid W short fibre nonwoven sheet with a width of approximately 300 mm.

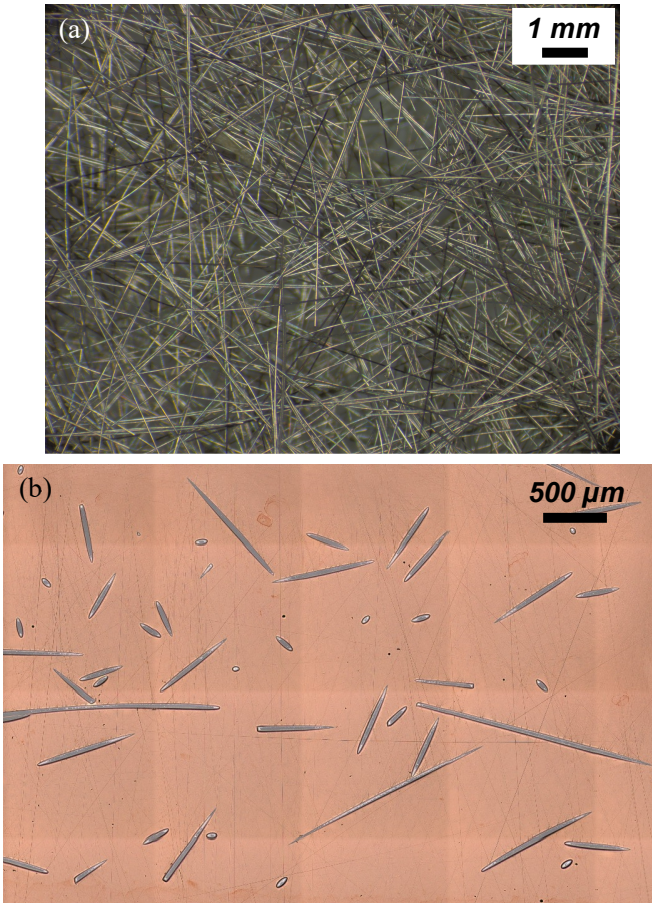

FIGURE 5.55: (a) Microscopic top view on a wet-laid W short fibre nonwoven preform (fibre diameter: 40 µm) and (b) optical microsection of a short W_f-Cu MMC fabricated through Cu infiltration of a wet-laid short W fibre nonwoven preform as illustrated in (a); the micrograph was prepared plane parallel to the infiltrated nonwoven sheet.

5.8 Chapter 5 summary

Within this chapter, work performed regarding the development of W_f-Cu MMCs intended for use as potentially advanced HSMs in highly loaded PFCs is described. In this respect, several aspects regarding such materials were discussed although a focus was put on the W_f-Cu MMC material manufacturing as well as the application of such materials in pipe configuration to PFC mock-ups that were HHF tested. In this context, the following main conclusions can be summarised:

- It has been demonstrated that fibrous W preforms for the manufacturing of W_f-Cu MMCs can be fabricated by means of well-established and industrially viable fibre processing techniques known from textile technology. Specifically, it has in this regard been demonstrated that multi-layered circular braids as preforms for W_f-Cu MMC pipe manufacturing can be fabricated. Moreover, it has been shown that yarns made out of thin W filaments with a diameter of 20 µm can be applied to such a preform fabrication process.

- It has been demonstrated that W_f-Cu MMCs with good material quality, i.e. with material properties acceptable for HHF applications, can be fabricated by means of liquid Cu melt infiltration techniques which can be regarded a viable and practicable fabrication method. In this context, however, it has been found that the processing conditions during the Cu melt infiltration have to be considered rather carefully in order that the beneficial mechanical properties of the reinforcing fibres are maintained. Investigations revealed that small quantities of impurities incorporated into the W fibre reinforcements during the Cu melt infiltration processing can deteriorate their mechanical performance significantly.

- The investigated W_f-Cu MMCs in pipe configuration were succesfully applied to actively water cooled W monoblock type PFC mock-ups that were tested under HHF loading. In this regard, several mock-ups were examined. One of them was loaded up to 1000 HHF pulses at $20\,MW\,m^{-2}$. Another mock-up was overloaded up to 100 HHF pulses at $25\,MW\,m^{-2}$ after screening up to a heat load of $32\,MW\,m^{-2}$. Both these mock-ups demonstrated a stable HHF performance without failure[59]. These results ultimately demonstrate the viability of W_f-Cu MMCs as HSMs in highly loaded PFCs.

[59] It should be highlighted that the abovementioned HHF loadings applied to the W monoblock type PFC mock-ups with W_f-Cu MMC heat sink pipe can indeed be regarded as high. In section 2.3, it has been mentioned that the ITER divertor target qualification criteria comprise the demonstration of component integrity for "only" 300 HHF load cycles at $20\,MW\,m^{-2}$ [50, 69].

Chapter 6

Tungsten-copper composites based on additively manufactured tungsten preforms

6.1 General remarks

As mentioned within the outline in Chapter 1, one class of novel W-Cu composite materials investigated within the present work are *W-Cu composites based on additively manufactured W preforms* (W_{AM}-Cu). *Additive manufacturing* (AM) is a term that describes manufacturing processes in which 3D objects are created by means of sequential deposition of layers under computer control. Such processes offer possibilities beyond the capabilities of conventional manufacturing technologies as parts with high geometrical complexity can be realised straightforwardly. In the more recent past, substantial progress has been achieved regarding the AM of metals. In this respect, *laser powder bed fusion* (LPBF) is a promising state-of-the-art technology[1] which allows the direct AM of a wide variety of metals without the need for binder phases. During such a process, powder material is selectively consolidated by means of a laser beam focused onto a powder bed as is schematically illustrated in Figure 6.1 [180]. A comprehensive summary of this technology can for example be found in reference [181].

6.2 Laser powder bed fusion of pure tungsten

In section 2.2.2, it has been described that W is currently considered the preferred PFM in magnetic confinement thermonuclear fusion devices mainly because of its low erosion during plasma exposure as well as its low retention of hydrogen isotopes. From

[1] In the literature, also other terms are used to designate this technology. Very often, the term *selective laser melting* (SLM) is used.

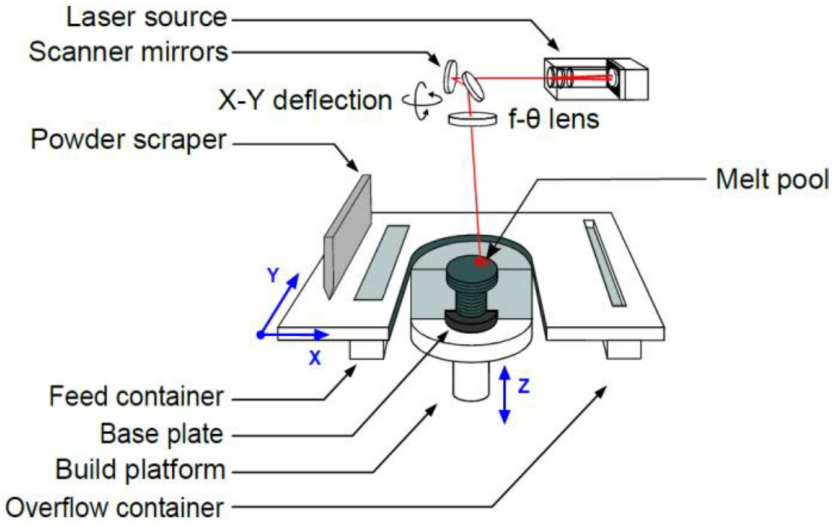

FIGURE 6.1: Schematic illustration of the LPBF process [180].

an engineering point of view, however, W is a challenging material to work with as it is an inherently hard and brittle metal. Established fabrication technologies for W are hence a limiting factor regarding the design and realisation of PFCs. Against this background, AM technologies may prove useful as they offer beneficial design flexibility through allowing the manufacture of W parts with almost arbitrary shape.

To date, only a few papers regarding AM of pure W can be found in the literature [182–188]. However, all these investigations report that W is a specifically challenging material for LPBF processes due to the intrinsic properties of this metal in combination with the high thermal gradients that are inevitably induced during LPBF processing. In the literature, it is reported that during LPBF processing spatial temperature gradients of approximately $10^2\,\mathrm{K\,mm^{-1}}$ to $10^4\,\mathrm{K\,mm^{-1}}$ as well as cooling rates higher than $10^4\,\mathrm{K\,s^{-1}}$ can be induced [181].

6.3 Experiments with low substrate preheating temperature

In the first instance, AM of pure W was investigated with an SLM MTT 250 HL LPBF facility[2] [189]. This facility is equipped with a 400 W fibre laser operating at a wavelength of 1075 nm. During operation, Ar was used as protective atmosphere within the device chamber while the O residue was kept as low as 0.1% during the build job. The laser was operated in focus ($z = 0$) while the focus diameter is approximately 100 µm.

In order to ensure acceptable flowability of the raw powder material during the AM process, plasma spheroidised pure W powder[3] was used. The results of the chemical

[2] located at Fraunhofer-Einrichtung für Gießerei-, Composite- und Verarbeitungstechnik IGCV, Augsburg, Germany

[3] supplier: LPW Technology Ltd., Runcorn, Cheshire, United Kingdom

composition analysis as well as the sizing distribution of this powder provided by the supplier are summarised in Table 6.1 and Table 6.2.

TABLE 6.1: Chemical composition of the used W powder.

Element	*wt.%*
W	> 99.99
Cr	< 0.001
Fe	< 0.001
Mo	< 0.001
Ni	< 0.001
O	0.01
Ta	< 0.002
Others	< 0.002

TABLE 6.2: Sizing distribution of the used W powder.

Volume percentiles	
Dv10	20.2 µm
Dv50	27.9 µm
Dv90	38.2 µm
Volume below	
10 µm	0.00%
15 µm	0.33%

In Figure 6.2, an SEM image of the used W powder is shown that illustrates the spherical shape of the individual particles [189]. Table 6.3 illustrates the investigated process

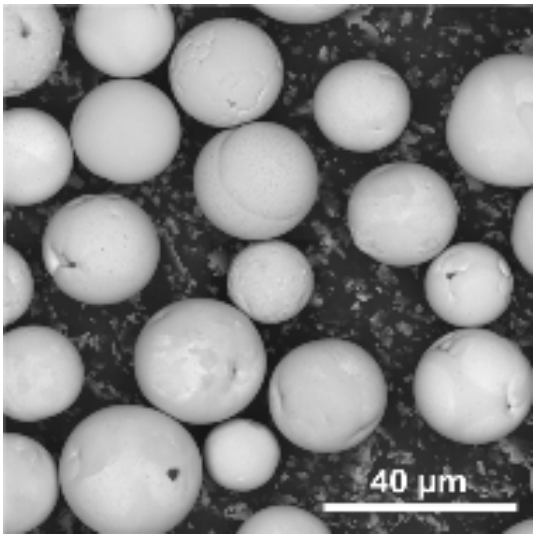

FIGURE 6.2: SEM image of the spheroidised W powder used for LPBF investigations [189].

parameters in terms of laser power and scanning speed. They range from 250 W to 400 W and 50 mm s^{-1} to 500 mm s^{-1}, respectively. Furthermore, Table 6.3 indicates the deposited *energy density* associated with these parameters and calculated according to the following expression:

$$E_\rho = \frac{P}{v\ s\ t} \tag{6.1}$$

where P is the laser power, v the scanning speed, s the scan line spacing and t the layer thickness. A scan line spacing of 80 µm, a layer thickness of 40 µm, preheating of the substrate plates to 200 °C and an alternating bidirectional (90°) laser scanning strategy were fixed during the manufacturing of LPBF W samples.

TABLE 6.3: Investigated LPBF process parameters in terms of laser power, laser scanning speed and deposited energy density [J mm^{-3}] according to Equation 6.1.

-	250 W	350 W	400 W
50 mm s^{-1}	1562.5	2187.5	2500
150 mm s^{-1}	520.8	729.2	833.3
300 mm s^{-1}	260.4	364.6	416.7
350 mm s^{-1}	223.2	-	-
400 mm s^{-1}	195.3	273.4	312.5
450 mm s^{-1}	-	243.1	277.8
500 mm s^{-1}	-	218.8	250

Cube-shaped samples with dimensions of approximately $10 \times 10 \times 10\,\text{mm}^3$ were built on stainless steel substrate plates by means of LPBF. In Figure 6.3, exemplary images of such cube-shaped samples after manufacturing are shown [189]. Figure 6.3a shows samples that were successfully built by means of LPBF while Figure 6.3b shows samples that could not be built as the deposited energy density was too high.

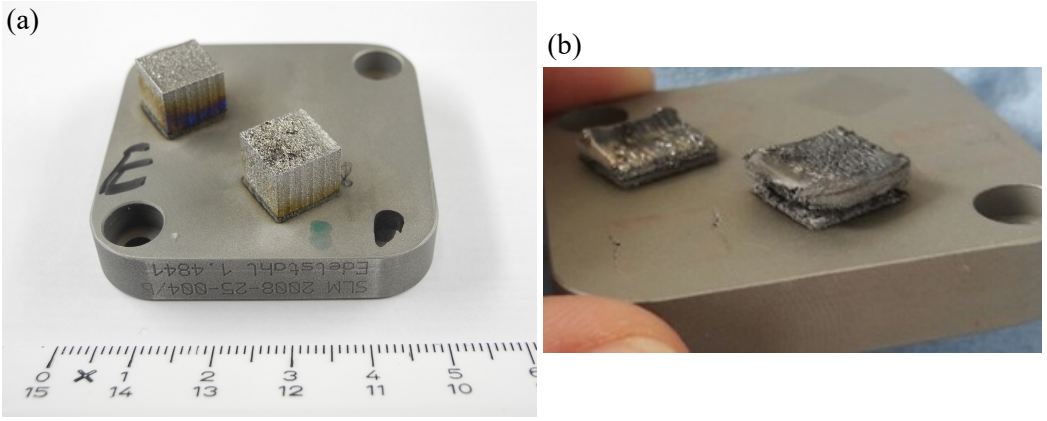

FIGURE 6.3: (a) Successfully manufactured cube-shaped LPBF W samples on stainless steel substrate plate and (b) samples that could not be built as the deposited energy density was too high [189].

An important prerequisite for a material to exhibit adequate thermophysical and mechanical properties is that the relative mass density is sufficiently high which means that the material exhibits a low residual porosity after manufacturing. That is the reason why this material parameter is commonly used as an optimisation objective for AM processes. Hence, the mass density of the produced LPBF W samples was measured by means of densimetry based on Archimedes' principle[4]. The results of these measurements are illustrated in Figure 6.4 [189]. In Figure 6.4a, the relative mass density is plotted against

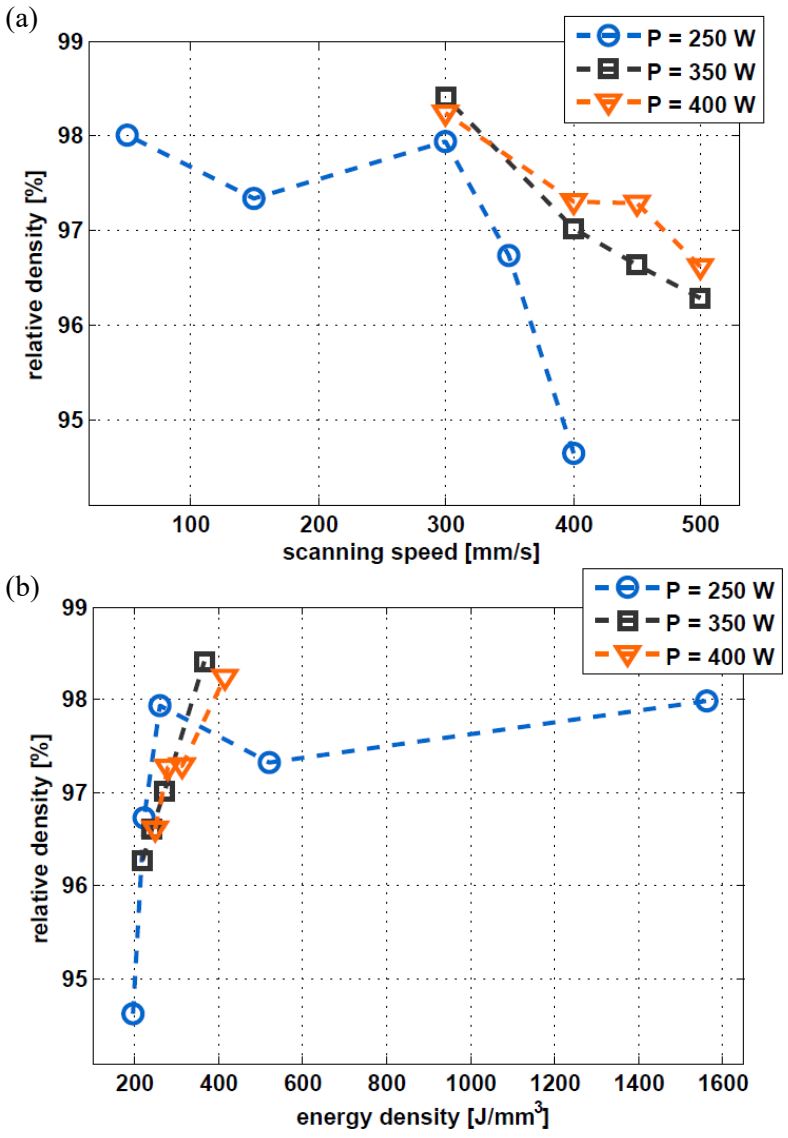

FIGURE 6.4: Measured relative mass density of LPBF W samples versus (a) laser scanning speed and (b) deposited energy density [189].

the applied laser scanning speed. It can be seen that, as expected, there is a trend of

[4]For these measurements, a dedicated density scale (ABS 220-4N, Kern & Sohn GmbH) was used. During the measurements, the samples were immersed in ethanol (Ethanol absolute for analysis EMSURE® ACS, ISO, Reag Ph Eur., Merck KGaA) at RT. The relative mass density values were calculated based on mass density measurements performed on a reference W sample (rolled W plate material, thickness $t = 4\,\mathrm{mm}$, supplier: A.L.M.T. Corp., Japan).

increasing mass density of the samples with decreasing laser scanning speeds. In Figure 6.4b, the relative mass density for the samples is plotted against the deposited energy density calculated according to Equation 6.1. Again, it can be observed that there is a trend of increasing mass density with increasing energy density. Moreover, it can be seen that for the samples produced with a laser power of 250 W no distinct increase in mass density could be observed for the relatively slow scanning speeds of $150\,\mathrm{mm\,s^{-1}}$ and $50\,\mathrm{mm\,s^{-1}}$, respectively.

In the following, some typical microsections of the produced LPBF W samples[5] are illustrated. Figure 6.5 shows optical microsections of samples produced with a laser power of 250 W, for three different scanning speeds, i.e. $400\,\mathrm{mm\,s^{-1}}$, $300\,\mathrm{mm\,s^{-1}}$ and $50\,\mathrm{mm\,s^{-1}}$, respectively [189]. Figure 6.5a illustrates that the sample produced with a scanning speed of $400\,\mathrm{mm\,s^{-1}}$ exhibits plainly visible and irregularly shaped porosity. From Figure 6.4, it can be seen that this sample showed an overall relative mass density of approximately 94.5%. Figure 6.5b illustrates a microsection of a sample produced with a laser power of 250 W and a scanning speed of $300\,\mathrm{mm\,s^{-1}}$. It can be seen that the sample shows considerably less porosity compared with Figure 6.5a which is also confirmed by the mass density measurements according to which the sample illustrated in Figure 6.5b exhibits a relative mass density of nearly 98%. Figure 6.5c shows an optical microsection of a sample again produced with a laser power of 250 W but with a rather low scanning speed of $50\,\mathrm{mm\,s^{-1}}$. These parameters yielded as well a sample with a relative mass density of nearly 98%. However, the microsections illustrated in Figure 6.5 do also show the presence of microcracks in the manufactured samples. Especially in Figure 6.5b, a network of microcracks can clearly be seen.

In Figure 6.6, typical optical microsections of LPBF W samples produced with the highest investigated laser power of 400 W are illustrated [189]. Figure 6.6a shows a microsection of a sample that has been produced with a scanning speed of $500\,\mathrm{mm\,s^{-1}}$. Some plainly visible porosity can be observed in the microsection while the mass density measurement of the sample showed a relative mass density of approximately 96.5%. Figure 6.6b shows a sample manufactured with slower scanning speed of $300\,\mathrm{mm\,s^{-1}}$ and hence a higher deposited energy density compared with Figure 6.6a. It can be seen that the microsection shows even less porosity compared to Figure 6.6a. However, both samples do also exhibit plainly visible microcracks as already observed for the samples illustrated in Figure 6.5. Figure 6.7 shows an SEM microsection (backscattered electron images) of the same sample as illustrated in Figure 6.6b. Again, the microcracks that have already been observed within the optical microscopy images can clearly be seen. Figure 6.7 furthermore reveals that the cracking occurs along the grain boundaries of the material. Moreover, it can be

[5] All microsections of LPBF W samples shown within the present work were prepared perpendicular to the building direction of the samples. In general, the metallographic preparation of these samples was performed by wet grinding with SiC abrasives up to a grit of P4000 and polishing with diamond suspension with a grain size of 1 µm as well as with colloidal silica suspension with a grain size of 0.04 µm.

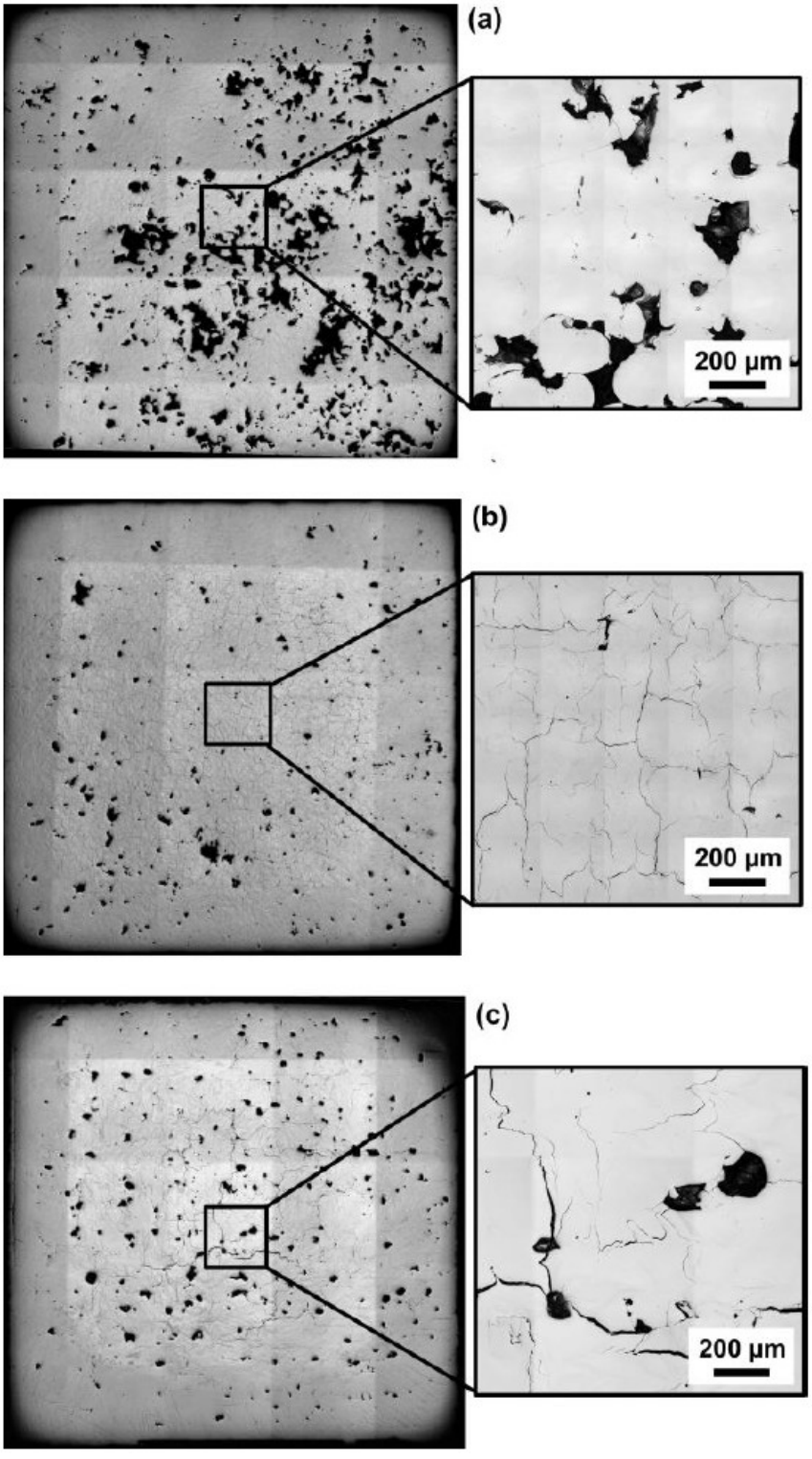

FIGURE 6.5: Optical microsections perpendicular to the building direction of LPBF W samples produced with a laser power of 250 W for three different laser scanning speeds, (a) 400 mm s^{-1}, (b) 300 mm s^{-1} and (c) 50 mm s^{-1} [189].

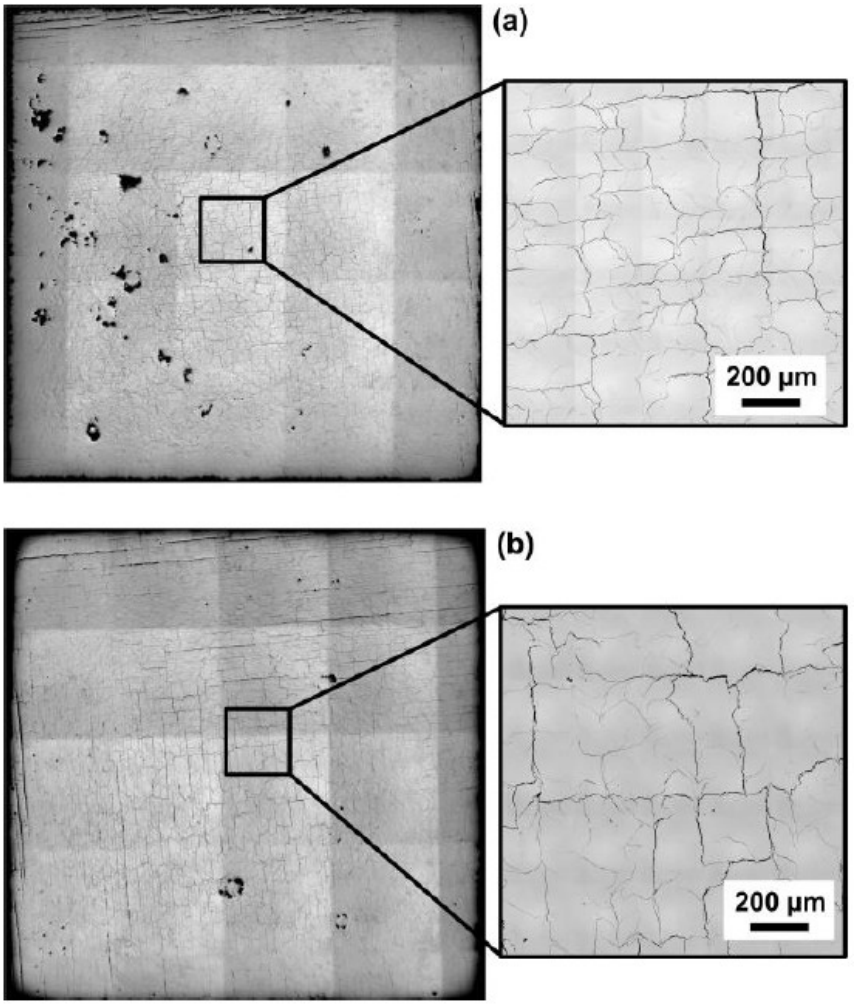

FIGURE 6.6: Optical microsections perpendicular to the building direction of LPBF W samples produced with a laser power of 400 W for two different laser scanning speeds, (a) 500 mm s^{-1} and (b) 300 mm s^{-1} [189].

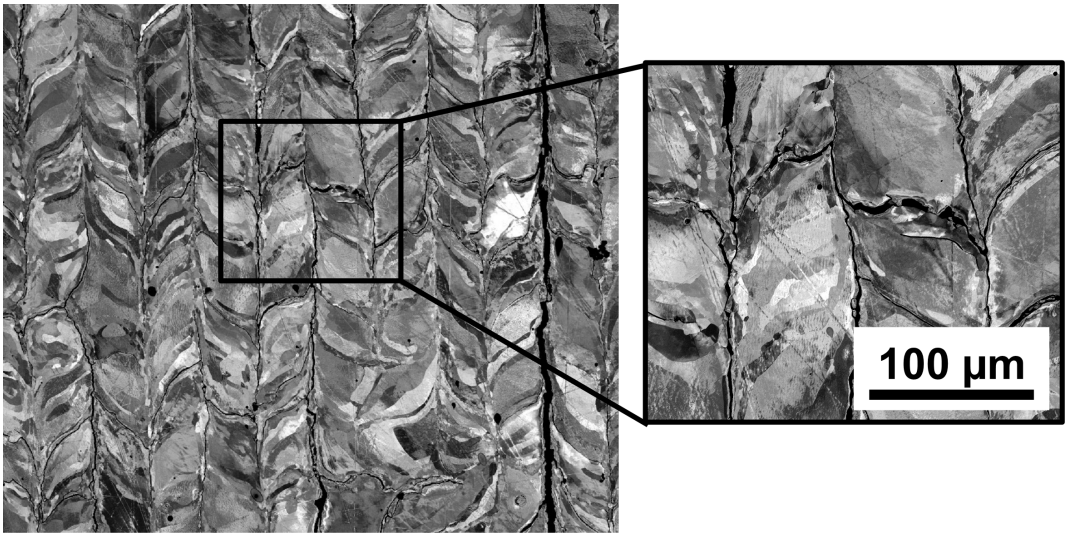

FIGURE 6.7: SEM microsection (backscattered electron images) perpendicular to the building direction of a LPBF W sample produced with a laser power of 400 W and a laser scanning speed of 300 mm s^{-1} [189].

seen that the larger grains are in principle confined by the laser melting track width and that they exhibit a characterisitc S-shape originating from the local temperature gradient across the scan track during the LPBF process as has also been observed in [190].

6.4 Experiments with high substrate preheating temperature

The abovementioned studies showed that W samples with a high relative mass density of approximately 98% can be consolidated directly by means of LPBF. However, metallographic investigations revealed that the material - especially samples with a high mass density – did exhibit pronounced microcracks which are expected to hamper the performance of the material. The microcrack formation was attributed to the intrinsic properties of W, especially its high DBTT, in combination with the high thermal gradients that occur during a LPBF process.

Against this background, the potentially positive influence of an elevated substrate preheating temperature during the LPBF process was furthermore investigated within the present work. In the literature, it was reported that a substrate preheating of 400 °C is not sufficient in order to mitigate the formation of microcracks within a W material during LPBF processing [183]. That is the reason why within the present work, LPBF with substrate preheating up to 1000 °C was investigated [191].

For these investigations, an Aconity*ONE* LPBF manufacturing facility was used[6]. It is equipped with a fibre laser operating at a wavelength of 1075 nm and an inductive heating system which can raise the substrate plate temperature up to 1000 °C. In order to facilitate such high preheating temperatures a reduced build platform with a diameter of 200 mm was used. During operation, Ar was used as protective atmosphere within the device chamber. The laser was operated in focus (z = 0) while the focus diameter is approximately 100 µm.

As raw powder material for the high-temperature LPBF investigations the same W powder in terms of supplier and specification as mentioned above regarding the low-temperature investigations was used. In terms of substrate preheating, the process was investigated for preheating temperatures of 600 °C, 800 °C and 1000 °C. The investigated process parameters in terms of laser power, laser scanning speed and substrate preheating are summarised in Table 6.4. As for the low-temperature investigations described in the previous section, the laser scanning strategy was fixed for all manufactured samples as 90° alternating bidirectional, the hatch spacing was held constant at 80 µm and the layer thickness was also fixed with 40 µm.

[6] located at Aconity3D GmbH, Herzogenrath, Germany

TABLE 6.4: Investigated LPBF process parameters in terms of substrate preheating, laser power and laser scanning speed.

Substrate preheating	*Laser power*	*Laser scanning speed*
600 °C	375 W	210 mm s^{-1} to 330 mm s^{-1}
600 °C	400 W	330 mm s^{-1} to 510 mm s^{-1}
800 °C	375 W	210 mm s^{-1} to 330 mm s^{-1}
800 °C	400 W	330 mm s^{-1} to 510 mm s^{-1}
1000 °C	375 W	210 mm s^{-1} to 330 mm s^{-1}
1000 °C	400 W	300 mm s^{-1} to 840 mm s^{-1}

With the parameters mentioned above, cube-shaped samples with dimensions of approximately $10 \times 10 \times 10\,\mathrm{mm}^3$ were manufactured on W substrate plates. In Figure 6.8, an image of such samples during the LPBF process can be seen [191]. The annealing colour of the consolidated material samples within the powder bed indicates their elevated temperature due to the fact that they are directly built on and bonded to the preheated substrate plate. In Figure 6.9, an exemplary image of LPBF W samples on a W sub-

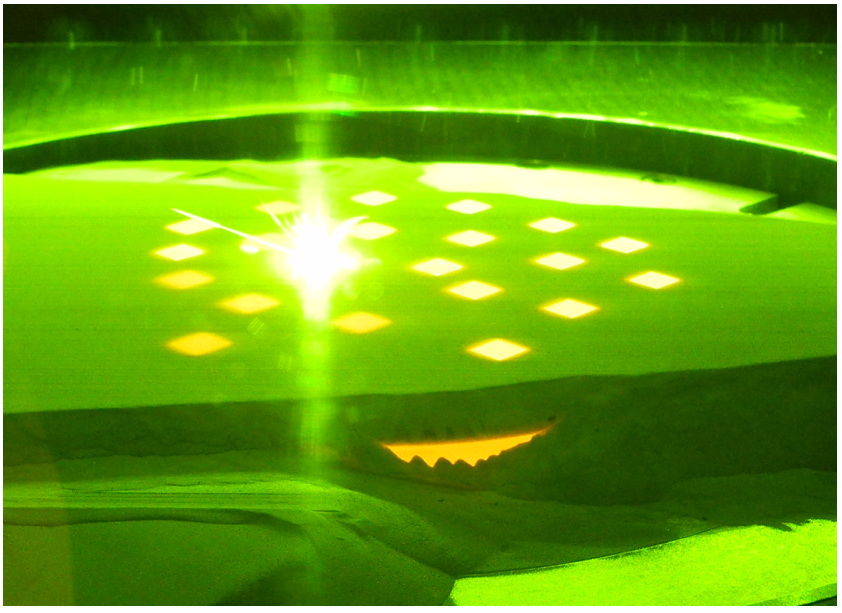

FIGURE 6.8: W samples during the LPBF process within the powder bed; the annealing colour of the consolidated material samples indicates their elevated temperature; the greenish colour of the image is due to the laser protection glass [191].

strate plate after manufacturing and powder removal is shown [191]. It is interesting to note that the laser beam melted cube-shaped samples do exhibit rather clean surfaces while the substrate plate seems to getter residual O and undergo oxidation during the heating within the device chamber.

The mass density of the investigated LPBF W samples was again determined by means of densimetry based on Archimedes' principle as described within the previous section

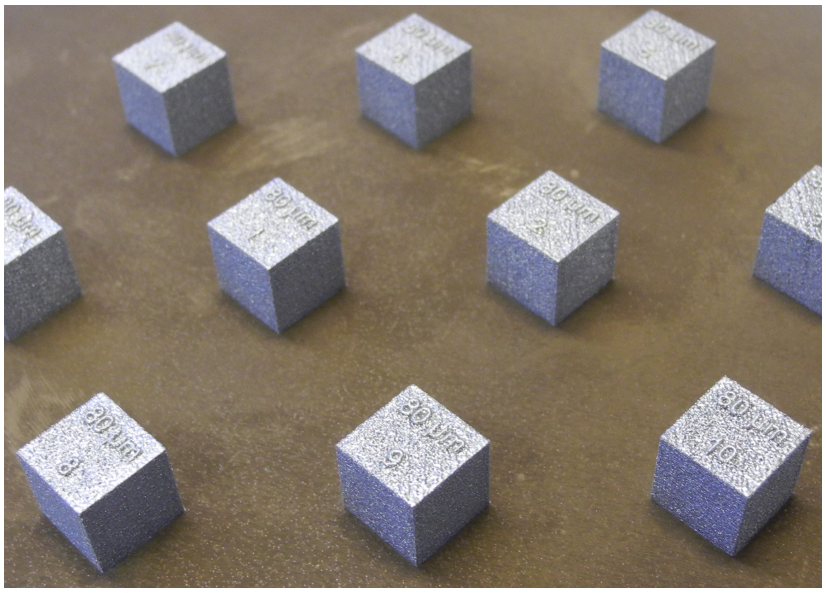

FIGURE 6.9: Typical cube-shaped LPBF W samples with an edge length of 10 mm on W substrate plate after the LPBF process and powder removal [191].

with respect to the low-temperature LPBF investigations. The relative mass densities of the samples are illustrated in Figure 6.10 where the density of the samples versus the applied energy density calculated according to Equation 6.1 is shown [191]. The illustration includes data of samples manufactured with different substrate preheating temperatures (600 °C, 800 °C, 1000 °C) as well as different laser powers (375 W, 400 W). Apart from the fact that Figure 6.10 confirms that pure W samples can be consolidated reasonably by means of LPBF several observations can be made in addition. On the one hand, it can be seen that there is a general trend of increasing mass density of the samples with increasing substrate preheating temperature. In this sense, it can be concluded that increased substrate preheating temperatures are in general beneficial for LPBF processing of pure W. On the other hand, it can be seen that for the investigated parameters energy densities of approximately $300\,\mathrm{J\,mm^{-3}}$ and higher are not suitable as such parameters lead to decreased densification of the material. Furthermore, it can be seen that the highest investigated preheating temperature of 1000 °C in combination with the high laser power of 400 W tend to result in the highest measured relative mass densities of the samples. As these two main process parameters have been regarded as most suited for the LPBF of pure W the corresponding parameter space was investigated down to energy densities of approximately $150\,\mathrm{J\,mm^{-3}}$. However, the data indicates that there is again a trend of slightly decreasing mass density for decreasing energy densities below approximately $200\,\mathrm{J\,mm^{-3}}$. This resembles a typical behaviour encountered with respect to material processing by means of LPBF which is characterised by a certain processing window that comprises manufacturing parameters yielding a high densification of the material. Usually, too low energy densities lead to interrupted melting tracks that in

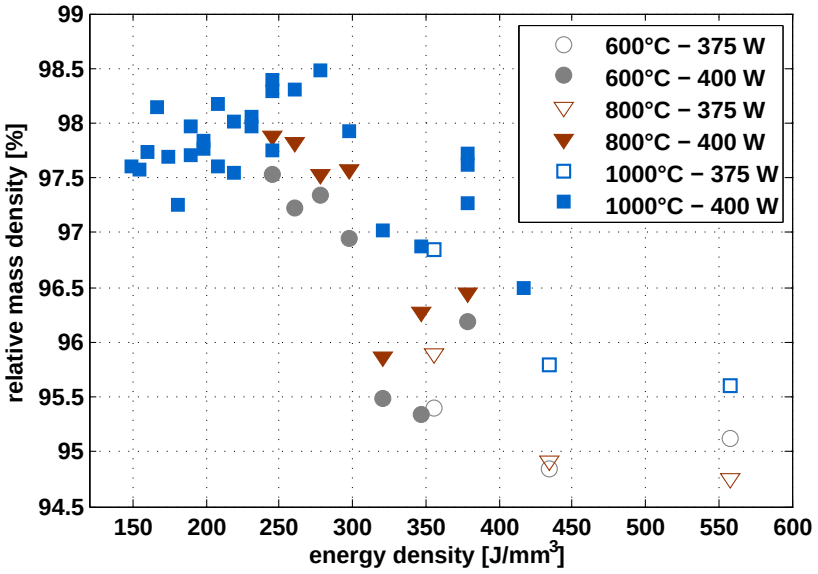

FIGURE 6.10: Measured relative mass density of LPBF W samples versus applied energy density; the illustration includes data of samples manufactured with different substrate preheating temperatures (600 °C, 800 °C, 1000 °C) as well as different laser powers (375 W, 400 W) [191].

turn imply porosity while excessive energy densities result in deep melting tracks with keyhole porosity formation [181]. Within the investigated parameter space, reasonable manufacturing parameters have been identified with a deposited energy density of approximately 250 J mm^{-3} for a laser power of 400 W.

In the following, typical optical microsections of the LPBF W samples are shown. In Figure 6.11, three samples are illustrated that were produced with a substrate preheating of 1000 °C and a laser power of 400 W [191]. For these two parameters, the boundaries of the investigated parameter space as well as a reasonable choice in terms of laser scanning speed are shown. In Figure 6.11a, a sample manufactured with a laser scanning speed of 300 mm s^{-1}, corresponding to an energy density of ca. 420 J mm^{-3}, is illustrated. It can be seen that the sample exhibits macroscopic defects, especially plainly visible porosity. In Figure 6.11b, a sample manufactured with a higher laser scanning speed of 510 mm s^{-1}, i.e. a lower energy density, is shown. It can be seen that the sample exhibits clearly less porosity, compared with the sample shown in Figure 6.11a, as is also confirmed by Archimedes' densimetry. In Figure 6.11c, a sample manufactured with a laser scanning speed of 840 mm s^{-1}, i.e. the highest laser scanning speed investigated within this work, is shown. It can be seen that the sample exhibits again slightly more porosity, compared with the sample shown in Figure 6.11b, which is also confirmed by Archimedes' densimetry.

The experiments described within this section were performed in order to investigate

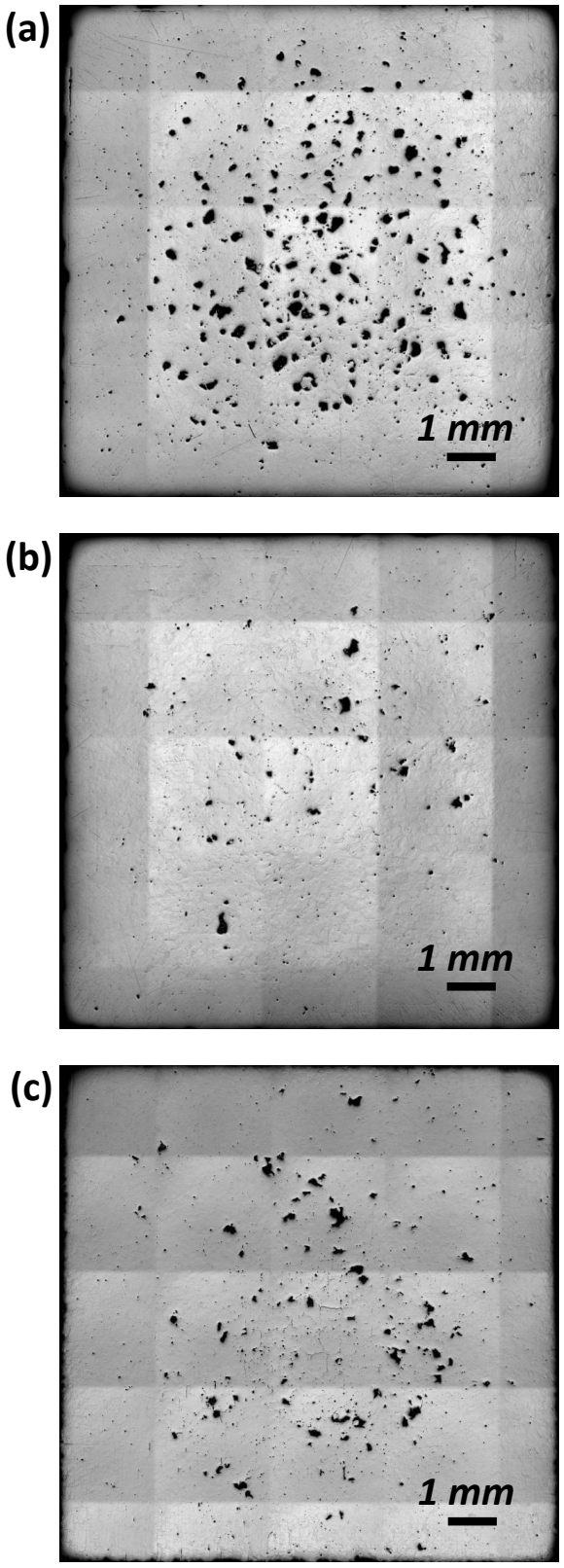

FIGURE 6.11: Optical microsections perpendicular to building direction of LPBF W samples produced with a substrate preheating of 1000 °C and a laser power of 400 W for three different laser scanning speeds, (a) 300 mm s^{-1}, (b) 510 mm s^{-1} and (c) 840 mm s^{-1} [191].

the potentially beneficial influence of an elevated substrate preheating temperature during the LPBF of pure W. Hence, microsections are shown in Figure 6.12 for samples manufactured with similar parameters but with different substrate preheating temperatures. Figure 6.12a is taken from the low-temperature investigations described above (cf.

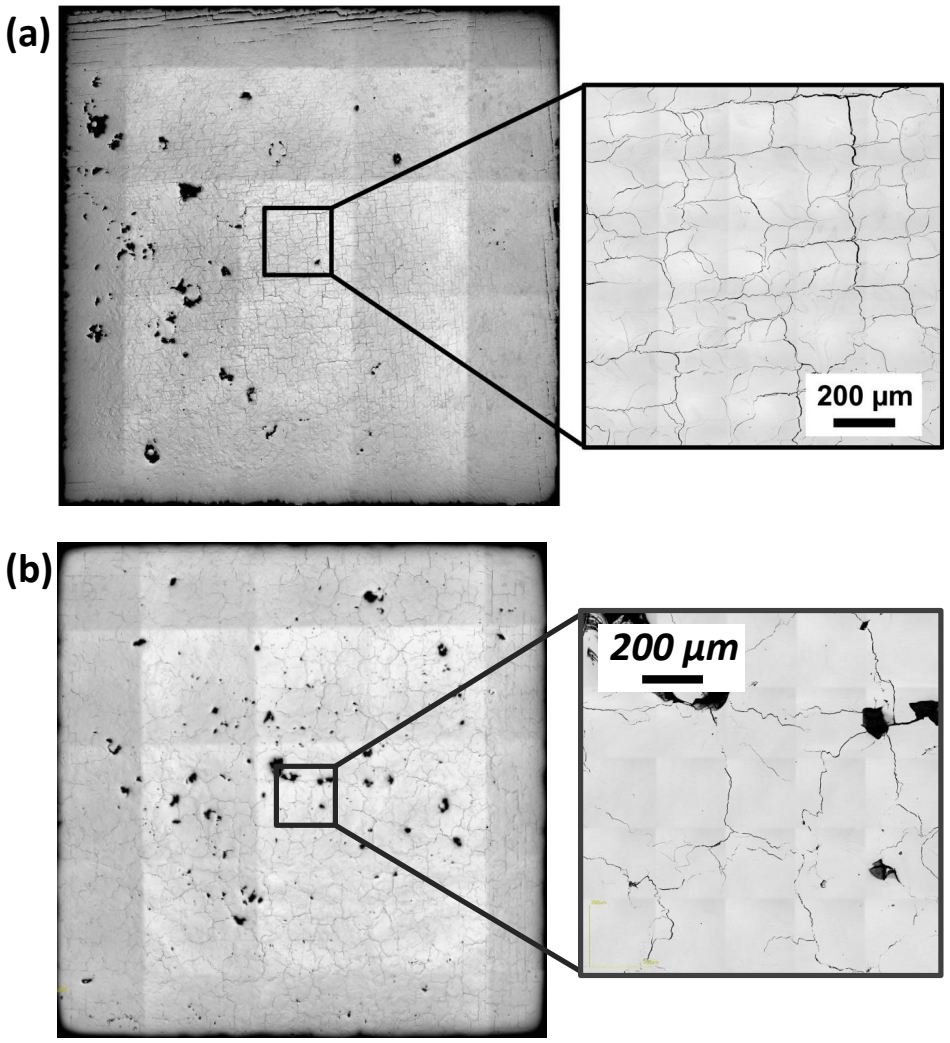

FIGURE 6.12: Optical microsections perpendicular to building direction of LPBF W samples manufactured with a substrate preheating of (a) 200 °C (laser power 400 W, laser scanning speeds 500 mm s^{-1}) [189] and (b) 1000 °C (laser power 400 W, laser scanning speeds 510 mm s^{-1}) [191].

Figure 6.6) and shows a sample that was manufactured with a substrate preheating of 200 °C while in Figure 6.12b a sample is shown that was manufactured with a substrate preheating of 1000 °C. The microsections illustrated in Figure 6.12 indicate that the crack defect formation is to some extent mitigated and crack density is reduced due to the substrate preheating but it is not completely inhibited. Furthermore, it can be seen that the cracking morphology is somewhat different. In Figure 6.12a, the cracks form a network that can directly be attributed to the scan tracks of the laser beam while this

is not apparently visible for the sample shown in Figure 6.12b, manufactured with a substrate preheating of 1000 °C.

6.5 Additively manufactured tungsten honeycomb structures

As has been mentioned above, one of the main advantages of AM technologies is that with such processes parts with almost any shape or geometry can be realised very flexibly by means of layerwise deposition of material. In order to demonstrate these possibilities thin-walled W honeycomb structures were manufactured directly by means of the investigated LPBF process with high substrate preheating temperature. In Figure 6.13, such

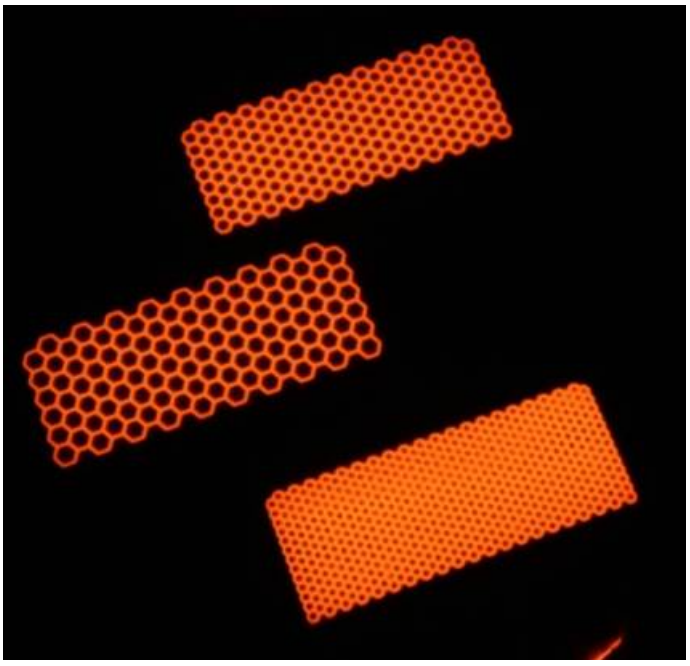

FIGURE 6.13: W honeycomb structures during LPBF process within the powder bed.

W honeycomb structures are shown during the LPBF process within the powder bed. An image of W honeycombs after the LPBF process is illustrated in Figure 6.14a [191]. In Figure 6.14b, the microscopic top view on an additively manufactured W honeycomb structure is illustrated. The struts of the W honeycomb structures shown in Figure 6.14 correspond to one single laser melting track. Furthermore, it should be mentioned that the issues with residual stresses and the corresponding crack defect formation as described above for bulk W material are expected to be less problematic for thin-walled structures as shown in Figure 6.14.

Moreover, the capabilities of LPBF were used to realise graded W honeycomb structures in which the honeycombs exhibited a varying wall thickness along the building direction. Such a specimen is illustrated in Figure 6.15. Figure 6.15a shows the top view on the

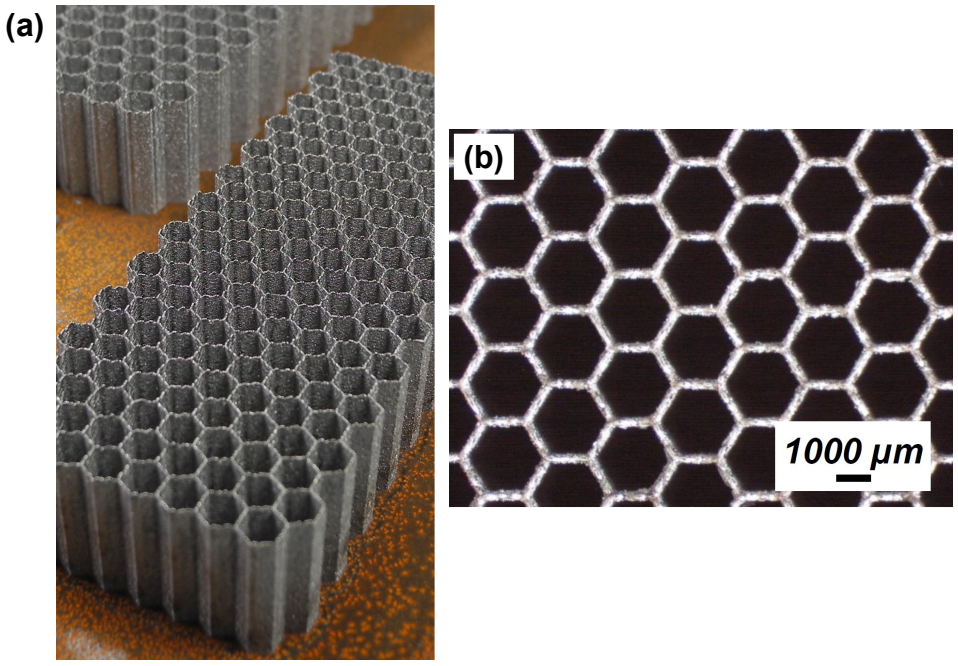

FIGURE 6.14: (a) W honeycomb structures on W substrate plate after LPBF process and powder removal and (b) microscopic top view on W honeycomb structure manufactured by means of LPBF [191].

structure while in Figure 6.15b the corresponding side view is shown. In Figure 6.15c, magnifications of the area indicated by the white rectangle in Figure 6.15b are shown including horizontal as well as vertical contour scans. The contour profiles illustrate the regular honeycomb structure as well as the graded wall thickness profile. Apart from that, in Figure 6.15d a cross section, as indicated by the white dashed line in Figure 6.15a, through the CAD model of this geometry is illustrated showing the increasing wall thickness of the honeycomb structure towards the bottom.

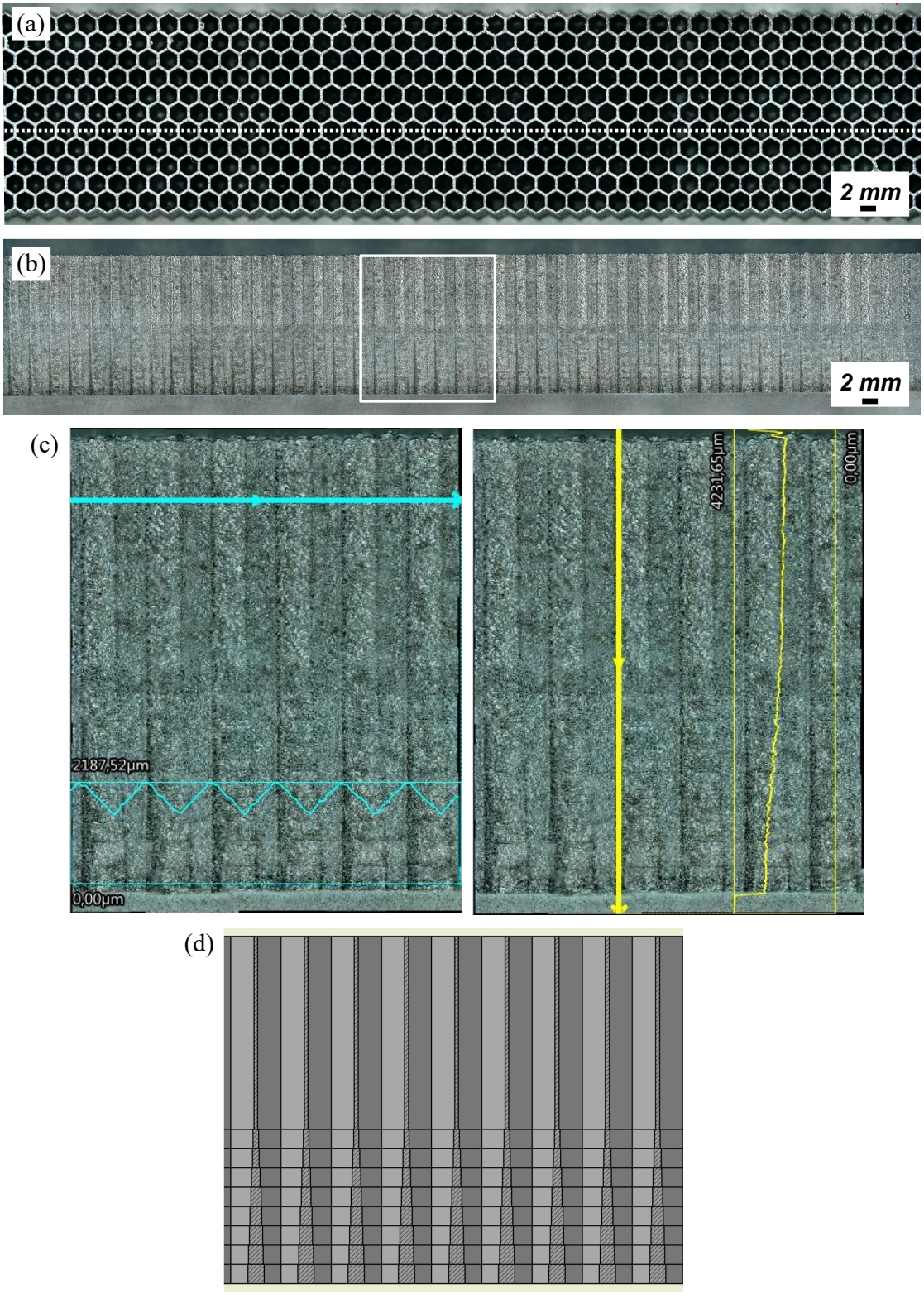

FIGURE 6.15: Graded W honeycomb structure: (a) Top and (b) side view of a specimen on W substrate plate after LPBF process and powder removal, (c) horizontal and vertical contour profiles of the honeycomb as well as (d) section through the CAD model (as indicated by the dashed white line in (a)) of the structure.

6.6 Composite materials based on additively manufactured tungsten

It has been mentioned within section 3.4 that the macroscopic properties of W-Cu MMCs can be tailored through the adjustment of the composite structure and that this can e.g. be exploited by adjusting the CTE in order to minimise thermally induced stresses due to a CTE mismatch within a component.
In this context, the design freedom allowed by AM technologies could be used to realise tailored W_{AM}-Cu composites. This approach allows a rather detailed control of the material distribution within a composite structure resulting in a tailored material behaviour that can be adjusted according to the loading situation within the material or a component. Such an approach to composite material design could leverage the potential of W-Cu MMCs for PFC applications even further.
In Figure 6.16, a W_{AM}-Cu composite based on an additively manufactured W honeycomb structure as illustrated in Figure 6.14 is shown while the composite structure was fabricated by means of a liquid Cu infiltration process [191]. Figure 6.16a and Figure 6.16b illustrate parallel and perpendicular microsections of the composite structure. In Figure 6.16c, an oblique view of the specimen is shown. Figure 6.16 demonstrates that tailored W-Cu composite structures based on additively manufactured W preforms are realisable. Furthermore, two aspects should be mentioned in this context. Figure 6.16 illustrates that the additively manufactured W structure is built onto a W substrate plate which could be a W PFM tile meaning that with such an approach an intimate bonding of the PFM to the W_{AM}-Cu heat sink could be realised which is highly desireable with regard to PFC applications. Furthermore, it has been described above that bulk LPBF W material exhibits defects, as e.g. microcracks, that are expected to hamper the performance of the material and it is questionable if such a material is suited for PFC applications as monolithic material. However, the concept of W_{AM}-Cu composites is rather based on thin-walled W structures that are additionally Cu infiltrated which means that they are embedded in a ductile matrix material. Hence, the issues with defects in LPBF W material might not be regarded that critical.

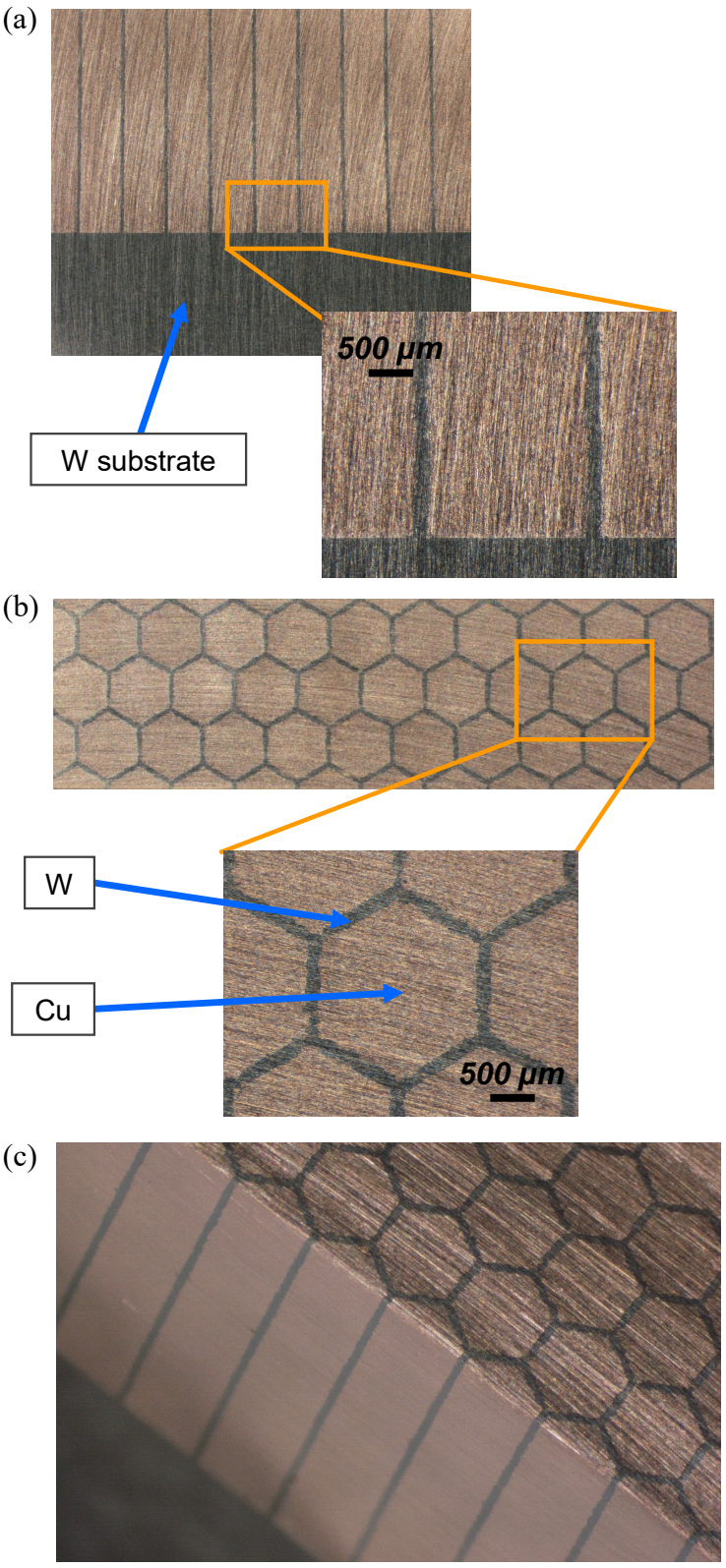

FIGURE 6.16: (a) Parallel and (b) perpendicular microsections of a melt infiltrated W_{AM}-Cu composite based on an additively manufactured W honeycomb structure [191]. In (c) an oblique view of the specimen is shown.

6.7 Potential for plasma-facing component design

Above it has been described that state-of-the-art AM technologies and the design freedom associated with these techniques could represent a possibility to create W_{AM}-Cu composite structures with tailored architecture according to the loading situation within a PFC. The question arises what a prudent W-Cu material distribution of a composite structure is in order to realise a better performing and more resilient PFC.
Hence, a methodology to optimise the material distribution in composite PFCs was developed in order to investigate the potential capabilities of W_{AM}-Cu composite structures. To that end, a custom-built thermoelastic *finite element* (FE) code was developed[7] that minimises thermally induced stresses due to steady-state HHF loads through tailoring a heterogeneous W-Cu material distribution. The basic strategy regarding this optimisation approach is described in the following. For further details, e.g. regarding the FE formulation, numerical details or the used material models the reader is referred to [192, 193].
A simplified PFC model as illustrated in Figure 6.17 was used to demonstrate the investigated optimisation approach [193]. The component was modelled in 2D with plane-

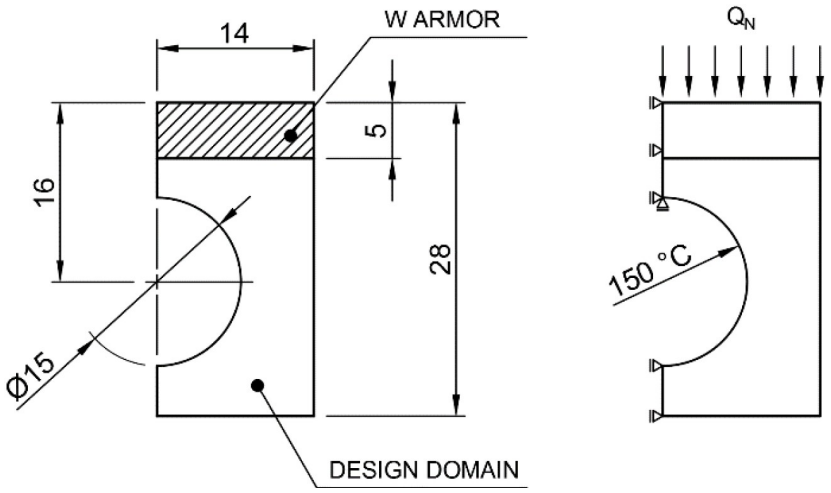

FIGURE 6.17: PFC model used for the W-Cu material distribution optimisation [193].

stress behaviour while the dimensions are comparable to the geometry of an ITER W monoblock [50,69]. The model shown in Figure 6.17 represents half of the PFC and takes advantage of the symmetry of the system. Moreover, a 5 mm thick W PFM armour was fixed.
The PFC model as illustrated in Figure 6.17 is discretised with a gridded FE mesh as is illustrated in Figure 6.18 [193]. Each element in the design domain is assigned a design variable that varies between 0.0 and 1.0. This variable gives the composition of the heterogeneous composite material within that element where 0.0 corresponds to Cu (alloy)

[7] This code was developed in the framework of a *Master's Thesis* that was supervised by the author in the course of the present work [192]. The major results of this thesis are published in [193].

and 1.0 to W. Intermediate values represent composite mixtures and the macroscopic behaviour of these mixtures is determined with a material model describing the elastic properties, the thermal conductivity as well as the CTE. For the computations, the fol-

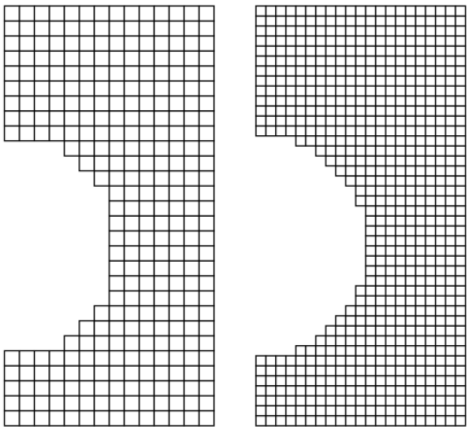

FIGURE 6.18: Gridded meshes applied to the PFC model illustrated in Figure 6.17 [193].

lowing boundary conditions were applied: A steady-state heat flux (Q_N) is applied at the surface of the W armour and nodes at the surface of the cooling channel are fixed to a heat sink temperature of 150 °C. Apart from that, thermal stress is calculated using a reference temperature T_0 at which the material is assumed to be stress-free[8].

As component integrity was regarded the most important aspect with respect to a PFC design the quantity to be optimised is the maximum thermal stress within the PFC induced by HHF loading. In this respect, the objective is the minimisation of *von Mises equivalent stress* which for a 2D, plane-stress domain can be calculated according to

$$\sigma_v^2 = \sigma_1^2 + \sigma_2^2 - \sigma_1\sigma_2 + 3\tau_{12}^2. \tag{6.2}$$

The optimisation problem is then formulated such that the peak von Mises stress in the PFC is minimised:

$$\begin{aligned} &min \;\; z \\ &subject\ to \;\; \sigma_v^{(e)} \leq z, \; e = 1, ..., n_{el} \end{aligned}$$

The applied formulation that yielded viable results treats stress locally meaning that an artificial variable z was minimized while the von Mises stress in each element was individually constrained to be less than or equal to z.

For the optimisation procedure derivatives of stress with respect to the design variables must be computed in addition to the current stress state in the component. In the

[8]The post-manufacturing stress state of W_{AM}-Cu composites is the result of residual stresses due to the AM process as well as the solidification shrinkage during Cu melt infiltration. It is expected that this stress state is rather complex while it has not yet been characterised experimentally.

context of optimisation problems this process is typically known as *sensitivity analysis*. For the solution of the optimisation problem the *method of moving asymptotes* (MMA) was chosen which is a nonlinear optimisation algorithm popular with respect to topology optimisation problems [194].

With the approach described above, optimisations were performed for a variety of conditions ($Q_N = 5\,\mathrm{MW\,m^{-2}}, 10\,\mathrm{MW\,m^{-2}}, 15\,\mathrm{MW\,m^{-2}}, 20\,\mathrm{MW\,m^{-2}}$; $T_0 = 150\,°\mathrm{C}, 400\,°\mathrm{C}, 650\,°\mathrm{C}, 900\,°\mathrm{C}, 1150\,°\mathrm{C}$) where it turned out that the heat flux and the stress-free reference temperature are indeed the most important design parameters. The reference configuration to which the optimised material distributions were compared is a monolithic W component. The results for this reference are illustrated in Figure 6.19 which summarises peak von Mises stresses for different applied heat fluxes [193]. Furthermore, stress and temperature distributions are in Figure 6.19b exemplarily illustrated for a heat loading of $15\,\mathrm{MW\,m^{-2}}$. Figure 6.20 shows exemplarily the progression of a W-Cu

(a)

Q_N (MW m^{-2})	σ_{max} (MPa)
5	260.5
10	576.1
15	922.5
20	1264.2

(b)

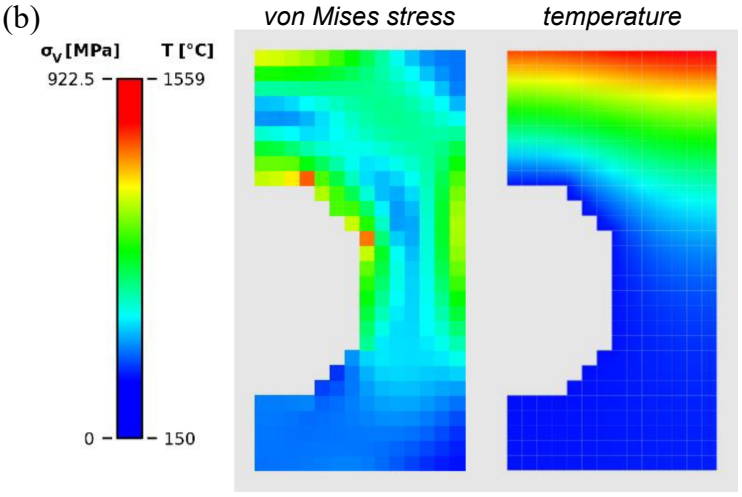

FIGURE 6.19: (a) Peak von Mises stress in a monolithic W reference domain for different applied heat fluxes and (b) von Mises stress (left) as well as temperature (right) distributions in the reference domain for an applied heat loading of $15\,\mathrm{MW\,m^{-2}}$ [193].

material distribution optimisation together with the corresponding stress fields for a load case with a heat loading of $Q_N = 10\,\mathrm{MW\,m^{-2}}$ and a stress-free reference temperature of $T_0 = 650\,°\mathrm{C}$ using a body-centred cubic (bcc) lattice structure material model [193]. In the material distribution plots in Figure 6.20, white represents Cu (alloy) and blue represents W. This means that darker shades of blue represent composite mixtures with higher W volume fractions. It can be seen that within 3 iterations, the peak von Mises stress has already decreased substantially. After 10 to 15 iterations, the material distribution and stress field have in principle stabilised resulting in a homogenised low stress state[9]. The peak von Mises stress reduction achieved through W-Cu material distribu-

[9] This convergence to a homogenised stress state seems to be reasonable. In the literature, such an optimisation behaviour has been termed the *axiom of uniform stress* and is regarded a fundamental rule in nature as wide areas of biological design behave according to this axiom [195].

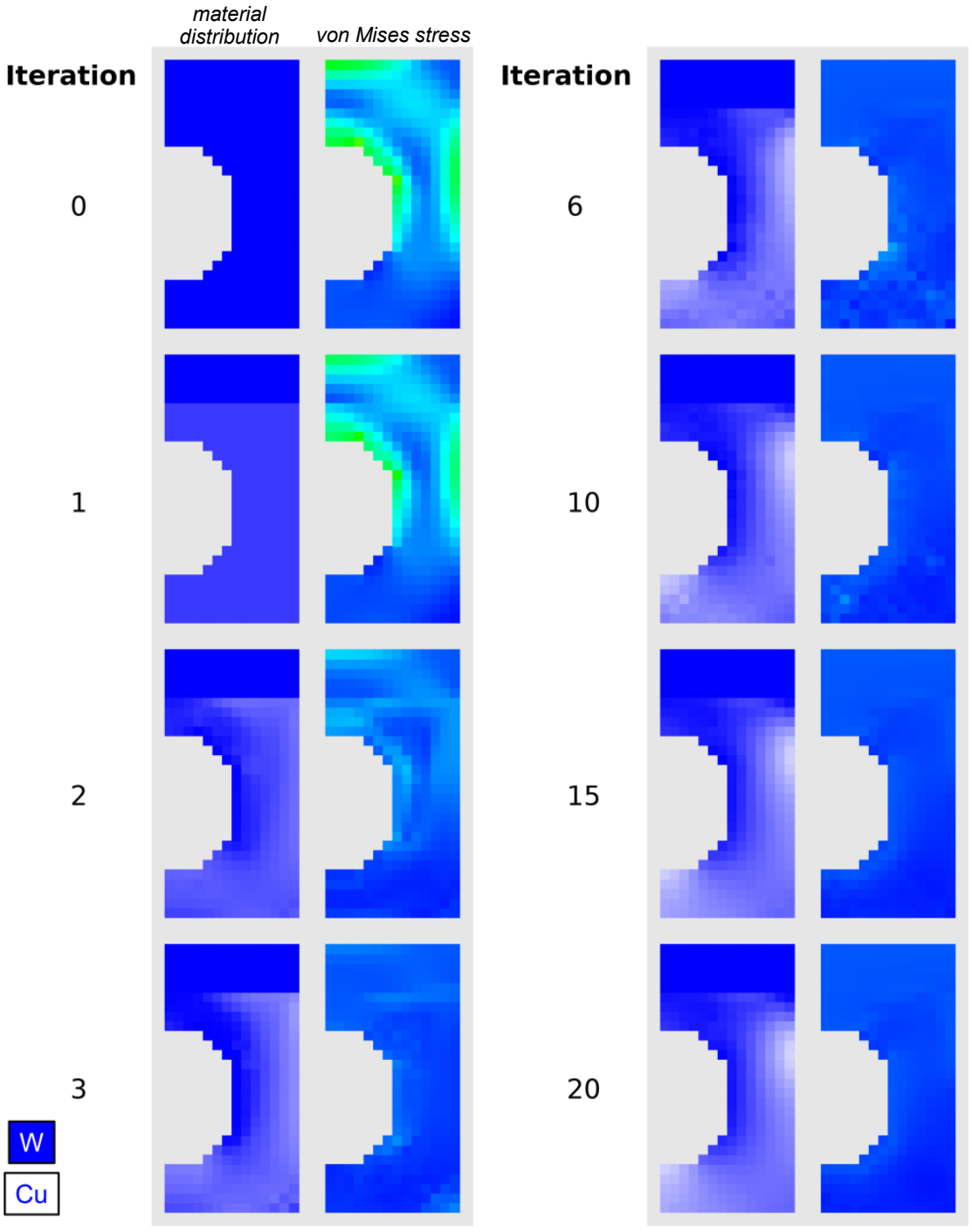

FIGURE 6.20: Iterations from an optimisation of a component for a heat loading of $10\,\mathrm{MW\,m^{-2}}$ as well as a stress free reference temperature of 650 °C; the left of each pair shows the material distributions (blue represents W, white represents Cu (alloy)) and the right of each pair shows the corresponding von Mises stress field (blue represents low stress states, green-/yellowish represents elevated stress levels) [193].

Q_N (MW m^{-2})	T_0 (°C)	σ_{max} (MPa)	Rel. $\Delta\sigma_{max}$ (%)
5	150	98.2	−62.3
5	400	42.9	−83.5
5	650	41.8	−84.0
5	900	42.6	−83.6
5	1150	41.6	−84.0
10	150	219.1	−62.0
10	400	84.9	−85.3
10	650	82.2	−85.7
10	900	87.2	−84.9
10	1150	88.4	−84.7
15	150	355.5	−61.5
15	400	177.9	−80.7
15	650	124.8	−86.5
15	900	139.7	−84.9
15	1150	139.9	−84.8
20	150	479.2	−62.1
20	400	370.4	−70.7
20	650	177.1	−86.0
20	900	185.6	−85.3
20	1150	198.8	−84.3

FIGURE 6.21: Peak von Mises stresses and stress reductions for PFC models optimised with a bcc lattice structure material model [193].

tion optimisation for different load cases using a bcc lattice structure material model is illustrated in Figure 6.21 [193]. A peak stress reduction of roughly 85% compared to the monolithic W reference configuration is typically achieved. Optimisation with an assumed stress-free temperature of $T_0 = 150\,°C$ was less effective but still resulted in stress reductions of roughly 60% for all investigated heat fluxes. These results indicate that PFC designs with optimised W-Cu material distributions could be very effective at reducing thermally induced stresses in order to ultimately enhance the resilience and integrity of such components. Furthermore, it should be mentioned that it was found that optimised designs do also exhibit reduced peak stresses over a wide range of off-nominal loading conditions [193].

Following optimisation, the resulting material distribution has to be translated into a manufacturable structure. An example for the feasibility of such a spatially heterogeneous distribution of W and Cu (alloy) is illustrated in Figure 6.22 which shows the cross-section of a bcc lattice structure component geometry (cell size: 2 mm) together with the optimisation result from which it was derived[10] [193].

[10]For this optimisation, the design variables were constrained to a maximum value of 0.7 in order to avoid regions with too high W volume fractions which are expected to be problematic for manufacturing due to the removal of residual powder after the LPBF process.

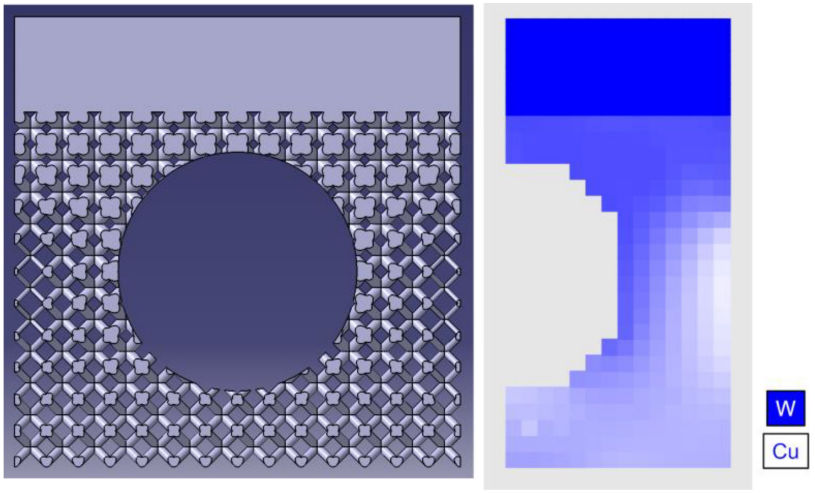

FIGURE 6.22: Sample optimised geometry implemented with a bcc lattice structure (left) as well as the optimisation result from which it was derived (right) [193].

6.8 Chapter 6 summary

Within this chapter, work performed regarding the development of W_{AM}-Cu MMCs based on additively manufactured W preforms is described. In this context, the AM of pure W by means of LPBF as well as the fabrication of W_{AM}-Cu MMCs was investigated. Furthermore, the potential of tailored W-Cu MMCs that could be realised with W_{AM}-Cu was discussed by means of a methodology for material distribution optimisation with respect to performance enhancement of PFCs. Against this background, the following main conclusions can be summarised:

- Pure W can be consolidated directly by means of LPBF up to relative mass densities of approximately 98%. However, it was found that the material does in general exhibit defects which are often encountered with respect to LPBF processing, like porosity and microcracks. The formation of microcracks was attributed to the intrinsic thermomechanical properties of W, especially its high DBTT, in combination with the high thermal gradients that inevitably occur during a LPBF process.

- LPBF experiments with substrate plate preheating temperatures up to 1000 °C revealed that such a preheating is beneficial for material consolidation during LPBF. However, it was found that there is no complete mitigation of microcrack formation.

- It has been shown that by means of LPBF thin-walled W structures with submillimeter resolution can be realised straightforwardly. This was demonstrated through the fabrication of W honeycomb structures which were also realised as graded structures with varying wall thickness.

- Furthermore, the processing of additively manufactured W structures to W_{AM}-Cu composite structures through Cu melt infiltration was demonstrated. This implies that tailored W-Cu composite structures based on additively manufactured W preforms are well realisable.

- Inspired by the design freedom that AM methods allow, a design methodology for PFCs was discussed which is based on a W-Cu material distribution optimisation technique. This numerical FE methodology predicts that for a tailored W-Cu material structure in a PFC heat sink peak stress reductions of up to 85% compared to an all-W reference component can be achieved under nominal HHF load conditions. These results indicate a high potential of W_{AM}-Cu for PFC design.

Chapter 7

Concluding Remarks

7.1 General conclusions

In Chapter 2 of the present work, the challenges and issues associated with the topic of power and particle exhaust with regard to future power-producing magnetic confinement thermonuclear fusion devices, like DEMO, have been described. In this context, it has been highlighted that the design and engineering of divertor target PFCs that need to be capable of withstanding intense particle, heat and neutron fluxes during fusion operation reliably represents a major challenge.
Specifically, it was in this context mentioned that the use of existing Cu alloys as structural divertor PFC heat sink materials is regarded a high impact design engineering risk with respect to a DEMO device. This is mainly due to the fact that Cu alloys suffer from property degradation under neutron irradiation, namely loss of ductility at lower as well as loss of strength at elevated operating temperatures. Because of the "show-stopper" nature of the divertor development it is required that alternatives to these existing materials for divertor PFC heat sink applications are developed.
Against this background, the present work reports on the development of W-Cu composites as advanced materials for PFC heat sink applications. Such materials are considered to hold a potential for improving the performance of highly loaded PFCs as they can in principle combine a high conductivity due to the Cu matrix with good high-temperature strength properties due to reinforcing W inclusions within the material. The latter aspect implies that such materials do rely on an inherently different strengthening mechanism compared to Cu alloys that mainly rely on work and precipitation hardening mechanisms which, however, are in general rather susceptible to thermally induced property degradation as well as effective only to a limited extent under neutron irradiation. Furthermore, W-Cu macroscopic composite material properties can - to some extent - be tailored by adjustment of the composite structure which can for example be exploited by reducing the CTE mismatch with respect to W in order to minimise thermal stress levels at PFM

to heat sink joints.

In this context, different types of W-Cu MMCs were investigated within the present work while the common feature of all these materials is that they are all fabricated according to the same manufacturing approach, i.e. liquid Cu melt infiltration of open porous W preforms. In more detail, W_p-Cu, W_f-Cu as well as W_{AM}-Cu MMCs were investigated. Various aspects regarding such materials were examined but a focus was put on their manufacturing as well as their potential applicability to PFC designs. The following conclusions regarding the different types of investigated W-Cu materials can be summarised:

W_p-Cu materials based on powder metallurgically produced W compacts represent a class of isotropic W-Cu MMCs characterised by a comparably simple manufacturing as well as sound thermophysical and -mechanical properties that can be varied according to the W-Cu composition of the material. The applicability of these materials has been demonstrated through the fabrication of W flat-tile type PFC mock-ups with W_p-Cu heat sink. It was found that the overall HHF performance of such a design was good but eventually limited due to typical flat-tile design issues inducing failure at the W/W_p-Cu bonding interface during cyclic heat loading at $20\,\mathrm{MW\,m^{-2}}$.

Regarding the W_f-Cu MMCs using high-strength drawn W fibres as reinforcement it can be stated that the fabrication of such MMCs was demonstrated including industrially viable fibre processing as well as Cu melt infiltration techniques. Furthermore, W_f-Cu MMCs in pipe configuration were successfully applied to W monoblock type PFC mock-ups. These mock-ups exhibited a very stable HHF performance during cyclic loading up to 1000 pulses at $20\,\mathrm{MW\,m^{-2}}$, cyclic loading up to 100 pulses at $25\,\mathrm{MW\,m^{-2}}$ as well as screening tests up to a heat load of $32\,\mathrm{MW\,m^{-2}}$. It should be highlighted that these HHF loadings can indeed be regarded as substantial. In section 2.3, it has been mentioned that the ITER divertor target qualification criteria comprise the demonstration of component integrity for 300 HHF load cycles at $20\,\mathrm{MW\,m^{-2}}$ [50, 69].

Apart from that, the possibility to realise W_{AM}-Cu MMCs based on additively manufactured W preforms was investigated. Such an approach makes use of the design freedom allowed by AM methods in order to realise materials that exhibit a tailored composite structure and hence a behaviour adjusted according to the loading situation within the material or a component. In this respect, the processing of additively manufactured thin-walled W honeycomb structures to W_{AM}-Cu composite structures through Cu melt infiltration was demonstrated which implies that tailored W-Cu composite structures based on additively manufactured W preforms are in principle realisable. Moreover, a design methodology for PFCs was discussed that is based on a W-Cu material distribution optimisation technique. This methodology predicts that for a tailored W-Cu composite material structure in a PFC heat sink significant peak stress reductions can be achieved under HHF loading. These results indicate that W_{AM}-Cu MMCs with tailored

composite structure might bear a high potential with respect to PFC applications.
Taking into consideration the abovementioned main results of the present work, the following overall conclusions can be drawn:

- W-Cu MMCs can be fabricated by means of liquid Cu (alloy) melt infiltration techniques with good material quality, i.e. with material properties acceptable for HHF applications in PFCs.
- W-Cu MMCs can be fabricated in a reasonable shape with respect to PFC heat sink applications.
- The reliable joining of W-Cu MMCs with W armour tiles can be realised, although it has to be investigated in more detail if the joining technologies proposed within the present work are applicable to divertor PFCs of future fusion devices, like DEMO.
- During the HHF tests of PFC mock-ups reported on within the present work no failure of the W-Cu MMC materials itself was observed which ultimately confirms the suitability of such materials for HHF applications.

Finally, the investigations reported on within the present work imply that W-Cu MMCs can be regarded as a class of viable and practicable advanced materials for heat sink applications in highly loaded PFCs as well as HHF applications in general.

7.2 Effects of neutron irradiation

In principle, it has been found within the present work that W-Cu MMCs represent a viable class of materials that hold a notable potential regarding their application to the heat sink of highly loaded PFCs. However, a major and critical criterion regarding the applicability of these MMCs in a nuclear fusion reactor is their behaviour under neutron irradiation. In a D-T fusion reactor, the energy of the neutrons created during the fusion reaction (cf. Equation 1.3) will be absorbed within the reactor wall, including the divertor PFCs. This in turn means, that the divertor PFC materials will be exposed to intense fusion neutron irradiation which compromises and degrades their thermophysical and -mechanical properties. This is mainly due to the following phenomena [196]:

- Incident neutrons cause accumulating atomic displacement damage within the PFC materials.
- Neutron irradiation can initiate nuclear reactions that transmute the atoms of a material. Eventually, this leads to a change in material structure and behaviour. In this context, nuclear reactions that produce gas species, mainly H and He, are considered as especially problematic. These gases can accumulate in materials over

long periods of time, e.g. at grain boundaries, which can lead to material swelling or embrittlement.

The deterioration of mechanical material properties under fusion neutron irradiation is a paramount concern regarding PFC materials. Above, it has been mentioned that the strengthening mechanism in W-Cu MMCs relies on a composite effect due to reinforcing W inclusions within the material. Against this background, the question arises if a composite can exhibit damage resilience when the ductility of the constituting phases is compromised through neutron irradiation induced embrittlement.
It is well-known that in composite materials extrinsic effects can contribute to the overall toughness of the material. Such effects are due to processes that cause absorption of energy within a composite material due to the interaction between the constituting phases. With respect to particle-reinforced composites, this is illustrated in Figure 7.1 which shows schematically possible fracture paths according to [106]. The illustrated phenomena are known to be capable of increasing the overall toughness of a particle-reinforced material through increasing the energy required for crack advance. Analogous

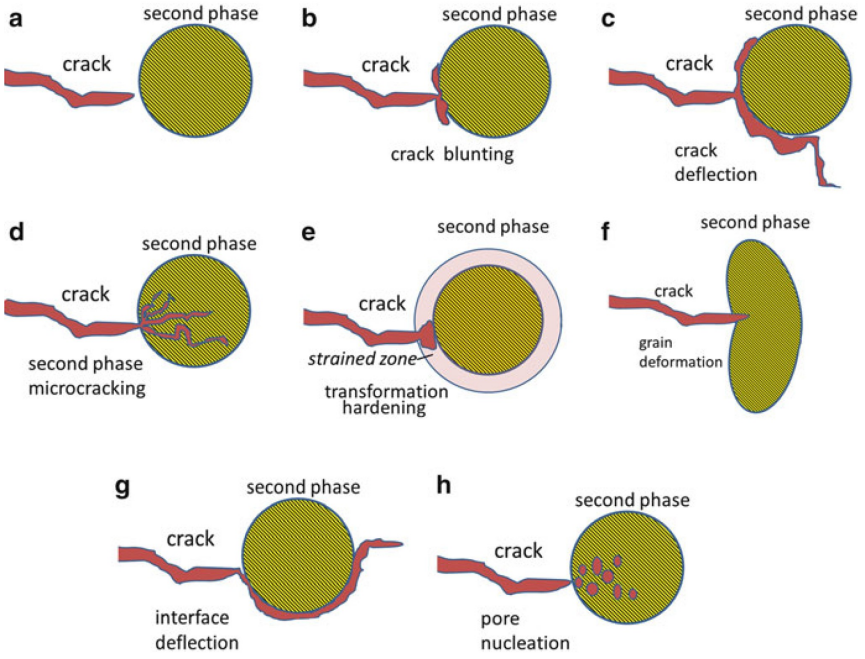

FIGURE 7.1: Possible fracture path interactions within a particle-reinforced composite according to [106]: (a) Crack approaching the second phase, (b) crack blunting, (c) crack deflection, (d) crack propagation into a second phase with microcracking, (e) induced transformation hardening, (f) grain deformation and plastic working, (g) interface deflection and (h) pore nucleation inside the second phase.

to the extrinsic toughening effects in particle-reinforced materials, there are also similar phenomena encountered in fibre-reinforced composites that are capable of increasing the overall material toughness. In Figure 7.2, these mechanisms are schematically illustrated [148]. The main effects in this respect are crack bridging, frictional fibre pull-out,

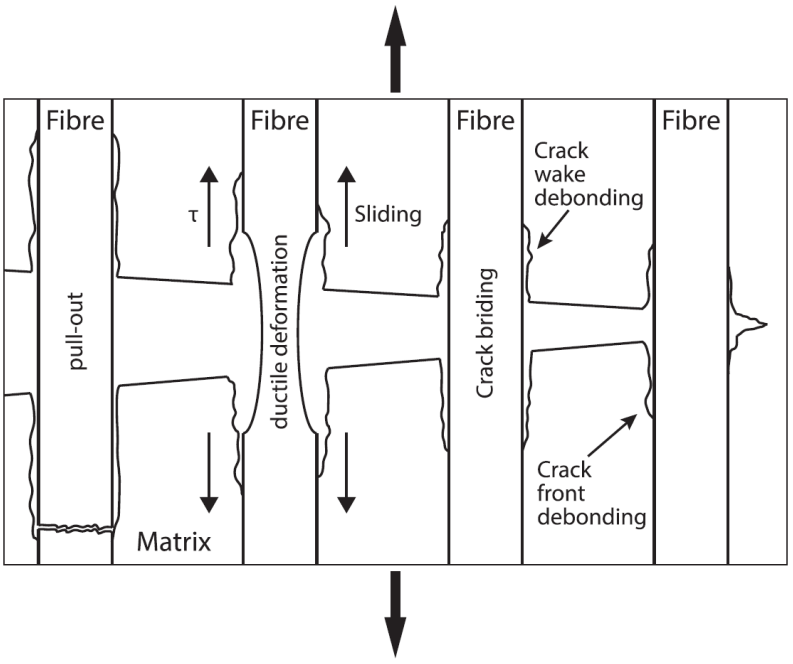

FIGURE 7.2: Possible toughening effects in fibre-reinforced composite materials [148].

fibre deformation and fibre debonding. Regarding the abovementioned extrinsic toughening effects, the nature and quality of the interface between the phases of a composite material is an important parameter that influences the overall toughness of a composite material fundamentally as it determines the fracture path and energy.

The materials investigated within the present work were not optimised with respect to their interface properties in order that toughening mechanisms as described above are fully exploited. It is furthermore questionable to what extent such extrinsic toughening mechanism occur in neutron irradiation embrittled W-Cu MMCs. Nevertheless, it can be stated that such toughening mechanism could imply an advantage if the intrinsic ductility of PFC materials cannot be maintained within a D-T fusion neutron environment. However, this topic has to be investigated through experiments that allow the judgement if such interface related toughening effects need to be exploited.

In order to contribute to the experimental investigation of neutron irradiation effects on W-Cu MMCs corresponding material samples were in the course of the present work provided for neutron irradiation experiments[1]. To that end, W_p-CuCrZr and W_f-CuCrZr material samples[2] for tensile testing with dimensions as illustrated in Figure 7.3 were manufactured. The samples were cut from plate material which was ground to the required thickness before the sample contours were cut by means of electrical discharge machining (EDM). The W_p-CuCrZr material exhibited a nominal composition of 70-

[1] neutron irradiation campaign within the EUROfusion work package materials (WPMAT), BR-2 research reactor, Mol, Belgium, irradiation dose: 1 dpa (in W), irradiation temperatures: 150 °C, 350 °C and 450 °C

[2] both materials were infiltrated with a CuCrZr matrix

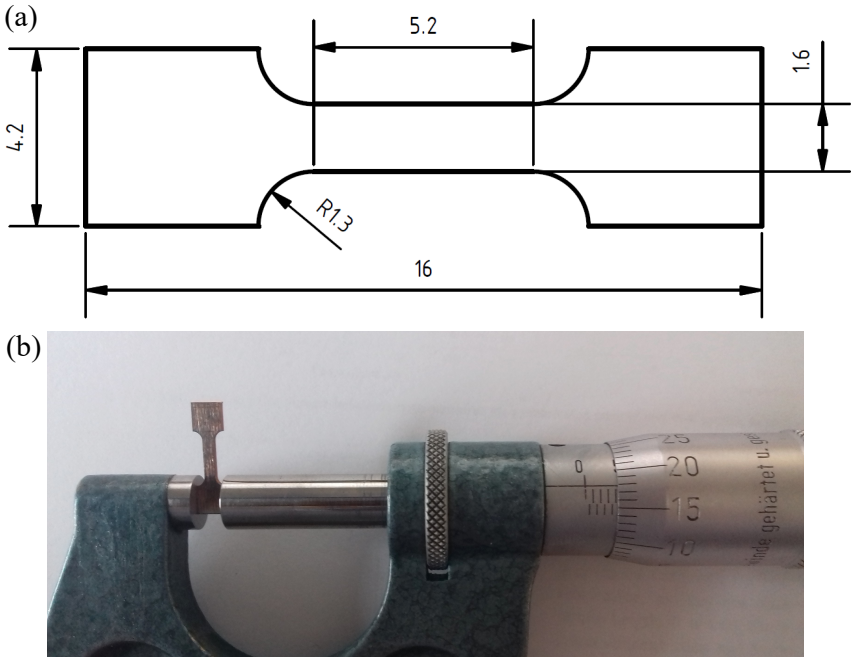

FIGURE 7.3: (a) Tensile sample dimensions and (b) a manufactured W_f-CuCrZr sample.

30wt.% W-CuCrZr. The W_f-CuCrZr material was UD reinforced with planar W fibre fabrics which in principle consisted of fibres with a diameter of 150 µm[3]. In Figure 7.4, an optical microsection of the gauge cross section of a W_f-CuCrZr tensile specimen is illustrated. Figure 7.4 shows that the W fibres are well embedded within the CuCrZr

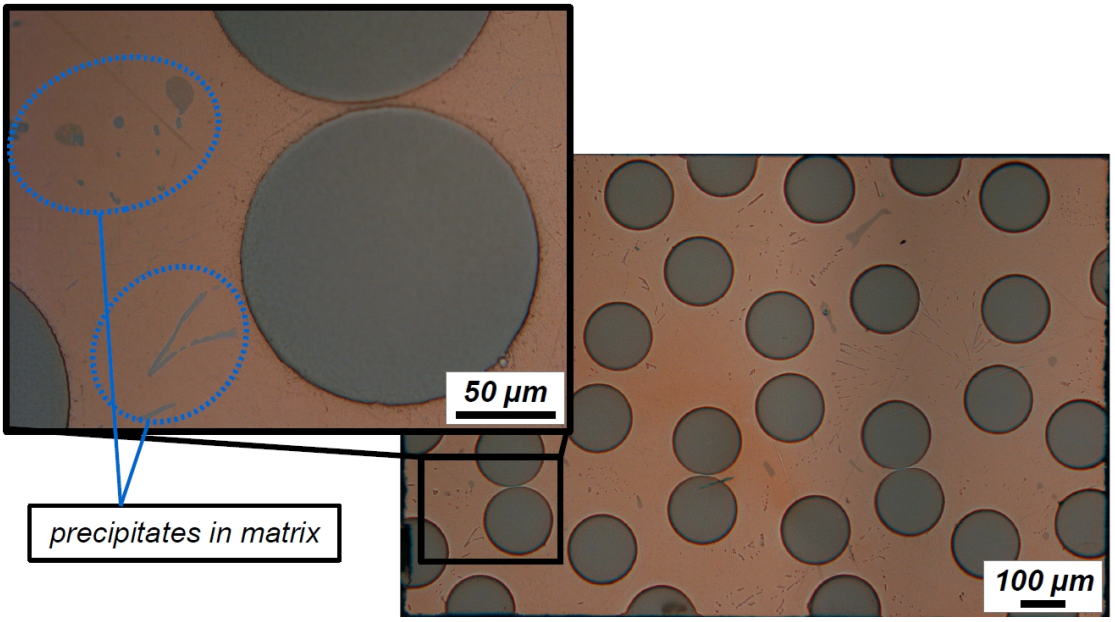

FIGURE 7.4: Optical microsection of the gauge cross section of a W_f-CuCrZr tensile specimen for neutron irradiation experiments.

[3] *Fabric 1* as described within reference [167] with a measured fibre spacing of 90 µm ± 12 µm was used for the W_f-CuCrZr sample fabrication.

matrix. Furthermore, the cross section indicates a fibre volume fraction of approximately 0.3 for the UD W fibre reinforcement. Apart from that, precipitates can be identified well within the CuCrZr matrix and are highlighted in the magnified image in Figure 7.4. In Figure 7.5, an optical microsection of the gauge cross section of a W_p-CuCrZr tensile specimen is illustrated. The two phases can clearly be distinguished while the microstructure is expectedly very similar to the ones illustrated in Figure 4.4.

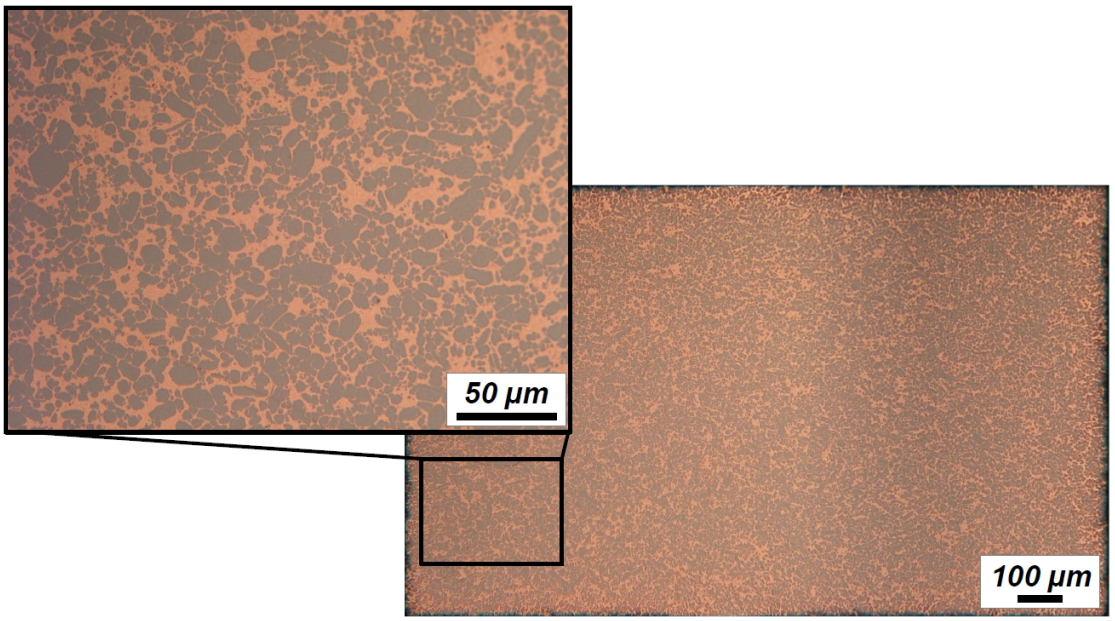

FIGURE 7.5: Optical microsection of the gauge cross section of a W_p-CuCrZr tensile specimen for neutron irradiation experiments.

7.3 Proposed future work

Several aspects have to be investigated in the future in order to forge ahead with the development of W-Cu MMCs for PFC applications in power-producing thermonuclear fusion devices. In general, the following aspects need to be considered:

- As mentioned in the previous section, it is regarded a crucially important aspect that the effects of fusion neutron irradiation on W-Cu MMCs are investigated. In this regard, it is especially important that the effects on the mechanical properties of the materials are examined.

- Moreover, the further optimisation and upscaling of industrially viable material fabrication have to be assessed.

- Furthermore, a detailed characterisation of material properties has to be conducted in order to establish a property database for W-Cu MMCs which can be used for the assessment of the materials and as input for design studies. In this context,

many different properties are actually decisive with respect to PFC applications including e.g. toughness, creep properties or details regarding failure mechanisms.

- Apart from that, reliable joining techniques for W-Cu MMCs that are applicable to divertor PFCs of future D-T fusion devices need to be qualified.
- Eventually, suitable and reliable non-destructive testing (NDT) methods for W-Cu MMCs and components comprising such materials need to be developed and qualified.

Regarding the different types of W-Cu MMCs investigated within the present work the following more specific and near term investigations are proposed:
With respect to the W_p-Cu MMCs, further material property characterisations should be performed including materials with different Cu alloy matrix materials (CuCrZr & CuCr) that exhibit different heat treatment conditions. Furthermore, possibilities to optimise and improve the joining of W_p-Cu materials to W should be investigated possibly also by exploiting the capabilities of this material class for realising functionally graded designs.
Regarding the W_f-Cu MMCs in pipe configuration, the optimisation of the fibrous W preform fabrication should be further investigated. In this regard, two aspects should be adressed. On the one hand, the possibility to produce triaxial braids with additional axial yarns should be tested in order that MMC pipes with adequate reinforcement in axial direction can be realised. Apart from that, it should in general be considered that a higher fibre volume fraction might be required in the W_f-Cu MMC pipes. This could for example be accomplished by developing and using W multifilaments with even more filaments than the yarns described within the present work. Apart from that, the upscaling of the fabrication process for W_f-Cu MMC pipes should be investigated. Within the present work, pipes with a length of approximately 200 mm were succesfully manufactured and tested. However, a full scale divertor target PFC in a future fusion reactor would most probably require longer heat sink pipes.
Regarding the short W_f-Cu material described in section 5.7, future work to further follow this material concept is proposed. In principle, short W_f-Cu could represent a viable material that combines the beneficial properties of drawn W fibres with a rather simple and straightforward material fabrication procedure. Hence, the potential of this composite should be investigated through the manufacture of material with reasonably high fibre volume fraction. Furthermore, property characterisation should be conducted in order to assess the potential of such materials.
Due to the promising results regarding the W-Cu material distribution optimisations in PFCs W_{AM}-Cu composites should be further investigated. On the one hand, the numerical optimisation procedures should be further applied and refined, e.g. by considering

more accurate boundary conditions or extension of the modelling to 3D domains. In this context, a sound experimental characterisation of W_{AM}-Cu composites is required as well in order to substantiate the optimisation results. Moreover, the translation of numerically optimised composite material distributions into manufacturable parts has to be accomplished. In this respect, the manufacturability of tailored W_{AM}-Cu MMCs has to be tested in order that a PFC mock-up comprising an optimised W_{AM}-Cu heat sink can be realised. Finally, HHF testing on such a mock-up has to be performed in order to confirm the expected beneficial features of a tailored W_{AM}-Cu MMC under HHF loading.

"It is a truism that technological development depends on advances in the field of materials."

Krishan K. Chawla

Appendix A

High-heat-flux test facility GLADIS

HHF testing represents an essential way to assess the performance of PFC materials and mock-ups under relevant thermomechanical loading conditions. Within the present work, the HHF test facility GLADIS (Garching Large Divertor Sample Test Facility) was used in this respect. GLADIS is a facility for the HHF testing of actively water cooled PFCs and is equipped with two individual ion sources for beam generation, each having a power of 1.1 MW. The main components of the facility as well as the arrangement of the ion sources are schematically illustrated in Figure A.1 [197]. The two ion sources are

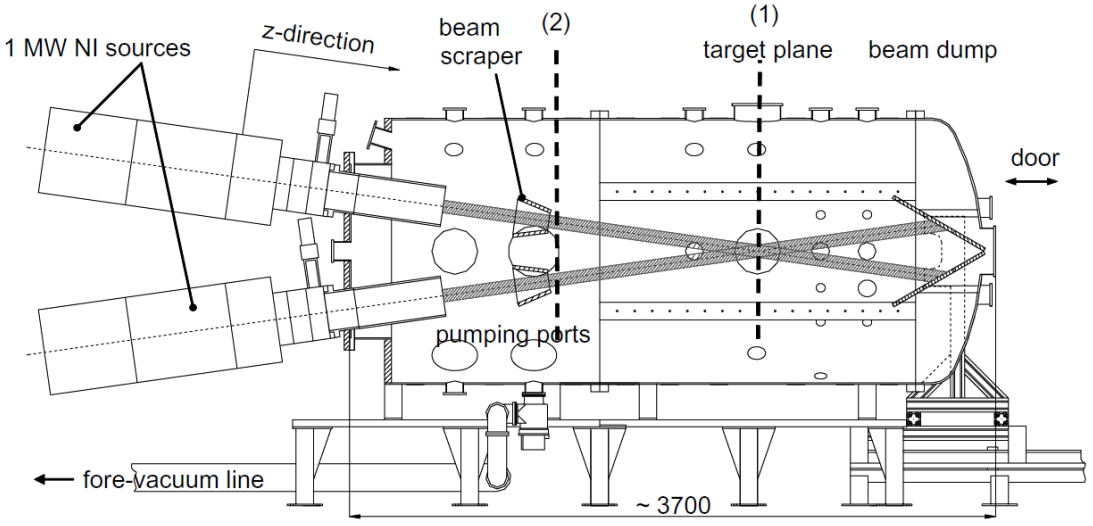

FIGURE A.1: Schematic cross section of the HHF test facility GLADIS illustrating the main components as well as the arrangement of the ion sources [197].

inclined at an angle of 8° with respect to the horizontal axis of the facility. Accordingly, the beams meet at a distance of 3 m from the ion source extraction grid. The ion sources were previously used as neutral beam heating systems in the stellarator experiment W7-AS. However, within GLADIS no ion removal system is used meaning that the beam imposing the load during HHF testing is a mixed beam of ions and neutrals. The beam profile in GLADIS is of Gaussian shape as is illustrated in Figure A.2 [197]. For further

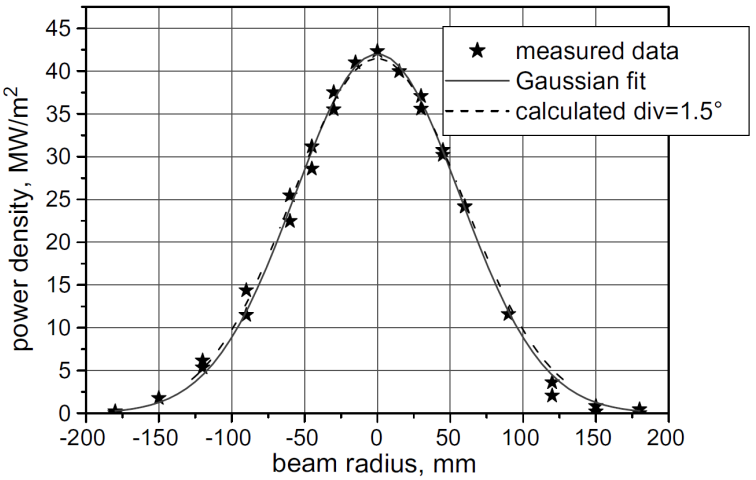

FIGURE A.2: Exemplary profile of a beam with a power of 876 kW at the target position in the HHF test facility GLADIS [197].

technical details regarding the design of GLADIS as well as important features, like diagnostics, control or data acquisition the reader is referred to [197]. In Figure A.3, a picture of GLADIS is shown [198].

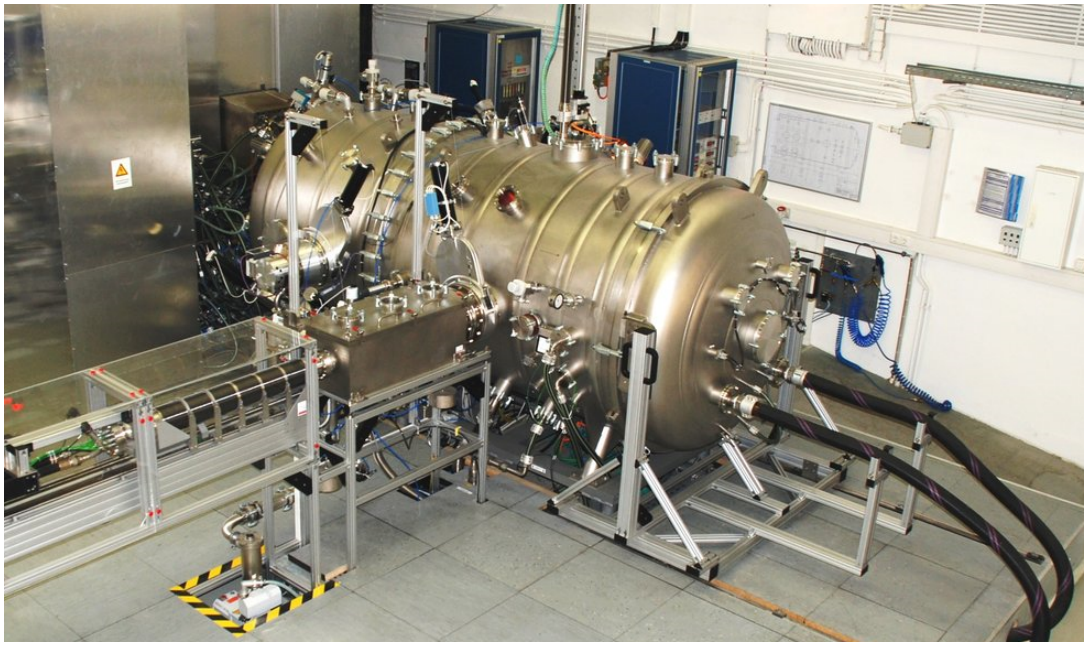

FIGURE A.3: Image of the HHF test facility GLADIS [198].

Appendix B

Numerical data and code

B.1 Thermophysical properties of W_p-Cu composites

TABLE B.1: Measured thermal diffusivity of W_p-Cu composites.

temperature [°C]	W_p-Cu 60-40wt.% [$mm^2\,s^{-1}$]	W_p-Cu 70-30wt.% [$mm^2\,s^{-1}$]	W_p-CuCrZr 70-30wt.% [$mm^2\,s^{-1}$]	W_p-Cu 85-15wt.% [$mm^2\,s^{-1}$]
50	84.09	81.42	71.08	66.67
100	81.67	80.71	71.11	65.04
150	80.80	78.35	70.31	63.54
200	78.52	76.49	68.93	62.06
250	77.07	74.88	68.23	60.95
300	75.41	73.46	67.34	59.80
350	74.24	71.91	66.21	58.60
400	73.00	70.64	65.45	57.74
450	71.68	69.24	64.44	56.52
500	70.47	67.90	63.75	55.61
550	69.10	66.43	62.67	54.75
600	67.31	64.59	61.64	53.81
650	66.59	64.26	60.58	52.78
700	65.32	63.29	59.53	51.96
750	64.28	61.67	57.74	51.06
800	62.98	60.55	56.71	50.35
850	61.38	59.37	54.82	49.68
900	60.31	58.47	53.17	49.15
950	59.59	57.30	51.00	48.29
1000	58.30	55.95	49.36	47.86

TABLE B.2: Thermal conductivity of W_p-Cu composites.

temperature [°C]	W_p-Cu 60-40wt.% [$W\,m^{-1}\,K^{-1}$]	W_p-Cu 70-30wt.% [$W\,m^{-1}\,K^{-1}$]	W_p-CuCrZr 70-30wt.% [$W\,m^{-1}\,K^{-1}$]	W_p-Cu 85-15wt.% [$W\,m^{-1}\,K^{-1}$]
50	259.18	242.26	211.96	185.09
100	254.23	242.74	214.63	182.80
150	253.36	237.37	213.77	179.86
200	248.15	233.77	211.97	177.57
250	245.69	230.75	211.59	175.77
300	242.61	228.68	211.21	174.46
350	240.82	225.63	209.35	172.23
400	238.83	223.71	209.18	171.56
450	236.33	220.93	207.56	169.12
500	235.01	219.22	207.55	168.47
550	232.09	216.01	205.67	167.01
600	228.52	212.32	204.22	166.07
650	227.91	212.93	202.06	164.07
700	225.87	211.94	200.65	163.41
750	223.93	207.99	194.82	161.60
800	221.35	205.94	192.95	160.56
850	217.69	203.87	188.31	160.12
900	215.65	202.32	184.06	159.52

TABLE B.3: Mass density of W_p-Cu composites used for the calculation of the thermal conductivity (cf. Equation 4.1) and determined according to a linear rule-of-mixture based on data from reference [121].

temperature [°C]	W_p-Cu 60-40wt.% [g cm^{-3}]	W_p-Cu 70-30wt.% [g cm^{-3}]	W_p-CuCrZr 70-30wt.% [g cm^{-3}]	W_p-Cu 85-15wt.% [g cm^{-3}]
50	13.18	14.31	14.28	16.43
100	13.16	14.29	14.26	16.42
150	13.14	14.28	14.25	16.40
200	13.12	14.25	14.22	16.38
250	13.10	14.24	14.21	16.37
300	13.08	14.22	14.19	16.35
350	13.06	14.20	14.17	16.34
400	13.03	14.17	14.15	16.32
450	13.01	14.15	14.13	16.30
500	12.99	14.13	14.12	16.28
550	12.96	14.11	14.10	16.27
600	12.93	14.09	14.07	16.24
650	12.91	14.06	14.05	16.23
700	12.88	14.04	14.03	16.21
750	12.85	14.01	14.00	16.18
800	12.82	13.98	13.97	16.16
850	12.78	13.95	13.94	16.14
900	12.75	13.92	13.91	16.12

TABLE B.4: Specific heat capacity of W_p-Cu composites used for the calculation of the thermal conductivity (cf. Equation 4.1) and determined according to a linear rule-of-mixture based on data from reference [121].

temperature [°C]	W_p-Cu 60-40wt.% [$J\,kg^{-1}\,K^{-1}$]	W_p-Cu 70-30wt.% [$J\,kg^{-1}\,K^{-1}$]	W_p-CuCrZr 70-30wt.% [$J\,kg^{-1}\,K^{-1}$]	W_p-Cu 85-15wt.% [$J\,kg^{-1}\,K^{-1}$]
50	233.93	207.95	208.84	168.97
100	236.60	210.43	211.63	171.20
150	238.65	212.21	213.41	172.58
200	240.94	214.41	216.21	174.67
250	243.38	216.47	218.27	176.18
300	246.01	218.93	221.03	178.39
350	248.43	220.96	223.09	179.89
400	251.06	223.42	225.86	182.11
450	253.44	225.43	227.91	183.59
500	256.80	228.42	230.64	186.07
550	259.15	230.40	232.73	187.53
600	262.51	233.39	235.43	190.01
650	265.20	235.62	237.37	191.60
700	268.48	238.54	240.29	194.03
750	271.16	240.77	241.05	195.61
800	274.17	243.23	243.51	197.31
850	277.41	246.12	246.40	199.72
900	280.36	248.52	248.82	201.39

TABLE B.5: Measured CTE of W_p-Cu composites.

temperature [°C]	W_p-Cu 60-40wt.% [$10^{-6}\,K^{-1}$]	W_p-Cu 70-30wt.% [$10^{-6}\,K^{-1}$]	W_p-Cu 85-15wt.% [$10^{-6}\,K^{-1}$]
100	11.60	11.24	8.40
150	11.73	11.06	8.31
200	11.87	11.04	8.40
250	12.00	11.07	8.52
300	12.10	11.10	8.57
350	12.10	11.10	8.57
400	12.10	11.03	8.57
450	12.07	11.00	8.57
500	12.10	11.00	8.58
550	12.10	11.00	8.59
600	12.07	10.93	8.60
650	12.04	10.87	8.58
700	12.13	11.03	8.52
750	12.23	11.17	8.35
800	12.36	11.33	8.18
850	12.47	11.44	8.00
900	12.57	11.58	7.84

B.2 Thermophysical properties of W_f-Cu composite

TABLE B.6: Thermal conductivity of W_f-Cu composite used for thermal FEA and determined with MFH computations as described within section 5.5 (fibre volume fraction: 0.12, fibre orientation according to braid as illustrated in Figure 5.11b).

temperature [°C]	W_f-Cu axial [$W\,m^{-1}\,K^{-1}$]	W_f-Cu hoop [$W\,m^{-1}\,K^{-1}$]	W_f-Cu radial [$W\,m^{-1}\,K^{-1}$]
20	364.91	373.25	364.51
100	358.3	366.99	357.89
200	350.65	359.73	350.22
300	342.97	352.47	342.52
400	335.71	345.46	335.25
500	328.44	338.45	327.97

TABLE B.7: Mass density of W_f-Cu composite (fibre volume fraction: 0.12) used for thermal FEA and determined according to a linear rule-of-mixture based on data from reference [121].

temperature [°C]	ρ [$g\,cm^{-3}$]
20	10.183
50	10.170
100	10.148
200	10.102
300	10.053
400	9.999
500	9.941

TABLE B.8: Specific heat capacity of W_f-Cu composite (fibre volume fraction: 0.12) used for thermal FEA and determined according to a linear rule-of-mixture based on data from reference [121].

temperature [°C]	c_p [$J\,kg^{-1}\,K^{-1}$]
20	319.348
50	321.005
100	324.320
200	329.983
300	337.077
400	344.144
500	352.611

B.3 Properties of W, pure Cu and CuCrZr

TABLE B.9: Thermophysical property data of W used for FEA and MFH analyses [59, 121].

temperature [°C]	λ [W m^{-1} K^{-1}]	ρ [g cm^{-3}]	c_p [J kg^{-1} K^{-1}]
20	173	19.30	129
50	170	19.29	130
100	165	19.28	132
150	160	19.27	133
200	156	19.25	135
250	151	19.24	136
300	147	19.23	138
350	143	19.22	139
400	140	19.20	141
450	136	19.19	142
500	133	19.18	144
550	130	19.17	145
600	127	19.15	147
650	125	19.14	148
700	122	19.13	150
750	120	19.11	151
800	118	19.10	152
850	116	19.08	154
900	114	19.07	155
950	112	19.06	156
1000	110	19.04	158
1100	108	19.01	160
1200	105	18.99	163
2000	93	-	-

TABLE B.10: Thermophysical property data of pure Cu used for FEA and MFH analyses [121].

temperature [°C]	λ [W m^{-1} K^{-1}]	ρ [g cm^{-3}]	c_p [J kg^{-1} K^{-1}]
20	401	8.940	388
50	398	8.926	390
100	395	8.903	394
150	391	8.879	398
200	388	8.854	401
250	384	8.829	406
300	381	8.802	410
350	378	8.774	415
400	374	8.744	419
450	371	8.713	424
500	367	8.681	430
550	364	8.647	435
600	360	8.612	441
650	357	8.575	447
700	354	8.536	453
750	350	8.495	459
800	347	8.453	466
850	344	8.409	472
900	340	8.363	479
950	337	-	487
1000	334	-	494

TABLE B.11: Thermophysical property data of CuCrZr used for MFH analyses [121].

temperature [°C]	λ [W m^{-1} K^{-1}]	ρ [g cm^{-3}]	c_p [J kg^{-1} K^{-1}]
20	318	8.900	390
400	347	8.716	427
500	346	8.665	437

TABLE B.12: Thermomechanical property data of W fibre used for MFH analyses [121].

temperature [°C]	CTE [10^{-6} K^{-1}]	Young's modulus [MPa]	Yield stress [MPa]	Hardening modulus [MPa]	Hardening exponent [-]
20	4.5	398	1596.7	1120.48	392.267
400	4.63	393	-	-	-

TABLE B.13: Thermomechanical property data of pure Cu used for MFH analyses [121].

temperature [°C]	CTE [10^{-6} K^{-1}]	Young's modulus [MPa]	Yield stress [MPa]	Hardening modulus [MPa]	Hardening exponent [-]
20	16.7	117	30.0	103.67	0.24013
400	18.2	98	-	-	-

TABLE B.14: Thermomechanical property data of CuCrZr used for MFH analyses [121].

temperature [°C]	CTE [10^{-6} K^{-1}]	Young's modulus [MPa]	Yield stress [MPa]	Hardening modulus [MPa]	Hardening exponent [-]
20	16.7	127.5	200.3	215.02	0.27256
400	18.1	113	-	-	-

Furthermore, a temperature-independent Poisson's ratio of 0.33 was used for pure Cu and CuCrZr as well as 0.29 for W.

B.4 Heat transfer coefficients used for thermal FEA

TABLE B.15: Heat transfer coefficient as a function of cooling channel wall temperature for cold-water cooling conditions ($T_{in} = 20\,°C$, $p_{static} = 10\,bar$, $v = 12\,m\,s^{-1}$, swirl tape insert with twist ratio of 2 and tape thickness of 0.8 mm).

wall temperature [°C]	heat transfer coefficient [$W\,m^{-2}\,K^{-1}$]
20	52.20
60	58.41
100	62.91
140	66.08
180	75.09
220	97.89
260	198.87
278.63	311.52

TABLE B.16: Heat transfer coefficient as a function of cooling channel wall temperature for cold-water cooling conditions ($T_{in} = 20\,°C$, $p_{static} = 10\,bar$, $v = 16\,m\,s^{-1}$, swirl tape insert with twist ratio of 2 and tape thickness of 0.8 mm).

wall temperature [°C]	heat transfer coefficient [$W\,m^{-2}\,K^{-1}$]
20	65.71
60	73.52
100	79.19
140	83.18
180	94.52
220	121.16
260	210.97
282.91	349.98

TABLE B.17: Heat transfer coefficient as a function of cooling channel wall temperature for hot-water cooling conditions ($T_{in} = 130\,°C$, $p_{in} = 40\,bar$, $v = 16\,m\,s^{-1}$, swirl tape insert with twist ratio of 2 and tape thickness of 0.8 mm).

wall temperature [°C]	heat transfer coefficient [$W\,m^{-2}\,K^{-1}$]
130	144.70
160	149.11
190	152.98
220	156.42
250	159.76
280	179.43
302.81	266.90

B.5 Code for heat transfer coefficient calculation

```
clear all
close all
clc
% Geometry %
pipe_inner_diameter = 1.2e-2; % [m]
t_tape = 0.8*(10^(-3)); % thickness of twisted tape [m]
twist_ratio = 2;
% Coolant conditions %
coolant_vel = 16; % average coolant velocity [m/s]
T = 403.15; % coolant temperature [K]
p = 4.0e6; % coolant pressure [Pa]
disp(['--> pipe inner diameter = ', num2str(pipe_inner_diameter), ' m']);
disp(['--> twist ratio = ', num2str(twist_ratio)]);
disp(['--> tape thickness = ', num2str(t_tape), ' m']);
disp(['--> coolant velocity = ', num2str(coolant_vel), ' m/s']);
disp(['--> coolant temperature = ', num2str(T), ' K']);
disp(['--> coolant pressure = ', num2str(p), ' Pa']);
% critical properties water (VDI-Waermeatlas, 2013, ISBN 9783642199813)
T_critical = 647.096; % [K]
p_critical = 220.64e5; % [Pa]
rho_critical = 322; % [kg m^-3]
[rho,lambda,dynamic_visc,kinematic_visc,Pr,cp,h] = waterprop(T,p); % determine↙
properties of water
[T_sat,rho_l,rho_g,h_l,h_g,s_l,s_g,cp_l,cp_g,dynamic_visc_l,dynamic_visc_g,↙
kinematic_visc_l,kinematic_visc_g] = waterprop_equilibrium(p); % determine equilibrium↙
properties of water
T_sub = T_sat - T; % subcooling [K]
h_vap = h_g - h_l; % enthalpy of vapourisation at given pressure [kJ kg^-1]
disp(['--> Prandtl number = ', num2str(Pr)]);
disp(['--> saturation temperature = ', num2str(T_sat), ' K']);
disp(['--> subcooling = ', num2str(T_sub), ' K']);
xsection = (pi*((pipe_inner_diameter/2)^2)) - (pipe_inner_diameter*t_tape); % cross↙
section [m^2]
k = sqrt((1+((pi/(2*twist_ratio))^2))); % swirl correction factor
disp(['--> flow area = ', num2str(xsection), ' m^2']);
disp(['--> swirl correction factor = ', num2str(k)]);
d_swirl = 4*((((pi*(pipe_inner_diameter^2))/4) - (t_tape*pipe_inner_diameter))/↙
((pi*pipe_inner_diameter) + (2*pipe_inner_diameter) - (2*t_tape))); % hydraulic↙
diameter [m]
disp(['--> hydraulic diameter = ', num2str(d_swirl), ' m']);
vel_swirl = coolant_vel*k; % swirl corrected velocity
Re_swirl = (rho*vel_swirl*d_swirl)/dynamic_visc; % swirl Reynolds number [-]
Re = (rho*coolant_vel*d_swirl)/dynamic_visc; % Reynolds number [-]
massflow = rho*xsection*coolant_vel; % [kg/s]
massflow_density = massflow/xsection; % [kg/s m^2]
disp(['--> mass flow = ', num2str(massflow), ' kg/s']);
disp(['--> mass flow density = ', num2str(massflow_density), ' kg/s m^2']);
disp(['--> Reynolds number = ', num2str(Re)]);
disp(['--> swirl Reynolds number = ', num2str(Re_swirl)]);
% The following correlations are taken from:
% Dimensional analysis of critical heat flux in subcooled water flow under one-side↙
heating conditions for fusion application,
% J. Boscary et al., Fusion Engineering and Design 43 (1998) 147-171
% Comparison between various thermal hydraulic tube concepts for the ITER divertor,
% I. Smid, J. Schlosser, J. Boscary, F. Escourbiac, G. Vieider, Fusion Technology 1996,↙
Pages 263-266, ISBN 9780444827623
i = 1;
for T_wall = T:1:673.15
    [rho_wall,lambda_wall,dynamic_visc_wall,kinematic_visc_wall,Pr_wall,cp_wall,h_wall]↙
= waterprop(T_wall,p); % determine properties of water at wall temperature
```

```
    Nu_fc = 1.15*0.027*((dynamic_visc/dynamic_visc_wall)^0.14)*(Re_swirl^0.8)*(Pr^↙
(1/3)); % Nusselt number [-]
    h_fc = (Nu_fc*lambda)/d_swirl; % forced convection heat transfer coefficient [W/m^2↙
K]
    T_wall_fc(i) = T_wall;
    htc_fc(i) = h_fc;
    hf_fc(i) = h_fc*(T_wall - T); % forced convection heat flux [W/m^2]
    i = i + 1;
end
j = 1;
hf_onb_bosc = 0;
hf_fc_comp = 1;
T_wall = T_sat;
while hf_onb_bosc <= hf_fc_comp
    hf_scb = 1e6*(((T_wall-T_sat)/(22.65*(exp(-(p/8700000)))))^2.8); % subcooled↙
boiling heat flux [W/m^2]
    htc_scb = hf_scb/(T_wall-T); % subcooled boiling heat transfer coefficient [W/m^2↙
K]
    hf_onb_bosc = 1082*((p/1e7)^1.156)*(((T_wall-T_sat)/0.556)^(1/(0.463*((p/1e7)^0.↙
0234)))); % nucleate boiling heat flux [W/m^2]
    hf_fc_comp = interp1(T_wall_fc, hf_fc, T_wall);
    hf_scb_vec(j) = hf_scb;
    hf_onb_bosc_vec(j) = hf_onb_bosc;
    htc_scb_vec(j) = htc_scb;
    hf_boil(j) = hf_scb - hf_onb_bosc;
    hf_fc_sum = interp1(T_wall_fc,hf_fc,T_wall);
    hf_sum(j) = sqrt(((hf_fc_sum)^2) + ((hf_boil(j))^2)); % heat flux [W/m^2]
    htc_sum(j) = hf_sum(j)/(T_wall-T); % heat transfer coefficient [W/m^2 K]
    T_wall_sum(j) = T_wall;
    T_onb = T_wall;
    j = j + 1;
    T_wall = T_wall + 1;
end
j = 1;
for T_wall = T_sat:1:673.15
    hf_scb = 1e6*(((T_wall-T_sat)/(22.65*(exp(-(p/8700000)))))^2.8); % subcooled↙
boiling heat flux [W/m^2]
    htc_scb = hf_scb/(T_wall-T); % subcooled boiling heat transfer coefficient [W/m^2↙
K]
    hf_scb_vec(j) = hf_scb;
    htc_scb_vec(j) = htc_scb;
    T_wall_scb(j) = T_wall;
    j = j + 1;
end
T_wall_conc = [[T:1:T_onb] [(T_onb+1):1:673.15]];
hf_conc = [hf_fc(T_wall_fc <= T_sat) hf_sum(T_wall_sum > T_sat) hf_scb_vec(T_wall_scb >↙
T_onb)];
htc_conc = [htc_fc(T_wall_fc <= T_sat) htc_sum(T_wall_sum > T_sat) htc_scb_vec↙
(T_wall_scb > T_onb)];
Ja = (rho_l/rho_g)*(cp*T_sub/h_vap); % Jakob number [-]
Bo_crit_Tong_uniform_swirl = 1.84*((d_swirl/(12.7e-3))^0.32)*(Re^(-0.6))*(1 + (0.00216*↙
((p/p_critical)^(1.8)))*(Re^(0.5))*Ja); % Boiling number [-]
wchf_Tong_uniform_swirl = Bo_crit_Tong_uniform_swirl*(coolant_vel*rho*h_vap);
wchf_Tong_oneside_swirl = 1.67*Bo_crit_Tong_uniform_swirl*(coolant_vel*rho*h_vap); %↙
critical heat flux [W/m^2]
disp(['--> critical heat flux = ', num2str(wchf_Tong_oneside_swirl), ' W/m^2']);
T_wall_critical = interp1(hf_conc,T_wall_conc,wchf_Tong_oneside_swirl);
htc_critical = wchf_Tong_oneside_swirl/(T_wall_critical - T);
hf_conc = hf_conc(hf_conc < wchf_Tong_oneside_swirl);
hf_conc = [hf_conc wchf_Tong_oneside_swirl];
```

```
T_wall_conc = T_wall_conc(hf_conc < wchf_Tong_oneside_swirl);
T_wall_conc = [T_wall_conc T_wall_critical];
htc_conc = htc_conc(hf_conc < wchf_Tong_oneside_swirl);
htc_conc = [htc_conc htc_critical];
disp('--------------------');
disp('wall temperature [K]: ');
disp(num2str(T_wall_conc'));
disp('--------------------');
htc_conc = htc_conc./1000;
disp('heat transfer coefficient [W/m^2K]: ');
disp(num2str(htc_conc'));
disp('--------------------');
disp('heat flux [W/m^2]: ');
disp(num2str(hf_conc'));
% plot %
figure1 = figure;
subplot1 = subplot(2,1,1,'Parent',figure1,'YGrid','on','XGrid','on');
box(subplot1,'on');
hold(subplot1,'all');
plot((T_wall_conc),hf_conc,'Parent',subplot1,'LineWidth',2.5,...
    'Color',[0 0.200000002980232 0.600000023841858])
ylabel('heat flux [W/m^2]');
subplot2 = subplot(2,1,2,'Parent',figure1,'YGrid','on','XGrid','on');
box(subplot2,'on');
hold(subplot2,'all');
plot((T_wall_conc),htc_conc,'Parent',subplot2,'LineWidth',2.5,...
    'Color',[0 0.200000002980232 0.600000023841858])
xlabel('wall temperature [K]');
ylabel('heat transfer coefficient [W/m^2K]');
```

Bibliography

[1] International Energy Agency, *World Energy Outlook 2015*. OECD/IEA, 2015, ISBN 978-92-64-24366-8. [Online]. Available: https://doi.org/10.1787/weo-2015-en

[2] *BP Statistical Review of World Energy 2018, 67th edition*, BP p.l.c., London, June 2018.

[3] International Energy Agency, *World Energy Outlook 2016*. OECD/IEA, 2016, ISBN 978-92-64-26495-3. [Online]. Available: https://doi.org/10.1787/weo-2016-en

[4] B.R. Martin, *Nuclear and Particle Physics*. John Wiley & Sons, 2006, ISBN 978-0-470-01999-3. [Online]. Available: https://doi.org/10.1002/0470035471

[5] A. Kamal, *Nuclear Physics*. Springer, 2014, ISBN 978-3-642-38654-1. [Online]. Available: https://doi.org/10.1007/978-3-642-38655-8

[6] E. Teller (Ed.), *Fusion, Volume 1, Magnetic Confinement, Part A*. Academic Press, 1981, ISBN 0-12-685201-4.

[7] K.S. Krane, *Introductory Nuclear Physics*. John Wiley & Sons, 1988, ISBN 0-471-80553-X.

[8] R.A. Gross, *Fusion Energy*. John Wiley & Sons, 1984, ISBN 0-471-88470-7.

[9] G.M. McCracken and P.E. Stott, *Fusion: The Energy of the Universe*, 2nd ed. Academic Press, 2012, ISBN 978-0-12-384656-3.

[10] W. Fundamenski, *Power Exhaust in Fusion Plasmas*. Cambridge University Press, 2010, ISBN 978-1-107-42421-0. [Online]. Available: https://doi.org/10.1017/CBO9780511770609

[11] P. Atkins and R. Friedman, *Molecular Quantum Mechanics*, 4th ed. Oxford University Press, 2008, ISBN 9780199274987.

[12] A. Piel, *Plasma physics - An Introduction to Laboratory, Space, and Fusion Plasmas*. Springer, 2010, ISBN 978-3-642-10490-9. [Online]. Available: https://doi.org/10.1007/978-3-642-10491-6

[13] W.M. Stacey, *Fusion - An Introduction to the Physics and Technology of Magnetic Confinement Fusion*. John Wiley & Sons, 1984, ISBN 0-471-88079-5.

[14] EUROfusion. [Online]. Available: https://www.euro-fusion.org/wpcms/wp-content/uploads/2013/08/CP13j-033-005-e1456216897771.jpg [accessed: 23-06-2017].

[15] EUROfusion. [Online]. Available: https://www.euro-fusion.org/wpcms/wp-content/uploads/2016/06/CP82j-348.jpg [accessed: 23-06-2017].

[16] P.H. Rebut and B.E. Keen, "The JET Experiment: Evolution, Present Status, and Prospects," *Fusion Technology*, vol. 11, no. 1, pp. 13–42, 1987. [Online]. Available: https://doi.org/10.13182/FST87-A24999

[17] M. Keilhacker et al., "High fusion performance from deuterium-tritium plasmas in JET," *Nuclear Fusion*, vol. 39, no. 2, pp. 209–234, 1999. [Online]. Available: https://doi.org/10.1088/0029-5515/39/2/306

[18] Max-Planck-Institut für Plasmaphysik. [Online]. Available: http://www.ipp.mpg.de/3894376/zoom-1436253890.jpg [accessed: 20-09-2017].

[19] Max-Planck-Institut für Plasmaphysik. [Online]. Available: http://www.ipp.mpg.de/2535674/zoom-1389887533.jpg [accessed: 20-09-2017].

[20] H.-S. Bosch et al., "Technical challenges in the construction of the steady-state stellarator Wendelstein 7-X," *Nuclear Fusion*, vol. 53, no. 12, p. 126001, 2013. [Online]. Available: https://doi.org/10.1088/0029-5515/53/12/126001

[21] H.-S. Bosch et al., "Final integration, commissioning and start of the Wendelstein 7-X stellarator operation," *Nuclear Fusion*, vol. 57, no. 11, p. 116015, 2017. [Online]. Available: https://doi.org/10.1088/1741-4326/aa7cbb

[22] A. Dinklage et al., "Magnetic configuration effects on the Wendelstein 7-X stellarator," *Nature Physics*, vol. 14, pp. 855–860, 2018. [Online]. Available: https://doi.org/10.1038/s41567-018-0141-9

[23] International Energy Agency, *World Energy Outlook 2017*. OECD/IEA, 2017, ISBN 978-92-64-28230-8. [Online]. Available: https://doi.org/10.1787/weo-2017-en

[24] D. Huy, M. Liedtke, C. Rongguo, G. Juan, Y. Liwen, *Supply and Demand of Lithium and Gallium*. Bundesanstalt für Geowissenschaften und Rohstoffe (BGR, Germany), Information Center of Ministry of Land and Resources (ICMLR, China), 2016, ISBN 978-3-943566-33-8.

[25] P.H. Rebut, "Perspectives on nuclear fusion," *Energy*, vol. 18, no. 10, pp. 1023–1031, 1993. [Online]. Available: https://doi.org/10.1016/0360-5442(93)90051-E

[26] A.A. Harms et al., *Principles of Fusion Energy: An Introduction to Fusion Energy for Students of Science and Engineering*. World Scientific, 2000, ISBN 981-02-4335-9.

[27] Max-Planck-Institut für Plasmaphysik. [Online]. Available: https://www.ipp.mpg.de/15144/zuendbedingungen [accessed: 17-04-2019].

[28] International Fusion Research Council (IFRC), "Status report on fusion research," *Nuclear Fusion*, vol. 45, no. 10A, pp. A1–A28, 2005. [Online]. Available: https://doi.org/10.1088/0029-5515/45/10A/001

[29] ASDEX Team, "The H-Mode of ASDEX," *Nuclear Fusion*, vol. 29, no. 11, pp. 1959–2040, 1989. [Online]. Available: https://doi.org/10.1088/0029-5515/29/11/010

[30] F. Wagner, "A quarter-century of H-mode studies," *Plasma Physics and Controlled Fusion*, vol. 49, no. 12B, pp. B1–B33, 2007. [Online]. Available: https://doi.org/10.1088/0741-3335/49/12B/S01

[31] ITER Physics Expert Group on Confinement and Transport et al., "Chapter 2: Plasma confinement and transport," *Nuclear Fusion*, vol. 39, no. 12, pp. 2175–2249, 1999. [Online]. Available: https://doi.org/10.1088/0029-5515/39/12/302

[32] M. Shimada et al., "Progress in the ITER Physics Basis - Chapter 1: Overview and summary," *Nuclear Fusion*, vol. 47, no. 6, pp. S1–S17, 2007. [Online]. Available: https://doi.org/10.1088/0029-5515/47/6/S01

[33] B. Bigot, "Nuclear Physics: Pull together for fusion," *Nature*, vol. 522, pp. 149–151, 2015. [Online]. Available: https://doi.org/10.1038/522149a

[34] J. Schwemmer, "Fusion: Abundant, Safe and Sustainable Energy for the Future," in *Climate Change – The New Economy, The United Nations Climate Change Conference - COP24 & CMP14*, G. Nichols-Roth, Ed., Katowice, Poland, 2–14 December 2018, pp. 42–45.

[35] ITER Organization. [Online]. Available: https://www.iter.org/proj/inafewlines [Accessed: 27-08-2018].

[36] ITER Organization. [Online]. Available: https://www.iter.org/img/resize-2000-70/all/content/com/gallery/media/7%20-%20technical/2009_04_29%20machine.jpg [Accessed: 28-10-2018].

[37] R. Aymar et al., "The ITER design," *Plasma Physics and Controlled Fusion*, vol. 44, no. 5, pp. 519–565, 2002. [Online]. Available: https://doi.org/10.1088/0741-3335/44/5/304

[38] ITER Organization. [Online]. Available: https://www.iter.org/sci/Goals [accessed: 27-08-2018].

[39] European Fusion Development Agreement (EFDA), "Fusion Electricity - A roadmap to the realisation of fusion energy," 2012, ISBN 978-3-00-040720-8.

[40] G. Federici et al., "DEMO design activity in Europe: Progress and updates," *Fusion Engineering and Design*, vol. 136, pp. 729–741, 2018. [Online]. Available: https://doi.org/10.1016/j.fusengdes.2018.04.001

[41] EUROfusion, "European Research Roadmap to the Realisation of Fusion Energy," 2018, ISBN 978-3-00-061152-0.

[42] J. Ongena et al., "Magnetic-confinement fusion," *Nature Physics*, vol. 34, pp. 398–410, 2016. [Online]. Available: https://doi.org/10.1038/nphys3745

[43] A. Kallenbach et al., "Tokamak operation with high-z plasma facing components," *Plasma Physics and Controlled Fusion*, vol. 47, no. 12B, pp. B207–B222, 2005. [Online]. Available: https://doi.org/10.1088/0741-3335/47/12B/S16

[44] R. Neu, "High-Z plasma facing components in fusion devices: boundary conditions and operational experiences," *Physica Scripta*, vol. T123, pp. 33–44, 2006. [Online]. Available: https://doi.org/10.1088/0031-8949/2006/T123/005

[45] F. Wagner et al., "Regime of Improved Confinement and High Beta in Neutral-Beam-Heated Divertor Discharges of the ASDEX Tokamak," *Phys. Rev. Lett.*, vol. 49, pp. 1408–1412, 1982. [Online]. Available: https://doi.org/10.1103/PhysRevLett.49.1408

[46] T.R. Barrett et al., "Progress in the engineering design and assessment of the European DEMO first wall and divertor plasma facing components," *Fusion Engineering and Design*, vol. 109-111, pp. 917–924, 2016. [Online]. Available: https://doi.org/10.1016/j.fusengdes.2016.01.052

[47] B. LaBombard et al., "Scaling of the power exhaust channel in Alcator C-Mod," *Physics of Plasmas*, vol. 18, p. 056104, 2011. [Online]. Available: https://doi.org/10.1063/1.3566059

[48] T. Eich et al., "Scaling of the tokamak near the scrape-off layer H-mode power width and implications for ITER," *Nuclear Fusion*, vol. 53, no. 9, p. 093031, 2013. [Online]. Available: https://doi.org/10.1088/0029-5515/53/9/093031

[49] A. Loarte and R. Neu, "Power exhaust in tokamaks and scenario integration issues," *Fusion Engineering and Design*, vol. 122, pp. 256–273, 2017. [Online]. Available: https://doi.org/10.1016/j.fusengdes.2017.06.024

[50] T. Hirai et al., "Use of tungsten material for the ITER divertor," *Nuclear Materials and Energy*, vol. 9, pp. 616–622, 2016. [Online]. Available: https://doi.org/10.1016/j.nme.2016.07.003

[51] J.H. You et al., "Conceptual design studies for the European DEMO divertor: Rationale and first results," *Fusion Engineering and Design*, vol. 109-111, pp. 1598–1603, 2016. [Online]. Available: https://doi.org/10.1016/j.fusengdes.2015.11.012

[52] J.H. You et al., "European divertor target concepts for DEMO: Design rationales and high heat flux performance," *Nuclear Materials and Energy*, vol. 16, pp. 1–11, 2018. [Online]. Available: https://doi.org/10.1016/j.nme.2018.05.012

[53] R.J. Quentmeyer, "Experimental Fatigue Life Investigation of Cylindrical Thrust Chambers, Technical Memorandum X-73665," NASA, Tech. Rep., 1977.

[54] K. Strauß, *Kraftwerkstechnik zur Nutzung fossiler, nuklearer und regenerativer Energiequellen*, 6th ed. Springer, 2009, ISBN 978-3-642-01430-7. [Online]. Available: https://doi.org/10.1007/978-3-642-01431-4

[55] J.K. Shultis and R.E. Faw, *Fundamentals of Nuclear Science and Engineering*. Marcel Dekker, 2002, ISBN 0-8247-0834-2.

[56] H. Zohm, "Assessment of DEMO challenges in technology and physics," *Fusion Engineering and Design*, vol. 88, no. 6-8, pp. 428–433, 2013. [Online]. Available: https://doi.org/10.1016/j.fusengdes.2013.01.001

[57] D. Naujoks, *Plasma-Material Interaction in Controlled Fusion*. Springer, 2006, ISBN 978-3-540-32148-4. [Online]. Available: https://doi.org/10.1007/3-540-32149-7

[58] R.E.H. Clark and D.H. Reiter, *Nuclear Fusion Research - Understanding Plasma-Surface Interactions*. Springer, 2005, ISBN 3-540-23038-6.

[59] C.J. Smithells, *Metals Reference Book*, 5th ed. Butterworths, 1976, ISBN 0408706279.

[60] E. Lassner and W.-D. Schubert, *Tungsten - Properties, Chemistry, Technology of the Element, Alloys, and Chemical Compounds*. Springer, 1999, ISBN 978-1-4613-7225-7. [Online]. Available: https://doi.org/10.1007/978-1-4615-4907-9

[61] D. Stork et al., "Developing structural, high-heat flux and plasma facing materials for a near-term DEMO fusion power plant: The EU assessment," *Journal of Nuclear Materials*, vol. 455, no. 1-3, pp. 277–291, 2014. [Online]. Available: https://doi.org/10.1016/j.jnucmat.2014.06.014

[62] J. Roth et al., "Recent analysis of key plasma wall interactions issues for ITER," *Journal of Nuclear Materials*, vol. 390-391, pp. 1–9, 2009. [Online]. Available: https://doi.org/10.1016/j.jnucmat.2009.01.037

[63] R. Neu et al., "The tungsten divertor experiment at ASDEX Upgrade," *Plasma Physics and Controlled Fusion*, vol. 38, no. 12A, p. A165, 1996. [Online]. Available: https://doi.org/10.1088/0741-3335/38/12A/013

[64] R. Neu, "Tungsten as a plasma facing material in fusion devices," Habilitationsschrift, Eberhard-Karls-Universität zu Tübingen, 2003.

[65] R. Neu et al., "Tungsten experiences in ASDEX Upgrade and JET," in *Proceedings of IEEE 25th Symposium on Fusion Engineering (SOFE)*, San Francisco, CA, USA, 10–14 June 2013. [Online]. Available: https://doi.org/10.1109/SOFE.2013.6635302

[66] S.J. Zinkle, "Applicability of copper alloys for DEMO high heat flux components," *Physica Scripta*, vol. 2016, no. T167, p. 014004, 2016. [Online]. Available: https://doi.org/10.1088/0031-8949/2015/T167/014004

[67] G. Federici et al., "European DEMO design strategy and consequences for materials," *Nuclear Fusion*, vol. 57, no. 9, p. 092002, 2017. [Online]. Available: https://doi.org/10.1088/1741-4326/57/9/092002

[68] C. Linsmeier et al., "Development of advanced high heat flux and plasma-facing materials," *Nuclear Fusion*, vol. 57, no. 9, p. 092007, 2017. [Online]. Available: https://doi.org/10.1088/1741-4326/aa6f71

[69] R.A. Pitts et al., "Physics conclusions in support of ITER W divertor monoblock shaping," *Nuclear Materials and Energy*, vol. 12, pp. 60–74, 2017. [Online]. Available: https://doi.org/10.1016/j.nme.2017.03.005

[70] P. Gavila et al., "High heat flux testing of EU tungsten monoblock mock-ups for the ITER divertor," *Fusion Engineering and Design*, vol. 98-99, pp. 1305–1309, 2015. [Online]. Available: https://doi.org/10.1016/j.fusengdes.2014.12.006

[71] G. Pintsuk et al., "Characterization of ITER tungsten qualification mock-ups exposed to high cyclic thermal loads," *Fusion Engineering and Design*, vol. 98-99, pp. 1384–1388, 2015. [Online]. Available: https://doi.org/10.1016/j.fusengdes.2015.01.037

[72] Fusion for Energy. [Online]. Available: http://fusionforenergy.europa.eu/mediacorner/newsview.aspx?content=1240 [accessed: 15-10-2018].

[73] G. Federici et al., "Overview of EU DEMO design and R&D activities," *Fusion Engineering and Design*, vol. 89, no. 7, pp. 882–889, 2014. [Online]. Available: https://doi.org/10.1016/j.fusengdes.2014.01.070

[74] M. Rieth and A. Hoffmann, "Influence of microstructure and notch fabrication on impact bending properties of tungsten materials," *International Journal of Refractory Metals and Hard Materials*, vol. 28, no. 6, pp. 679–686, 2010. [Online]. Available: https://doi.org/10.1016/j.ijrmhm.2010.04.010

[75] J. Boscary et al., "Design improvement of the target elements of Wendelstein 7-X divertor," *Fusion Engineering and Design*, vol. 87, no. 7, pp. 1453–1456, 2012. [Online]. Available: https://doi.org/10.1016/j.fusengdes.2012.03.034

[76] M. Matsukawa et al., "Status of JT-60SA tokamak under the EU-JA Broader Approach Agreement," *Fusion Engineering and Design*, vol. 83, no. 7, pp. 795–803, 2008. [Online]. Available: https://doi.org/10.1016/j.fusengdes.2008.06.047

[77] M. Missirlian et al., "The WEST project: Current status of the ITER-like tungsten divertor," *Fusion Engineering and Design*, vol. 89, no. 7, pp. 1048–1053, 2014. [Online]. Available: https://doi.org/10.1016/j.fusengdes.2014.01.050

[78] Deutsches Kupferinstitut, "Werkstoff-Datenblatt CuCr1Zr - CW106C (2.1293)," 2005. [Online]. Available: https://www.kupferinstitut.de/fileadmin/user_upload/kupferinstitut.de/de/Documents/Shop/Verlag/Downloads/Werkstoffe/Datenblaetter/Niedriglegierte/CuCr1Zr.pdf

[79] M. Li and S.J. Zinkle, "Physical and Mechanical Properties of Copper and Copper Alloys," in *Comprehensive Nuclear Materials*, R.J.M. Konings, Ed. Elsevier, 2012, ch. 4, pp. 667–690, ISBN 978-0-08-056033-5. [Online]. Available: https://doi.org/10.1016/B978-0-08-056033-5.00122-1

[80] S.A. Fabritsiev et al., "Neutron spectrum and transmutation effects on the radiation damage of copper alloys," *Fusion Engineering and Design*, vol. 36, no. 4, pp. 505–513, 1997. [Online]. Available: https://doi.org/10.1016/S0920-3796(96)00700-4

[81] F.A. Garner et al., "Response of solute and precipitation strengthened copper alloys at high neutron exposure," *Journal of Nuclear Materials*, vol. 191-194, pp. 386–390, 1992. [Online]. Available: https://doi.org/10.1016/S0022-3115(09)80072-X

[82] K.K. Chawla, *Composite Materials: Science and Engineering*, 3rd ed. Springer, 2013, ISBN 978-0-387-74364-6. [Online]. Available: https://doi.org/10.1007/978-0-387-74365-3

[83] R.E Shalin (Ed.), *Polymer Matrix Composites*. Chapman & Hall, 1995, ISBN 978-94-010-4229-1. [Online]. Available: https://doi.org/10.1007/978-94-011-0515-6

[84] D. Hull and T.W. Clyne, *An Introduction to Composite Materials*, 2nd ed. Cambridge University Press, 1996, ISBN 0-521-38855-4. [Online]. Available: https://doi.org/10.1017/CBO9781139170130

[85] N. Chawla and K.K. Chawla, *Metal Matrix Composites*, 2nd ed. Springer, 2013, ISBN 978-1-4614-9547-5. [Online]. Available: https://doi.org/10.1007/978-1-4614-9548-2

[86] U.G.K. Wegst et al., "Bioinspired structural materials," *Nature Materials*, vol. 14, pp. 23–36, 2015. [Online]. Available: https://doi.org/10.1038/nmat4089

[87] S. Mannan et al., "Correlations between axial stiffness and microstructure of a species of bamboo," *Royal Society Open Science*, vol. 4, no. 1, 2017. [Online]. Available: https://doi.org/10.1098/rsos.160412

[88] S. Rawal, "Metal-Matrix Composites for Space Applications," *The Journal of The Minerals, Metals & Materials Society*, vol. 53, no. 4, pp. 14–17, 2001. [Online]. Available: https://doi.org/10.1007/s11837-001-0139-z

[89] H.-J. Dudek et al., "SiC-Fibre Reinforced Titanium Alloys: Processing, Interfaces and Mechanical Properties," in *Developments in the Science and Technology of Composite Materials: Fourth European Conference on Composite Materials*, Stuttgart, Germany, 25–28 September 1990, pp. 339–344, ISBN 978-94-009-0787-4. [Online]. Available: https://doi.org/10.1007/978-94-009-0787-4

[90] D.R. Pank and J.J. Jackson, "Metal-Matrix Composite Processing Technologies for Aircraft Engine Applications," *Journal of Materials Engineering and Performance*, vol. 2, no. 3, pp. 341–346, 1993. [Online]. Available: https://doi.org/10.1007/BF02648820

[91] R. Leucht and H.-J. Dudek, "Properties of SiC-fibre reinforced titanium alloys processed by fibre coating and hot isostatic pressing," *Materials Science and Engineering: A*, vol. 188, no. 1, pp. 201–210, 1994. [Online]. Available: https://doi.org/10.1016/0921-5093(94)90373-5

[92] S.A. Singerman and J.J. Jackson, "Titanium Metal Matrix Composites for Aerospace Applications," in *Superalloys*, R.D. Kissinger et al., Ed. The Minerals, Metals & Materials Society, 1996, pp. 579–586, ISBN 9780873393522.

[93] C. Leyens et al., "Continuous Fiber Reinforced Titanium Matrix Composites: Fabrication, Properties and Applications," *Advanced Engineering Materials*, vol. 5,

no. 6, pp. 399–410, 2003. [Online]. Available: https://doi.org/10.1002/adem.200310093

[94] D.B. Miracle, "Metal matrix composites – From science to technological significance," *Composites Science and Technology*, vol. 65, no. 15, pp. 2526–2540, 2005. [Online]. Available: https://doi.org/10.1016/j.compscitech.2005.05.027

[95] J.M. Berthelot, *Composite Materials - Mechanical Behavior and Structural Analysis*. Springer, 1998, ISBN 0-387-98426-7.

[96] S. Nemat-Nasser and M. Hori, *Micromechanics - Overall Properties of Heterogeneous Materials*. North-Holland, 1993, ISBN 978-0-444898814.

[97] J.L. Auriault, "Effective Macroscopic Description for Heat Conduction in Periodic Composites," *International Journal of Heat and Mass Transfer*, vol. 26, no. 6, pp. 861–869, 1983. [Online]. Available: https://doi.org/10.1016/S0017-9310(83)80110-0

[98] P.W. Chung et al., "Homogenization of Temperature-Dependent Thermal Conductivity in Composite Materials," *Journal of Thermophysics and Heat Transfer*, vol. 15, no. 1, pp. 10–17, 2001. [Online]. Available: https://doi.org/10.2514/2.6590

[99] M. Kamiński, "Homogenization technique for transient heat transfer in unidirectional composites," *Communications in Numerical Methods in Engineering*, vol. 19, no. 7, pp. 503–512, 2003. [Online]. Available: https://doi.org/10.1002/cnm.608

[100] Y.M. Shabana and N. Noda, "Numerical evaluation of the thermomechanical effective properties of a functionally graded material using the homogenization method," *International Journal of Solids and Structures*, vol. 45, no. 11, pp. 3494–3506, 2008. [Online]. Available: https://doi.org/10.1016/j.ijsolstr.2008.02.012

[101] A.H. Muliana and J.S. Kim, "A two-scale homogenization framework for nonlinear effective thermal conductivity of laminated composites," *Acta Mechanica*, vol. 212, no. 3, pp. 319–347, 2010. [Online]. Available: https://doi.org/10.1007/s00707-009-0264-2

[102] Y. Asakuma and T. Yamamoto, "Effective thermal conductivity of porous materials and composites as a function of fundamental structural parameters," *Computer Assisted Methods in Engineering and Science*, vol. 20, no. 2, pp. 89–98, 2013.

[103] C. Karch, "Micromechanical Analysis of Thermal Expansion Coefficients," *Modeling and Numerical Simulation of Material Science*, vol. 4, no. 3, pp. 104–118, 2014. [Online]. Available: https://doi.org/10.4236/mnsms.2014.43012

[104] W. Tian et al., "Mean-field homogenization based approach to evaluate macroscopic coefficients of thermal expansion of composite materials," *International Journal of Heat and Mass Transfer*, vol. 102, pp. 1321–1333, 2016. [Online]. Available: https://doi.org/10.1016/j.ijheatmasstransfer.2016.07.036

[105] S. Schindler et al., "Numerical homogenization of elastic and thermal material properties for metal matrix composites (MMC)," *Continuum Mechanics and Thermodynamics*, vol. 29, no. 1, pp. 51–75, 2017. [Online]. Available: https://doi.org/10.1007/s00161-016-0515-0

[106] R.M. German, *Particulate Composites - Fundamentals and Applications*. Springer, 2016, ISBN 978-3-319-29915-0. [Online]. Available: http://dx.doi.org/10.1007/978-3-319-29917-4

[107] T. Sadowski (Ed.), *Multiscale Modelling of Damage and Fracture Processes in Composite Materials*. Springer, 2005, ISBN 978-3-211-29558-8. [Online]. Available: https://doi.org/10.1007/3-211-38102-3

[108] M.N. Tamin (Ed.), *Damage and Fracture of Composite Materials and Structures*. Springer, 2012, ISBN 978-3-642-23658-7. [Online]. Available: https://doi.org/10.1007/978-3-642-23659-4

[109] L. Banks-Sills, *Interface Fracture and Delaminations in Composite Materials*. Springer, 2018, ISBN 978-3-319-60326-1. [Online]. Available: https://doi.org/10.1007/978-3-319-60327-8

[110] D.L. McDanels, "Tungsten Fiber Reinforced Copper Matrix Composites: A review, Technical Paper 2924," NASA, Tech. Rep., 1989.

[111] S.T. Peters (Ed.), *Handbook of Composites*, 2nd ed. Springer, 1998, ISBN 9781461563891. [Online]. Available: http://dx.doi.org/10.1007/978-1-4615-6389-1

[112] A. v. Müller et al., "Melt infiltrated tungsten-copper composites as advanced heat sink materials for plasma facing components of future nuclear fusion devices," *Fusion Engineering and Design*, vol. 124, pp. 455–459, 2017. [Online]. Available: https://doi.org/10.1016/j.fusengdes.2017.01.042

[113] R. Kieffer and W. Hotop, *Pulvermetallurgie und Sinterwerkstoffe*. Springer, 1948, ISBN 978-3-540-01339-6.

[114] R. Imm and G. Stempel, "Der Einfluß der Porosität auf einige Eigenschaften von Wolfram/Kupfer-Kontaktwerkstoffen," *Materialwissenschaft und Werkstofftechnik*, vol. 7, no. 10, pp. 376–380, 1976. [Online]. Available: https://doi.org/10.1002/mawe.19760071007

[115] W. Schatt, K.-P. Wieters and B. Kieback, *Pulvermetallurgie - Technologien und Werkstoffe*, 2nd ed. Springer, 2007, ISBN 978-3-540-23652-8. [Online]. Available: https://doi.org/10.1007/978-3-540-68112-0

[116] K. Rosan, *European Copper Materials - Comparison between DIN and EN*, 2nd ed. DIN Deutsches Institut für Normung e.V., Beuth, 2011, ISBN 978-3-410-17628-2.

[117] Deutsches Kupferinstitut, "Niedriglegierte Kupferwerkstoffe - Eigenschaften, Verarbeitung, Verwendung," 2012. [Online]. Available: https://www.kupferinstitut.de/fileadmin/user_upload/kupferinstitut.de/de/Documents/Shop/Verlag/Downloads/Werkstoffe/i008.pdf

[118] D. Kohtz, *Wärmebehandlung Metallischer Werkstoffe - Grundlagen und Verfahren*. Springer, 1994, ISBN 978-3-540-62165-2. [Online]. Available: https://doi.org/10.1007/978-3-642-46835-3

[119] A. Thompson et al., "X-Ray Data Booklet," Center for X-Ray Optics and Advanced Light Source, Lawrence Berkeley National Laboratory, University of California Berkeley, 2009.

[120] P. von Böckh and T. Wetzel, *Heat Transfer - Basics and Practice*. Springer, 2012, ISBN 978-3-642-19183-1. [Online]. Available: https://doi.org/10.1007/978-3-642-19183-1

[121] "ITER Structural Design Criteria for In-vessel Components, Appendix A, Materials Design Limit Data, G 74 MA 8 01-05-28 W 0.2," 2013.

[122] Deutsches Kupferinstitut, "Werkstoff-Datenblatt Cu-OFE - CW009A," 2005. [Online]. Available: https://www.kupferinstitut.de/fileadmin/user_upload/kupferinstitut.de/de/Documents/Shop/Verlag/Downloads/Werkstoffe/Datenblaetter/Kupfer/Cu-OFE.pdf

[123] E. Tejado et al., "The thermo-mechanical behaviour of W-Cu metal matrix composites for fusion heat sink applications: The influence of the Cu content," *Journal of Nuclear Materials*, vol. 498, pp. 468–475, 2018. [Online]. Available: https://doi.org/10.1016/j.jnucmat.2017.08.020

[124] E. Tejado et al., "Evolution of mechanical performance with temperature of W/Cu and W/CuCrZr composites for fusion heat sink applications," *Materials Science and Engineering: A*, vol. 712, pp. 738–746, 2018. [Online]. Available: https://doi.org/10.1016/j.msea.2017.12.054

[125] J.H. You et al., "Thermal and mechanical properties of infiltrated W/CuCrZr composite materials for functionally graded heat sink application," *Journal*

of Nuclear Materials, vol. 438, no. 1, pp. 1–6, 2013. [Online]. Available: https://doi.org/10.1016/j.jnucmat.2013.03.005

[126] V.R. Barabash et al., "Specification of CuCrZr alloy properties after various thermo-mechanical treatments and design allowables including neutron irradiation effects," *Journal of Nuclear Materials*, vol. 417, no. 1, pp. 904–907, 2011. [Online]. Available: https://doi.org/10.1016/j.jnucmat.2010.12.158

[127] D. Munz and Y.Y. Yang, "Stress Singularities at the Interface in Bonded Dissimilar Materials Under Mechanical and Thermal Loading," *Journal of Applied Mechanics*, vol. 59, pp. 857–861, 1992. [Online]. Available: https://doi.org/10.1115/1.2894053

[128] D. Munz and Y.Y. Yang, "Stresses near the free edge of the interface in ceramic-to-metal joints," *Journal of the European Ceramic Society*, vol. 13, no. 5, pp. 453–460, 1994. [Online]. Available: https://doi.org/10.1016/0955-2219(94)90024-8

[129] J.H. You and H. Bolt, "Analysis of singular interface stresses in dissimilar material joints for plasma facing components," *Journal of Nuclear Materials*, vol. 299, no. 1, pp. 1–8, 2001. [Online]. Available: https://doi.org/10.1016/S0022-3115(01)00680-8

[130] J. Schlosser et al., "Technologies for ITER divertor vertical target plasma facing components," *Nuclear Fusion*, vol. 45, no. 6, pp. 512–518, 2005. [Online]. Available: https://doi.org/10.1088/0029-5515/45/6/013

[131] C.B. Baxi and H. Falter, "Analytical prediction of thermal performance of hypervapotron and its application to ITER," in *Fusion Technology 1992 - Proceedings of the 17th Symposium on Fusion Technology*, C. Ferro et al., Ed., Rome, Italy, 14–18 September 1992, pp. 186–190, ISBN 0 444 89995 2.

[132] F. Escourbiac et al., "Experimental optimisation of a hypervapotron® concept for ITER plasma facing components," *Fusion Engineering and Design*, vol. 66-68, pp. 301–304, 2003. [Online]. Available: https://doi.org/10.1016/S0920-3796(03)00172-8

[133] M. Merola et al., "ITER plasma-facing components," *Fusion Engineering and Design*, vol. 85, no. 10, pp. 2312–2322, 2010. [Online]. Available: https://doi.org/10.1016/j.fusengdes.2010.09.013

[134] D. Rupp and S.M. Weygand, "Experimental investigation of the fracture toughness of polycrystalline tungsten in the brittle and semi-brittle regime," *Journal of Nuclear Materials*, vol. 386-388, pp. 591–593, 2009. [Online]. Available: https://doi.org/10.1016/j.jnucmat.2008.12.184

[135] D. Rupp and S.M. Weygand, "Anisotropic fracture behaviour and brittle-to-ductile transition of polycrystalline tungsten," *Philosophical Magazine*, vol. 90, no. 30, pp. 4055–4069, 2010. [Online]. Available: https://doi.org/10.1080/14786435.2010.504198

[136] D. Rupp et al., "Fracture toughness and microstructural characterization of polycrystalline rolled tungsten," *International Journal of Refractory Metals and Hard Materials*, vol. 28, no. 6, pp. 669–673, 2010. [Online]. Available: https://doi.org/10.1016/j.ijrmhm.2010.05.006

[137] T. Hirai et al., "Status of technology R&D for the ITER tungsten divertor monoblock," *Journal of Nuclear Materials*, vol. 463, pp. 1248–1251, 2015. [Online]. Available: https://doi.org/10.1016/j.jnucmat.2014.12.027

[138] J.M. Kazaroff and R.S. Jankovsky, "Cyclic Hot Firing of Tungsten-Wire-Reinforced, Copper-Lined Thrust Chambers, Technical Memorandum 4214," NASA, Tech. Rep., 1990.

[139] D.L. McDanels et al., "Stress-Strain Behavior of Tungsten-Fiber-Reinforced Copper Composites, Technical Note D-1881," NASA, Tech. Rep., 1963.

[140] D.L. McDanels, "Electrical resistivity and conductivity of tungsten-fiber-reinforced copper composites, NASA Technical Note D-3590," NASA, Tech. Rep., 1966.

[141] D.L. McDanels et al., "Analysis of Stress-Rupture and Creep Properties of Tungsten-Fiber-Reinforced Copper Composites, Technical Note D-4173," NASA, Tech. Rep., 1967.

[142] A. Kelly and W.R. Tyson, "Tensile properties of fibre-reinforced metals: copper/-tungsten and copper/molybdenum," *J. Mech. Phys. Solids*, vol. 13, pp. 329–350, 1965.

[143] A. Herrmann et al., "Interfacial optimization of tungsten fibre-reinforced copper for high-temperature heat sink material for fusion application," *Journal of Nuclear Materials*, vol. 386–388, pp. 453–456, 2009, fusion Reactor Materials. [Online]. Available: https://doi.org/10.1016/j.jnucmat.2008.12.138

[144] A. Herrmann, "Interface Optimization of Tungsten Fiber-Reinforced Copper for Heat Sink Application," Ph.D. dissertation, Technische Universität München, 2009.

[145] A. Herrmann et al., "Design and evaluation of an optimized W/Cu interlayer for W monoblock components," *Fusion Engineering and Design*, vol. 86, no. 1, pp. 27–32, 2011. [Online]. Available: https://doi.org/10.1016/j.fusengdes.2010.07.018

[146] Z. Hu et al., "Preparation and anisotropic compressive deformation behaviors of tungsten fiber reinforced Cu-Zn matrix composite," *Materials Science and Engineering: A*, vol. 708, pp. 43–49, 2017. [Online]. Available: https://doi.org/10.1016/j.msea.2017.09.110

[147] S.W.H. Yih and C.T. Wang, *Tungsten - Sources, Metallurgy, Properties, and Applications*. Plenum Press, 1979, ISBN 0-306-31144-5.

[148] J. Riesch et al., "Development of tungsten fibre-reinforced tungsten composites towards their use in DEMO — potassium doped tungsten wire," *Physica Scripta*, vol. 2016, no. T167, p. 014006, 2016. [Online]. Available: https://doi.org/10.1088/0031-8949/T167/1/014006

[149] J. Riesch et al., "Tensile behaviour of drawn tungsten wire used in tungsten fibre-reinforced tungsten composites," *Physica Scripta*, vol. 2017, no. T170, p. 014032, 2017. [Online]. Available: https://doi.org/10.1088/1402-4896/aa891d

[150] D. Terentyev et al., "Mechanical properties of as-fabricated and 2300 °C annealed tungsten wire tested up to 600 °C," *International Journal of Refractory Metals and Hard Materials*, vol. 66, pp. 127–134, 2017. [Online]. Available: https://doi.org/10.1016/j.ijrmhm.2017.03.011

[151] J. Riesch et al., "Properties of drawn W wire used as high performance fibre in tungsten fibre-reinforced tungsten composite," *IOP Conference Series: Materials Science and Engineering*, vol. 139, p. 012043, 2016. [Online]. Available: https://doi.org/10.1088/1757-899X/139/1/012043

[152] R. Neu et al., "Tungsten fibre-reinforced composites for advanced plasma facing components," *Nuclear Materials and Energy*, vol. 12, pp. 1308–1313, 2017. [Online]. Available: https://doi.org/10.1016/j.nme.2016.10.018

[153] D.W. Petrasek, "High-Temperature Strength of Refractory-Metal Wires and Consideration for Composite Applications, Technical Note D-6881," NASA, Tech. Rep., 1972.

[154] E.A. Winsa et al., "Predicted Inlet Gas Temperatures for Tungsten Fiber Reinforced Superalloy Turbine Blades, Technical Memorandum 73842," NASA, Tech. Rep., 1978.

[155] P. Melnyk and J.N. Fleck, "Tungsten Wire/FeCrAlY Matrix Turbine Blade Fabricaion Study, CR-159788," NASA, Tech. Rep., 1979.

[156] D.W. Petrasek et al., "Tungsten Fiber Reinforced FeCrAlY - A First Generation Composite Turbine Blade Material, Technical Memorandum 79094," NASA, Tech. Rep., 1979.

[157] D.W. Petrasek and R. Signorelli, "Tungsten Fiber Reinforced Superalloys - A Status Review, Technical Memorandum 82590," NASA, Tech. Rep., 1981.

[158] J.R. Lewis, "Design Overview of Fiber-Reinforced Superalloy Composites for the Space Shuttle Main Engine, CR-168185," NASA, Tech. Rep., 1983.

[159] D.W. Petrasek and J.R. Stephens, "Fiber Reinforced Superalloys for Rocket Engines, Technical Memorandum 100880," NASA, Tech. Rep., 1988.

[160] F.J. Ritzert and R.L. Dreshfield, "Progress Toward a Tungsten Alloy Wire/High Temperature Alloy Composite Turbine Blade, Technical Memorandum 105901," NASA, Tech. Rep., 1992.

[161] "DIN 60000: Textilien - Grundbegriffe," 1969, DK 677.1/.5: 001.4.

[162] T. Gries et al., *Textile Technology - An Introduction*, 2nd ed. Carl Hanser Verlag, 2015, ISBN 978-1-56990-565-4. [Online]. Available: https://doi.org/10.3139/9781569905661

[163] P. Potluri and S. Nawaz, "Developments in braided fabrics," in *Specialist Yarn and Fabric Structures*, R.H. Gong, Ed. Elsevier, 2011, ch. 14, pp. 333–353, ISBN 978-0-85709-393-6. [Online]. Available: https://doi.org/10.1533/9780857093936.333

[164] G.D. Roberts et al., "Design and Testing of Braided Composite Fan Case Materials and Components, Technical Memorandum 2009-215811," NASA, Tech. Rep., 2009.

[165] J.P. Carey, *Handbook of Advances in Braided Composite Materials*. Woodhead Publishing, 2017, ISBN 978-0-08-100369-5. [Online]. Available: https://doi.org/10.1016/C2014-0-03943-3

[166] C. Cherif (Ed.), *Textile Materials for Lightweight Constructions - Technologies, Methods, Materials, Properties*. Springer, 2016, ISBN 978-3-662-46341-3. [Online]. Available: https://doi.org/10.1007/978-3-662-46341-3

[167] H. Gietl et al., "Textile preforms for tungsten fibre-reinforced composites," *Journal of Composite Materials*, vol. 52, no. 28, pp. 3875–3884, 2018. [Online]. Available: https://doi.org/10.1177/0021998318771149

[168] Y. Han, "Mechanical Behavior of Doped Tungsten Wire: The Effects of Heat Treatment," Master's Thesis, Technische Universität München, 2014.

[169] A. v. Müller et al., "The effects of heat treatment at temperatures of 1100 °C to 1300 °C on the tensile properties of high-strength drawn tungsten fibres," *Nuclear Materials and Energy*, vol. 16, pp. 63–167, 2018. [Online]. Available: https://doi.org/10.1016/j.nme.2018.06.003

[170] M. Ilg, "Mechanical and Microstructural Characterisation of Potassium Doped Tungsten Fibers after Different Heat Treatments," Diplomarbeit, Technische Universität München, 2016.

[171] J. R. Stephens, "Effects of Interstitial Impurities on the Low-Temperature Tensile Properties of Tungsten, Technical Note D-2287, 1964," NASA, Tech. Rep., 1964.

[172] J. Coenen et al., "Improved pseudo-ductile behavior of powder metallurgical tungsten short fiber-reinforced tungsten (W_f/W)," *Nuclear Materials and Energy*, vol. 15, pp. 214–219, 2018. [Online]. Available: https://doi.org/10.1016/j.nme.2018.05.001

[173] A. H. Fritz and G. Schulze (Ed.), *Fertigungstechnik*, 10th ed. Springer, 2012, ISBN 978-3-642-29785-4. [Online]. Available: https://doi.org/10.1007/978-3-662-46555-4

[174] R.E. Berger, "Centrifugal casting of metal matrix composites," Ph.D. dissertation, University of California, Berkeley, United States, 1994.

[175] M. van Geldern, "Herstellung von hochschmelzenden Metallmatrix-Verbundwerkstoffen durch Schleudergießen," Ph.D. dissertation, Friedrich-Alexander-Universität Erlangen-Nürnberg, Germany, 2005.

[176] Y. Nishida and G. Ohira, "Modelling of infiltration of molten metal in fibrous preform by centrifugal force," *Acta Materialia*, vol. 47, no. 3, pp. 841–852, 1999. [Online]. Available: https://doi.org/10.1016/S1359-6454(98)00393-0

[177] M. Mutschler, "Design of a laboratory scale device for centrifugal infiltration of cylindrical tungsten fibre preforms with copper," Semesterarbeit, Technische Universität München, 2015.

[178] T. Mori and K. Tanaka, "Average stress in matrix and average elastic energy of materials with misfitting inclusions," *Acta Metallurgica*, vol. 21, no. 5, pp. 571–574, 1973. [Online]. Available: https://doi.org/10.1016/0001-6160(73)90064-3

[179] G. Kellie (Ed.), *Advances in Technical Nonwovens*. Woodhead Publishing, 2016, ISBN 978-0-08-100575-0.

[180] K. Kempen et al., "Process Optimization and Microstructural Analysis for Selective Laser Melting of AlSi10Mg," in *Solid Freeform Fabrication Proceedings*, 2011, pp. 484–495.

[181] J.P. Kruth et al., "Additive Manufacturing of Metals via Selective Laser Melting - Process Aspects and Material Developments," in *Additive manufacturing: Innovations, Advances, and Applications*, T.S. Srivatsan and T.S. Sudarshan, Ed. CRC Press, 2016, ch. 3, pp. 69–99, ISBN 978-1-4987-1478-5.

[182] K. Deprez et al., "Rapid additive manufacturing of MR compatible multipinhole collimators with selective laser melting of tungsten powder," *Medical physics*, vol. 40, no. 1, p. 012501, 2013. [Online]. Available: https://doi.org/10.1118/1.4769122

[183] A. Iveković et al., "Selective laser melting of tungsten and tungsten alloys," *International Journal of Refractory Metals and Hard Materials*, vol. 72, pp. 27–32, 2018. [Online]. Available: https://doi.org/10.1016/j.ijrmhm.2017.12.005

[184] T. Kurzynowski et al., "Selective Laser Melting of Pure Tungsten," in *Proceedings of the Fraunhofer Direct Digital Manufacturing Conference*, Berlin, Germany, March 2016.

[185] I. Smolina et al., "Properties of pure tungsten samples fabricated by SLM," in *Interdisciplinary nature of scientific research, Conference book*, J. Szreka, Ed., Wroclaw, Poland, March 2014, pp. 337–340, ISBN 978-83-7493-863-1.

[186] D. Wang et al., "Dense Pure Tungsten Fabricated by Selective Laser Melting," *Applied Sciences*, vol. 7, no. 4, p. 430, 2017. [Online]. Available: https://doi.org/10.3390/app7040430

[187] C. Tan et al., "Selective laser melting of high-performance pure tungsten: parameter design, densification behavior and mechanical properties," *Science and Technology of Advanced Materials*, vol. 19, no. 1, pp. 370–380, 2018. [Online]. Available: https://doi.org/10.1080/14686996.2018.1455154

[188] R. Enneti et al., "Direct Metal Laser Sintering/Selective Laser Melting of Tungsten Powders," *International Journal of Powder Metallurgy*, vol. 53, no. 4, pp. 23–31, 2017.

[189] A. v. Müller et al., "Microstructural investigations of tungsten manufactured by means of laser beam melting," in *Proceedings of the 6th International Conference on Additive Technologies*, Nürnberg, Germany, November 2016, pp. 61–66, ISBN 978-961-285-537-6.

[190] B. Vrancken et al., "Study of the influence of material properties on residual stress in selective laser melting," in *Proceedings of the Solid Freeform Fabrication Symposium*, Austin, Texas, USA, 2013, pp. 1–15.

[191] A. v. Müller et al., "Additive manufacturing of pure tungsten by means of selective laser beam melting with substrate preheating temperatures up to 1000 °C," *Nuclear Materials and Energy*, vol. 19, pp. 184–188, 2019. [Online]. Available: https://doi.org/10.1016/j.nme.2019.02.034

[192] B. Curzadd, "Topology optimization of tungsten/copper structures for plasma-facing component applications," Master's Thesis, Technische Universität München, 2018.

[193] B. Curzadd et al., "Topology optimization of tungsten/copper structures for plasma-facing component applications," *Nuclear Fusion*, 2019. [Online]. Available: https://doi.org/10.1088/1741-4326/ab1ff5

[194] K. Svanberg, "The method of moving asymptotes — a new method for structural optimization," *International Journal for Numerical Methods in Engineering*, vol. 24, no. 2, pp. 359–373, 1987. [Online]. Available: https://doi.org/10.1002/nme.1620240207

[195] C. Mattheck, *Design in Nature - Learning from Trees*. Springer, 1998, ISBN 978-3-540-62937-5. [Online]. Available: https://doi.org/10.1007/978-3-642-58747-4

[196] M.R. Gilbert et al., "Neutron-induced dpa, transmutations, gas production, and helium embrittlement of fusion materials," *Journal of Nuclear Materials*, vol. 442, no. 1, Supplement 1, pp. S755–S760, 2013. [Online]. Available: https://doi.org/10.1016/j.jnucmat.2013.03.085

[197] H. Greuner et al., "High heat flux facility GLADIS:: Operational characteristics and results of W7-X pre-series target tests," *Journal of Nuclear Materials*, vol. 367-370, pp. 1444 – 1448, 2007. [Online]. Available: https://doi.org/10.1016/j.jnucmat.2007.04.004

[198] Max-Planck-Institut für Plasmaphysik. [Online]. Available: https://www.ipp.mpg.de/3930218/gladis [accessed: 24-06-2019].